
# Fragment based drug discovery for SOD1-ALS and solution X-ray scattering studies on the copper chaperone for SOD1 (hCCS) and its functional complexes with SOD1

Thesis submitted in accordance with the requirements of the University of Liverpool for the degree of Doctor in Philosophy

by

Gareth Wright

November 2011

Amyotrophic lateral sclerosis (ALS) is a fatal disease of the nervous system. The majority of ALS cases are have no attributable genetic link, however approximately 10% are familial and 20 % of these result from mutations in the SOD1 gene. How SOD1 mutation manifests as the ALS phenotype is not clear however the enzyme does gain an aggregative property characterised by SOD1 inclusions in the brain and spinal cord. Drug treatment for sporadic and familial ALS is currently limited to palliatives and there is currently no specific treatment for SOD1 mediated ALS. In order to find molecules that may be of use in the development of SOD1 therapeutics a crystallographic screening pipeline was set up to assess binding of small molecules to both wild-type and SOD1 mutants.

Using *in silico* studies and previous crystallographic work as a starting point, this method revealed several low molecular weight compounds (Mr 183 – 310 $gMol^{-1}$) that have SOD1 binding activity. These molecules belong to three distinct classes: catecholamine, quinazoline and fluorouridine and occupy two distinct binding sites on the surface of the SOD1 β-barrel in an area known to be important in disease pathogenesis.

The incorporation of copper into biological macromolecules such as SOD1 is essential for the viability of most organisms. However, copper is toxic and therefore the intracellular free copper concentration is kept to an absolute minimum. The Copper Chaperone for SOD1 (CCS) is the major pathway for SOD1 copper loading and transfer of an intrasubunit disulphide bond known to stabilise SOD1.

Using small angle X-ray scattering combined with online size exclusion chromatography high quality data were acquired for both homodimeric hCCS and the functionally critical hCCS-SOD1 heterodimer. SAXS measurements were made of the hCCS complex with wild-type SOD1 and the disease relevant L38V and I113T SOD1 mutants. A rigid body modelling approach enabled exploration of the conformational dynamics of each species. Homodimeric hCCS is found to adopt positions that would facilitate initial copper acquisition and transfer from domain I to domain III. This domain III is also found in positions that would allow disulphide and copper transfer to SOD1 in the heterodimeric complex. The hCCS-I113T SOD1 complex has characteristics which are convergent with a view of ALS initiated by improperly matured SOD1.

# Table of contents

# Acknowledgements

Thank you to my supervisors Prof. Samar Hasnain and Dr Richard Strange for direction and encouragement.

Many thanks to Dr Guenter Grossmann for excellent help with the practicalities of SAXS, numerous paper redrafts and a lot of 5 am chocolate at the synchrotron.

Many of the novel SOD1 binding compounds described in the first half of this work were synthesised by Dr Neil Kershaw for which, along with many useful discussions, I am very grateful.

A big thank you to Mr Mark Prescott and Dr Mark Wilkinson for mass spectrometry on a heap of proteins.

Thank you to all members, past and present, of labs C & D in the University of Liverpool Biosciences building whose trade in consumables and expertise made a lot of this work possible.

Thank you to Clare, my mum and dad and all my family for tons of support over three years.

# List of Figures

# List of Tables

# Glossary of Abbreviations

| Abbreviation | Full name |
|---|---|
| ADMET | Absorption, distribution, metabolism, excretion and toxicity |
| ALS | Amyotrophic lateral sclerosis |
| CCS | Copper chaperone for SOD1 |
| $D_{max}$ | Maximum intra-particle dimension |
| DMF | Dimethylformamide |
| DMSO | Dimethyl sulfoxide |
| DTT | Dithiothreitol |
| ESI-MS | Electrospray ionisation mass spectroscopy |
| EXAFS | Extended X-ray absorption fine structure |
| fALS | Familial amyotrophic lateral sclerosis |
| FBDD | Fragment-based drug discovery |
| 5-FUrd | 5-Fluorouridine |
| ICP-MS | Inductively coupled plasma mass spectrometry |
| IPTN | Isoproteranol |
| ITC | Isothermal titration calorimetry |
| MDQ | 4-(4-methyl-1,4-diazepan-1-yl)quinazoline |
| MDTQ | 4-(4-methyl-1,4-diazepan-1-yl)-2-(trifluoromethyl)quinazoline |
| MPQ | 4-(4-methylpiperazin-1-yl)quinazoline |
| MPTQ | 4-(4-methylpiperazin-1-yl)-2-(trifluoromethyl)quinazoline |
| NMR | Nuclear magnetic resonance |
| PCR | Polymerase chain reaction |
| PDB | Protein data bank |
| Rg | Radius of gyration |
| sALS | Sporadic amyotrophic lateral sclerosis |
| SAXS | Small-angle X-ray scattering |
| SOD1 | Human Cu/Zn superoxide dismutase-1 |
| TDP-43 | Tar DNA binding protein-43 |

# Chapter I

## ALS, SOD1 and drug development

### 1.1 Amyotrophic Lateral Sclerosis

Amyotrophic lateral sclerosis (ALS) is an idiopathic neuropathy of humans characterised by death of the upper and lower motor neurons leading to muscle atrophy, paralysis and death [1]. ALS has an incidence of 3.0 and 2.4 per 100,000 person years for men and women respectively in Europe [2]. This is reflected in other population registries where information is available [3] and equates to approximately a 1 in 500 probability of an individual developing ALS over their life span. These figures can be compared with those pertaining to multiple sclerosis 4.2 per 100,000, Parkinson's disease 14 per 100,00 [4] and Alzheimer's disease 750 per 100,000 [5].

Symptoms that give rise to initial presentation are varied but can be divided roughly into bulbar onset and limb onset. Bulbar onset effects 42% [6] of patients and is characterised by dysarthria, dysphagia or sialorrhoea [7]. Limb onset ALS is seen in 58% [6] of cases and is associated with muscle weakness or atrophy, fasciculations and cramps [7]. A small minority of patients present initially with respiratory weakness not associated with bulbar or limb symptoms [8]. As the disease progresses fatigue and reduced activity become common [9]. Malnutrition and sialorrhoea, arising from an inability to swallow, together with reduced respiratory function and uncontrolled expression of emotion [10] are observed in the later stages. Death usually arises from respiratory failure often associated with pneumonia [11].

ALS is inexorably progressive with 70 - 80% of patients dying within 5 years of the onset of symptoms [6]. Although there is a slight preponderance of ALS in men rather than women its occurrence is largely unpredictable. Approximately 90% of ALS cases are sporadic and have no clearly attributable cause [12].

## 1.2 Familial Amyotrophic Lateral Sclerosis and associated proteins

The remaining 10% of ALS cases have a genetic link with one of several susceptibility loci that have varying degrees of genetic penetrance and resultant disease severity [13]. A small number of familial amyotrophic lateral sclerosis (fALS) cases have been observed to show an autosomal recessive inheritance pattern [14,15] but the majority are autosomal dominant [16-18].

While 13 ALS loci have been discovered only 6 have a substantive pathological connection with known proteins. Alsin is a GTPase regulator encoded by the ALS2 gene at position q33 on chomosome 2 and is responsible for an early onset, recessive form of ALS resulting from C-terminal truncation [14,19] . The SEXT gene at 9q34 encodes the senataxin protein, several mutations in which have been found to determine an early onset form of ALS with slow disease progression [16]. Mutations in the OPTN gene at locus 10p15 which encodes optineurin, previously implicated in open angle glaucoma, have been associated with an autosomal dominant ALS characterised by late onset [20]. Similarly, two point mutations in the VAPB locus at 20q13 have been discovered to be responsible for an autosomal dominant atypical form of ALS associated with adult onset spinal muscular atrophy [21,22].

TDP-43 (Tar DNA Binding Protein-43) and FUS (Fused In Sarcoma) are nucleic acid binding proteins coded for at loci at chromosomal locations 1p36 [23] and 16p11 [24] respectively. Both of these proteins were first identified through implications in other diseases. The FUS locus was found to undergo a translocation in liposarcoma tumours that created a chimeric protein together with the transcription regulator CHOP [24]. *Ou et al* discovered that TDP-43 binds to and represses transcription from the HIV long terminal repeat sequence TAR [25]. Autozygosity mapping subsequently uncovered a direct connection between mutation of these two protein and fALS [18,26]. Interestingly, TDP-43 had previously been observed to form a major component of intracellular inclusions found in the brain and spinal cord of patients with sporadic ALS and frontotemporal lobar degeneration [27]. Mutations in the TDP-43 sequence were also found in cases of sALS [18].

### 1.3 SOD1 genetics

Approximately 20% of familial ALS cases are associated with mutations in the superoxide dismutase-1 (SOD1) encoding gene found on chromosome 21 at location q22.1 [17]. Mutation in the SOD1 gene therefore accounts for 1 – 2% of all ALS cases which is the highest proportion of any of the known causative genetic elements.

To date there are 159 documented ALS causing SOD1 mutations [28]. An affected individual's life expectancy after initial onset of symptoms is defined, to a large extent, by the mutation [29,30]. These mutations are diverse in nature and include amino acid deletion [31] and insertion [32], deletion of base pairs in the 3' untranslated region [33], premature truncation [34] and amino acid substitution [17], the latter of which is by far the most common. These mutations are for the most part dominantly inherited [17] with individuals heterozygous for the pathogenic mutation. However, homozygous sufferers have been observed indicating a possible recessive inheritance pattern [35,36] which, surprisingly, in one case was associated with a juvenile onset and rapid disease progression [35].

### 1.4 Superoxide and SOD1 catalytic function

The existence of the superoxide radical ($O_2^-$) was first postulated by Linus Pauling in 1931 as an aside to his work on the quantum mechanics of the chemical bond [37]. It is produced *in vivo* as a result of the aberrant univalent reduction of dioxygen by leaky electron transport in mitochondrial oxidative phosphorylation [38]. Superoxide is easily converted into the highly toxic hydroxyl radical (•OH) and peroxynitrite ($ONOO^-$). Up to 2% of electrons passing through the electron transport chain are lost to the environment so reactive oxygen species, including superoxide, would quickly render the cell dysfunctional and lead to necrosis without a neutralisation strategy. The superoxide dismutase class of enzymes catalyse the dismutation of superoxide to dioxygen and hydrogen peroxide [39] and are employed to deal with this toxic threat.

Human SOD1 (EC 1.15.1.1) when fully mature contains one copper and one zinc ion per monomer [40]. The redox potential of copper in the SOD1 active site enables it to efficiently catalyse the dismutation of the superoxide radical to dioxygen and hydrogen peroxide by cycling back and forth between the Cu(I) and Cu(II) oxidation states according to the two

step reaction [39]:

$$O_2^- + Cu^{2+}ZnSOD \rightarrow O_2 + Cu^{1+}ZnSOD$$
$$O_2^- + Cu^{1+}ZnSOD + 2H^+ \rightarrow H_2O_2 + Cu^{2+}ZnSOD$$

This reaction is very efficient and proceeds at almost the diffusional limit with a rate constant of $10^9$ $M^{-1}$ $s^{-1}$ [41] as opposed to spontaneous dismutation which operates at $10^5$ $M^{-1}$ $s^{-1}$ [42].

SOD1 is a structurally conserved protein present in widely divergent species [43,44] and is constitutively expressed in almost all human cells [45] underscoring the biological importance of this enzyme. It is found predominantly in the cytosol [46] and mitochondrial intermembrane spaces of eukaryotic cells [47] but also in the nucleus, peroxisomes and lysosomes [48].

### 1.5 SOD1 structure

Human SOD1 is a 32 kDa homodimer composed of two non-covalently associated 153 amino acid subunits. The first structure of SOD1 was that of the bovine enzyme determined at 2.0 Å resolution in 1982 [49]. The wild-type human protein was described at 2.5 Å resolution in 1992 with a focus on designing thermally stable recombinant SOD1 proteins for therapeutic use combating free radical mediated disease [50]. This was followed in 2006 by a 1.07 Å atomic resolution structure of wild-type native human SOD1 [51].

These studies indicated each SOD1 monomer is composed of an eight strand anti-parallel Greek key β-barrel connected by seven loops of varying length (Figure 1.1). Loop IV (residues 49 - 83) is the largest and houses Asp83, His63, His71 and His80 which coordinate zinc in a tetrahedral conformation (Figure 1.2). This loop, termed the zinc loop, extends past the metal binding sites and contains a short 1½ turn α-helix (56 – 61) that is anchored to the β-barrel by an intrasubunit disulphide bond between Cys57 and Cys146. Loop VII (120 – 143), termed the electrostatic loop, also contains a 1½ turn α-helix and at its N-terminus His120 coordinates copper along with His46 and His48 of strand 4 of the β-barrel (Figure 1.2).

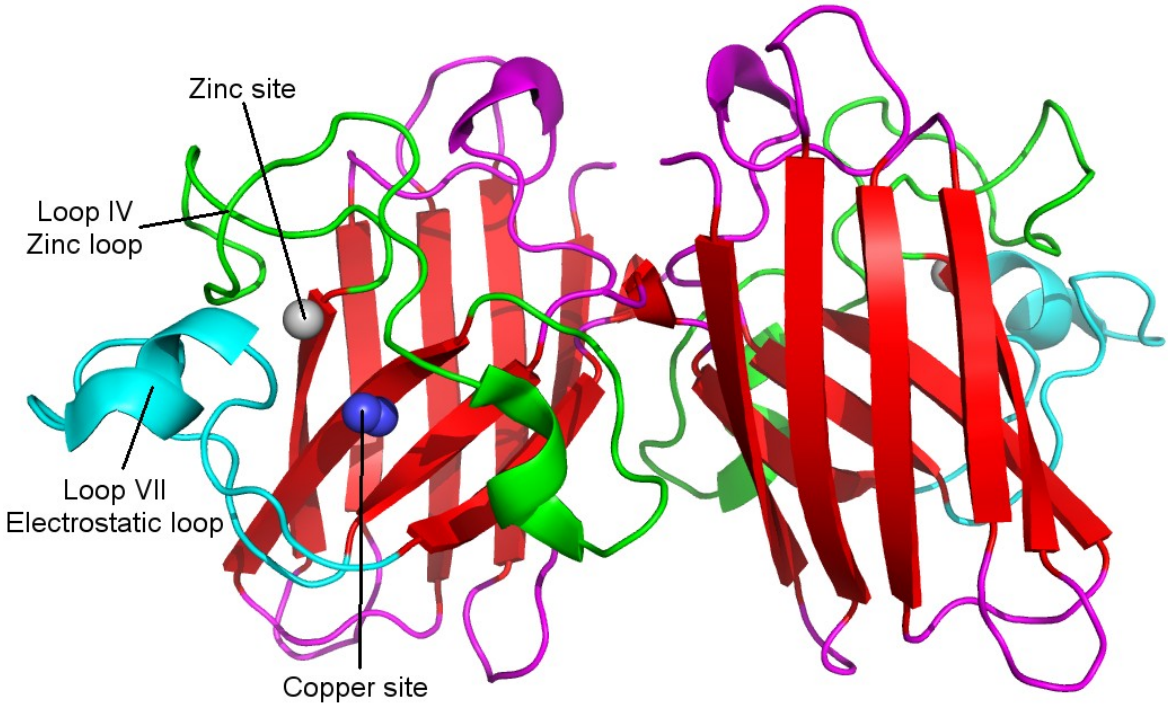


Figure 1.1. The structure of human SOD1. The SOD1 β-barrel is highlighted in red. Loops are highlighted purple except loop IV and VII, the zinc and the electrostatic loops which are highlighted green and cyan respectively. The copper and zinc sites are shown withblue and grey spheres respectively. PDB ID: 2C9V [51].

When the copper ion is oxidised His63 acts as a bidentate bridging ligand between the two metal ions and copper is coordinated in an irregular tetrahedral fashion. On reduction copper moves 1.0 Å away from His63 and is coordinated only by the imidazole group nitrogens of His46, His48, and His120 in a planar triangular conformation (Figure 1.2).

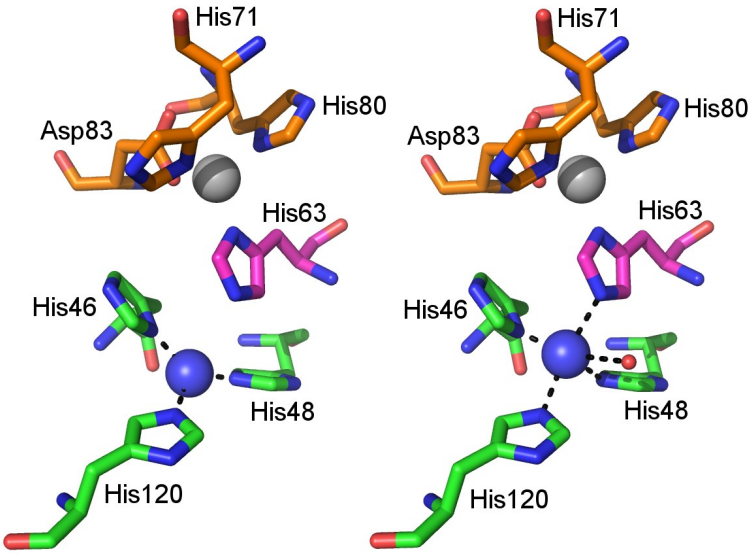


Figure 1.2. Detail of the SOD1 copper and zinc binding sites. Copper coordinating histidine residues are shown green with the bridging histidine purple. Zinc coordinating residues are shown in orange. The change in the position of the copper ion when in the reduced (left) and oxidised (right) forms can be observed. Co-ordination between copper and nitrogens is marked with a black dashed line as is co-ordination by a single water molecule in the Cu(II) state.

The N and C termini of the SOD1 polypeptide form short protrusions from the β-barrel and together with sections of loops IV and VI comprise the dimer interface. This region is stabilised largely by hydrophobic interactions between the dimer counterparts.

### 1.6 SOD1 fALS disease pathogenesis

fALS associated SOD1 mutations are located throughout the full length of the 153 amino acid SOD1 primary sequence including zinc [52,53] and copper [54,55] site substitutions (Figure 1.3).

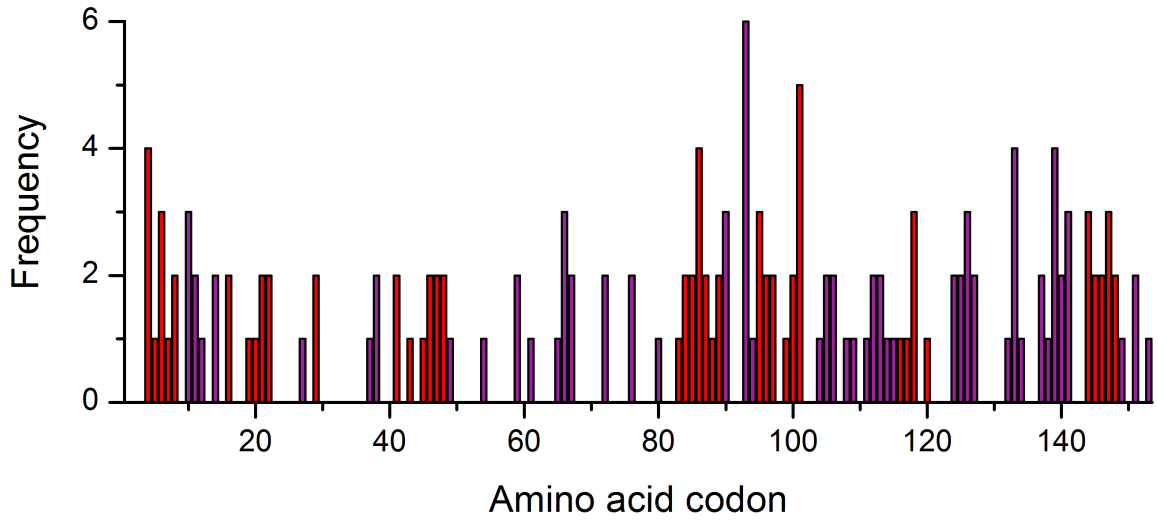


Figure 1.3. Distribution of fALS associated mutations throughout the SOD1 open reading frame. Mutations found in loop regions are coloured purple and mutations found in the β-barrel are coloured red. The height of each bar represents the number of novel SOD1 mutations found at that particular site.

Indeed, 81 codons (53%) have one or more documented fALS mutations. A close inspection of their position indicates a 20% increased probability that a residue will have one or more mutations inside the β-barrel than in a loop (0.46 and 0.66 respectively). However strand 3 of the β-barrel (amino acids 30 - 36) is suspiciously free of mutations and is the longest unmutated region. On the other hand there are obvious hotspots not only in the β-barrel but in loops VI and VII, the electrostatic loop.

While each mutation carries an increased probability of the individual following a particular disease course there is no discernible correlation between the biochemical and structural characteristics of mutant SOD1 and patient phenotype [30,56]. For example, mutant

SOD1 proteins have been observed to have dismutase activities varying from approaching nil up to 150% of the wild-type protein. This does not correlate with disease characteristics such as age of onset and life span after onset of symptoms [57-59]. Therefore, disruption of dismutase activity cannot be the root cause of SOD1 associated ALS. If human SOD1 does not have an unknown function, distinct from its dismutase activity, that is deleteriously affected by these mutations it must gain a characteristic that it does not posses in its wild-type form.

This notion is supported by a number of observations of transgenic mice. Those expressing fALS-associated human SOD1 mutants develop ALS-like symptoms in early adulthood [60,61] and these symptoms result irrespective of the presence, absence or expression level of wild-type SOD1 [61]. Those expressing or over-expressing only human wild-type protein display no ALS-like symptoms [62,63] as do those completely deficient in the enzyme [64].

Large SOD1 filled aggregates are observed in the spinal cord neurons of fALS effected individuals and fALS associated SOD1 mutant transgenic mice [65-68]. These aggregates interfere with axonal transport [69,70], cause aberrant apoptosis [71], damage the mitochondria [72] and sequester the proteasome [73]. The SOD1 toxic gain of function could be the ability to aggregate however the mechanism which facilitates this aggregation is not currently known or the reason it specifically effects motor neurons.

At first glance SOD1 aggregation appears counter-intuitive given that wild-type fully metallated SOD1 remains correctly folded at temperatures approaching boiling point [74]. However, introduction of fALS associated SOD1 mutations was found to decrease the thermal stability as determined by differential scanning calorimetry [74]. Similarly, partial metallation of wild-type and mutant SOD1 proteins was also found to decrease thermal stability [74] with loss of the zinc ion from wild-type SOD1 substantially promoting monomerisation [75] and self organisation into amyloid-like structures [76,77] and soluble aggregates [78,79].

Each SOD1 monomer contains one intramolecular disulphide bond between cysteines 57 and 146 [49]. This bond is transferred from CCS (Copper Chaperone for SOD1) [80] during the copper loading process [81] or by a CCS-independent pathway [82]. In fALS associated SOD1 mutant proteins this bond is susceptible to reduction by glutathione at near physiological

levels [83]. Disulphide reduction was observed to promote SOD1 monomerisation [83] particularly when the protein was partially zinc metallated [75]. SOD1 monomerisation has been shown to precede aggregation [84,85] and introduction of a inter-subunit disulphide bond or a chemical crosslink between adjacent Cys111 residues was observed stabilise the protein and prevent polymerisation *in vitro* [86,87].

Thus destabilisation of the SOD1 dimer resulting from demetallation, disulphide reduction or a combination of both, appears to be a central characteristic of fALS associated mutants. This is corroborated by structural and computational molecular dynamics data that indicate a change in the nature of the dimer interface [88,89], increased dimer instability [85] and a loss of structural integrity in the zinc binding and electrostatic loop regions [90] on reduction or metal removal.

### 1.7 Available SOD1 fALS therapeutics and review of clinical trials in progress

The relatively low incidence of ALS classifies it as an orphan disease and consequently it has attracted little attention in terms of therapeutics development from traditional drug development agencies. Currently, Riluzole is the only approved drug for the treatment of ALS. It is known to increase life expectancy for an ALS sufferer by two months on average [91]. There are currently no available drugs specifically targeted to fALS or SOD1 mediated fALS.

Clinical and pre-clinical trials of SOD1 mediated fALS therapeutics have met with almost complete failure, however some recent studies are worthy of note. Arimoclomol is currently undergoing phase II/III clinical trials [92]. It is a co-inducer of heat shock proteins that enables the clearing of SOD1 aggregates by over-expression of protein chaperones and has been observed to prolong life expectancy in fALS mouse models by 22% when used in pre and early symptomatic individuals [93,94]. However, when this drug was tested against late stage ALS mouse models, that exhibit a greater degree of similarity to human patients initially presenting with ALS, it did not have any life prolonging effect [95].

A second therapeutic approach currently in development silences gene expression and reduces the target protein concentration as old protein is degraded. This could practically be achieved by nucleic acid hybridisation [96] or chemical inhibition. SOD1 antisense

oligonucleotides able to bind nascent SOD1 mRNA, prevent translation and increase survival time in rat G93A models after direct infusion into the ventricular system have been documented [97]. Phase I clinical trials are ongoing for this therapy but while efficacious in animal models, this delivery method has obvious penalties for future patient comfort and care. Similarly, antisense expressing viral systems have successfully transduced the CNS although their ability to retard disease progression is disputed [98,99].

Pyrimethamine, is a common drug used for the treatment of protozoal infections such as malaria and toxoplasmosis. It is reported to reduce SOD1 levels in G93A SOD1 mouse [100]. In an initial 18 week, seven person clincial trial, this compound was observed to reduce blood lymphocyte SOD1 levels by 30 – 60% for non-A4V patients [100]. Conversely, pyrimethamine was not observed to reduce SOD1 expression in wild-type mice nor abrogate SOD1 synthesis in cell models [101] however this compound is currently undergoing phase I/II clinical trials.

The lack of efficacious fALS targeted therapeutics and the inherent problems associated with those strategies currently in the drug development pipeline provide a clear need for a drug discovery program targeted to SOD1.

# Chapter II

## Drug discovery and crystallographic theory

### 2.1 Fragment based rational drug design

A traditional approach to drug development takes a defined biological target and screens millions of drug-like compounds for interactions using a minaturisable assay [102]. While this methodology has been valuable in generating many of the therapeutics discovered in the 20th century it is inherently limited by the inverse relationship between molecular complexity and lead discovery [103], and the low success ratio of lead optimisation [104]. The large infrastructure investment needed for the successful completion of an initial screen, lead optimisation and arrival at a potential drug-like compound, even before clinical or toxicity trials begin, is prohibitive for all but the largest pharmaceutical companies. This effectively stalls drug development for diseases where there are low numbers of affected individuals or the end market is perceived to be too small to compensate for initial outlay [105].

An alternative approach screens low molecular weight compounds for relatively weak binding to the target [106], which may not have been identified by a *in vitro* assay, using a structure based technique such as NMR or X-ray crystallography [107]. These small molecules are then grown or linked to produce larger molecules that have strong site specific binding [108] characterised by increased ligand efficiency [109]. Throughout this process it is possible to engineer in Lipinsky 'Rule of 5' [110] compliance including hydrophilicity, low number of rotatable binds, low molecular weight (<500 Da), 5 or lower hydrogen bond donors or acceptors and other ADMET properties which will facilitate activity.

### 2.2 Crystallographic fragment-based drug discovery

The relative ease with which crystallisation and single crystal X-ray diffraction structure determination proceeds means crystallography is an ideal tool to feed information into the drug development pipeline throughout its course. Its use in initial ligand screening [107] enables the site of interaction to be determined unambiguously at the outset and directs

how chemical space should be probed during optimisation [111].

### 2.3 Crystallisation, compound soaking and data collection

A prerequisite for crystallographic protein structure determination is diffracting crystals. Crystallisation is the ordered precipitation of solute from a solution by nucleation followed by growth. Throughout this work SOD1 was crystallised by the hanging drop vapour diffusion method (Figure 2.1A). Protein solution at a sufficiently high concentration was mixed 1:1 with the a precipitant solution and suspended over a reservoir of the precipitant solution. Initially the concentration of precipitant, [ppt], is given by

$$[ppt_{reservoir}] = 2[ppt_{drop}]$$

As water evaporates from the drop and condenses in the reservoir solution, this becomes

$$[ppt_{reservoir}] = [ppt_{drop}]$$

with a concomitant doubling of the protein concentration in the drop. This concentration shift pushes the drop from the unsaturated phase to the supersaturated phase (Figure 2.1B). The degree of supersaturation is the key-point in crystallisation experiment and can be affected by temperature, pH, protein concentration and precipitant concentration. Very high supersaturation will promote disordered expulsion of protein from solution leading to amorphous precipation however if supersaturation cannot be achieved crystal nucleation will not take place. Nucleation is often a very slow process but its necessity can circumvented by addition of pre-existing seed crystals. The SOD1 crystals used in the following chapter were grown from seeds originally acquired from apo-H48Q SOD1 crystallisation and were transferred into the drop after equilibration.

Protein crystal production for a ligand screening program is complicated by a need to produce crystals which are resistant to the solvents commonly used in soaking experiments, such as dimethyl sulfoxide (DMSO) or dimethylformamide (DMF). The crystal must also have sufficiently large solvent pores to allow movement of the small molecules through the crystal lattice. These two attributes can be mutually exclusive with less dense crystal forms more liable to dissolve in organic solvents.

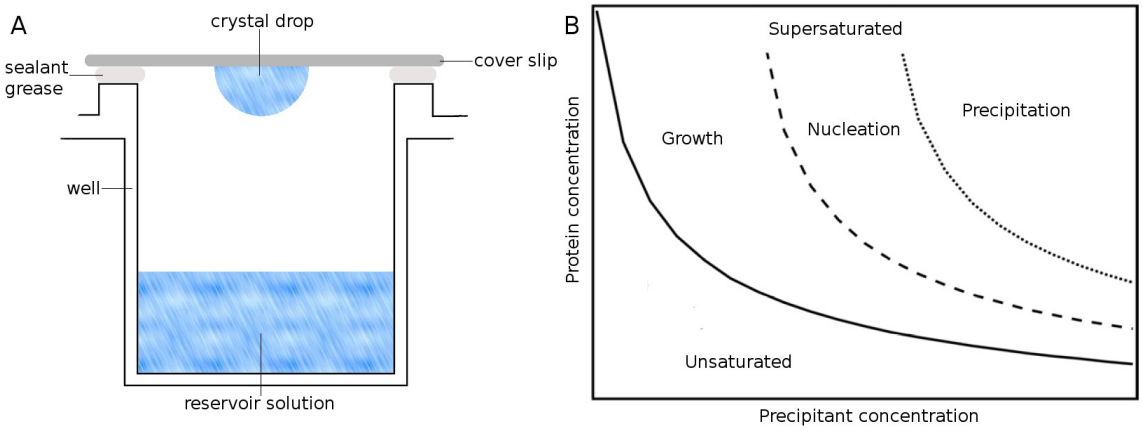


Figure 2.1 (A) Hanging drop vapour diffusion. (B) Phase diagram of protein crystallisation driven by precipitant concentration.

Crystallographic data collection often takes place with the crystal in a stream of nitrogen gas at 100 K. This reduces the effects of radiation damage and means a single crystal is sufficient to collect all the data necessary for structure determination. While this reduces the demand for protein and ligand it is essential that the ligand be included in any aqueous cryoprotectant solutions in order that bound ligand is not dispersed during cryoprotection.

The data presented in the following chapter were collected at two crystallographic beamlines: Proxima 1 at SOLEIL, Paris, France and IO3 at DIAMOND, Oxfordshire, England. Details of data collection and processing can be found in the Materials and Methods chapter.

## 2.4 Crystallographic theory

The minutiae of crystallographic theory are available in numerous canonical texts and it is not the purpose of this work to review available information however, what follows is a brief description of that which is necessary to understand the work presented in chapter III.

The distribution of electrons ($\rho$) at a point (x, y, z) within a unit cell (with volume $V$) of a crystal can be described as the Fourier sum of its structure factors ($F_{hkl}$).

$$\rho(x,y,z)=\frac{1}{V}\sum_{h}\sum_{k}\sum_{l}F_{hkl}\,e^{-2\pi i(hk+ky+lz)}$$

## 2.5 Data reduction, scaling & merging

The first stage in the process of creating a model of a biomolecule by X-ray diffraction crystallography is data reduction. That is, indexing of reflections to correct *h*, *k* and *l* values, unit cell parameter refinement and assessment of the intensity of reflections by background subtracted integration. The outcome of this process is a data set consisting of the Miller indices of each reflection (*hkl*), its intensity ($I_{hkl}$) and standard uncertainty ($\sigma I_{hkl}$). Throughout this work data reduction was performed with iMOSFLM [112] or HKL2000 [113].

The intensity of each reflection can be affected by the intensity of the incident beam and variability in the beam's path length through the crystal as it is moved into different orientations. It cannot be assumed therefore, that the intensities measured directly from the diffraction image are consistent across the whole data set. This problem is eliminated by observing reflections with known index across more than one frame and scaling the dataset so that identical reflections have identical intensity throughout. This task was performed here using the programs SCALA [114] or HKL2000.

## 2.6 Isomorphous phasing

As stated previously, the electron density within a crystal unit cell can be expressed as the equation in Section 2.4 where the structure factor amplitudes and phases are implicit in the term $F_{hkl}$. This equation can be reformulated as

$$\rho(x, y, z) = \frac{1}{V} \sum_{h} \sum_{k} \sum_{l} |F_{hkl}| e^{-2\pi i (hk + ky + lz - \alpha'_{hkl})}$$

which gives electron density at coordinate (*x*, *y*, *z*) of the real lattice as a function of measured structure factor amplitudes $|F_{hkl}|$ and phases ($\alpha'_{hkl}$). The structure factor amplitude is proportional to the square root of its intensity ($I_{hkl}^{1/2}$) which can be directly measured during data collection however the phase of a diffracted ray arriving at the detector during an experiment cannot be directly measured. This phase information must be calculated for each reflection in order to derive a model of electron density from a series of diffraction images.

The phase problem is a major hurdle when the structure of a new protein is being experimentally determined. It is solved most frequently by isomorphous replacement, anomalous diffraction or molecular replacement methods. However, a protein crystal soaked in a putative ligand is unlikely to deviate hugely from the structure of the native crystal. A crystallographic approach to fragment based drug discovery necessitates that the structure of the target protein has already been solved. If this is the case the structure of the ligand-protein complex can be solved using phase information taken from the native protein structure by isomorphous molecular replacement in conjunction with experimentally measured intensities from the complex.

In the following chapter the structure of SOD1 with eight ligands is presented. Each ligand is described bound to SOD1 in both the $P2_1$ and and $C222_1$ space groups. These structures were solved using previously existing SOD1 models with PDB codes 2VOA [90] and 1UXL [89] respectively. Four structures of L38V SOD1 were found to pack in the $P2_12_12_1$ space group. These structures were solved by isomorphous phasing using a pre-existing but unpublished model of $P2_12_12_1$ native L38V SOD1 which was itself solved by molecular replacement using the program MOLREP [115].

**2.7 Refinement**

Isomorphous phasing allows one to generate a rough electron density map of the protein-ligand complex under investigation. At this point structure factors can be calculated from the model taking into account the sum of diffractive contributions from individual atoms ($j$) with elemental scattering factor ($f_j$) at a particular position ($x_j$, $y_j$, $z_j$) in the unit cell.

$$F_{hkl} = \sum_{j=1} f_j \, e^{2\Pi i (hx_j + ky_j + lz_j)}$$

The model becomes more detailed as components are added to reflect experimentally observed electron density. As a result the phases computed from it also improve and thus the subsequent model computed from the original structure factor amplitudes and latest phase information also improves. In this cycle of model refinement and structure factor recalculations the model becomes increasingly a mirror of the real molecule with

calculated amplitudes $|F^c|$ approaching observed amplitudes $|F^o|$. The structures presented in the following chapter were constructed with successive rounds of manual model building in COOT [116] and refinement with REFMAC5 [117].

# Chapter III

## Crystallographic screening of small molecules for SOD1 binding

### 3.1 SOD1 screening pipeline

Using a crystallographic approach to compound screening and lead optimisation we hope to find compounds that bind to and consequently change the pathogenic characteristic of SOD1, with the aim of producing target specific therapeutics. In practice this involves co-crystallisation of SOD1 with a number of putative ligands and subsequent determination of the structure of the SOD1-ligand complex.

The screening of small molecules for SOD1 binding took place against the dimer interface mutant I113T. The II13T mutation was one of the first 11 SOD1 mutations implicated in ALS [17]. It is one of the most common SOD1 gene mutations and has been reported in nine countries. It is by far the most common mutation in the UK [118,119] and is associated with extreme phenotypic variation [120,121] and incomplete penetrance [122]. This mutant is known to be extremely prone to aggregation *in vitro* as a result of metal loss [78].

I113T SOD1 crystals in the $P2_1$ space group were grown from seed at pH 5. This crystal form is densely packed and can diffract up to atomic resolution [123,51], with 1.0 Å currently the highest documented resolution, and is resistant to low concentrations of dimethyl sulfoxide (DMSO). If binding was observed in the crystal structure with I113T the compound was soaked into wild-type, L38V [17] and H48Q [55] SOD1 crystals at pH 5. L38V is located in the loop connecting strands 3 and 6 of the SOD1 β-barrel and H48Q is a copper site mutant. In order to discount ligand binding through crystal lattice contacts the compound was also tested against I113T SOD1 crystals in the $C222_1$ space group grown at pH 8. This ligand soaking pipeline afforded a robust assessment of binding against a representative selection of SOD1 mutants at high resolution and at physiologically relevant conditions. As a result every ligand soaking experiment was repeated at least five times. A complete list of the compounds analysed for SOD1 binding is presented in Appendix IV.

### 3.2 Small molecule library screen

An initial screen for SOD1 binding compounds met with limited success. The screen used was the Rigaku Activesite Library of 384 diverse compounds. This selection of low molecular weight compounds is solubilised in 100% DMSO. The crystal soaking procedure must be carried out in a buffer solution that prevents crystals dissolving. In practice this means mixing the compound solution and the crystal soaking buffer prior to soaking. The majority of the compounds used in the screen were not soluble in less than 100% DMSO unless their concentration was below the low millimolar range. Consequently, the amount of compound available for binding to SOD1 during the soaking experiment was also low and therefore few hits were discovered [123].

### 3.3 4-(4-methyl-1,4-diazepan-1-yl)-2-(trifluoromethyl)quinazoline (MDTQ)

As part of their ongoing research into the pathogenesis and amelioration of SOD1 related fALS *Antonyuk et al* reported a diverse group of molecules which were found to bind SOD1 [123]. One of these compounds, 4-(4-methyl-1,4-diazepan-1-yl)-2-(trifluoromethyl)quinazoline hereafter called MDTQ, was found to occupy a binding site over the SOD1 Trp32. MDTQ is composed of a quinazoline ring system with an homopiperazine group connected at C4 and a trifluoromethyl at C2 (Figure 3.1). MDTQ has good solubility in aqueous buffers removing the necessity to use strong solvents such as DMSO.

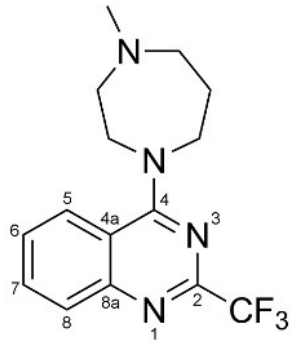


Figure 3.1. The structure of MDTQ (4-(4-methyl-1,4-diazepan-1-yl)-2-(trifluoromethyl) quinazoline). The quinazoline numbering system is shown, Mr 310.14 g $Mol^{-1}$.

In the structure presented by *Antonyuk et al* [123], the tri-fluromethyl group of MDTQ interacts with L38V SOD1 through two hydrogen bonds with Glu100. The quinazolene double ring system was also hydrogen bonded with Ser98. MDTQ bound L38V SOD1 with the long axis of its quinazoline ring system running parallel with the Trp32 indole group maximising any stacking interaction.

MDTQ was entered into the SOD1 screening pipeline in order to asses the methodology's efficacy, determine if MDTQ universally binds all SOD1 mutants and to characterise its pharmacophore properties. Table 3.1 shows the crystallographic statistics for five SOD1-MDTQ structures.

Figure 3.2A indicates the position of MDTQ binding between strands 3 and 6 on the surface of the I113T SOD1 Greek-key β-barrel. As previously reported the trifluoromethyl group protrudes into a cleft created by the side chains of Lys30, Glu100 and Ser98 (Figure 3.2B). This group has possible hydrogen bonding interactions with the side chain hydroxyl

of Ser98 and the backbone amide groups of Val31 and Ile99 (Figure 3.2D). Another hydrogen bond with the Glu100 carboxylic acid was postulated previously however in this structure the donor-acceptor distance is 4.6 Å. The Ser98 side chain also acts as a hydrogen bond donor to a MDTQ quinazoline ring nitrogen. These interactions are summarised in table 3.2.

| SOD1 variant | **I113T** | **I113T** | **wild-type** | **L38V** | **H48Q** |
|---|---|---|---|---|---|
| Resolution (Å) | 1.29 | 2.00 | 2.20 | 1.45 | 1.59 |
| Space group | $P2_1$ | $C222_1$ | $P2_1$ | $P2_12_12_1$ | $P2_1$ |
| pH | 5.0 | 8.0 | 5.0 | 5.0 | 5.0 |
| Unit cell parameters: | | | | | |
| a (Å) | 38.5 | 165.1 | 39.0 | 49.9 | 38.7 |
| b (Å) | 68.1 | 203.6 | 68.0 | 67.7 | 68.3 |
| c (Å) | 49.9 | 144.5 | 49.6 | 74.1 | 50.3 |
| α (°) | 90.0 | 90.0 | 90.0 | 90.0 | 90.0 |
| β (°) | 104.8 | 90.0 | 104.4 | 90.0 | 105.2 |
| γ (°) | 90.0 | 90.0 | 90.0 | 90.0 | 90.0 |
| Completeness (%) | 99.1 (95.6) | 98.7 (98.5) | 98.2 (92.0) | 99.9 (99.5) | 97.6 (91.5) |
| Redundancy | 4.1 (3.5) | 3.6 (3.5) | 3.3 (3.0) | 6.2 (5.6) | 3.6 (3.6) |
| R-merge (%) | 8.8 (65.5) | 10.2 (58.9) | 29.3 (45.1) | 9.8 (67.6) | 7.9 (24.3) |
| I/σ | 9.54 (2.2) | 9.51 (2.1) | 3.1 (1.9) | 9.8 (2.3) | 10.1 (3.6) |
| Rfact / Rfree (%) | 14.9 / 21.4 | 20.6 / 24.2 | 22.2 / 33.8 | 18.6 / 22.0 | 22.8 / 26.9 |
| RMS bond (Å) | 0.015 | 0.015 | 0.021 | 0.014 | 0.014 |

Table 3.1. Single crystal X-ray diffraction data collection, processing and model refinement statistics for MDTQ bound to human recombinant SOD1.

By virtue of its dimeric nature, SOD1 contains two Trp32 binding sites per molecule. In the structure presented in Figure 3.2, MDTQ adopts a different conformation at each site. Hydrogen bonding interactions are preserved in both conformations with the exception of the Ser98 hydrogen bond which switches acceptors between the nitrogens distal and proximal to the MDTQ homopiperazine group (Figure 3.2B and C respectively). In both cases, binding is likely to be strengthened though aromatic π-π interactions between the MDTQ quinazoline ring system and the indole moiety of Trp32. The homopiperazine ring extends into the solvent in each case. Figure 3.2B shows good electron density around this group indicating a possible stabilising hydrogen bond with the Glu21 side chain carboxylic acid group although the donor-acceptor distance is 4.6 Å (Figure 3.2D). The second conformation shows little electron density (Figure 3.2C) indicating this group is freely able to rotate around the N-C4 bond connecting it to the quinazoline rings.

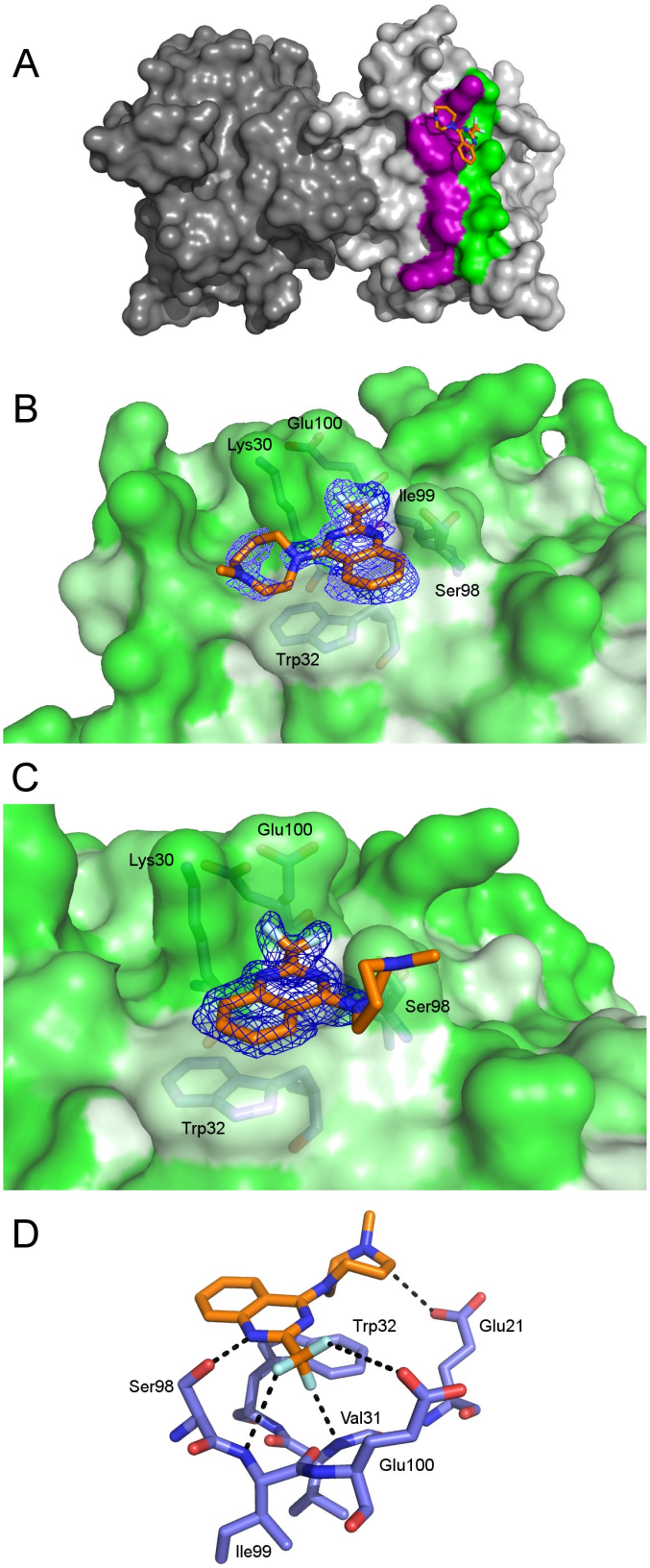


Figure 3.2. MDTQ bound to I113T SOD1. (A) MDTQ with respect to the SOD1 dimer in grey and light grey, strands 3 and 6 of the SOD1 β-barrel are coloured purple and green respectively. (B) $2F_o$-$F_c$ electron density map of MDTQ contoured at 1σ at the Trp32 binding site with the SOD1 surface coloured by amino acid hydrophobicity according Eisenberg's consensus hydrophobicity scale [124] and (C) the second conformation of MDTQ at the Trp32 of the opposing I113T SOD1 dimer. (D) Hydrogen bonding between I113T SOD1 and MDTQ shown with black dashed lines.

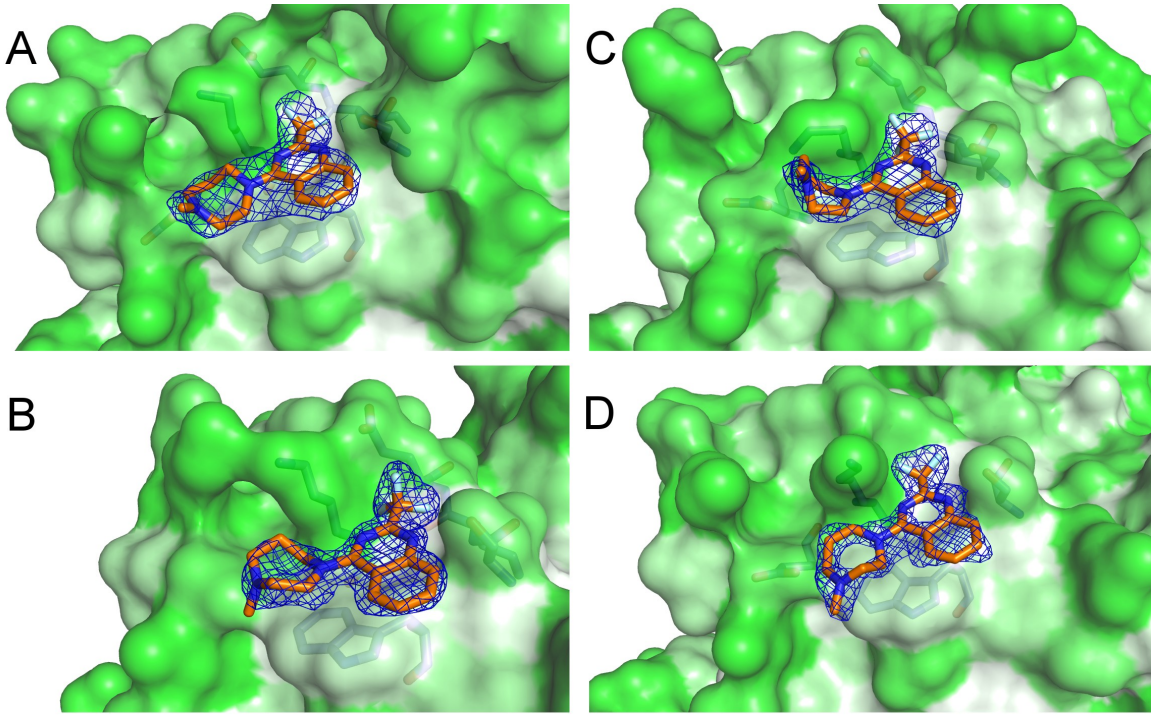


Figure 3.3. MDTQ bound to multiple SOD1 mutants. $2F_o$-$F_c$ electron density maps contoured at 1σ of MDTQ bound at the Trp32 site in (A) I113T SOD1 pH 8 $C222_1$ crystal structure (B) L38V SOD1 in the $P2_12_12_1$ form, (C) wild-type SOD1 and (D) H48Q SOD1 grown at pH 5 in the $P2_1$ form.

| Donor | I113T | wtSOD1 | L38V | H48Q | I113T pH8 | Acceptor |
|---|---|---|---|---|---|---|
| Ser98-OH | 2.7 Å | 3.0 Å | 2.7 Å | 2.9 Å | 2.8 Å | N-Quinazoline |
| Ser98-OH | 2.7 Å | 2.6 Å | 2.8 Å | 2.5 Å | 2.5 Å | F-Trifluoromethyl |
| Ile99-NH | 3.6 Å | 3.7 Å | 3.4 Å | 3.8 Å | 3.3 Å | F-Trifluoromethyl |
| Val31-NH | 3.2 Å | 3.5 Å | 4.1 Å | 3.3 Å | 3.2 Å | F-Trifluoromethyl |
| Glu100-COOH | 4.6 Å | 4.2 Å | 4.7 Å | 3.1 Å | 3.9 Å | F-Trifluoromethyl |

Table 3.2. Summary of potential hydrogen bonding in between MDTQ and SOD1. In the case of the I113T $P2_1$ structure values indicate the canonical orientation presented in Figure 3.2B.

Figure 3.3 describes the binding of MDTQ to three SOD1 variants. In each case the MDTQ molecule is found in the published orientation. Electron density for the ligand is good indicating that binding to SOD1 is not pH or SOD1 mutant dependent.

To probe the nature of MDTQ binding three derivatives with modified pharmacophore properties were synthesised. The following two sections describe the binding of two of these compounds, MPQ and MDQ, to recombinant SOD1.

### 3.4 4-(4-methylpiperazin-1-yl)quinazoline (MPQ)

The quinazoline based compound 4-(4-methylpiperazin-1-yl)quinazoline (MPQ) differs from MDTQ in that the trifluoromethyl group at C2 is not present and the homopiperazine at C4 is replaced with a methylpiperazine (Figure 3.4). Table 3.3 shows crystallographic statistics for various SOD1 proteins complexed with MPQ.

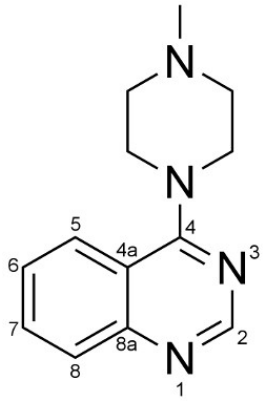


Figure 3.4. The structure of MPQ (4-(4-methylpiperazin-1-yl)quinazoline). The quinazoline numbering is system shown, Mr 228.14 g $Mol^{-1}$.

| SOD1 variant | **I113T** | **I113T** | **wild-type** | **L38V** | **H48Q** |
|---|---|---|---|---|---|
| Resolution (Å) | 1.24 | 1.93 | 1.35 | 1.33 | 1.53 |
| Space group | $P2_1$ | $C222_1$ | $P2_1$ | $P2_12_12_1$ | $P2_1$ |
| pH | 5.0 | 8.0 | 5.0 | 5.0 | 5.0 |
| Unit cell parameters: | | | | | |
| a (Å) | 38.7 | 166.3 | 38.8 | 50.1 | 38.6 |
| b (Å) | 68.1 | 203.8 | 68.5 | 67.8 | 68.1 |
| c (Å) | 50.0 | 144.5 | 50.0 | 74.4 | 49.6 |
| α (°) | 90.0 | 90.0 | 90.0 | 90.0 | 90.0 |
| β (°) | 104.7 | 90.0 | 104.5 | 90.0 | 104.5 |
| γ (°) | 90.0 | 90.0 | 90.0 | 90.0 | 90.0 |
| Completeness (%) | 99.9 (99.9) | 99.5 (95.5) | 94.1 (69.6) | 95.2 (77.3) | 95.2 (94.4) |
| Redundancy | 4.1 (3.4) | 3.7 (3.0) | 3.47 (2.6) | 6.08 (3.37) | 3.7 (3.8) |
| R-merge (%) | 8.2 (68.9) | 9.2 (52.0) | 5.4 (42.8) | 8.4 (59.8) | 7.2 (11.5) |
| I/σ | 14.4 (1.7) | 12.3 (2.0) | 13.3 (2.2) | 10.81 (1.73) | 12.2 (3.8) |
| Rfact / Rfree (%) | 13.9 / 17.5 | 17.2 / 20.4 | 13.6 / 18.1 | 17.3 / 23.3 | 19.4 / 23.2 |
| RMS bond (Å) | 0.014 | 0.015 | 0.013 | 0.013 | 0.014 |

Table 3.3. Single crystal X-ray diffraction data collection, processing and model refinement statistics for MPQ bound to SOD1.

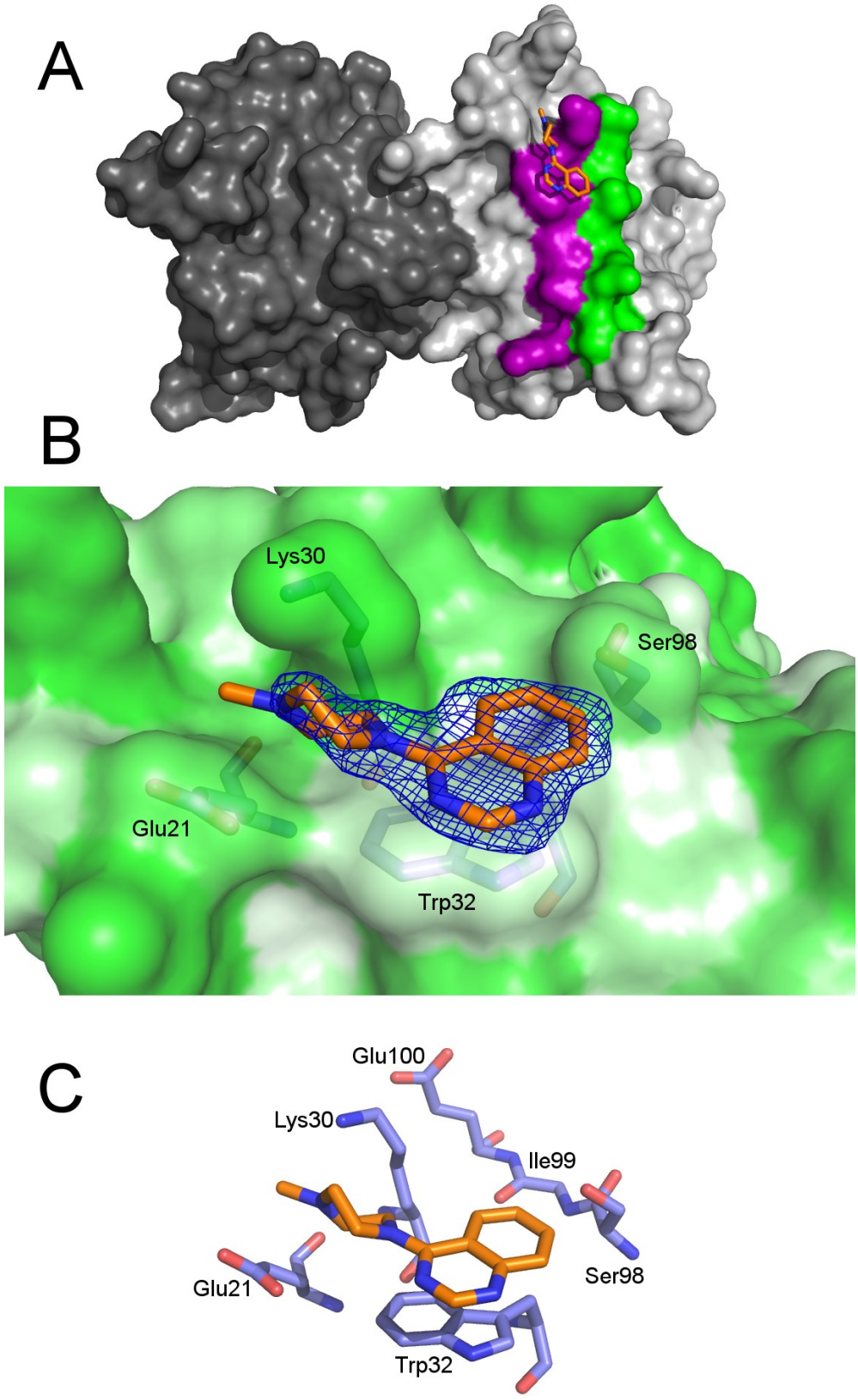


Figure 3.5. MPQ bound to I113T SOD1. (A) MPQ with respect to the SOD1 dimer in grey and light grey, strands 3 and 6 of the SOD1 β-barrel are coloured purple and green respectively. (B) $2F_o$-$F_c$ electron density map of MPQ contoured at 1σ at the Trp32 binding site with the SOD1 surface coloured by amino acid hydrophobicity and (C) Stick diagram of MPQ bound over the I113T SOD1 Trp32.

Figure 3.5A shows the mode of binding of MPQ to I113T on the surface of strand 3 of the SOD1 β-barrel. This compound occupies roughly the same space as MDTQ roughly 3.5 Å above the Trp32 indole. MPQ binding at this site differs however from that of MDTQ presented in the previous section in that the quinazoline nitrogen atoms are not involved in hydrogen bonding with SOD1 and face out from the β-barrel. The methylpiperazine is positioned between the side-chains of Glu21 and Lys30, 3.5 Å from each, with a possible hydrogen bond between the Glu21 carboxyl and methylpiperazine nitrogen (Figure 3.5C).

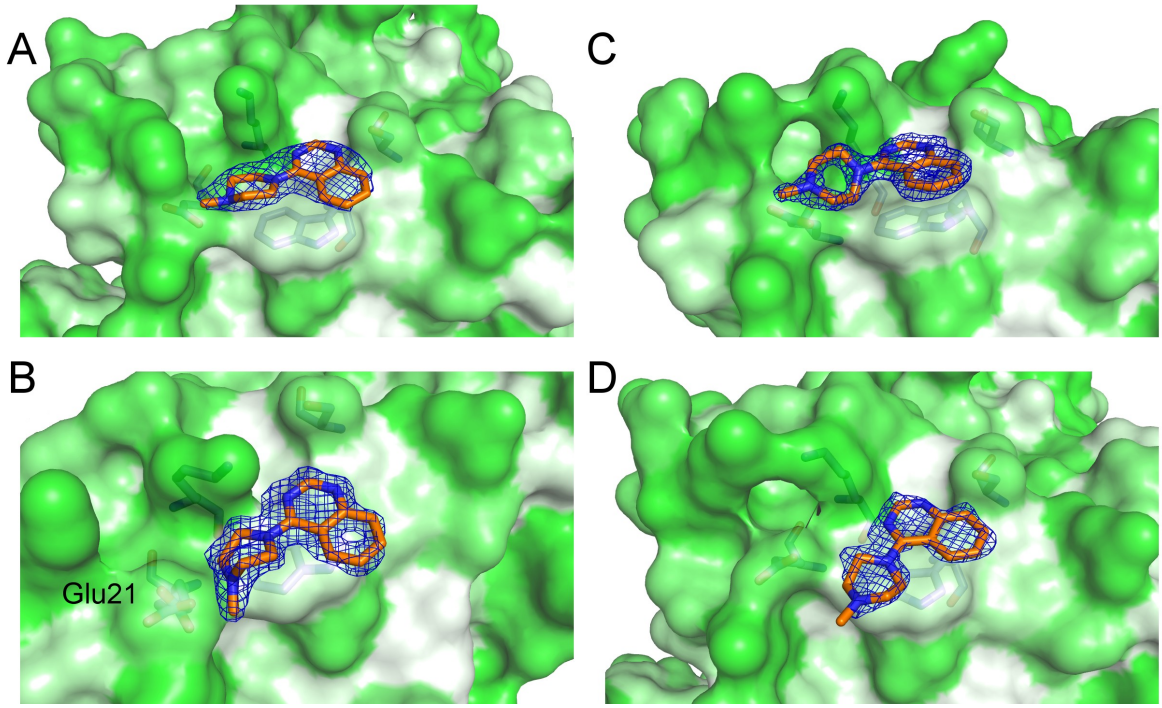


Figure 3.6. MPQ bound to multiple SOD1 mutants. $2F_o$-$F_c$ electron density maps contoured at 1σ of MPQ bound at the Trp32 site in (A) I113T SOD1 pH 8 $C222_1$ crystal structure (B) L38V SOD1 in the $P2_12_12_1$ form, (C) wild-type SOD1 and (D) H48Q SOD1 grown at pH 5 in the $P2_1$ form.

MPQ was analysed for binding against other SOD1 variants as per the screening pipeline described previously. In each instance, MPQ binds at the Trp32 site in the orthodox fashion with N1 of the quinazoline rings forming a hydrogen bond with Ser98 and a potential hydrogen bond between MPQ's methylpiperazine group and Glu21 (Figure 3.6). This hydrogen bond has length 2.9 - 3.4 Å and in the case of L38V SOD1 induces a change in the conformation of Glu21 drawing its side-chain carboxyl closer to the methylpiperazine nitrogen (Figure 3.6B).

### 3.5 4-(4-methyl-1,4-diazepan-1-yl)quinazoline (MDQ)

Figure 3.7 describes the structure of 4-(4-methyl-1,4-diazepan-1-yl)quinazoline (MDQ). This compound is very similar to MDTQ with an unmodified homopiperazine group at C4 but the trifluoromethyl at quinazoline ring position C2 is removed. Like the previous two compounds, MDQ has good solubility in aqueous buffers. This compound was entered in to the SOD1 screening pipeline (Table 3.4) and, as expected, was found to interact with SOD1 at the Trp32 site on the surface of strand 3 of the β-barrel (Figure 3.8A).

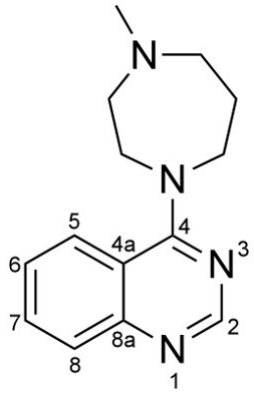


Figure 3.7. The structure of MDQ (4-(4-methyl-1,4-diazepan-1-yl)quinazoline). The quinazoline numbering system is shown, Mr 242.15 g $Mol^{-1}$.

Figure 3.8B shows the unbiased electron density of the MDQ quinazoline rings above and parallel to the Trp32 indole. In contrast to MPTQ and MPQ, there is no electron density associated with the homopiperazine group outside outside the N-C4 bond. This bond cannot move independently of the quinazoline system and allows us to positively determine the orientation of the MDQ molecule. There are no hydrogen bonds between this compound and SOD1 (Figure 3.8C) indicating that the only force keeping this molecule in place is a hydrophobic interaction between the aromatic Trp32 indole and the quinazoline ring moieties. Repeating this binding experiment against other SOD1 variants yields similar results (Figure 3.9B, C and D). At pH 8 however there is clear electron density around the homopiperazine group although there are no hydrogen bonding partners within a reasonable distance that could prevent this groups free rotation (Figure 3.9A).

| **Variant** | **I113T** | **I113T** | **wild-type** | **L38V** | **H48Q** |
|---|---|---|---|---|---|
| Resolution (Å) | 1.22 | 2.29 | 1.35 | 1.21 | 1.6 |
| Space group | $P2_1$ | $C222_1$ | $P2_1$ | $P2_12_12_1$ | $P2_1$ |
| pH | 5.0 | 8.0 | 5.0 | 5.0 | 5.0 |
| Unit cell parameters: | | | | | |
| a (Å) | 38.0 | 165.0 | 38.3 | 50.6 | 38.8 |
| b (Å) | 68.2 | 202.9 | 68.1 | 68.1 | 68.3 |
| c (Å) | 49.0 | 144.1 | 49.3 | 74.3 | 50.4 |
| α (°) | 90.0 | 90.0 | 90.0 | 90.0 | 90.0 |
| β (°) | 104.1 | 90.0 | 104.3 | 90.0 | 105.4 |
| γ (°) | 90.0 | 90.0 | 90.0 | 90.0 | 90.0 |
| Completeness (%) | 97.3 (87.2) | 99.4 (96.8) | 95.5 (76.8) | 98.1 (90.9) | 96.4 (95.3) |
| Redundancy | 3.5 (2.8) | 7.1 (6.5) | 3.4 (2.3) | 8.9 (4.9) | 3.6 (3.8) |
| R-merge (%) | 8.0 (52.2) | 14.9 (83.9) | 7.1 (35.6) | 9.5 (75.7) | 14.0 (48.4) |
| I/σ | 9.7 (1.9) | 11.52 (2.14) | 10.52 (2.14) | 12.82 (2.06) | 6.3 (2.3) |
| Rfact / Rfree (%) | 12.5 / 15.9 | 16.4 / 21.7 | 16.5 / 21.8 | 15.7 / 20.1 | 25. 6 / 30.1 |
| RMS bond (Å) | 0.014 | 0.015 | 0.014 | 0.012 | 0.016 |

Table 3.4. Single crystal X-ray diffraction data collection, processing and model refinement statistics for MDQ bound to SOD1.

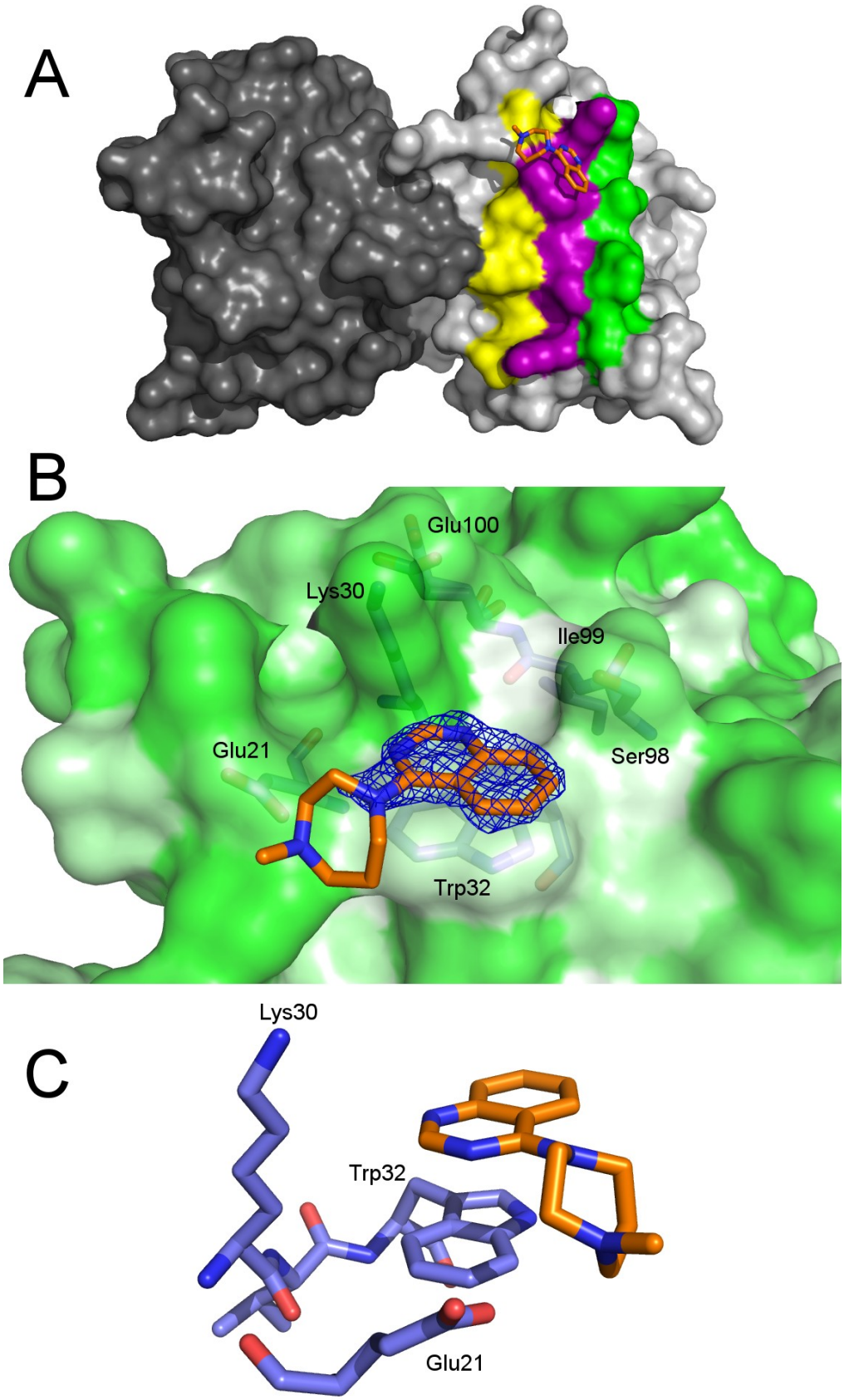


Figure 3.8. MDQ bound to I113T SOD1. (A) MDQ with respect to the SOD1 dimer in grey and light grey, strands 2, 3 and 6 of the SOD1 β-barrel are coloured yellow, purple and green respectively. (B) $2F_o$-$F_c$ electron density map of MDQ contoured at 1σ at the Trp32 binding site with the SOD1 surface coloured by amino acid hydrophobicity and (C) Stick model of I113T SOD1 with MDQ bound over Trp32.

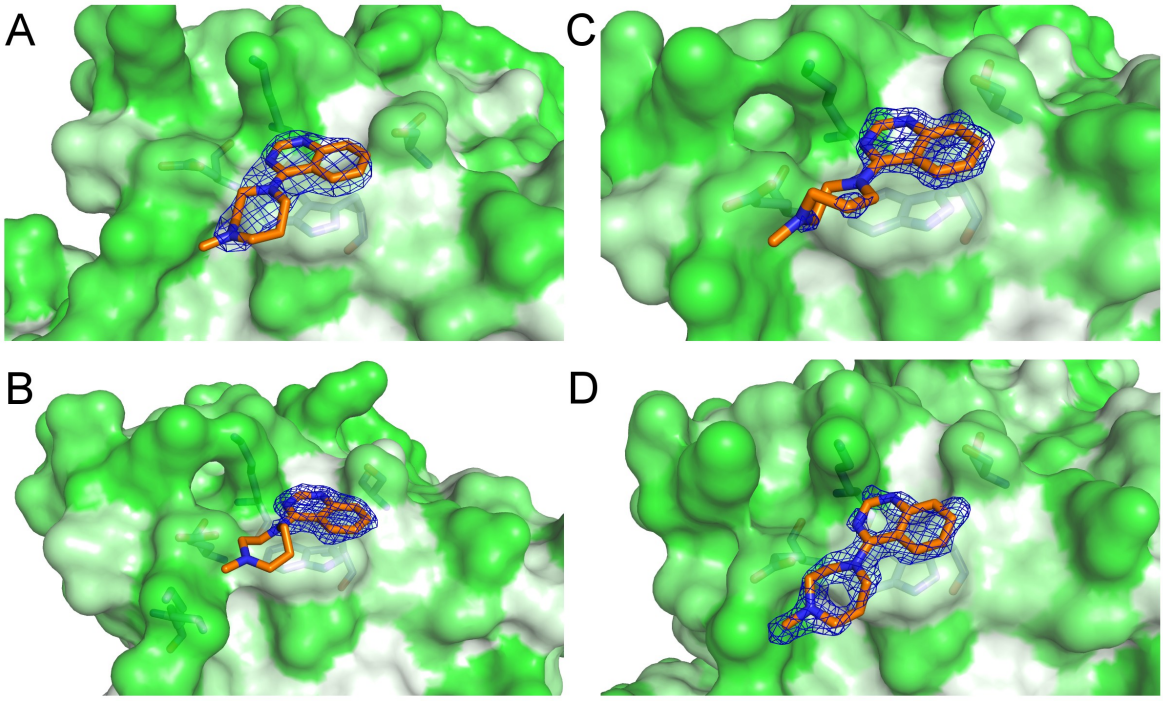


Figure 3.9. MDQ bound to multiple SOD1 mutants. $2F_o$-$F_c$ electron density maps contoured at 1σ of MDQ bound at the Trp32 site in (A) I113T SOD1 pH 8 $C222_1$ crystal structure (B) L38V SOD1 in the $P2_12_12_1$ form, (C) wild-type SOD1 and (D) H48Q SOD1 grown at pH 5 in the $P2_1$ form.

### 3.6 4-(4-methylpiperazin-1-yl)-2-(trifluoromethyl)quinazoline (MPTQ)

The compound presented in Figure 3.10, 4-(4-methylpiperazin-1-yl)-2-(trifluoromethyl)quinazoline (MPTQ) is another quinazoline derivative which differs from the original MDTQ compound published by *Antonyuk et al* [123] only by the omission of a carbon and two hydrogens from the homopiperazine moiety to form methylpiperazine (Figure 3.10). This change brings about a reduction in molecular mass from 310.14 to 296.12 $gMol^{-1}$ and an increase in ClogP of 2.75 to 2.77 for MDTQ and MPTQ respectively. MPTQ has a much lower solubility in water than MDTQ despite such small changes in physical characteristics. Consequentially, this compound could not be used at the 50 mM crystal soaking concentration which is standard in much published ligand soaking work and has been used thoughout this study. In practice the maximum concentration at which MPTQ could be used was 1 mM as there is a trade-off between crystallisation precipitant and solubilising agent concentrations that can be used in the soaking buffer, in this case ammonium sulphate and DMSO.

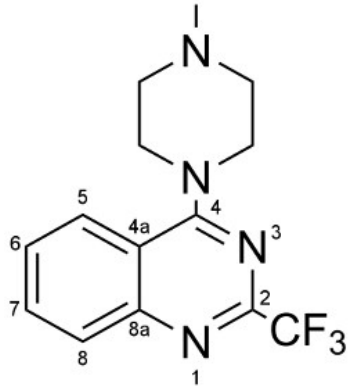


Figure 3.10. The structure of MPTQ (4-(4-methylpiperazin-1-yl)-2-(trifluoromethyl)quinazoline). The quinazoline numbering system is shown, Mr 296.12 $gMol^{-1}$.

The structure presented in Figure 3.11 and described in Table 3.5 is the result of one such experiment using low concentration MPTQ soaking in to I113T SOD1 at pH 5. While there is little density around both the quinazoline and methylpiperazine groups, the trifluoromethyl group can be seen in the Lys30-Ser98-Glu100 pocket. As with MDTQ, this compound should make hydrogen bonds with the backbone amide groups of Val31 and Ile99 together with the Glu100 carboxylic acid group. Low occupancy of MPTQ at the Trp32 site was replicated in L38V, H48Q and wild-type SOD1 crystal structures.

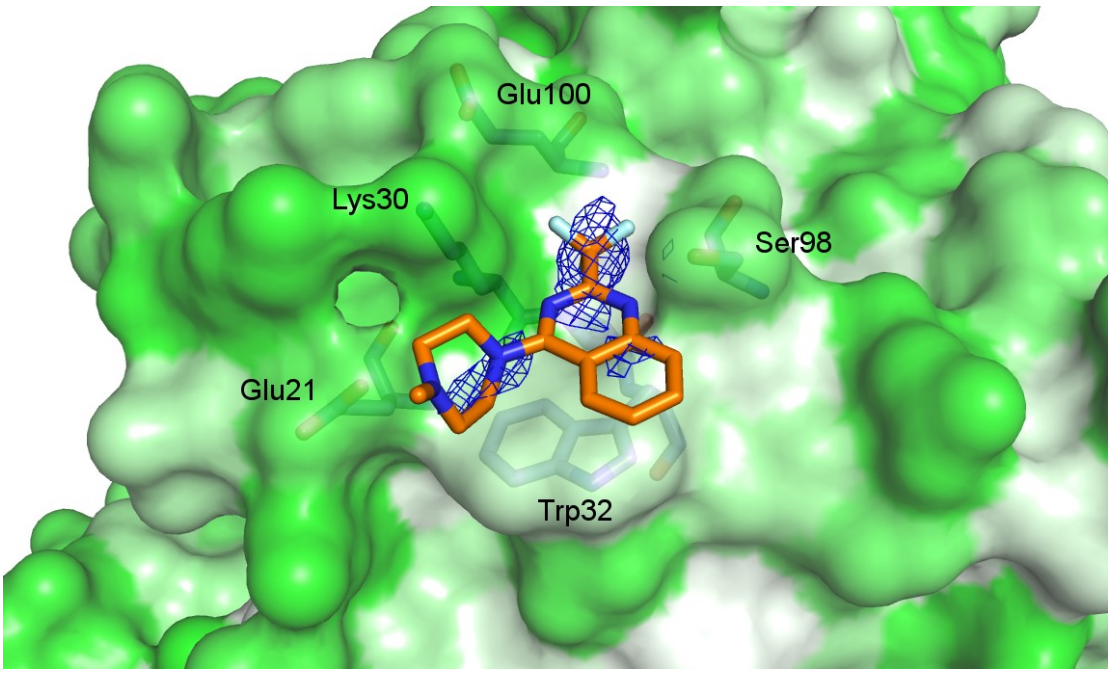


Figure 3.11. MPTQ bound to I113T SOD1. $2F_o$-$F_c$ electron density map contoured at 1σ of MPTQ with partial occupancy at the Trp32 site in the $P2_1$ crystal structure I113T SOD1 at pH 5.

| **Variant** | **I113T** |
|---|---|
| Resolution (Å) | 1.57 |
| Space group | $P2_1$ |
| pH | 5.0 |
| Unit cell parameters: | |
| a (Å) | 30.6 |
| b (Å) | 68.0 |
| c (Å) | 50.6 |
| α (°) | 90.0 |
| β (°) | 105.6 |
| γ (°) | 90.0 |
| Completeness (%) | 98.1 (90.6) |
| Redundancy | 3.6 (3.1) |
| R-merge (%) | 8.6 (62.9) |
| I/σ | 11.1 (2.1) |
| Rfact / Rfree (%) | 17.4 / 21.5 |
| RMS bond (Å) | 0.015 |

Table 3.5. Single crystal X-ray diffraction data collection, processing and model refinement statistics for MPTQ bound to SOD1.

### 3.7 Quinazoline Summary

The quinazoline ring system is a versatile scaffold used in many therapeutic applications including antibacterials [125], antimalarials [126], cancer treatments [127] and analgesics [128]. *Antonyuk et al* previously documented an interaction between SOD1 and the quinazoline derivative 4-(4-methyl-1,4-diazepan-1-yl)-2-(trifluoromethyl)quinazoline (MDTQ) [123]. Here we have observed this compound binding to wild-type and fALS associated SOD1 proteins in different crystal environments. To probe the nature of this interaction three similar compounds were synthesized, varying only by substitution at C2 and C4, and their binding to SOD1 was analysed. All three compounds occupy a similar binding site over Trp32 and, where compound solubility was not a problem, showed good electron density indicating a high level of occupancy. When the C2 trifuoromethyl group is removed these compounds are not locked in position by extensive hydrogen bonding the Ile99, Val31 and Glu100. All four compounds benefit strongly from a hydrophobic stacking interaction with the Trp32 indole. This maybe the only force keeping MPQ and MDQ in place, other than a possible hydrogen bond with the carboxyl side chain of Glu100. Substitution at C4 has little effect on binding and in many cases this group is able to rotate around the N-C4 covalent bond.

### 3.8 5-Fluorouridine

Fluorinated pyrimidine analogues, such as 5-fluorouracil, are widely used as anti-tumor therapeutics. 5-Fluorouracil is a member of the antimetabolite class of cancer treatments and exerts an effect by conversion to 5-fluorouridine which is in turn phosphorylated. The resulting compound forms a stable complex with thymidylate synthase inhibiting deoxythymidine monophosphate synthesis or is incorporated into nascent mRNA where it disrupts much of its normal function [129].

5-Fluorouridine is a nucleoside derivative composed of a single uracil ring substituted at C5 with fluorine and a ribose ring at N3 (Figure 3.12). While it is a more potent anti-tumor agent than 5-fluorouracil and the highly similar 5-fluoro-2'deoxyuridine it is not in clinical use due to strong associated side effects.

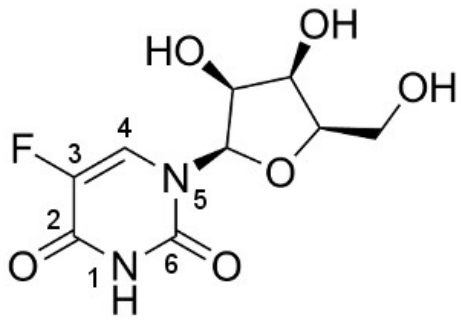


Figure 3.12. The structure of 5-fluorouridine. The pyrimidine numbering system is shown. Mr 262.02 $gMol^{-1}$.

*Nowak et al* highlighted 5-fluorouridine as a potent inhibitor of *in vitro* SOD1 aggregation [130]. This group used *in silico* methods to find compounds with a potential to bind at a hydrophobic pocket at the SOD1 dimer interface centred on Val7, Gly146 and Val147 from opposing monomers [131]. By occupying this site a perceived instability in the SOD1 mutant dimer that promotes monomerisation was abrogated and aggregation propensity was returned to a level equivalent to that seen in the wild-type protein. The uracil moiety was prevalent in this first group of compounds which were then further modified for greater specificity, activity and improved ADME properties [130]. 5-Fluorouridine was a member of this second cohort and was observed to reduce conversion of the A4V mutant SOD1 dimer to higher molecular weight aggregates to approximately 5 % over a 48 hour period compared with 50 % over 4 hours for A4V SOD1 solely.

5-Fluorouridine and other compounds from both studies described above [130,131] have great promise as SOD1 therapeutic leads but have never been directly visualised *in situ* at the Val7-Gly146-Val147 pocket. This compound was entered into the SOD1 screening pipeline not only to gain important structural information regarding its mode of binding with the aim of further optimisation but also to gain an improved understanding of SOD1 related fALS pathogenesis. Crystallographic data relating to this compound bound to several SOD1 variants are presented in Table 3.6.

| **Variant** | **I113T** | **I113T** | **wild-type** | **L38V** | **H48Q** |
|---|---|---|---|---|---|
| Resolution (Å) | 1.06 | 1.95 | 1.28 | 1.24 | 1.53 |
| Space group | $P2_1$ | $C222_1$ | $P2_1$ | $P2_12_12_1$ | $P2_1$ |
| pH | 5.0 | 8.0 | 5.0 | 5.0 | 5.0 |
| Unit cell parameters: | | | | | |
| a (Å) | 38.0 | 165.2 | 38.6 | 50.0 | 38.7 |
| b (Å) | 68.1 | 203.2 | 68.2 | 67.6 | 68.0 |
| c (Å) | 49.1 | 144.4 | 50.2 | 74.0 | 50.5 |
| α (°) | 90.0 | 90.0 | 90.0 | 90.0 | 90.0 |
| β (°) | 104.2 | 90.0 | 105.1 | 90.0 | 105.6 |
| γ (°) | 90.0 | 90.0 | 90.0 | 90.0 | 90.0 |
| Completeness (%) | 87.8 (68.2) | 99.9 (99.5) | 96.4 (74.5) | 91.0 (56.0) | 99.7 (99.7) |
| Redundancy | 2.4 (1.6) | 7.0 (6.5) | 3.5 (2.5) | 5.8 (2.4) | 3.6 (3.6) |
| R-merge (%) | 7.0 (41.7) | 11.9 (68.1) | 5.4 (47.5) | 7.4 (48.7) | 8.0 (26.2) |
| I/σ | 7.5 (1.5) | 12.0 (2.8) | 18.7 (1.9) | 12.8 (1.7) | 9.7 (4.1) |
| Rfact / Rfree (%) | 16.2 / 20.0 | 17.6 / 20.9 | 12.8 (17.8) | 15.0 / 19.0 | 20.7 / 24.4 |
| RMS bond (Å) | 0.015 | 0.014 | 0.014 | 0.014 | 0.015 |

Table 3.6 Single crystal X-ray diffraction data collection, processing and model refinement statistics for 5-fluorouridine bound to SOD1.

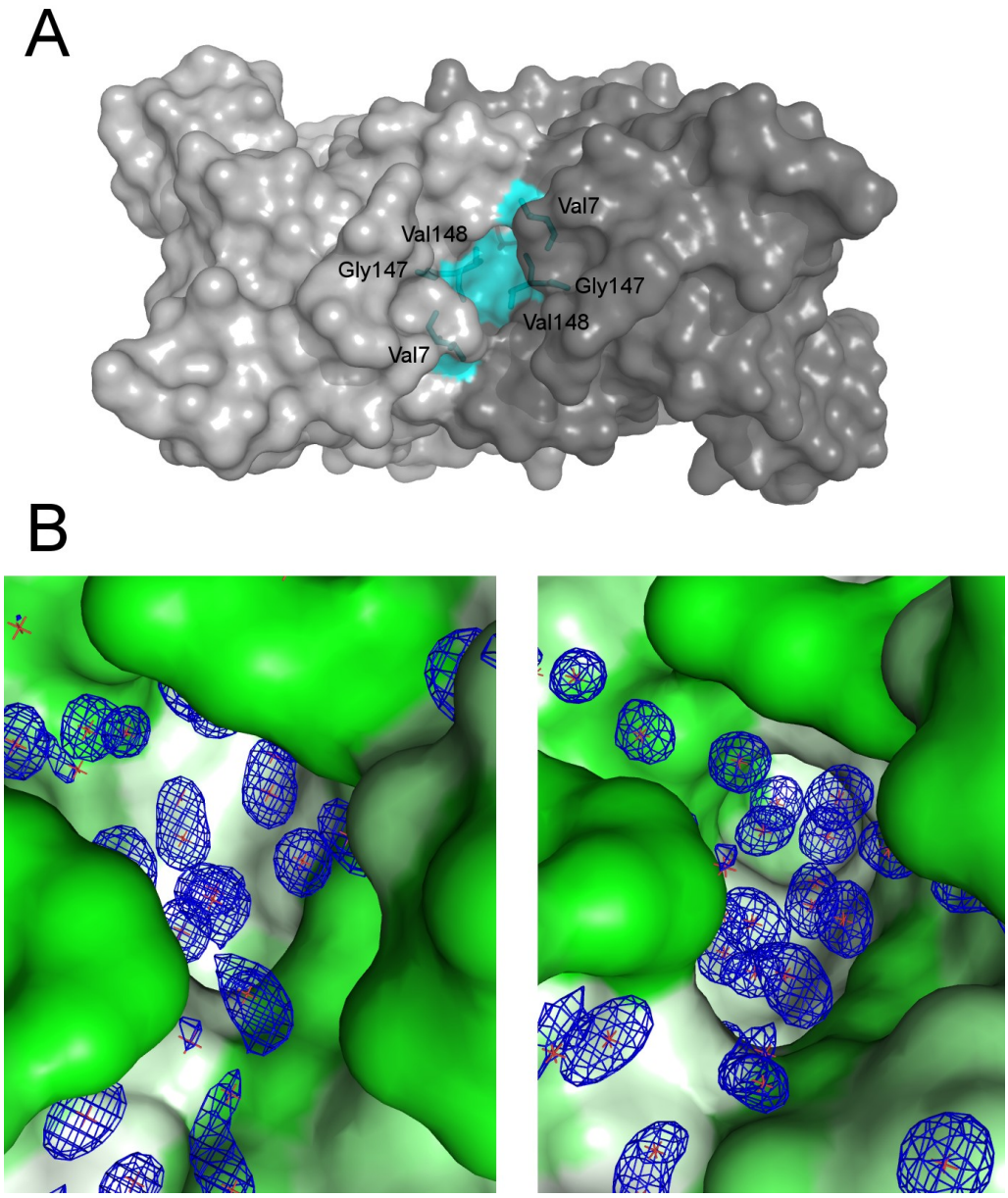


Figure 3.13. The I113T dimerisation region hydrophobic pocket after crystal soaking with 5-fluorouridine. (A) The position of the Val7-Gly146-Val147 pocket with residues highlighted cyan and (B) $2F_o$-$F_c$ electron density maps contoured at 1σ of solvent in this pocket in the I113T SOD1 crystal structure after soaking with 50 mM 5-fluorouridine for 2 hours. The pocket is shown from two angles with no sign of electron density corresponding to 5-fluorouridine.

Figure 3.13A shows the location of the Val7-Gly146-Val147 pocket at the SOD1 dimer interface. This pocket is again shown in Figure 3.13B with electron density from the solved crystal structure of I113T SOD1 soaked in 50 mM 5-fluorouridine for 2 hours. While there is an abundance of water molecules at this site there is no electron density which could represent 5-fluorouridine. Soaking this compound into different SOD1 variants at both pH 5 and 8 achieved the same negative result at this site.

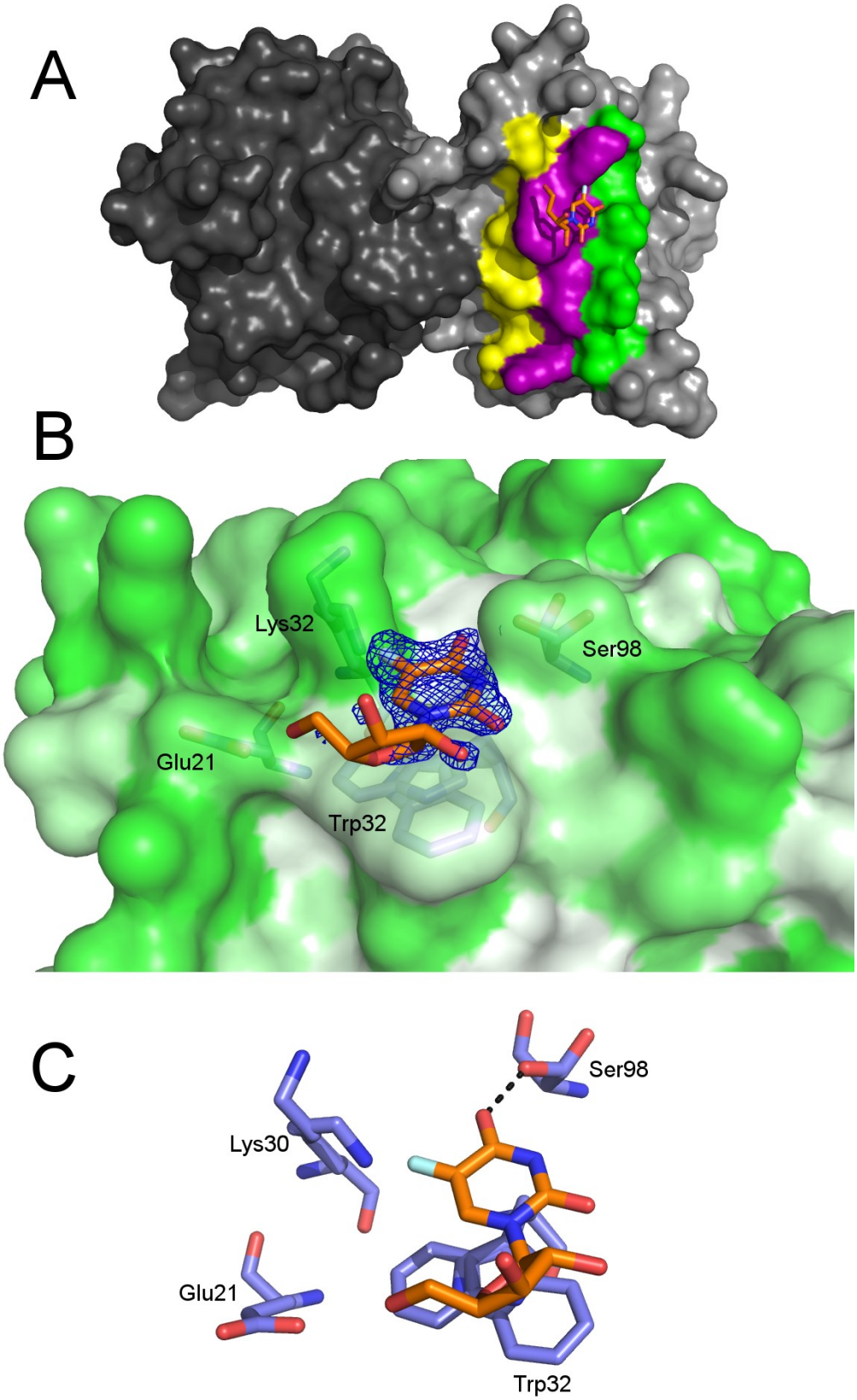


Figure 3.14. 5-Fluorouridine bound to I113T SOD1. (A) 5-Fluorouridine with respect to the SOD1 dimer in grey and light grey, strands 2, 3 and 6 of the SOD1 β-barrel are coloured yellow, purple and green respectively. (B) $2F_o$-$F_c$ electron density map of 5-fluorouridine contoured at 1σ at the Trp32 binding site with the SOD1 surface coloured by amino acid hydrophobicity and (C) Hydrogen bonding between I113T SOD1 and 5-fluorouridine shown with black dashed line.

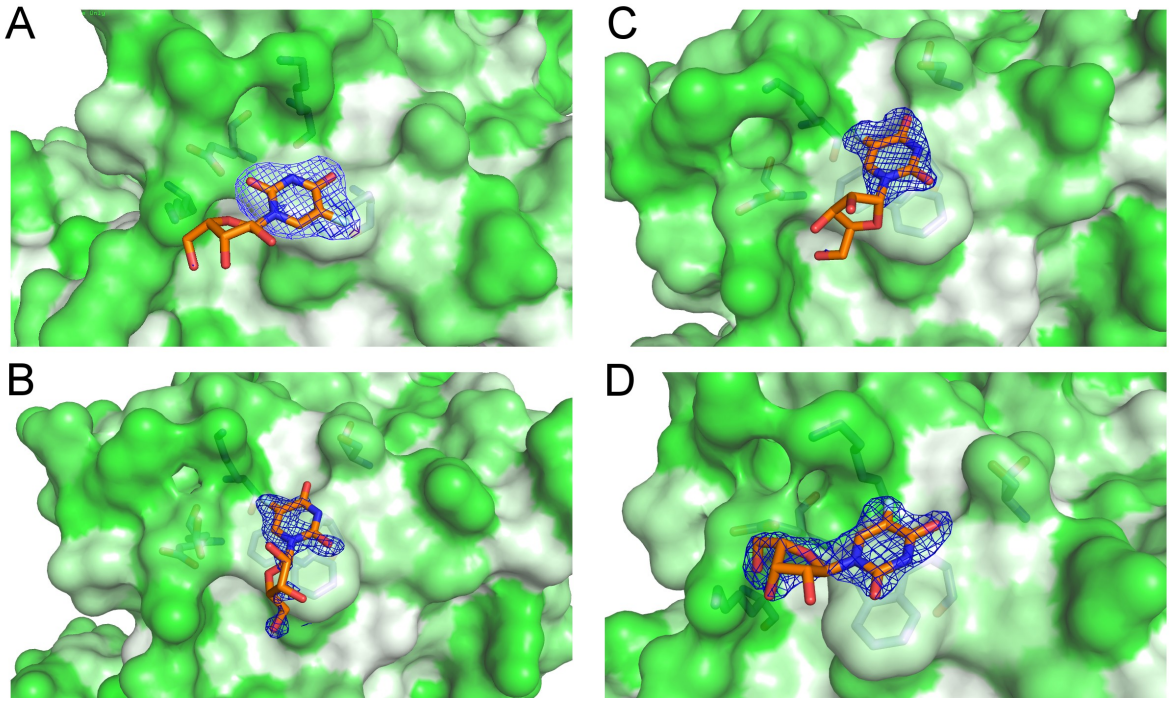


Figure 3.15. 5-Fluorouridine bound to multiple SOD1 mutants. $2F_o$-$F_c$ electron density maps contoured at 1σ of 5-fluorouridine bound at the Trp32 site in (A) I113T SOD1 pH 8 $C222_1$ crystal structure (B) L38V SOD1 in the $P2_12_12_1$ form, (C) wild-type SOD1 and (D) H48Q SOD1 grown at pH 5 in the $P2_1$ form.

During the course of structure refinement it became clear that 5-fluorouridine does bind SOD1 at the Trp32 site (Figure 3.14). This is not unsurprising given the ability of tryptophan to engage molecules in non-specific stacking interactions however 5-fluorouridine also potentially makes a hydrogen bond between the C2 carbonyl and the Ser98 side-chain (Table 3.7).

| **Donor** | **I113T** | **wtSOD1** | **L38V** | **H48Q** | **Acceptor** |
|---|---|---|---|---|---|
| Ser98-OH | 3.7 Å | 3.9 Å | 4.3 Å | 4.4 Å | O=C2-5-Fluorouridine |

Table 3.7 Summary of potential hydrogen bonding between 5-fluorouridine and SOD1 at the Trp32 site. A value is not shown for 5-fluorouridine bound in the $C222_1$ structure as the hydrogen bond distances are too large.

5-Fluorouridine's interaction with the I113T Trp32 site is mediated though the pyrimidine ring and its substituents. In the structure presented there is very little electron density that can be attributed to the ribose ring and there are no available bonding partners indicating it is freely able to rotate around N3-C bond.

Analysis of 5-fluorouridine bound at the Trp32 site in crystal structures of L38V, H48Q

and wild type SOD1 in the $P2_1$ crystal form grown at pH 5 indicates this binding is repeatable and consistent in form (Figure 3.15B, C and D). In each case there is good electron density associated with the pyrimidine group, which forms two hydrogen bonds with the SOD1 Lys30 and Ser98 side-chains. Conversely, 5-fluorouridine binding at pH 8 is of a slightly different character. In this case the uracil ring is rotated over Trp32 bringing the C6 carbonyl into hydrogen bonding distance (3.6 Å) with the Glu21 side-chain carboxyl. Again the ribose group shows little electron density when contoured at 1σ.

To summarise, 5-fluorouridine was predicted to bind to SOD1 at a pocket close to the dimerisation region. This compound was observed to effectively inhibit SOD1 mutant aggregation *in vitro* [130]. Here we are unable to find any evidence of that this compound binds at the predicted site. This is despite numerous crystal soaking experiments against several SOD1 variants. One can however observe some electron density attributable to 5-fluorouridine at the Trp32 binding site described by *Antonyuk et al* [123] and explored in detail in the previous sections.

### 3.9 Isoproteranol

Isoproteranol is a licensed sympathomimetic inotropic drug used in the treatment of several cardiac conditions and asthma [132] although in the latter case it has largely been superseded by newer therapeutics due to complications arising from dosing [133]. It is a synthetic catecholamine and isopropyl derivative of epinephrine (Figure 3.16) which acts on the β1 and β2 adrenergic receptor.

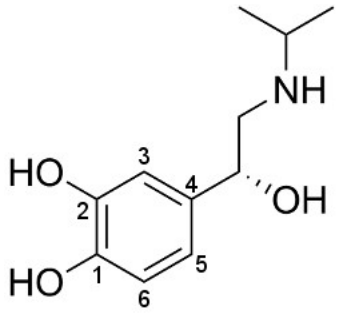


Figure 3.16. The structure of isoproteranol (also known as: Isoprenaline, Isuprel and Medihaler-iso). 211.3 $gMol^{-1}$.

Isoproteranol was also proposed as a SOD1 binding compound targeted to the Val7-Gly146-Val147 pocket [130]. This is particularly interesting in light of recent findings implicating isoproteranol in effective down regulation of SOD1 mRNAs in Wistar rat myocardium tissue following 7 days of repeated dosing [134]. While this effect has not been researched in man and may result from a number possible non-specific processes this compound is clearly worth investigation in regard to its potential interaction with SOD1. Isoproteranol was soaked into crystals of SOD1 and the bound structures were analysed for ligand binding (Table 3.8).

Figure 3.17 shows the Val7-Gly146-Val147 pocket of I113T SOD1 after crystal soaking with isoproteranol. The result is much the same as that described in the previous section dealing with 5-fluorouridine, while electron density associated with ordered water molecules is clearly visible there is nothing which represents the ligand.

Isoproteranol can however be found at four other unique sites in this structure. Three of these are in regions where the ligand makes contacts with more than one SOD1 dimer and can be discounted as artefacts of crystal packing. Figure 3.17 describes the remaining site in a groove created by the short loop II connecting strands 2 and 3 of SOD1 β-barrel.

Binding is repeatable, not SOD1 mutant specific and pH independent (Figure 3.18 and 3.19).

| **Variant** | **I113T** | **I113T** | **wild-type** | **L38V** | **H48Q** |
|---|---|---|---|---|---|
| Resolution (Å) | 1.45 | 2.2 | 1.34 | 1.53 | 1.53 |
| Space group | $P2_1$ | $C222_1$ | $P2_1$ | $P2_1$ | $P2_1$ |
| pH | 5.0 | 8.0 | 5.0 | 5.0 | 5.0 |
| Unit cell parameters: | | | | | |
| a (Å) | 37.9 | 165.1 | 38.3 | 38.0 | 38.2 |
| b (Å) | 68.0 | 203.5 | 68.0 | 67.8 | 67.9 |
| c (Å) | 49.3 | 144.6 | 50.5 | 49.9 | 49.7 |
| α (°) | 90.0 | 90.0 | 90.0 | 90.0 | 90.0 |
| β (°) | 104.0 | 90.0 | 105.3 | 104.6 | 104.4 |
| γ (°) | 90.0 | 90.0 | 90.0 | 90.0 | 90.0 |
| Completeness (%) | 98.0 (94.2) | 99.7 (98.6) | 98.7 (87.3) | 99.7 (99.7) | 99.7 (99.7) |
| Redundancy | 3.6 (3.4) | 7.4 (7.3) | 3.79 (3.27) | 3.5 (3.6) | 3.5 (3.6) |
| R-merge (%) | 5.3 (26.0) | 14.9 (91.2) | 6.8 (42.1) | 11.1 (31.3) | 7.1 (16.0) |
| I/σ | 15.2 (4.3) | 13.32 (2.82) | 10.99 (2.60) | 6.9 (3.1) | 11.8 (6.1) |
| Rfact / Rfree (%) | 15.7 / 18.8 | 19.5 / 23.1 | 18.1 / 19.7 | 24.3 / 30.0 | 20.0 / 22.8 |
| RMS bond (Å) | 0.016 | 0.014 | 0.015 | 0.015 | 0.015 |

Table 3.8. Single crystal X-ray diffraction data collection, processing and model refinement statistics for isoproteranol bound to SOD1.

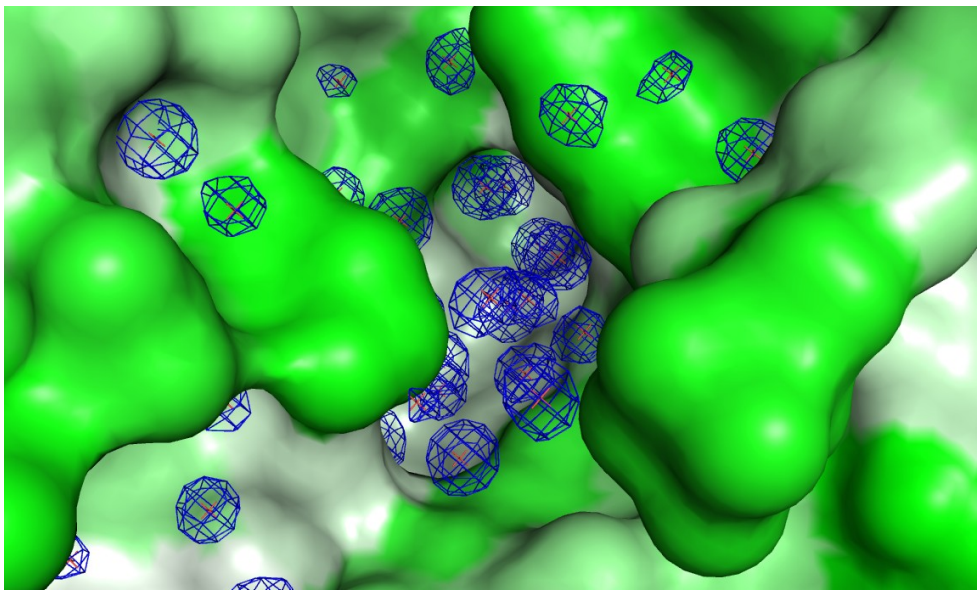

Figure 3.17. The I113T dimerisation region hydrophobic pocket after crystal soaking with isoproteranol. $2F_o$-$F_c$ electron density map contoured at 1σ of the I113T SOD1 Val7-Gly146-Val147 pocket with solvent after 2 hours soak in 50 mM isoproteranol.

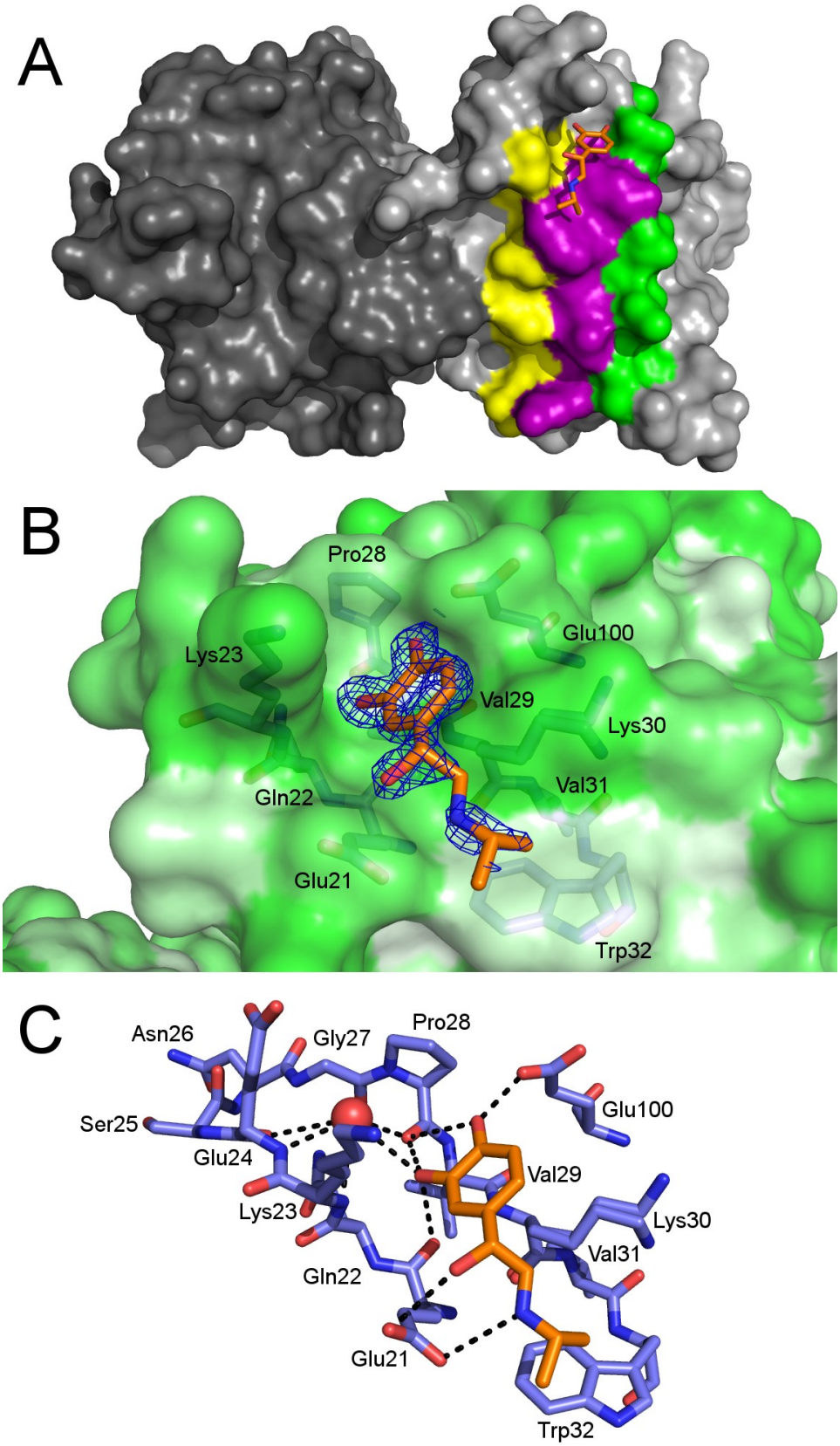


Figure 3.18. Isoproteranol bound to I113T SOD1. (A) Isoproteranol with respect to the SOD1 dimer in grey and light grey, strands 2, 3 and 6 of the SOD1 β-barrel are coloured yellow, purple and green respectively. (B) $2F_o$-$F_c$ electron density map of isoproteranol contoured at 1σ at the β-barrel loop II site with the SOD1 surface coloured by amino acid hydrophobicity and (C) Hydrogen bonding between I113T SOD1 and isoproteranol shown with black dashed lines. A single water molecule is also shown as a red sphere.

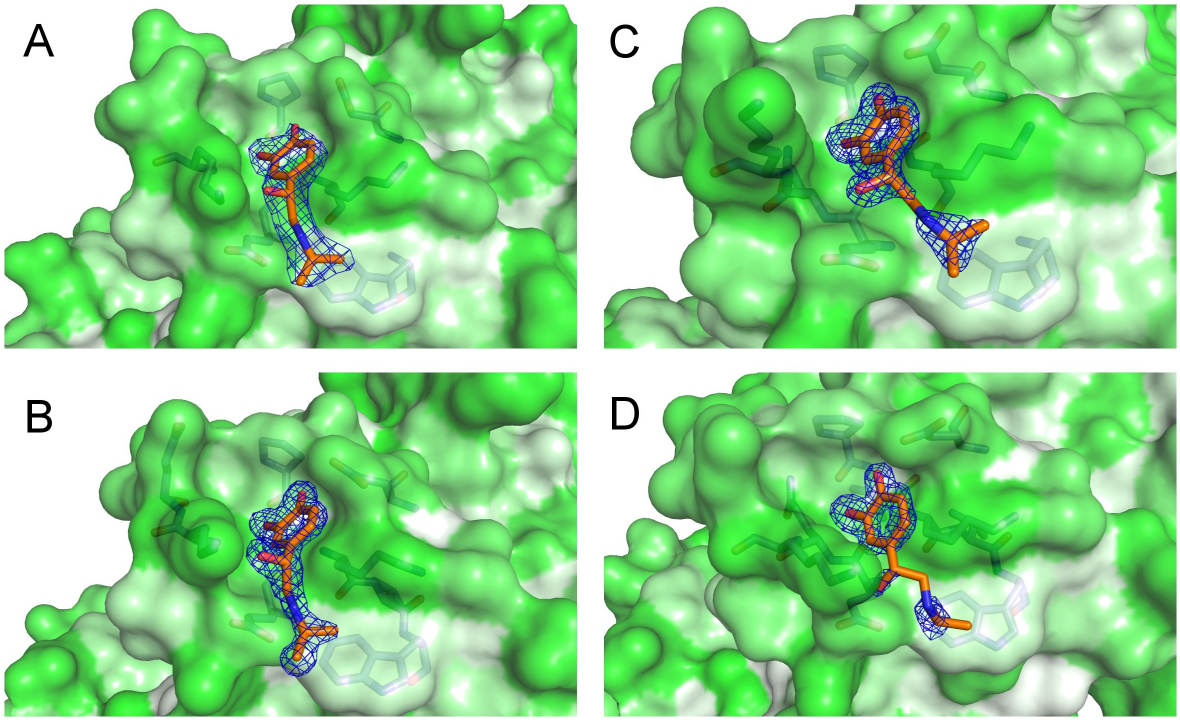


Figure 3.19. Isoproteranol bound to multiple SOD1 mutants. $2F_o$-$F_c$ electron density maps contoured at 1σ of the loopII/catecholamine pocket with Isoproteranol bound in (A) I113T SOD1 pH 8 $C222_1$ crystal structure (B) L38V SOD1 , (C) wild-type SOD1 and (D) H48Q SOD1 grown at pH 5 in the $P2_1$ form.

| Donor | I113T | wtSOD1 | L38V | H48Q | I113T pH8 | Acceptor |
|---|---|---|---|---|---|---|
| Isoproteranol C1-OH | 2.4 Å | 2.6 Å | 2.6 Å | 2.5 Å | 3.6 Å | COOH-Glu100 |
| Isoproteranol C1-OH | 3.4 Å | 3.2 Å | 3.2 Å | 3.4 Å | 3.4 Å | O=C-Pro28 |
| Isoproteranol C2-OH | 2.8 Å | 2.8 Å | 2.7 Å | 2.9 Å | 3.1 Å | O=C-Pro28 |
| Isoproteranol C2-OH | 3.1 Å | 3.1 Å | 3.2 Å | 3.2 Å | 3.4 Å | O=C-Glu21 |
| Isoproteranol C2-OH | 3.3 Å | 3.4 Å | 3.3 Å | 3.4 Å | 3.3 Å | $H_2O$ |
| Isoproteranol tail-OH | 3.1 Å | 3.6 Å | 4.3 Å | 3.1 Å | 4.7 Å | O=C-Glu21 |
| Isoproteranol tail-NH | 3.5 Å | 3.6 Å | 3.3 Å | 4.1 Å | 3.7 Å | O=C-Glu21 |

Table 3.9. Summary of potential hydrogen bonding interactions between SOD1 and isoproteranol in the loop II binding site.

This site is close to but distinct from the Trp32 binding site and the interaction has several features that distinguish it from those described in the previous sections. Isoproteranol sits in a hydrophilic groove created by Glu21, Lys23, Pro28, Lys30 and Glu100. The catechol head group is an obvious hydrogen bond donor to the carboxyl and carbonyl groups of Glu21, Glu100 and Pro28 together with a single water molecule which fills the groove adjacent to Pro28 (Table 3.9). Also, the amine and hydroxyl groups of the tail interact with the Glu21 carboxyl. The isopropyl tail sits above Trp32 and may benefit from a

hydrophobic interaction with the Trp32 indole however its occupancy is lower than the rest of the molecule indicating a degree of flexibility. In an unbound SOD1 structure the Lys30 side-chain is able to move freely and is not visible after the β or γ carbon. Here space is limited by the presence of isoproteranol and the fully visible Lys30 side chain is forced to move towards Ser98. Other than this deformation the SOD1 dimer remains unperturbed with a whole molecule RMSD of 0.26 Å compared with the atomic resolution crystal structure of wild-type SOD1 (2C9V) [51] (Figure 3.20).

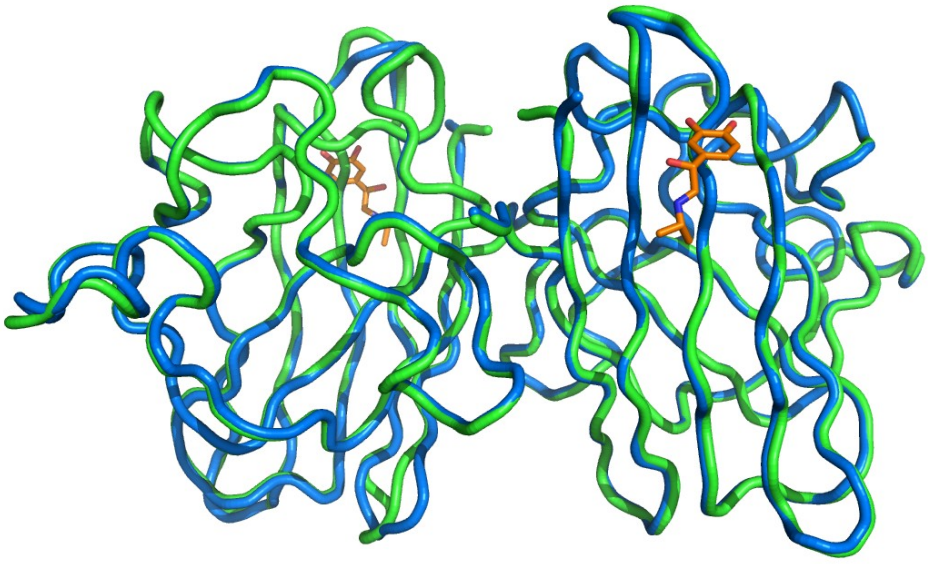

Figure 3.20. Comparison of I113T SOD1 in the native and isoproteranol bound states. Structural alignment, RMSD = 0.25 Å, of I113T SOD1 with isoproteranol bound at the loop II site (blue and orange) with the structure of wild-type SOD1 (2C9V) (green). In each case the protein backbone is represented as a ribbon.

To summarise, we find that isoproteranol does not occupy the Val7-Gly146-Val147 pocket in any of the SOD1 structure presented here. In each of these structures, isoproteranol can be found at multiple positions some of which are attributed to crystal lattice contacts however one site is not lattice dependent. Ligand binding at this loop II site is likely to create several hydrogen bonds with the protein and each of the ligand's four possible hydrogen bond donor groups are involved in this interaction.

The elucidation of a catechol binding site at loop II of the SOD1 β-barrel opens the possibility to bind a large number of biologically relevant molecules in this position. What follows is a description of two such compounds; the hormones adrenaline and dopamine.

### 3.10 Adrenaline

Adrenaline is a member of the biogenic amine group of excitatory neurotransmitters and acts on the α and β adrenergic receptors. It is found in the neurons of the medulla and project into the thalamus and hypothalamus. Neurones that use adrenaline are found less frequently in the brain than those that utilise the other catecholamine neurotransmitters [135]. Adrenaline is a licensed drug and used frequently in the treatment of asthma [136], bronchiolitis [137], anaphylaxis [138] and angioedema [139].

Adrenaline is structurally very similar to isoproteranol; a catechol head group with hydroxyl and amine substitutions in the tail. In fact the only difference between these two drugs is the presence of an isopropyl group at the terminus of the molecules tail (Figure 3.21). This similarity ensured that crystal soaking experiments would be successful however adrenaline has low solubility in aqueous solutions at neutral pH due to a lack of polarity. This characteristic prevented an assessment of adrenaline binding to SOD1 at physiological pH. Crystallographic statistics for adrenaline bound in SOD1 crystals grown at pH 5 are presented in Table 3.10 and the related structures displayed in Figures 3.22 and 3.23.

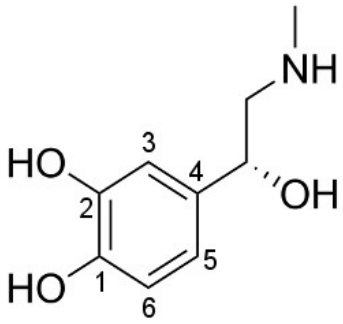


Figure 3.21. The structure of adrenaline (epinephrine, Twinject and Epipen). Mr 183.2 $gMol^{-1}$.

Figure 3.22A and B indicate that, as expected, adrenaline binds in the same loop II groove as isoproteranol. Figure 3.22C and Table 3.11 describe the hydrogen bonding interactions between I113T SOD1 and adrenaline. Glu21, Pro28, Glu100 and the loop II ordered water molecule all act as hydrogen bond acceptors in partnership with adrenaline's catechol hydroxyls. The carboxyl side-chain of Glu21 also interacts with the adrenaline's tail amine and hydroxyl groups. Comparison with the hydrogen bonds made by isoproteranol reveals these interactions are conserved with only slight changes in bond lengths discernible.

| **Variant** | **I113T** | **wild-type** | **L38V** | **H48Q** |
|---|---|---|---|---|
| Resolution (Å) | 0.98 | 1.6 | 1.25 | 1.49 |
| Space group | $P2_1$ | $P2_1$ | $P2_1$ | $P2_1$ |
| pH | 5.0 | 5.0 | 5.0 | 5.0 |
| Unit cell parameters: | | | | |
| a (Å) | 38.3 | 38.4 | 38.5 | 38.4 |
| b (Å) | 68.1 | 68.3 | 68.2 | 68.2 |
| c (Å) | 50.2 | 50.8 | 50.7 | 50.2 |
| α (°) | 90.0 | 90.0 | 90.0 | 90.0 |
| β (°) | 104.7 | 105.0 | 105.9 | 105.0 |
| γ (°) | 90.0 | 90.0 | 90.0 | 90.0 |
| Completeness (%) | 97.0 (71.3) | 99.6 (99.6) | 97.9 (89.3) | 99.7 (99.0) |
| Redundancy | 3.6 (2.0) | 2.8 (2.7) | 3.5 (2.7) | 3.6 (3.6) |
| R-merge (%) | 4.4 (51.7) | 9.2 (44.8) | 7.6 (41.4) | 6.7 (15.9) |
| I/σ | 14.7 (4.16) | 6.3 (1.9) | 9.4 (2.3) | 13.0 (6.6) |
| Rfact / Rfree (%) | 13.8 / 15.4 | 21.4 / 25.9 | 22.2 / 25.1 | 20.2 / 22.9 |
| RMS bond (Å) | 0.014 | 0.014 | 0.014 | 0.015 |

Table 3.10.Single crystal X-ray diffraction data collection, processing and model refinement statistics for adrenaline bound to SOD1.

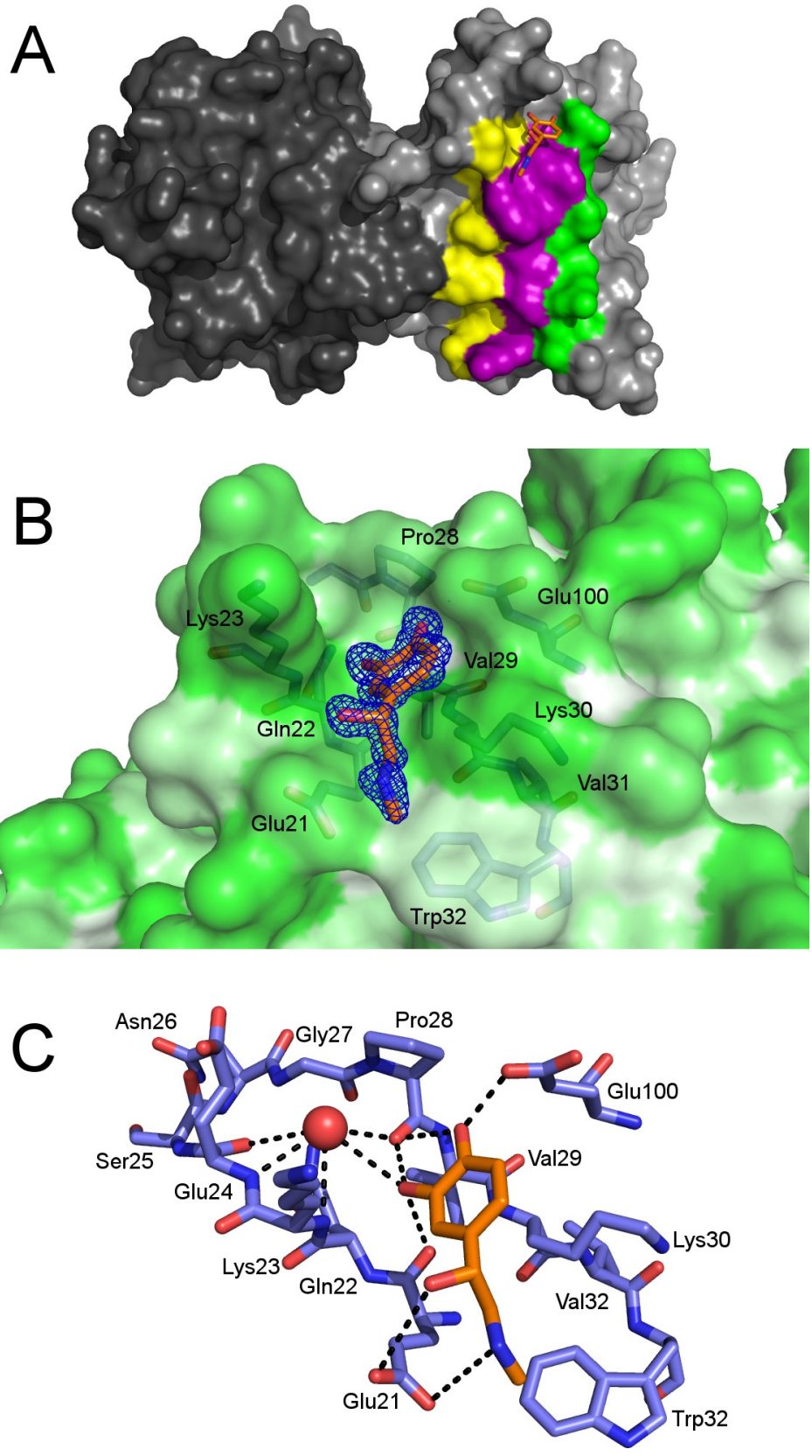


Figure 3.22. Adrenaline bound to I113T SOD1. (A) Adrenaline with respect to the SOD1 dimer in grey and light grey, strands 2, 3 and 6 of the SOD1 β-barrel are coloured yellow, purple and green respectively. (B) $2F_o$-$F_c$ electron density map of adrenaline contoured at 1σ at the Trp32 binding site with the SOD1 surface coloured by amino acid hydrophobicity and (C) hydrogen bonding between I113T SOD1 and adrenaline shown with black dashed lines. A single water molecule is also shown as a red sphere.

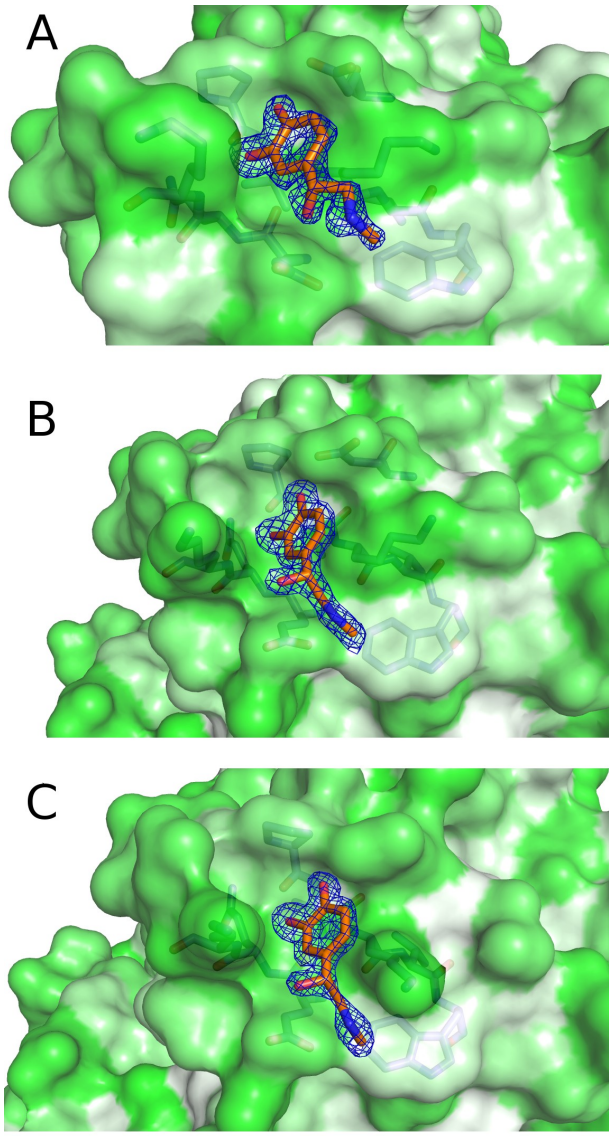


Figure 3.23. Adrenaline bound to multiple SOD1 mutants. $2F_o$-$F_c$ electron density maps contoured at 1σ of adrenaline bound at the loop II site in (A) L38V SOD1 in the $P2_12_12_1$ form, (B) wild-type SOD1 and (C) H48Q SOD1 grown at pH 5 in the $P2_1$ form.

| Donor | I113T | wtSOD1 | L38V | H48Q | Acceptor |
|---|---|---|---|---|---|
| Adrenaline C1-OH | 2.6 Å | 2.5 Å | 2.8 Å | 2.6 Å | COOH-Glu100 |
| Adrenaline C1-OH | 3.2 Å | 3.1 Å | 3.4 Å | 3.2 Å | O=C-Pro28 |
| Adrenaline C2-OH | 2.8 Å | 2.7 Å | 2.7 Å | 2.7 Å | O=C-Pro28 |
| Adrenaline C2-OH | 3.2 Å | 3.2 Å | 3.3 Å | 3.2 Å | O=C-Glu21 |
| Adrenaline C2-OH | 3.4 Å | 3.3 Å | 3.3 Å | 3.4 Å | $H_2O$ |
| Adrenaline tail-OH | 4.0 Å | 4.3 Å | 2.8 Å | 3.9 Å | COOH-Glu21 |
| Adrenaline tail-NH | 4.0 Å | 3.3 Å | 3.9 Å | 3.5 Å | COOH-Glu21 |

Table 3.11. Summary of potential hydrogen bonding interactions between I113T SOD1 and adrenaline in the loop II binding site.

### 3.11 Dopamine

Dopamine is a biogenic amine neurotransmitter and a critical intermediate in the synthesis of adrenaline and noradrenaline from tyrosine and L-dihydroxyphenylalanine [135]. Unlike isoproteranol and adrenaline, dopamine acts upon specific G-protein coupled receptors in dopaminergic neurones rather than adrenergic receptors. These neurones are found throughout the brain, where they are involved in working memory [140], the heart, where stimulation can increase myocardial contractility and cardiac output, and the kidneys where they effect diuresis and natriuresis [141].

The dopaminergic nervous system is implicated in a plethora of common disease states. These include: hypertension, obesity [141], attention deficit disorder [142], schizophrenia [143] and drug dependence [144]. These neurones are also critically affected in Parkinson's disease (PD). Analogous to ALS, PD involves the selective death of a subset of CNS neurones in the brain's substantia nigra. While the etiology of PD is not clearly understood there are indications that an interaction between dopamine and α-synuclein promotes amyloid deposition and cell death [145].

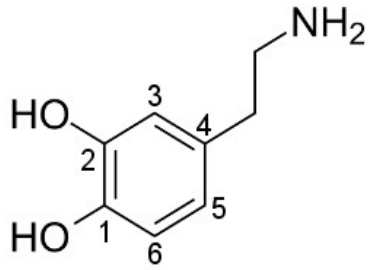


Figure 3.24. The structure of dopamine. Mr 153.2 $gMol^{-1}$.

Like isoproteranol and adrenaline, dopamine follows the catecholamine blueprint with a catechol head group attached to a tail substituted with an amine group (Figure 3.24). Dopamine does not contain a tail hydroxyl as seen in the previous two compounds and this reduces the number of potential hydrogen bonds between the ligand and Glu21.

Figure 3.25 shows the binding of dopamine to I113T SOD1 at the loop II groove and Table 3.12 shows related crystallographic statistics. As expected there is good electron density around the catechol head group which makes typical hydrogen bonds with the Glu21 and Pro28 carbonyls, the Glu100 carboxyl and the loop II ordered water molecule (Figure

3.25C and Table 3.13). Binding is replicated with slight changes in conformation in structures with other SOD1 variants and near physiological pH (Figure 3.26). While these bonds are conserved with respect to isoproteranol and dopamine, the hydroxyl hydrogen donor is switched in each case as the plane of the catechol group is rotated 180 º (Figure 3.27).

| **Variant** | **I113T** | **I113T** | **wild-type** | **L38V** | **H48Q** |
|---|---|---|---|---|---|
| Resolution (Å) | 1.00 | 1.90 | 1.89 | 1.53 | 1.55 |
| Space group | $P2_1$ | $C222_1$ | $P2_1$ | $P2_1$ | $P2_1$ |
| pH | 5.0 | 8.0 | 5.0 | 5.0 | 5.0 |
| Unit cell parameters: | | | | | |
| a (Å) | 38.4 | 165.4 | 38.6 | 38.6 | 38.7 |
| b (Å) | 68.0 | 203.4 | 68.2 | 67.1 | 67.9 |
| c (Å) | 49.9 | 144.6 | 50.9 | 52.3 | 50.5 |
| α (º) | 90.0 | 90.0 | 90.0 | 90.0 | 90.0 |
| β (º) | 104.8 | 90.0 | 105.8 | 106.7 | 105.7 |
| γ (º) | 90.0 | 90.0 | 90.0 | 90.0 | 90.0 |
| Completeness (%) | 96.8 (80.4) | 97.0 (82.4) | 92.9 (65.2) | 99.8 (99.9) | 99.8 (98.8) |
| Redundancy | 3.7 (2.7) | 7.0 (5.2) | 2.7 (1.5) | 3.6 (3.6) | 3.6 (3.4) |
| R-merge (%) | 4.7 (58.7) | 11.3 (64.5) | 9.9 (31.8) | 16.7 (53.9) | 8.0 (53.9) |
| I/σ | 16.4 (1.6) | 12.52 (1.62) | 6.6 (2.0) | 6.3 (2.2) | 14.0 (2.1) |
| Rfact / Rfree (%) | 15.8 / 18.2 | 20.0 / 23.2 | 23.9 (29.3) | 29.8 / 34.3 | 19.9 / 23.7 |
| RMS bond (Å) | 0.015 | 0.016 | 0.016 | 0.015 | 0.015 |

Table 3.12. Single crystal X-ray diffraction data collection, processing and model refinement statistics for dopamine bound to SOD1.

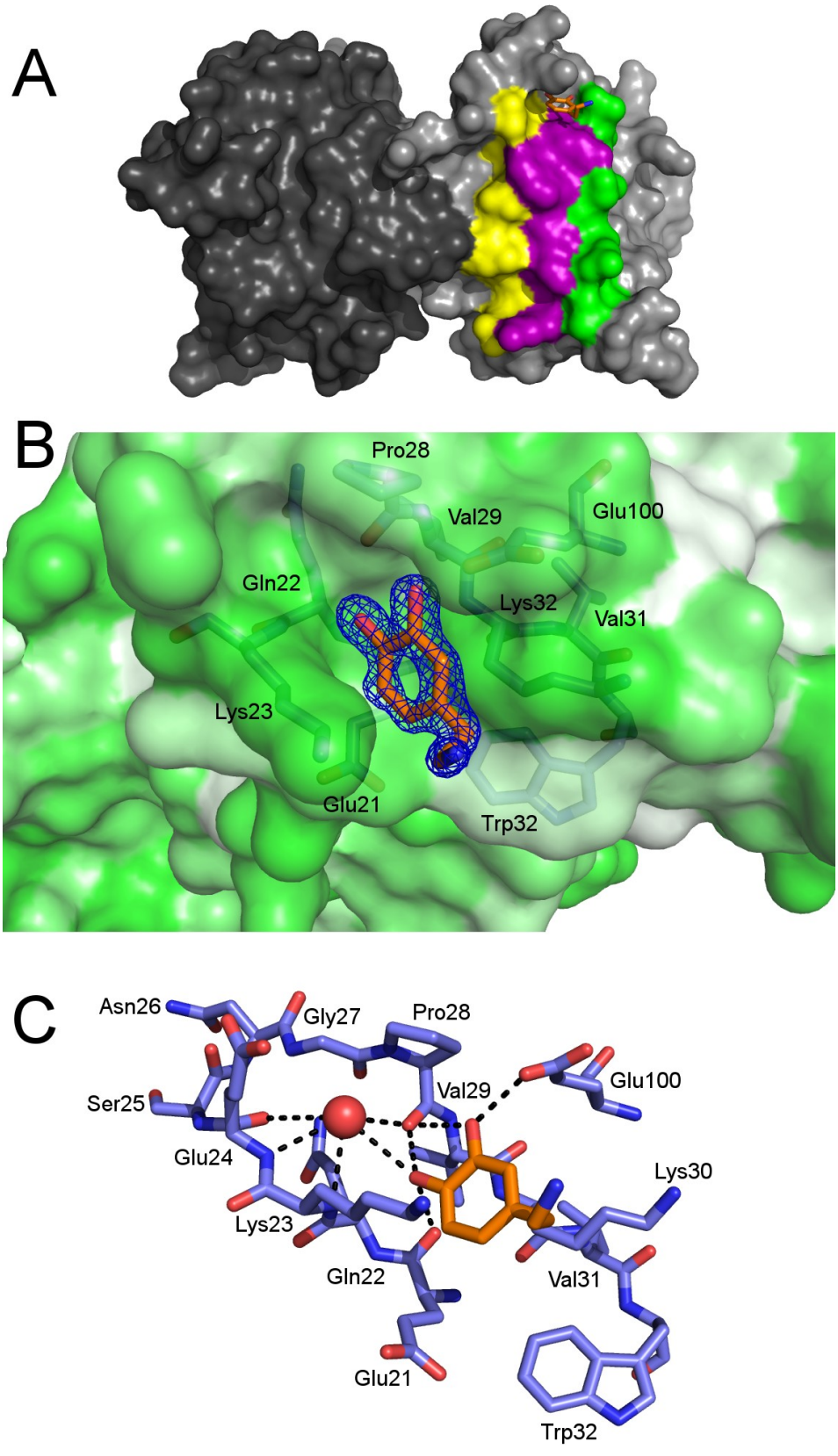


Figure 3.25. Dopamine bound to I113T SOD1. (A) Dopamine with respect to the SOD1 dimer in grey and light grey, strands 2, 3 and 6 of the SOD1 β-barrel are coloured yellow, purple and green respectively. (B) $2F_o$-$F_c$ electron density map of dopamine contoured at 1σ at the Trp32 binding site with the SOD1 surface coloured by amino acid hydrophobicity and (C) hydrogen bonding between I113T SOD1 and dopamine shown with black dashed lines, a single water molecule is also shown as a red sphere.

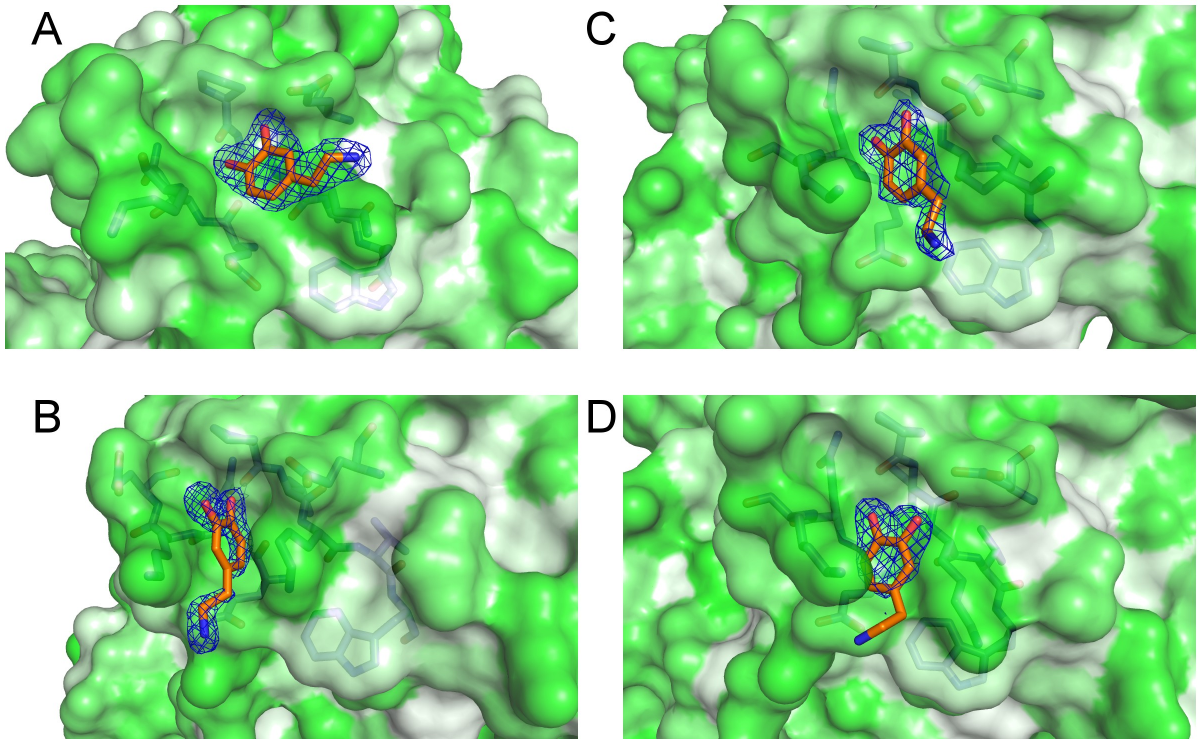


Figure 3.26. Dopamine bound to multiple SOD1 mutants. $2F_o$-$F_c$ electron density maps contoured at 1σ of the SOD1 loop II pocket with dopamine bound in (A) I113T SOD1 pH 8 $C222_1$ crystal structure (B) L38V SOD1, (C) wild-type SOD1 and (D) H48Q SOD1 grown at pH 5 in the $P2_1$ form.

| Donor | I113T | wtSOD1 | L38V | H48Q | I113T pH8 | Acceptor |
|---|---|---|---|---|---|---|
| Dopamine C1-OH | 2.8 Å | 2.7 Å | 2.2 Å | 2.9 Å | 2.5 Å | O=C-Pro28 |
| Dopamine C1-OH | 3.2 Å | 3.0 Å | 4.0 Å | 3.4 Å | 3.1 Å | O=C-Glu21 |
| Dopamine C1-OH | 3.3 Å | 3.4 Å | 2.9 Å | 3.3 Å | 3.4 Å | $H_2O$ |
| Dopamine C2-OH | 2.6 Å | 2.9 Å | - | 3.2 Å | 2.5 Å | COOH-Glu100 |
| Dopamine C2-OH | 3.3 Å | 3.3 Å | - | 4.5 Å | 3.4 Å | O=C-Pro28 |

Table 3.13. Summary of potential hydrogen bonding interactions between SOD1 and dopamine in the loop II binding site.

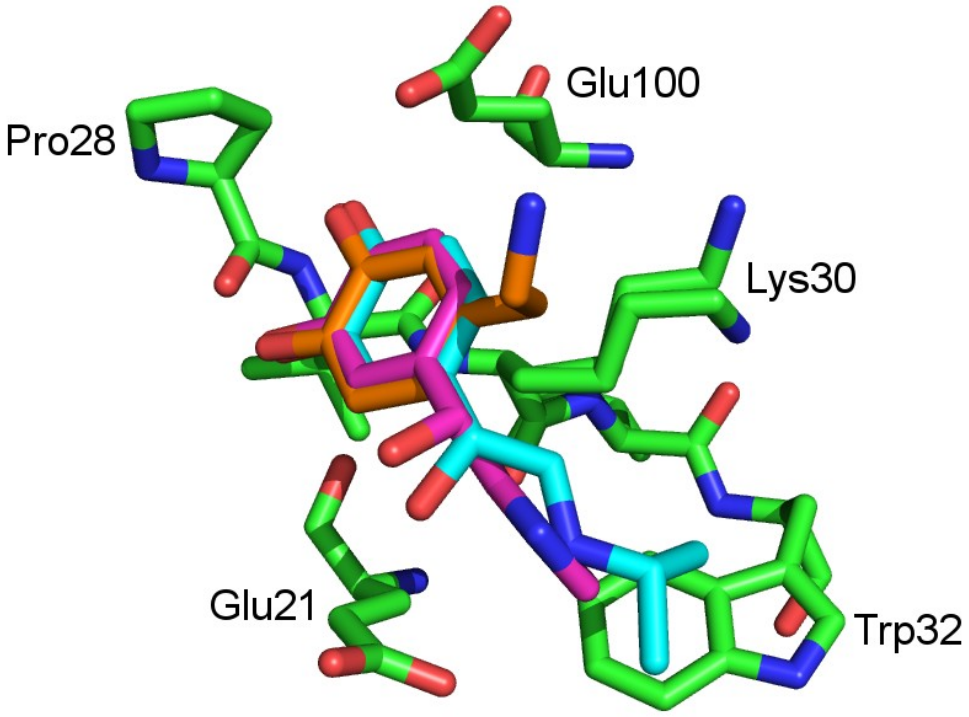


Figure 3.27. Comparison of I113T SOD1 structures with bound catecholamines; isoproteranol (cyan), adrenaline (purple) and dopamine (orange).

The reason for this shift in orientation appears to be the lack of hydrogen bonding with the Glu21 carboxyl through a tail hydroxyl. The dopamine tail is therefore untethered and projects into solvent away from Trp32. Electron density is, surprisingly, clearly defined for this part of the molecule (Figure 3.25B) possibly as a result of repulsion from Lys23 and Lys30 side chains.

### 3.12 An *in vitro* assay to monitor SOD1 aggregation

While the etiology of SOD1 related fALS is currently ambiguous the disease manifests with particular phenotypic characteristics. Motor neurone cell death leading to a deterioration of muscle control, atrophy and ultimately death are the primary traits of all ALS sufferers. The knowledge that the SOD1 gene is mutated in a subset of cases [17] led to the observation that SOD1 protein accumulates as high molecular weight inclusions in the motor neurones of these individuals [68] and in mouse transgenic models [146]. In addition, fALS associated SOD1 mutant protein has been found to be destabilised and aggregation prone *in vitro* particularly when demetallated and disulphide reduced [78,86]. *Banci et al* observed that apo-I113T SOD1 undergoes a gradual but progressive disappearance of the dimeric form concomitant with evolution of higher molecular weight species when the protein was analysed by size exclusion chromatography after incubation at physiologically relevant concentration, pH and temperature [78]. This work is recreated in Figure 3.28.

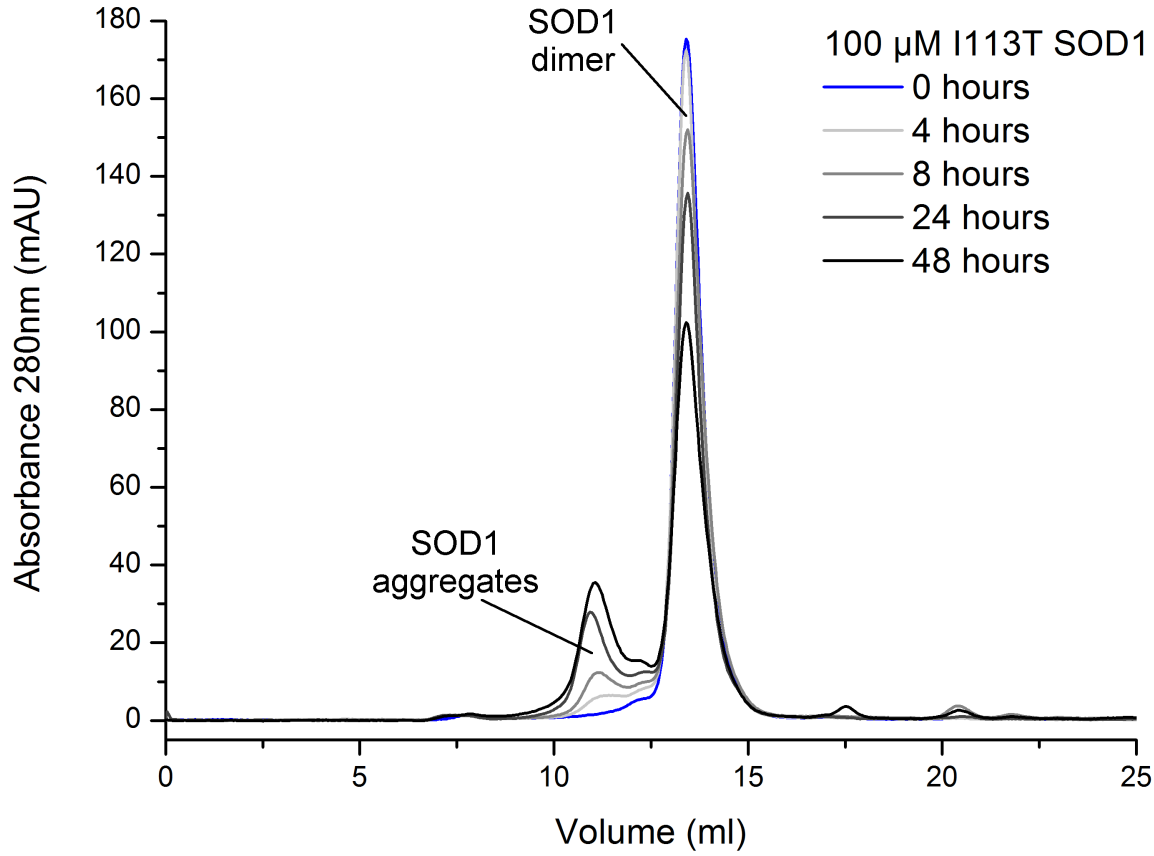


Figure 3.28. Aggregation of I113T SOD1 monitored by size exclusion chromatography. Apo-I113T SOD1 (100 µM) in Tris-HCl 20 mM, NaCl 150 mM was incubated for the indicated time at 37°C before 300 µl was was loaded onto a Superose 12 10/300 gel filtration column.

Lansbury and co-workers have used this system to determine the effect of an intersubunit disulphide bond on A4V SOD1 aggregation [86] and the effect of putative SOD1 binding compounds on aggregation [130,131]. Indeed, 5-fluorouridine and isoproteranol were both assayed for aggregation inhibition by quantifying how much dimeric apo-A4V SOD1 remained after incubation with the compound in comparison with an untreated protein control. In both cases more than 95 % of A4V SOD1 was in the dimeric form when assayed. Although size exclusion chromatography is generally low though-put technique the small number of compounds presented in the previous sections allows their biological activity to be characterised using this methodology. The experimental conditions used in this study are explained below.

The intracellular concentration of SOD1 has been estimated to be in the low μM range [84]. To fully represent this and in order to make valid comparisons with the work of *Nowak et al* [130] and *Banci et al* [78] apo-SOD1 was used at 25 μM and 100 μM concentrations thoughout. Physiological pH was maintained using Tris buffered saline and assays were incubated at 37 ºC.

As can been seen in Figure 3.27, extensive dimer loss can be discerned after 48 hours. At this time point a large peak corresponding to high molecular weight soluble SOD1 aggregates is also clearly visible. While a shorter time period (4 hours) was assessed in each case, the extent of aggregation after such a short incubation time prevented an assessment of compound effectiveness. As a result, 48 hours was used throughout as the standard incubation period.

With no information concerning ligand binding affinities directly available from the crystal structure of a protein-ligand complex it is difficult to determine the concentration of ligand that should be used to measure its biological activity. Given that two of the compounds presented here have previously demonstrated aggregation inhibition activity at a 1:3 SOD1 to ligand molar ratio [130], those conditions are replicated here. A 1:30 ratio is also presented in each case.

In order that ligands be allowed time to dock before the onset of aggregation a 15 minute incubation period with the ligand was effected before 5 mM EDTA was added to initiate

aggregation. This is fully in accordance with the previous work of Lansbury and co-workers [130,131].

As described, adrenaline has limited solubility in aqueous buffers at neutral pH. Similarly, 4-(4-methylpiperazin-1-yl)-2-(trifluoromethyl)quinazoline (MPTQ) has very limited solubility without the presence of DMSO. As a result neither of these compounds were assayed for aggregation inhibition.

In the previous sections, I113T SOD1 was used as an screening test case for ligand binding. *Banci et al* used I113T SOD1 to demonstrate the inherently aggregation prone nature of SOD1 mutants [78]. Figures 3.29 – 3.34 A and B show *in vitro* I113T SOD1 aggregation in the presence of each of the compounds presented in the previous section under the conditions described above, with noted exceptions, as monitored by size exclusion chromatography. These experiments were repeated with each SOD1 binding compound using L38V SOD1 (Figures 3.29 – 3.34 C and D).

The alanine to valine amino acid substitution at position 4 of the SOD1 polypeptide is the most common SOD1 mutant in North America and is widely regarded to manifest with the severest ALS phenotype [147]. The A4V mutation is found at the SOD1 dimer interface [148] and may exert its pathogenic effect by perturbation of the interface or distortion of the SOD1 β-barrel. When isoproteranol and 5-fluorouridine were previously analysed for aggregation inhibition they were assayed against a recombinant A4V protein [130]. This protein was expressed in *E. coli* as a glutathione S-transferase fusion protein from which it was cleaved during protein purification [86]. Cleavage occurs using a derivative of human rhinovirus 3C protease at the site Leu-Glu-Val-Leu-Phe-Gln-Gly-Pro between glutamate and glycine [149]. Thus, removal of the fusion protein leaves the peptide Gly-Pro-Leu-Gly-Ser N-terminal to the SOD1 primary alanine. Given over 50 % of SOD1 amino acids are found to have ALS related mutations and the N-terminus of SOD1 is found close to the dimerisation region it is conceivable that addition of extra amino acids may effect the protein's properties particularly relating to its aggregation propensity. In order to fully characterise the compounds presented earlier and to act as a control for aggregation assays using I113T and L38V SOD1 an identical construct was cloned, expressed and purified according to published methodology [86]. This SOD1 protein, with the A4V mutation and 5 extra N-terminal amino acids, is hereafter termed A4V+ SOD1. The 6 SOD1 binding

compounds tested for aggregation inhibition with I113T and L38V SOD1 were examined in an identical fashion with apo-A4V+ SOD1 (E and F in Figures 3.29 – 3.34).

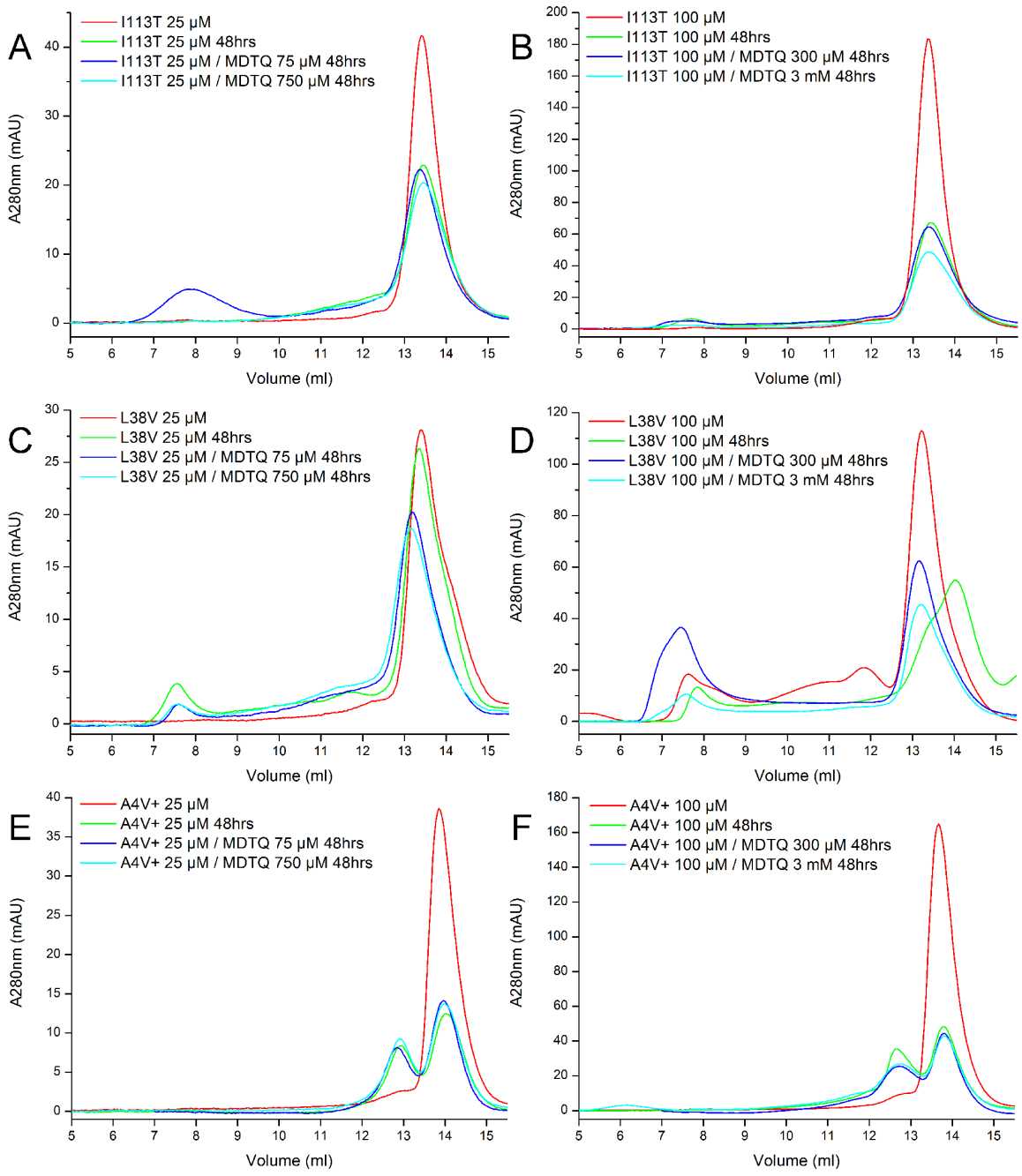


Figure 3.29. Aggregation of recombinant SOD1 in the presence of MDTQ monitored by SEC. apoSOD1 at t=0 hrs is presented in each case (red) with apoSOD1 after 48 hrs incubation at 37 ºC (green) compared with identical samples containing 1:3 (blue) and 1:30 (cyan) concentrations of MDTQ. (A) I113T 25 µM (B) I113T 100 µM (C) L38V 25 µM (D) L38V100 µM (E) A4V+ 25 µM (F) A4V+ 100 µM.

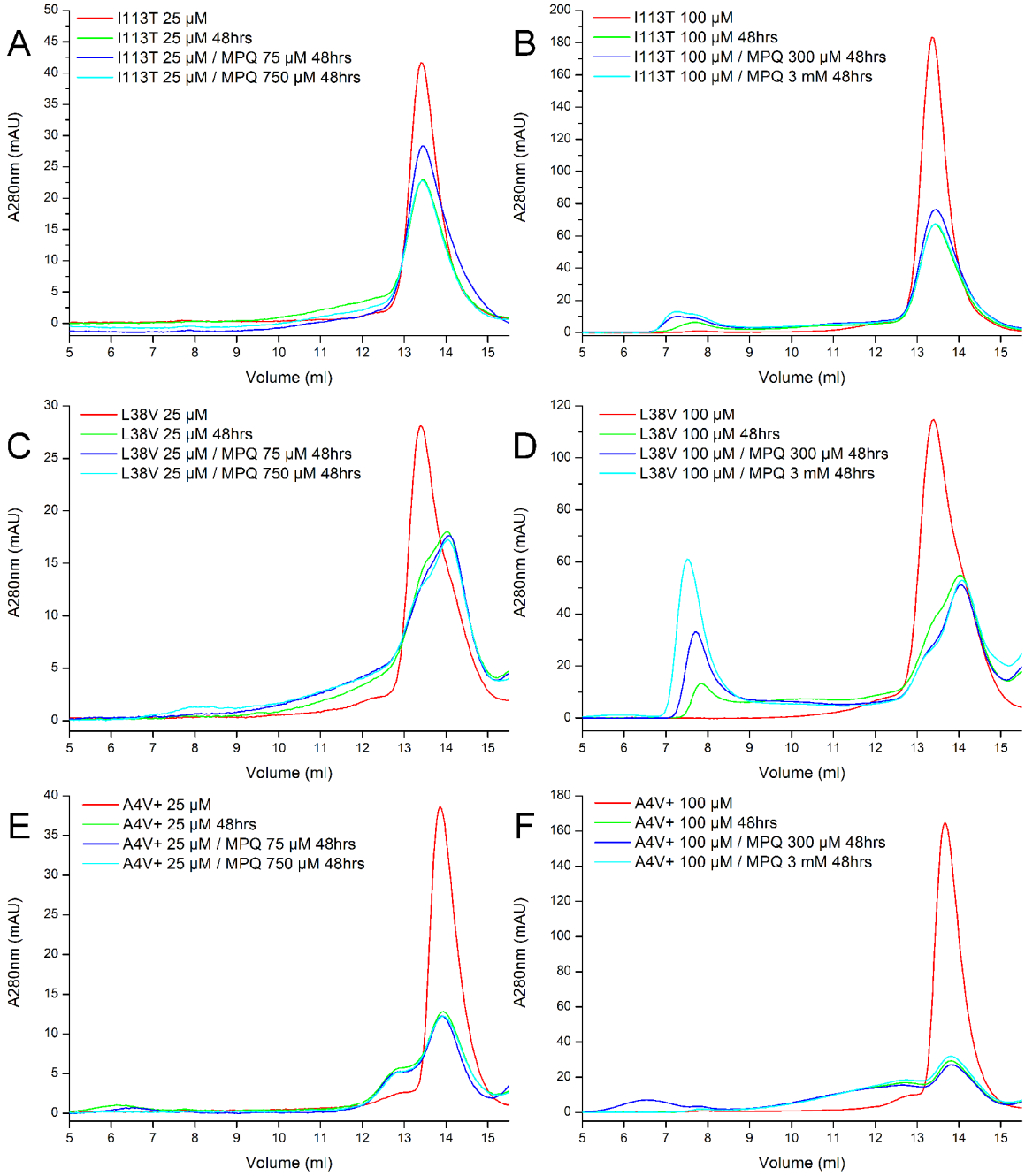


Figure 3.30 Aggregation of recombinant SOD1 in the presence of MPQ monitored by SEC. apoSOD1 at t=0 hrs is presented in each case (red) with apoSOD1 after 48 hrs incubation at 37 ºC (green) compared with identical samples containing 1:3 (blue) and 1:30 (cyan) concentrations of MPQ. (A) I113T 25 µM (B) I113T 100 µM (C) L38V 25 µM (D) L38V100 µM (E) A4V+ 25 µM (F) A4V+ 100 µM.

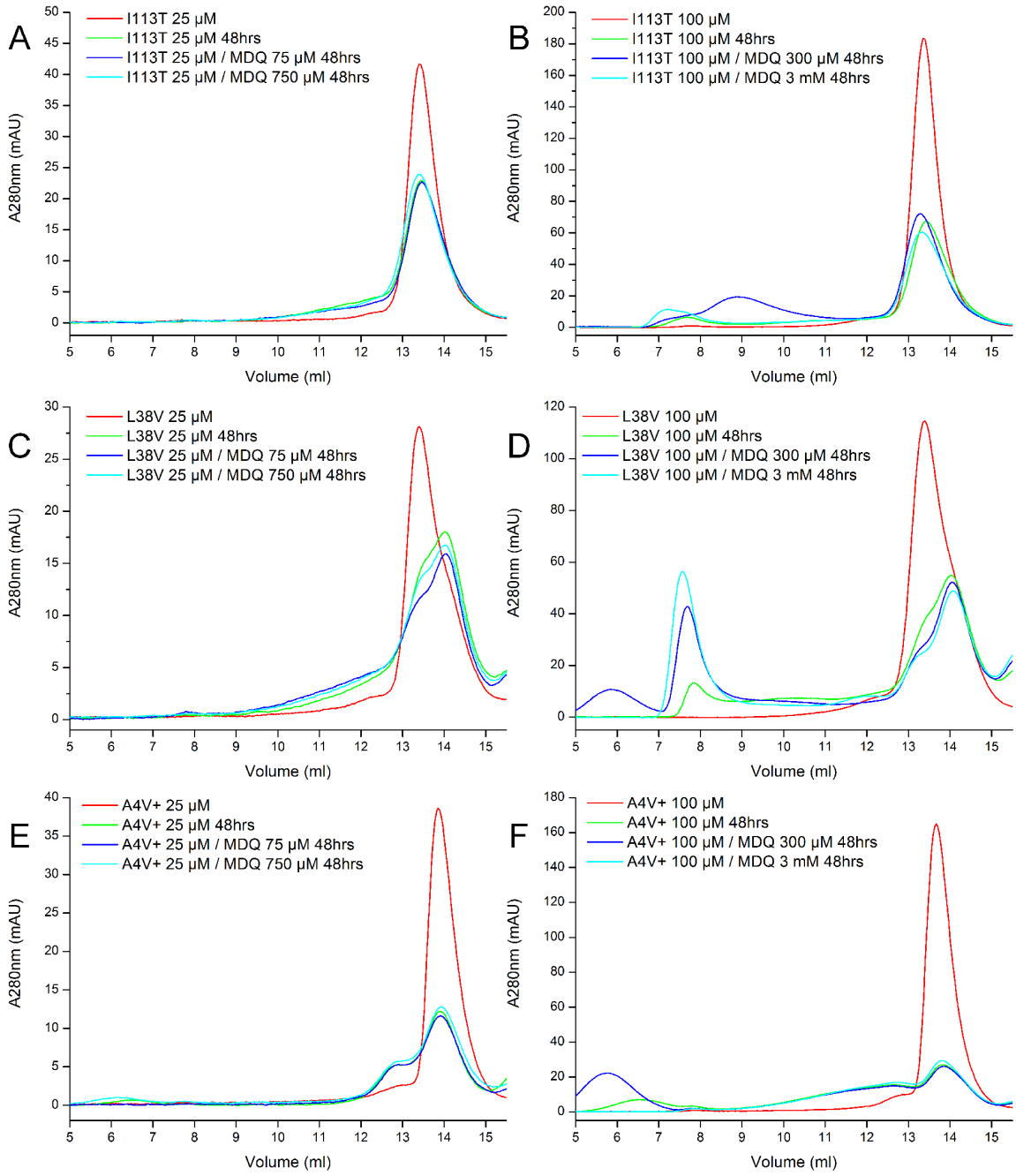


Figure 3.31 Aggregation of recombinant SOD1 in the presence of MDQ monitored by SEC. apoSOD1 at t=0 hrs is presented in each case (red) with apoSOD1 after 48 hrs incubation at 37 ºC (green) compared with identical samples containing 1:3 (blue) and 1:30 (cyan) concentrations of MDQ. (A) I113T 25 µM (B) I113T 100 µM (C) L38V 25 µM (D) L38V100 µM (E) A4V+ 25 µM (F) A4V+ 100 µM.

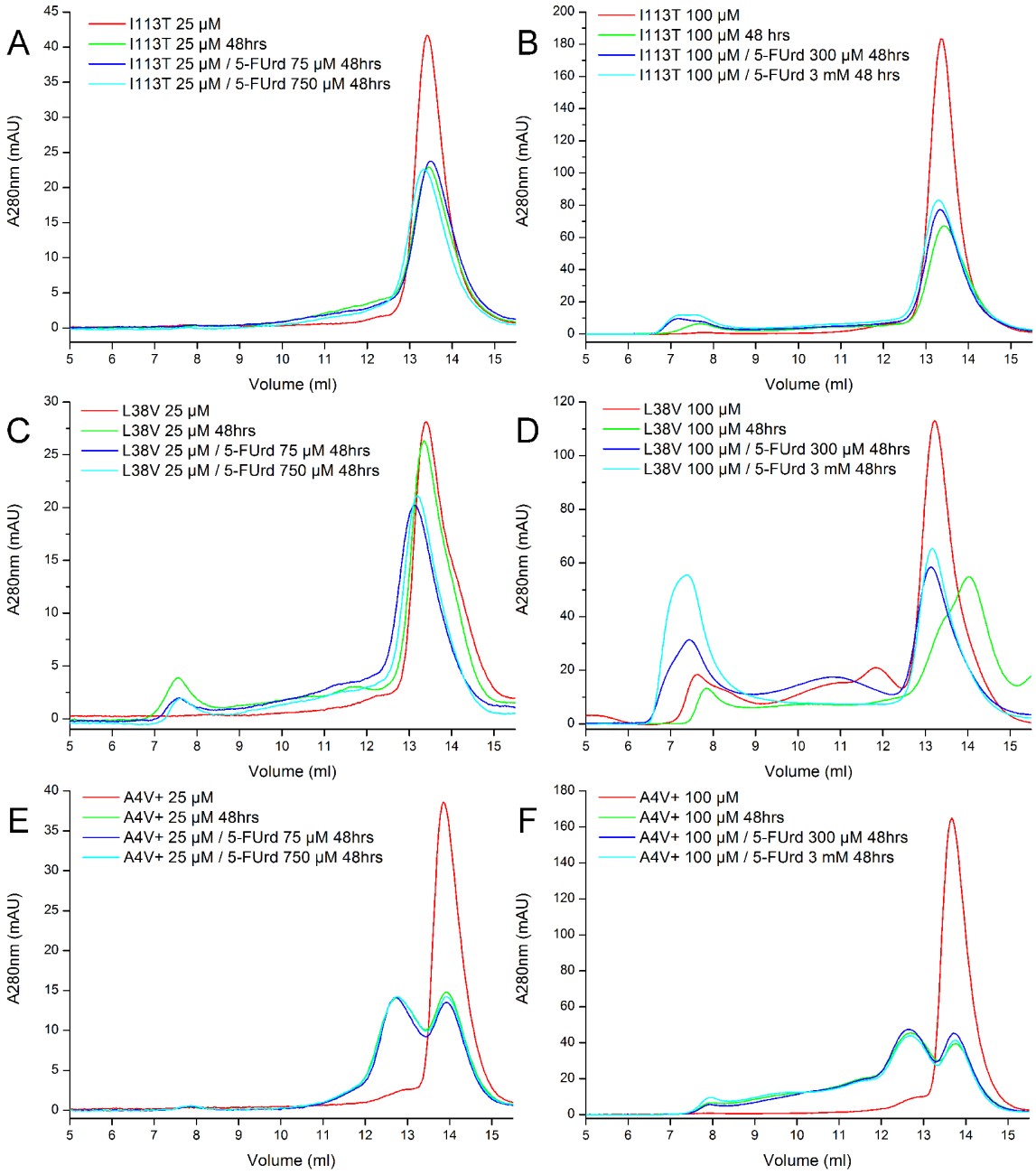


Figure 3.32 Aggregation of recombinant SOD1 in the presence of 5-fluorouridine monitored by SEC. apoSOD1 at t=0 hrs is presented in each case (red) with apoSOD1 after 48 hrs incubation at 37 ºC (green) compared with identical samples containing 1:3 (blue) and 1:30 (cyan) concentrations of 5-fluorouridine. (A) I113T 25 µM (B) I113T 100 µM (C) L38V 25 µM (D) L38V100 µM (E) A4V+ 25 µM (F) A4V+ 100 µM.

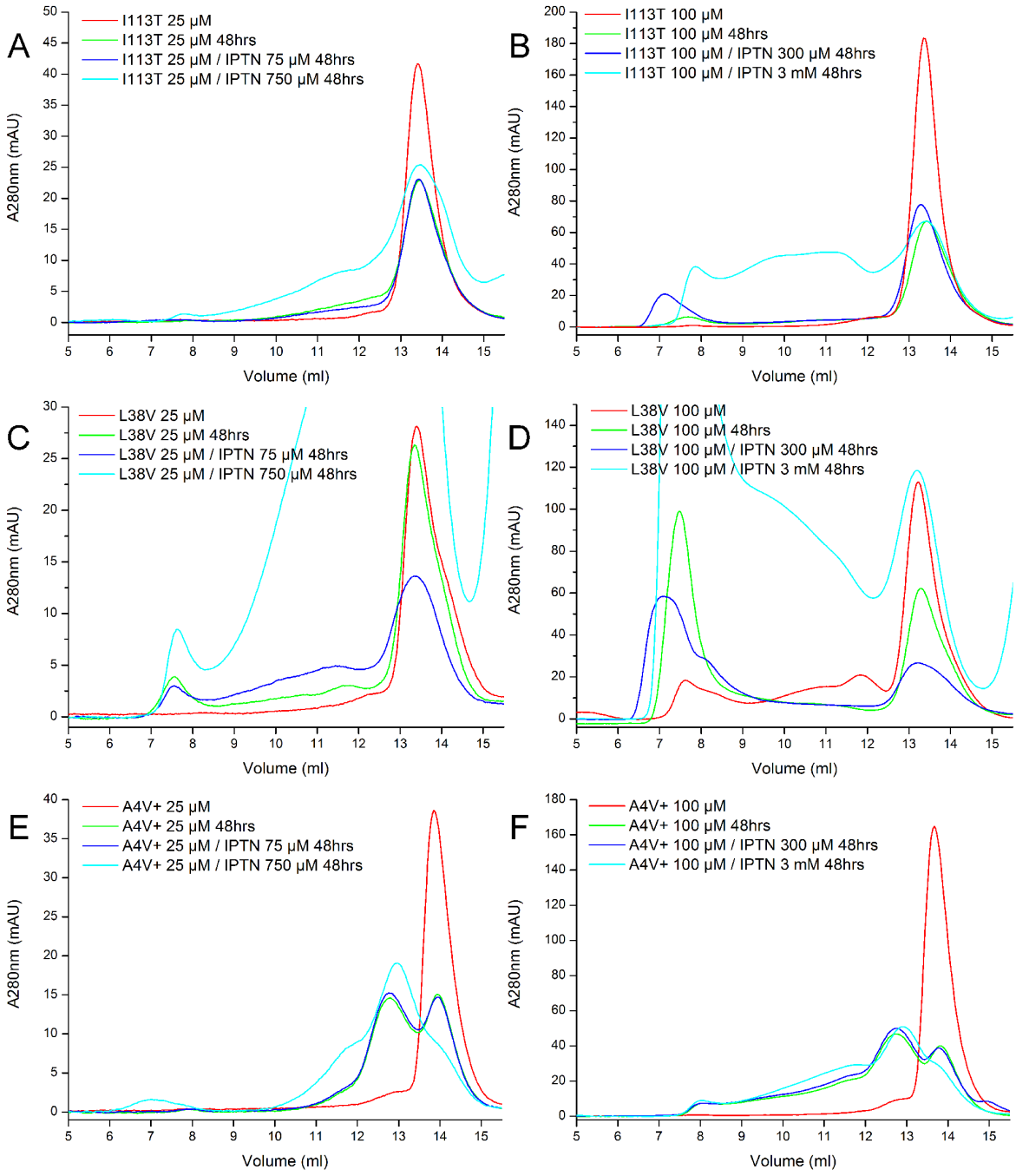


Figure 3.33 Aggregation of recombinant SOD1 in the presence of isoproteranol monitored by SEC. apoSOD1 at t=0 hrs is presented in each case (red) with apoSOD1 after 48 hrs incubation at 37 ºC (green) compared with identical samples containing 1:3 (blue) and 1:30 (cyan) concentrations of isoproteranol. (A) I113T 25 µM (B) I113T 100 µM (C) L38V 25 µM (D) L38V100 µM (E) A4V+ 25 µM (F) A4V+ 100 µM.

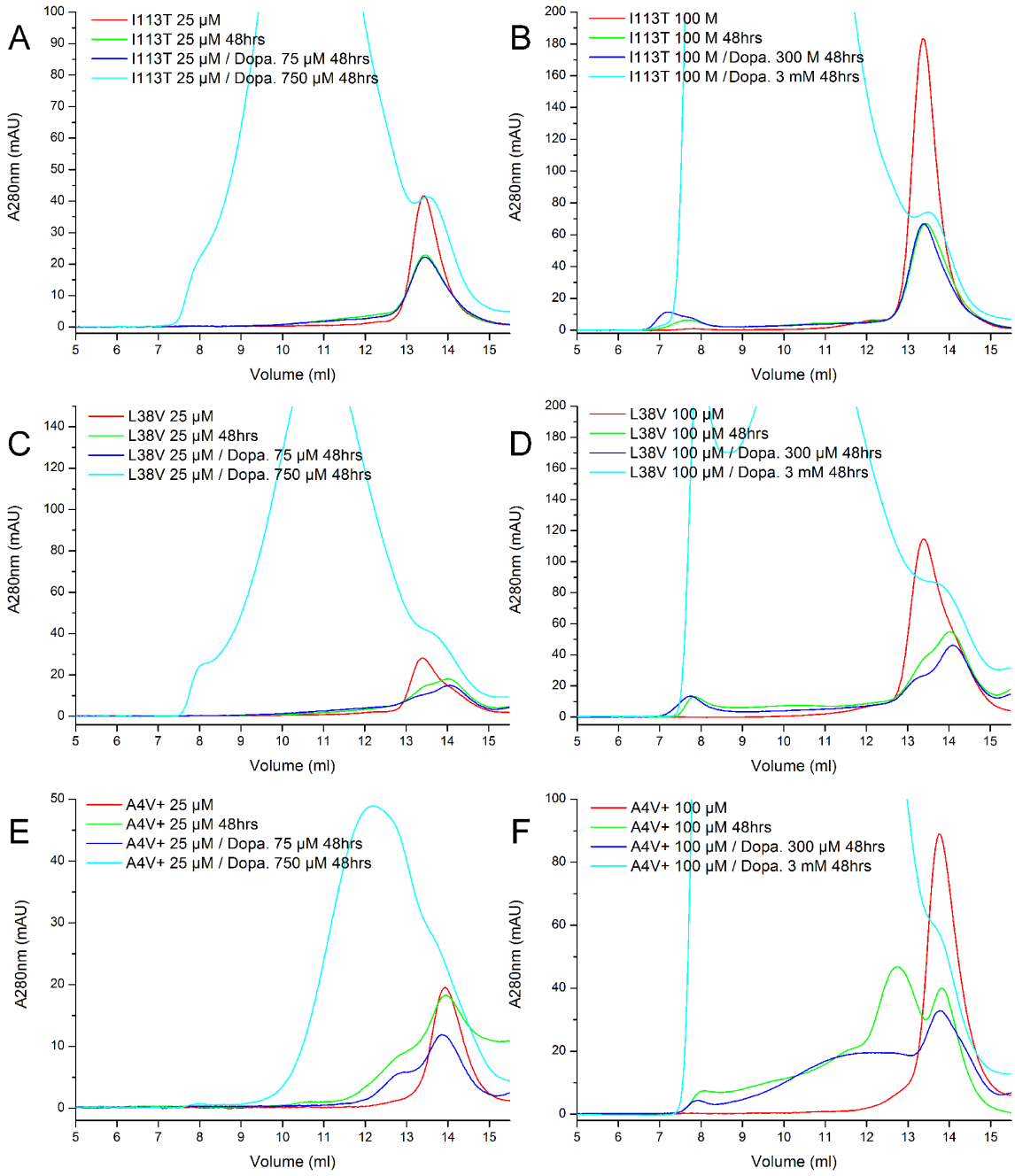


Figure 3.34 Aggregation of recombinant SOD1 in the presence of dopamine monitored by SEC. apoSOD1 at t=0 hrs is presented in each case (red) with apoSOD1 after 48 hrs incubation at 37 ºC (green) compared with identical samples containing 1:3 (blue) and 1:30 (cyan) concentrations of dopamine. (A) I113T 25 µM (B) I113T 100 µM (C) L38V 25 µM (D) L38V100 µM (E) A4V+ 25 µM (F) A4V+ 100 µM.

When apo-SOD1 is analysed by SEC a single peak corresponding to the apo dimer is observed (Figures 3.29 – 3.34 red lines). Following incubation at 37 ºC the height and area of this peak is reduced corresponding to the SOD1 dimer moving into higher molecular weight oligomers (Figures 3.29 – 3.34 green lines). In the case of the three quinazolene derivatives tested here, I113T, L38V and A4V+ SOD1 aggregation is not inhibited by addition of a 1:3 and 1:30 molar ratio (Figures 3.29 – 3.31). This is demonstrated by the similar dimer peak heights when comparing the apo-SOD1 control after 48 hours and those of containing compound. In most cases there is a slight decrease in dimer prevalence at high compound concentration.

Neither isoproteranol, 5-fluorouridine or dopamine (3.32 - 3.34) exhibit any SOD1 aggregation inhibition as determined by observation of the SOD1 dimer peak height and area. Figures 3.33 and 3.34 both exhibit strong absorbance in the 7 – 13 ml region when high catecholamine concentrations are used seemingly indicating an vast increase in the prevalence of high molecular weight SOD1 species. This is likely an artefact of strong UV absorption by catecholamine oxidation products but indicates the presence of the compound in higher molecular weight species. These species must be either SOD1-compound complexes or compound-compound complexes.

# Chapter IV

## Discussion of small molecule SOD1 binding and the effect upon SOD1 aggregation *in vitro*

### 4.1 The SOD1 screening pipeline

Appendix IV illustrates the 43 compounds screened here for SOD1 binding using a crystallographic approach. Including the Rigaku ActiveSite library this amounts to approximately 450 compounds. This throughput would not have been possible without efficient protein expression and reliable protein crystallisation. The system implemented here allows compounds to be tested against SOD1 proteins which belong to each of the major SOD1 mutation groups; dimer interface, copper site, loop and the wild-type prototype.

### 4.2 The SOD1 tryptophan-32 binding site

4-(4-methyl-1,4-diazepan-1-yl)-2-(trifluoromethyl)quinazoline (MDTQ) is patented as a modulator of ALS. This compound was found to bind to G93A SOD1 at a site over Trp32 with its trifluoromethyl moiety embedded in a cavity created by Val31, Ser98 and Glu100 [123]. Here the binding of MDTQ at this site has been confirmed by single crystal X-ray diffraction structure determination and found to occur in a variety of SOD1 mutants as well as the wild-type form.

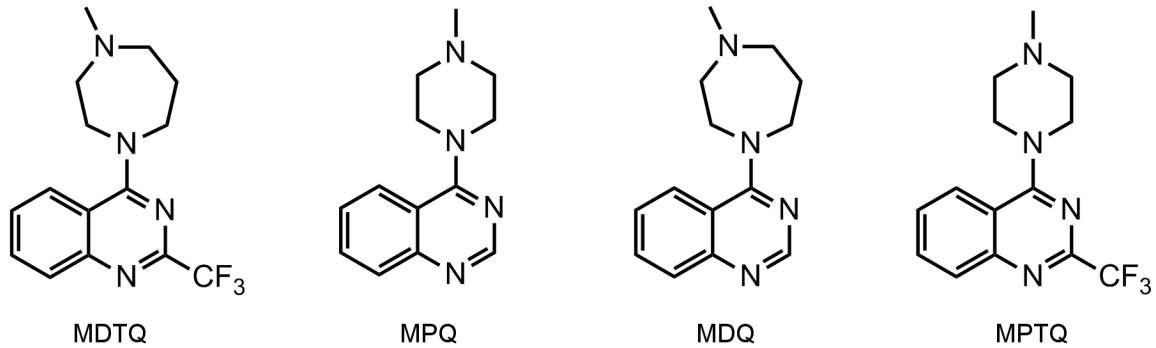


Figure 4.1. The structures of four SOD1 binding quinazoline derivatives.

Figure 4.1 shows the four quinazoline bases compounds found to bind SOD1 during the course of this study. Modification of two of the groups substituted on the central quinazoline ring of MDTQ had disparate effects on its interaction with SOD1. Removal of a carbon from the homopiperazine group to form 4-(4-methylpiperazin-1-yl)-2-(trifluoromethyl)quinazoline (MPTQ) severely affected the compound's solubility, limiting its availability in soaking experiments, but did not change its mode of binding. Removal of the trifluoromethyl group on C2 to form 4-(4-methylpiperazin-1-yl)quinazoline (MPQ) or 4-(4-methyl-1,4-diazepan-1-yl)quinazoline (MDQ) prevents formation of 3 hydrogen bonds between this group and the protein. As can been seen in Figures 3.6 and 3.9, in both cases the quinazoline ring system slightly shifts position away from Ser98 perhaps in order to maximise the hydrophobic interaction with the Trp32 indole. This prevents formation of the Ser98-quinazoline N1 hydrogen bond. It seems reasonable that ablation of these bonds will weaken the overall interaction between ligand and protein.

Analysis of SOD1 protein aggregation in the presence of these quinazoline derivatives indicated no obvious effect when compared to a control. Similarly, 5-fluorouridine was also found to bind at the Trp32 site and form hydrogen bonds with Lys30 and Ser98. This compound also had no effect on SOD1 dimer loss.

### 4.3 The SOD1 loop II binding site

Figure 4.2 shows the structure of the three catecholamine compounds found here to bind at a site in the groove created by amino acids Glu21 – Trp32 at the loop II region of the SOD1 β-barrel.

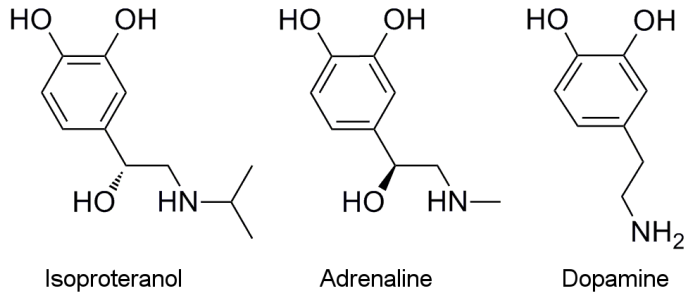


Figure 4.2. The structures of three SOD1 binding catecholamines.

Each of these compounds is capable of making several hydrogen bonding interactions

between the catechol head group and SOD1. One ordered water that sits in loop II is also important in this regard. Interactions between the tail amine and hydroxyl groups with Glu21 appear to dictate the conformation of the catechol head group as described in Figure 3.26. Dopamine does not make hydrogen bonds between tail and Glu21 indicating that its affinity for the loop II site will be reduced in comparison with isoproteranol and adrenaline.

When isoproteranol and dopamine are assayed for their effect on SOD1 aggregation we find that both compounds seem to promote formation of high molecular weight species as determined by the increased 280nm absorption at high compound concentrations in the 7 – 13 ml region of their respective SEC traces. Dopamine shows extraordinarily high absorption in this region possibly arising from the non-specific effects of dopamine toxicity mediated by its oxidation products dopa-quinone and indolequinones or formation of melanin [150].

**4.4 Lansbury compounds and contrary results**

The course which leads from SOD1 mutation to motor neurone cell death and ALS is not clearly delineated. This is despite the best efforts of many people over the course of nearly two decades since its first implication as causative factor in ALS. SOD1 aggregation and the resulting disruption of cellular process is heavily implicated in disease pathogenesis however as it is the only indisputable and unifying cell level disease characteristic preceding cell death. SOD1 polymerisation resulting from a monomerisation event leading to aggregation prone monomers has been proposed as the pathogenic mechanism [151].

This concept takes a lead from observation of mutant transthyretin (TTR) behaviour in the neurodegenerative disease familial amyloid polyneuropathy (FAP) [152]. This disease initiates with dissociation of tetrameric TTR followed by conformational changes to the monomer and aggregation of these modified monomers into fibrillar oligomers [153]. Small molecule inhibition of TTR tetramer dissociation has been shown to reduce aggregates *in vitro* and in patient trials [154].

Isoproteranol and 5-fluorouridine were identified through an *in silico* screen for molecules targeting the SOD1 dimer interface pocket created by amino acids Val7, Gly146 and

Val147 [130]. These molecules aimed to inhibit SOD1 monomerisation by replicating the effect of an artificial intersubunit disulphide bond created by the mutation V148C [86]. Validation of their effect was monitored by observing the quantity of dimeric SOD1 remaining after a period of time [130]. Here we find that isoproteranol and 5-fluorouridine bind at sites proximal but distinct in the loop II region on the surface of the SOD1 β-barrel. This area is distant from the dimerisation region and the result questions the monomerisation hypothesis as the cause of SOD1 aggregation. If both compounds exert a protective effect on dimeric SOD1 as published by *Nowak et al* [130] and, as neither compound induces large conformational changes, that effect must exert itself at the site, or close to the site, at which the compound binds. As a result the protective effect is likely an inhibition of non-native dimer contacts that take place in the loop II region rather than inhibition of monomerisation that ultimately leads to polymerisation. This strongly implicates the loop II region in SOD1 mediated fALS pathogenicity.

### 4.5 Loop II and Trp32 in SOD1 pathology and implications

The Trp32-loop II region of SOD1 (Figure 4.3) has previously been found to form one of three crucial determinants of SOD1 aggregation *in vitro* [155]. This is corroborated by analysis of the SOD1 primary sequence using tools designed to predict regions with a propensity for aberrant multimerisation [156].

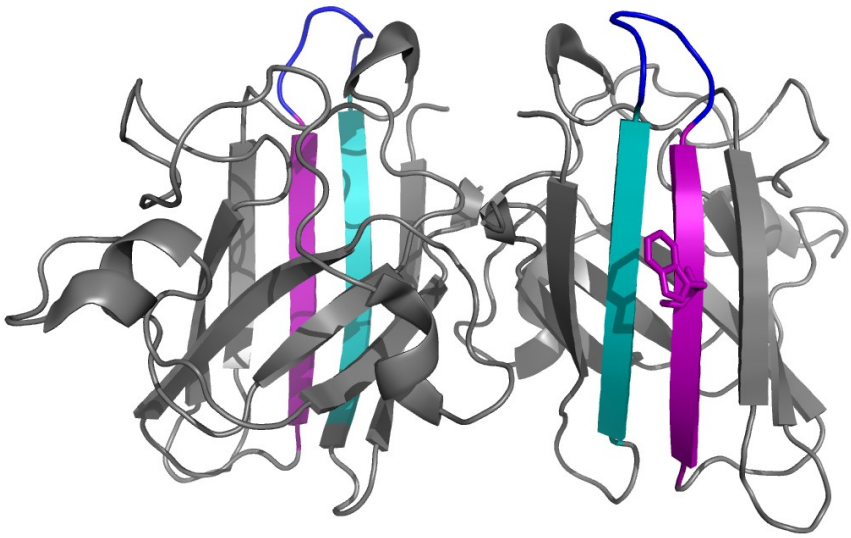

Figure 4.3. The SOD1 dimer (2C9V). β-strand 2 and 3 are highlighted turquoise and purple respectively and loop II in blue. SOD1 Trp32 is also shown in purple.

The single SOD1 tryptophan is unusually solvent exposed on the surface of the SOD1 β-

barrel. *Zhang et al* noted in 2003 that bicarbonate was able to induce covalent aggregation of wild-type SOD1 by tryptophan oxidation [157]. Using β-strand 3 peptide mimetics this group was able to determine that SOD1 Trp32 could be modified to hydroxytryptophan, kynurenine and N-formylkynurenine [158]. This was followed by observations on wild-type human SOD1 isolated from erythrocytes confirming that oxidatively modified SOD1 comprises 20 – 30 % of the total cellular pool and that Trp32 in particular can be modified by the addition of one or two oxygen atoms [159].

These findings are novel with respect to SOD1 biology but become especially interesting in light of experiments using a W32F SOD1 mutant. This amino acid substitution prevents the formation of covalently bonded SOD1 aggregates *in vitro* [157] and prolongs the life expectancy of spinal cord-dorsal root ganglia cell cultures. In the latter case, cells transfected with a G93A/W32F double mutant expression plasmid had comparable life expectancies with those expressing wild-type SOD1 driven by the same system and almost twice that of those expressing a G93A single mutant [159]. These results are corroborated by recent findings that fALS associated SOD1 mutants are unable to propagate SOD1 misfolding in mouse transgenic models when expressed as a double mutant with W32S [160].

### 4.6 Affinity & NMR experiments

Affinity, efficiency, efficacy and specificity are of critical importance alongside ADMET properties in any drug development pipeline from initial hit through optimisation to a compound that could be a candidate for clinical trials. One method to ensure that successive iterations of a compound are changing the compounds characteristics in the desired way is to measure the strength of ligand binding. The change in free entropy ($\Delta S$) and enthalpy ($\Delta H$) on ligand binding are often used as a measure of affinity [161]. During the course of this work each of the compounds presented as binding to SOD1 were analysed by isothermal titration calorimetry and, in the case of isoproteranol, one-dimensional NMR spectroscopy. Despite good electron density in the crystal structures, high quality protein samples and highly pure ligand no data regarding the affinity of any of these compounds could be gleaned.

### 4.7 Prospects and further work

The catecholamine and quinazoline compounds presented here represent excellent initial scaffolds upon which groups can be added in order to increase specificity and affinity. Each of the compounds presented has a molecular weight below 310 $gMol^{-1}$ and could be reduced even further to those groups which appear critical to binding. The catechol head group and the trifluoromethyl attached to a planar aromatic moiety are the groups which appear to make the most contacts with the peptide. Their binding site proximity together with the disease importance attached to this region encourages the notion of a chimeric or linked compound to take advantage of both sites. Fragment linking is not without difficulties however, due to the reduction of rotational freedom encountered during fragment binding often the binding affinities of linked compounds are not of the expected strength [162].

A key factor in the growth of these compounds into SOD1 therapeutics is development of an assay to determine their biological effect. The SEC aggregation assay deployed in this work has previously been used with respect to SOD1 however the contradictory results obtained here question both the results and the assay. A cell model for SOD1 toxicity has been developed and has been used in targeted drug development [163], as have transgenic mouse models [164]. While these are more expensive and each has limitations in terms of throughput they are undoubtedly a better representation ALS neurones.

# Chapter V

## An introduction to the human copper chaperone for SOD1 and small-angle X-ray scattering

### 5.1 Copper metabolism

The evolutionary shift to aerobic respiration resulted in the need for organisms to utilise an element with high redox potential. As the atmosphere became more oxidising this demand could not be filled by iron, which was converted into the insoluble iron (III) form. It could be fulfilled by the newly bioavailable copper which was well suited to the task [165]. As a result of this change and the subsequent proliferation and evolution of aerobic organisms, copper became an essential element for the vast majority of species [166]. In humans copper is an essential cofactor of enzymes involved in respiration, iron transport and free radical scavenging among others.

While copper's redox properties are a solution to one set of problems it is also the cause of another set. Free soluble copper is a source of oxidative stress because it generates reactive oxygen species through Fenton chemistry [167]. Consequently, the intracellular free copper concentration must be kept at a minimum. It is known to be ~$10^{-18}$ M in yeast cells which equates to less than one free copper atom per cell [168]. Under these circumstances it is very unlikely that a newly synthesised copper binding protein will find an amenable copper cofactor.

### 5.2 The membrane bound copper transporter and metallochaperones

The metallochaperones are a group of soluble intracellular proteins that are responsible for the chelation and movement of metal ions from their entry into the cell to their target protein [169]. Copper metallochaperones are involved in three pathways i) secretory/iron uptake, ii) activation of cytochrome c oxidase and iii) activation of SOD1. Each pathway begins with copper uptake by one of the copper transporter family (Ctr); in humans this is hCTR1 [170]. Copper then passes along an increasing affinity gradient that prevents binding

by cytoplasmic low molecular weight metal chelators such as metallothionine and glutathione [171].

Copper transport by human CTR1 is inhibited by silver but not divalent metal ions indicating that Cu(I) is the substrate [172]. hCTR1 is an integral membrane protein and forms a homotrimer with a central pore [173]. Each monomer has an extracellular N-terminus and an cytoplasmic C-terminus [174]. This cytoplasmic region is known to exchange Cu(I) with the *S. cerevisiae* cytoplasmic, secretory pathway metallochaperone Atx1 [175]. This protein in turn delivers Cu(I) to the Atx1-like domain of the membrane bound secretory vesicle protein Ccc2 [176,177]. In an analogous system, reliant on Cox17, copper is delivered to the intermembrane space of the mitochondria where it is shuttled along inner membrane proteins before transfer to cytochrome c oxidase [178].

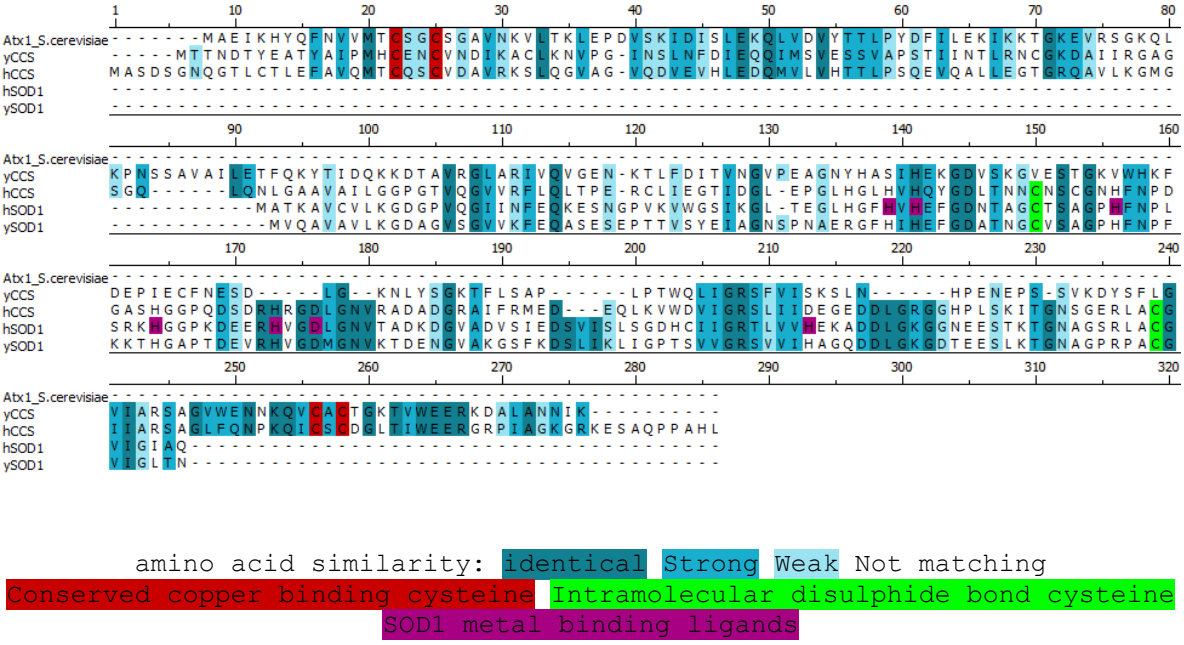


Figure 5.1. Multiple protein sequence alignment CCS and SOD1 proteins. *S. cerevisiae* Atx1 (GI:1255959), yCCS/LYS7 (GI:729967), hCCS (GI:49456811), hSOD1 (GI:49456443) and ySOD1 (GI:1015812) generated using BLOSUM [179].

Human SOD1 is found in the cytoplasm and the mitochondrial intermembrane space [46,180]. In each of these locations Copper Chaperone for SOD1 (hCCS) interacts directly with SOD1 and can load copper into the nascent protein [181-183]. hCCS was first discovered as a homolog of a yeast protein (Lys7/yCCS) that specifically delivered copper to yeast SOD1, indeed, hCCS is 26% identical to yeast yCCS (Figure 5.1) and displays similar domain architecture [182].

### 5.3 Domain architecture of hCCS

Domain I of both hCCS (residues 1 - 80) and yCCS shows considerable homology to the *S. cerevisiae* Atx1 protein (Figure 5.2A). This region contains a conserved MXCXXC motif seen at the N-terminal region of several copper transport proteins [184-186]. This motif has been shown to bind Cu(I) [187,188] and other metal ions [189,190]. Removal of this domain from the yCCS protein does not eliminate its activity as a domain II/III truncation protein could effectively complement a LYS7Δ strain [191]. However, under copper limited conditions domain I is essential for LYS7Δ complementation [191]. Conversely, domain I was proved essential for human CCS functioning with deletion of this domain ablating activation of SOD1 *in vivo* in embryonic fibroblasts [192].

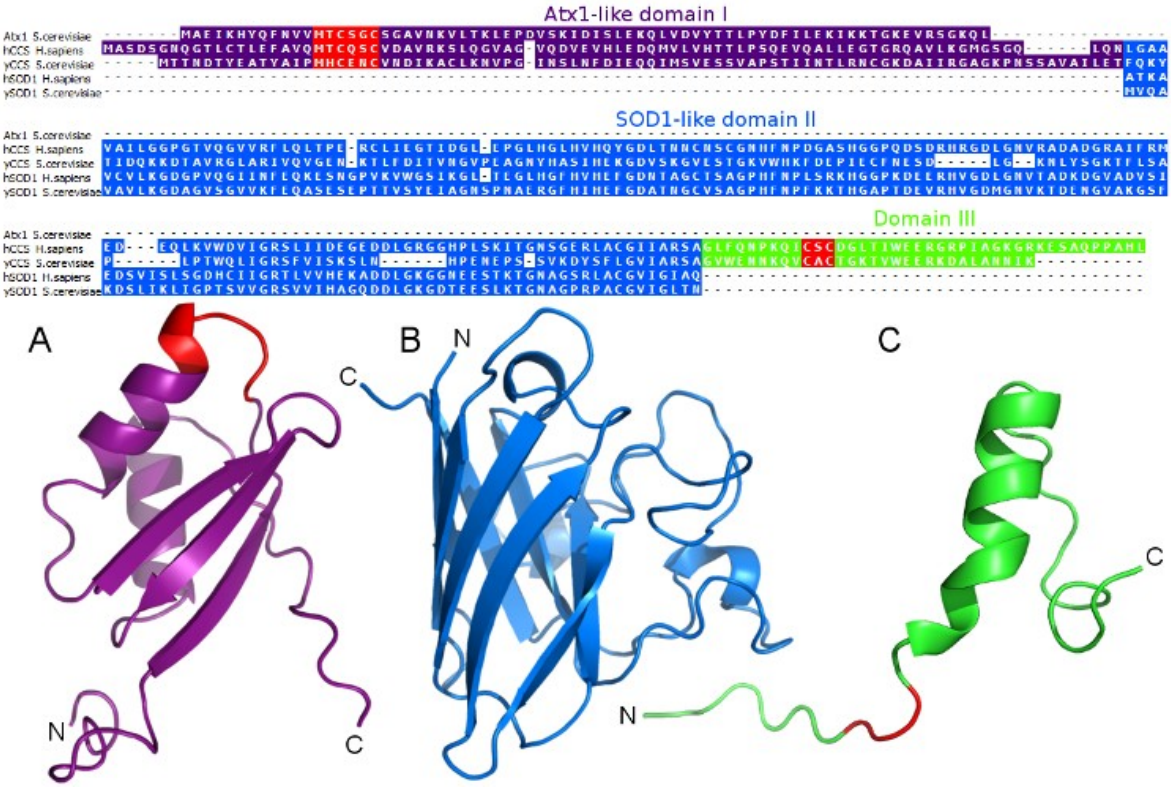


Figure 5.2. Structures of the three hCCS domains. (A) NMR structure of the Atx-1 like domain I (2CRL), (B) crystal structure of SOD1-like domain II monomer (1DO5) and (C) the predicted structure of domain III. Copper-binding regions are indicated in red. Taken from *Wright et al* [193].

Domain II (residues 85 - 234) exhibits 50% identity to wild-type hSOD1 (Figure 5.2B). Similarity between these proteins extends to the catalytic copper and structural zinc binding sites of SOD1 (Figure 5.1, purple residues). The metal coordinating amino acids are intact in hCCS except for the residue corresponding to histidine 120 which is replaced

by aspartic acid. The reverse mutation at this site bestows superoxide scavenging activity on yeast CCS but the native protein is not functional as a dismutase [194]. This arrangement proposes a copper binding site in CCS similar to that of SOD1 and seems to be an obvious protagonist in the transfer of copper to its destination. However, these residues were not required for SOD1 activation when tested in the yeast system [191]. Crystallographic studies on hCCS domain II found that this pseudo-copper site was not occupied but the zinc site was occupied [195]. The presence of zinc in the SOD1-like site was subsequently confirmed by EXAFS [196].

hCCS domain II also houses two cysteine residues that align with those involved in the SOD1 intramolecular disulphide bond (Figure 5.1, green residues). This disulphide bond is present in the crystal structure and anchors strand eight of the β-barrel to the disulphide loop as in SOD1 [195].

Domain III (residues 235 – 274, Figure 5.2C) is very highly conserved among CCS proteins from different species and was proven essential for yCCS function under all conditions [191]. It contains a CXC motif that binds Cu(I) and is essential for transfer of copper to SOD1 [191]. Based on XAS data and recombinant CCS copper content, *Eisses et al* proposed this motif could interact with the MXCXXC of domain I or another domain III from a CCS homodimer partner [197]. These interactions are likely to occur under non-limiting copper conditions via a di-, tri-, or tetra-nuclear copper cluster [196].

Equally important for the maturation of SOD1 is the oxidation of its intramolecular disulphide bond [75]. While formation of this bond can be catalysed by oxygen [80] and reduced glutathione [82], CCS is the primary catalyst for most organisms and is the only system in yeast [80,198]. Crystallisation of a ySOD1 H48F mutant in heterodimeric complex with yCCS revealed a disulphide bond between ySOD1 Cys57 and yCCS domain III Cys229 [199]. This finding demonstrates a possible mechanism by which SOD1 acquires an intramolecular disulphide bond concomitantly with copper loading.

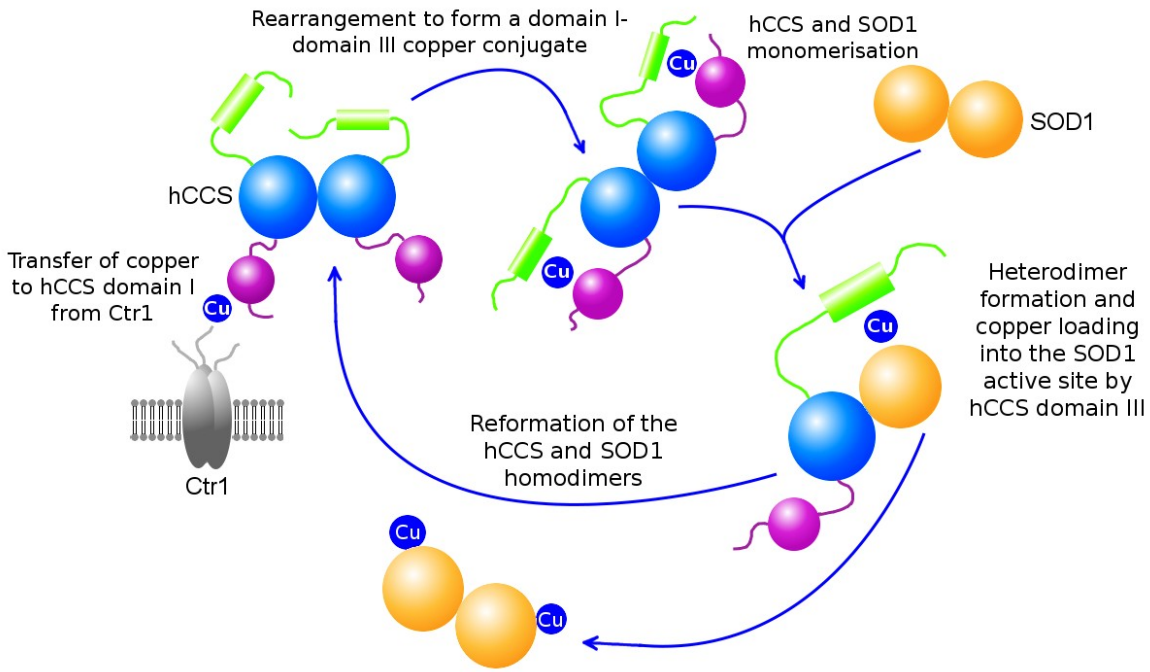


Figure 5.3. The accepted mechanism of SOD1 copper loading by hCCS.

To summarise, hCCS appears to contain one zinc ion in domain II at the SOD1 analogous site. The domain II copper site is not necessary for function and is not necessarily occupied. Figure 5.3 describes the function of hCCS in SOD1 activation. Domain I sequesters copper from the environment or CtrI and passes it to domain III. A hetero-complex is formed through an interaction between CCS domain II and SOD1. Copper loaded domain III then forms an intermolecular disulphide bond with SOD1 Cys57 and transfers copper to the SOD1 active site. Subsequent reorganisation of this disulphide creates the SOD1 internal disulphide and enables separation of the hetero-complex.

## 5.4 X-ray scattering

X-ray scattering and X-ray crystallography are related techniques that exploit the elastic scattering of X-rays by electrons in matter. Both rely on measurement of the intensity and angle of deflection of X-rays scattered by the sample. The fundamental difference is the nature of the substance under investigation. Crystallography utilises the periodicity of the crystalline lattice and the superposition property of electromagnetic radiation to enable atomic level characterisation of the sample. X-ray scattering on the other hand measures isotropic scattering and does not require the sample to be crystalline. In fact scattering can be performed on any non-crystalline material including liquids, gasses, amorphous solid

and, most importantly for protein characterisation, molecules in solution [200].

### 5.5 X-ray scattering by biological macromolecules in solution

Protein in solution is of primary interest to the structural biologist and although the principles of X-ray scattering hold regardless of the state of the sample what follows is concerned with small angle X-ray scattering (SAXS) from protein solutions. In a sufficiently large volume and concentration of such a solution all orientations of the solute molecule are present simultaneously. Thus scattering occurs radially around the beam and is equivalent to the scattering from a single particle averaged over all orientations according to the Debye equation [201]

$$I(q) = \int_V \int \rho(r_1)\rho(r_2)\frac{\sin qr_{12}}{qr_{12}} dr_1 dr_2$$

where $r_{12}$ describes the spatial distance between scattering atoms $\rho(r_1)$ and $\rho(r_2)$ in volume $V$ with $q$, momentum transfer, given by the equation

$$q = \frac{4\pi \sin\theta}{\lambda}$$

where, $\lambda$ is wavelength and $\theta$ is half the angle between the incident and scattered radiation. The highest intensity $(I)q$ is found parallel to the incident beam ($2\theta = 0$) and decreases as $2\theta$ increases. A characteristic scattering profile is obtained by subtracting scattering by the buffer from that of the protein solution and plotting intensity against momentum transfer. The lowest angle part of this curve is dictated by the radius of gyration, $R(g)$ which is the root mean squared distance of each scatterer from the molecule's centre. At low $q$, scattering can be approximated by the Guinier approximation [202]

$$I(q) = I(0)\exp\frac{(-q^2 R_g^2)}{3}$$

Thus $R(g)$ can be calculated by

$$R(g)=\sqrt{-3\mathrm{m}}$$

where m is the gradient of the Guinier plot, $I(q)$ vs $q^2$. Linearity of the Guinier region gives a good indication of sample monodispersity.

A Fourier transform of the scattering profile gives the pair distance distribution function, $p(r)$. The $p(r)$ function is given by

$$p(r)=\frac{1}{2\pi^2}\int_0^\infty I(q)qr\sin(qr)dq$$

and describes the frequency of intra-atomic lengths and the scattering particle's maximum linear dimension [202], $D_{max}$. A plot of this function is useful when appraising the overall shape and anisometry of a molecule.

### 5.6 *Ab initio* shape restoration from the scattering curve

While precise atomic co-ordinates cannot be gleaned from SAXS data, a representative three dimensional molecular envelope can be constructed from a scattering profile without previous knowledge of protein structure. Several algorithms have been developed for *ab initio* shape restoration. The most widely used of these generate models using beads to fill a volume defined by the deduced scattering parameters in a way that produces a scattering profile which approaches that obtained experimentally. An inherent flaw in this approach is that many diverse models can be generated that fit the experimental data. This can be overcome to some extent by repetition of the method and averaging the pool of structures.

GASBOR, the shape restoration algorithm exploited in the following chapters creates a three dimensional model by finding a chain-compatible spatial arrangement of dummy residues that fits the scattering profile up to 0.5 $Å^{-1}$ [203]. Dummy residues are centred on hypothetical $C_\alpha$ atoms and must be at most 3.8 Å from its nearest neighbour ensuring compactness and connectivity. A final model is condensed from a spherical assembly of dummy residues by a cyclic simulated annealing protocol until further optimisation does

not change a goal function which incorporates the described constraints.

### 5.7 Rigid body modelling

A SAXS model can be thought of as a low resolution envelope in which one can fit high resolution structures. For proteins with multiple domains connected by flexible linkers or subunits this is the aim of rigid body modelling against SAXS data and can provide more detailed information than space filling *ab initio* models solely. As with *ab initio* methods, rigid body modelling attempts to minimise the difference between experimental and theoretical scattering by changing the relative orientations of domains. If steric and electrostatic restraints are applied to limit translation and rotational domain shifts, models can be generated which represent conformational variations of these mobile domains thus indicating possible dynamic features.

Here the programs BUNCH and CORAL [204] have been used to fit known domain structures against experimentally obtained scattering profiles. These programs model full-length proteins as rigid domains linked by flexible chains of dummy $C_\alpha$ atoms [204]. Each rotation or translation of a domain changes its scattering amplitude so that the scattering intensity, $I(q)$ of the complex is given by

$$I(q)=\left\langle \left| \sum_{k=1}^{K} A^{(k)}(q) \right|^{(2)} \right\rangle_{\Omega}$$

where $A^{(k)}(q)$ is the scattering amplitude of the $k^{th}$ rigid body and $< >_\Omega$ accounts for spherical averaging in reciprocal space. Each model is assessed for its goodness of fit to the experimental intensity, $I_{exp}(q)$ by the magnitude of

$$\chi^2=\frac{1}{N-1}\sum_j \left[ \frac{I_{\exp}(q_j)-cI(q_j)}{\sigma(q_j)} \right]^2$$

where $\sigma(q_j)$ is the experimental error at momentum transfer ($q_j$), $N$ is the number of experimental points and c is a scaling factor.

## 5.8 Summary

While the yeast CCS homolog has been characterised structurally and biochemically hCCS is still relatively unknown. Structural information regarding this protein is limited to a 2.75Å resolution crystal structure of the central SOD1-like domain [195] and a NMR structure of domain I deposited in the Protein Data Bank by the RIKEN structural genomics initiative. Full length hCCS has never been directly observed and the conformational dynamics of this entire class of proteins are completely uncharacterised. Similarly, details of the interaction between hSOD1 and hCCS are sparse. The two successive chapters describe the cloning, expression and purification of recombinant hCCS from an *E. coli* host. This is followed by characterisation of hCCS in solution by small angle X-ray scattering. Finally the functionally crucial heterodimeric complex formed by hCCS and SOD1 is characterised using SAXS and the implications of this work are discussed.

# Chapter VI

## Solution X-ray scattering studies on hCCS and SOD1

### 6.1 Expression of recombinant hCCS in *Escherichia coli* and purification

DNA coding for wild-type human CCS was amplified from an EST clone and inserted, using a ligation dependent cloning approach, into the pET-24d derived plasmid pETM-11 to yield the expression plasmid pETM11-hCCS. Expression from this plasmid is driven by T7 RNA polymerase on induction with a suitable inducer [205]. Recombinant human CCS expressed as described is fused with a hexa-histidine tag that facilitates purification of the protein by nickel affinity chromatography [206].

Expression of recombinant protein from the pETM-11 vector incorporates the amino acid sequence Glu-Asn-Leu-Tyr-Phe-Gln-Gly-Ala prior to its N-terminus. This sequence is the target site for TEV (tobacco etch virus) protease [207] and can be used to remove the extra amino acids which form the protein's poly-histidine tag. Cleavage takes place between the Gln-Gly residues leaving glycine and alanine N-terminal to the primary methionine. Recombinant hCCS can then be purified to homogeneity by removal of the free poly-histidine tag and 6His-TEV protease from the solution by reapplication to the NiNTA column (Figure 6.1).

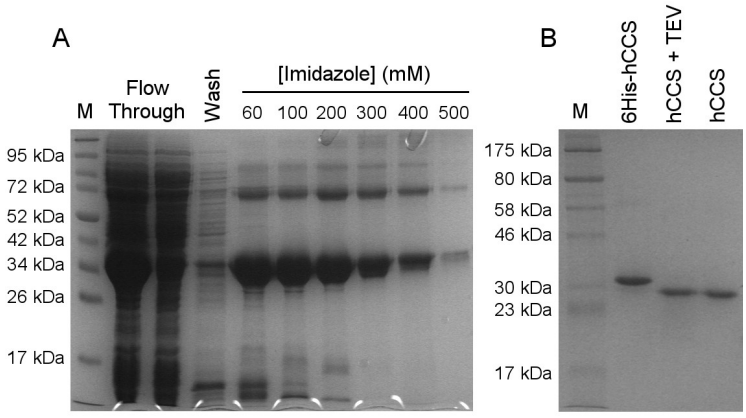


Figure 6.1. Purification of recombinant hCCS. (A) SDS-PAGE separation of fractions from the purification of polyhistidine tagged hCCS by nickel affinity chromatography. (B) SDS-PAGE separation of samples from the digestion of 6His-hCCS by TEV protease followed by reverse purification on a NiNTA column. Digestion was performed on ~50mg 6His-hCCS at 4°C with 100µg/ml TEV protease overnight. SDS-PAGE separation in both cases was performed with 12% resolving-4% stacking Tris-glycine protein gels and stained with coomassie stain.

Purification of hCCS by this method yields ~90 mg/l of liquid culture and the protein can be concentrated over 25 mg/ml. The protein has a molecular mass of 29.168 kDa (Figure 6.2) which compares very well with the predicted peptide molecular mass of 29.1687 kDa. It contains a stoichiometric amount of zinc but negligible copper as determined by electrospray ionisation mass spectroscopy (ESI-MS) and inductively coupled plasma mass spectrometry (ICP-MS) respectively. When the protein is examined by size exclusion chromatography a dominant peak at ~60 kDa is observed indicating that hCCS produced in this way is predominantly dimeric (Figure 6.3). However tetrameric protein is also observed, as previously described by *Winkler et al* [208] and *Rae et al* [209].

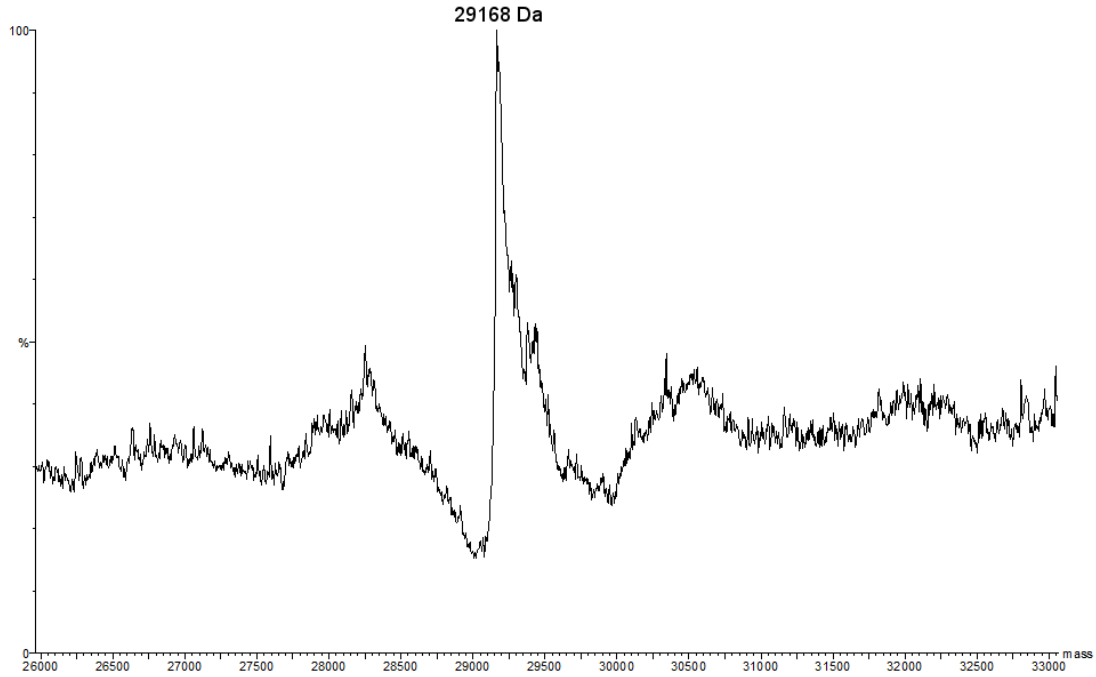


Figure 6.2. Electrospray ionisation mass spectrometry of recombinant hCCS.

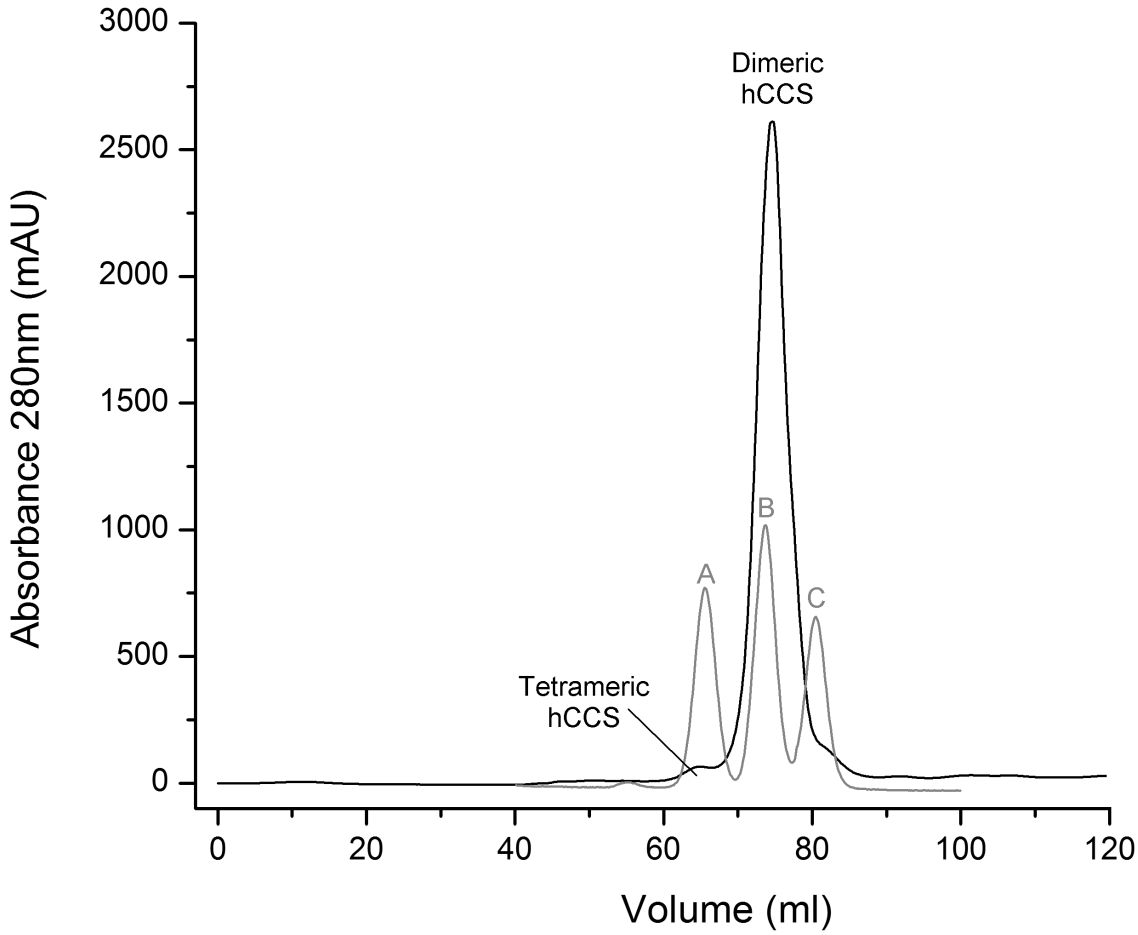


Figure 6.3. Size exclusion chromatography profile of recombinant hCCS. Fractions from NiNTA chromatography suspected to contain hCCS were pooled, concentrated to 2 ml, loaded and separated on a calibrated Superdex 200 16/60 gel filtration column with an ÄKTA purifier with flow rate of 1 ml/min at 20 $^{o}$C under reducing conditions. The column was calibrated (grey) with A - aldolase 158 kDa (65.5 ml), B – bovine serum albumin 67 kDa (73.5 ml) and C - ovalbumin 43 kDa (80.5 ml). A characteristic peak at ~74 ml is observed corresponding to the hCCS dimer (black).

The structure of the apo-hCCS domain I, deposited in the Protein Data Bank by the RIKEN structural genomics initiative (PDB ID: 2CRL), shows no sign of oligomerisation. This rules out domain I as the possible dimerisation site when it is in the copper-apo form. The yeast CCS homolog is known to form a dimer through the interaction of its SOD1-like domains [210]. Similarly, hCCS truncated to comprise only domain II exhibited a similar domain interface in the crystal structure to that of SOD1 [195]. We can infer therefore that full length hCCS in the copper depleted state forms a dimer with domain II as the interface. This point is important to emphasise as the following sections deals with the interpretation of small angle scattering data where dimerisation through domain II was imposed while modelling hCCS in solution.

### 6.2 hCCS small angle X-ray scattering and assignment of scattering parameters

Scattering experiments were performed on the SWING beamline at Synchrotron SOLEIL, Paris. This beamline incorporates an online size exclusion chromatography HPLC system for the separation of proteins immediately prior to exposure to the X-ray beam [211]. This synthesis of techniques eliminates the contribution of higher or lower molecular weight species from the scattering profile of the species under investigation. This was deemed especially important for hCCS as tetrameric protein exists in solution and large molecular weight aggregates form spontaneously. These species would disproportionally affect deduced scattering parameters as the intensity of scattering is proportional to the square of the total number of electrons which constitute the scatterer.

The apparatus allows the user to take numerous exposures over the course of protein elution. Initial analysis of the hCCS elution profile described in terms of the forward scattering intensity, $I(0)$, which is directly related to the concentration and molecular weight of the protein, indicates a major peak corresponding to the hCCS dimer preceded by that of the tetramer (Figure 6.4). The radius of gyration, $R(g)$, attains a steady value over the dimer peak but increases sharply moving toward the tetramer and higher molecular weights. This graph confirms the suspicion that SAXS measurement of the hCCS dimer in bulk solution is impractical due to the contribution from these species. Deduced SAXS parameters would be an average of every species in the heterogeneous sample. Using this graph one can estimate the $R(g)$ of dimeric and tetrameric hCCS to be approximately 30 Å and 40 Å respectively.

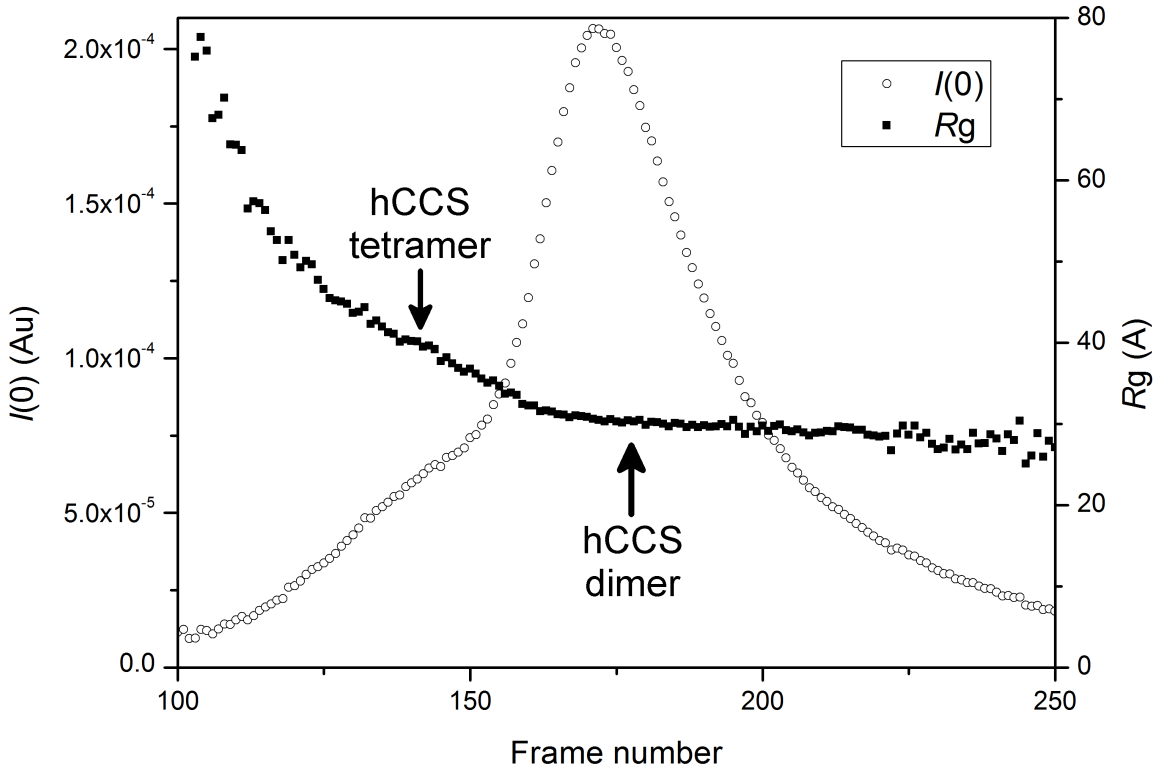


Figure 6.4. Size exclusion chromatography profile of hCCS described by radius of gyration and forward scattering intensity, $R(g)$ and $I(0)$. Frames 168 – 175 were averaged and used for the subsequent analysis. Adapted from *Wright et al* [193].

A region of this elution profile over the hCCS dimer peak with steady $R(g)$ values was averaged. The resulting single scattering profile is shown in Figure 6.5. Further manipulation of this data yields the Guinier plot in Figure 6.6, distance distribution function Figure 6.7 and Kratky plot Figure 6.8.

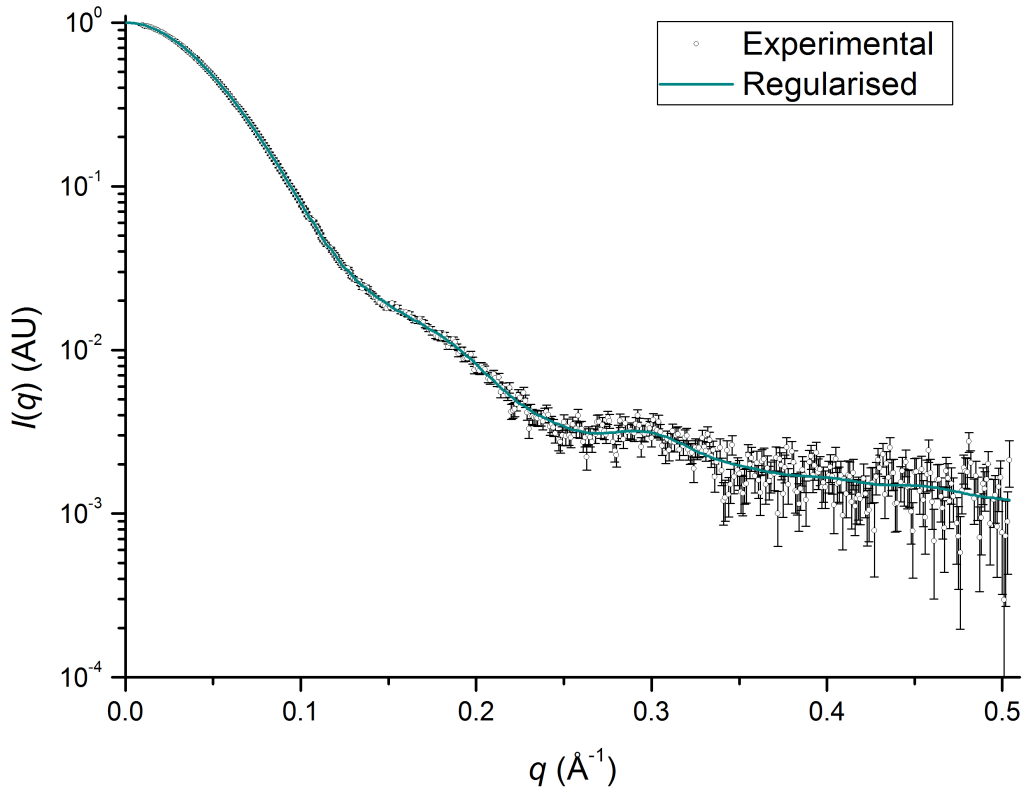


Figure 6.5. Solution X-ray scattering profile of hCCS. Experimentally obtained scattering curve with errors is in black while the smoothed scattering profile obtained by back-transform of the $p(r)$ (Figure 6.7) is cyan.

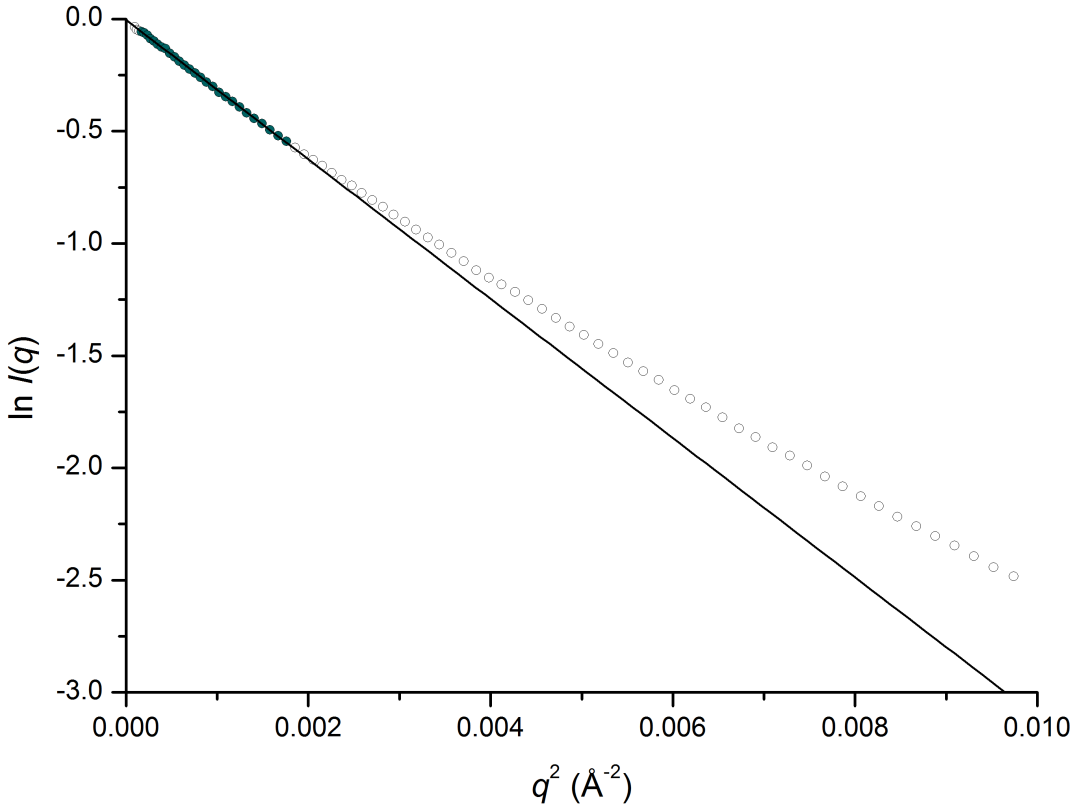


Figure 6.6. Guinier plot of X-ray scattering from hCCS. Data points (4 - 30) used in the Guinier approximation are highlighted cyan.

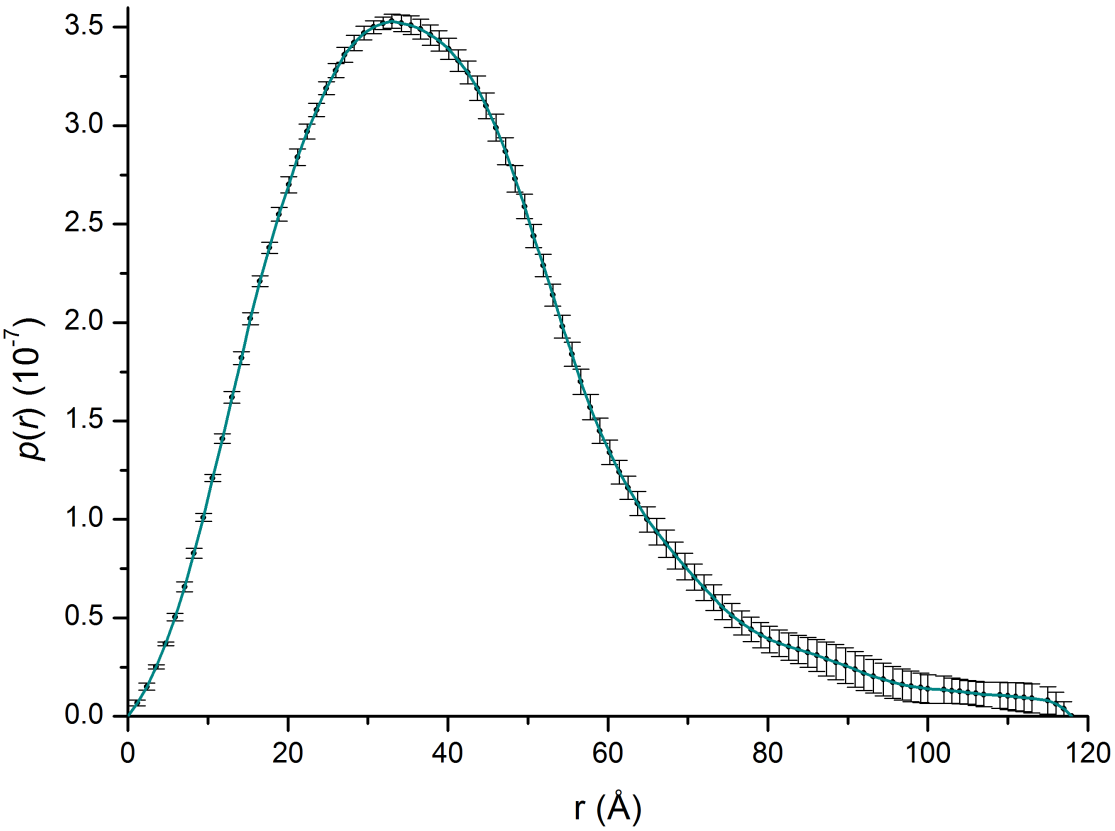


Figure 6.7. hCCS distance distribution function, $p(r)$. Errors are increased by a factor of 10.

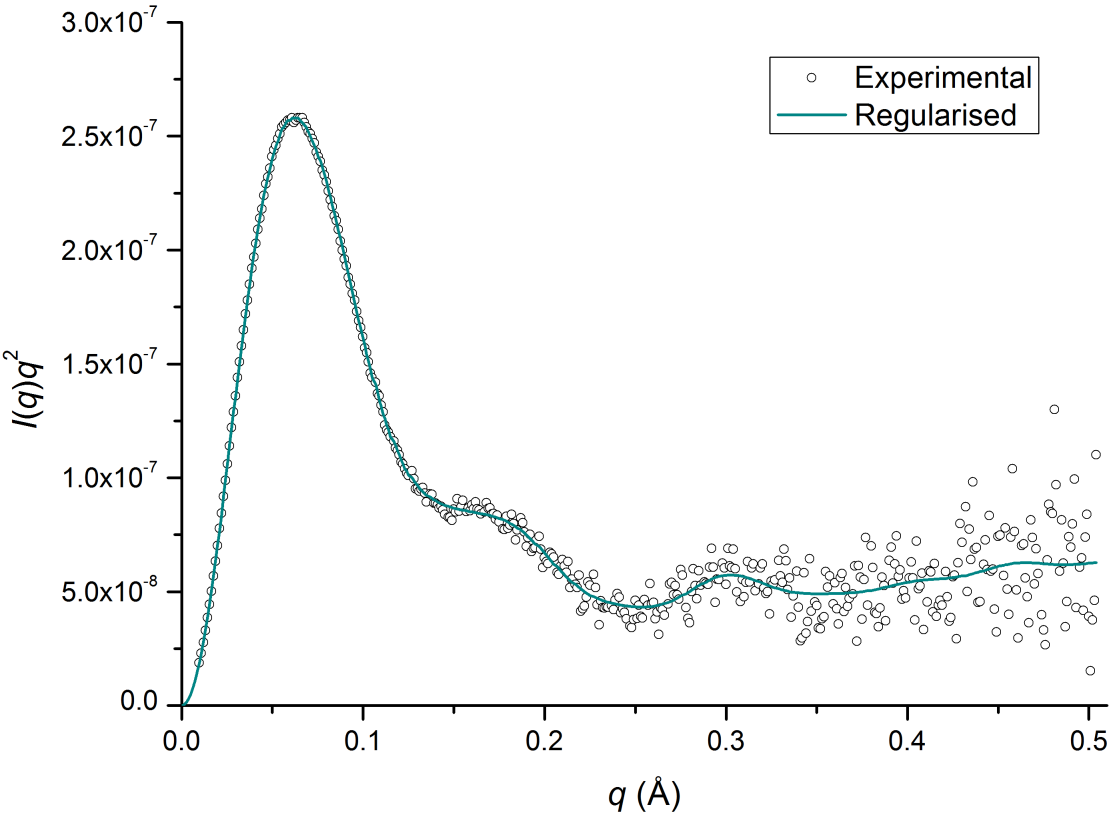


Figure 6.8. hCCS Kratky plot.

Figure 6.6 shows the Guinier plot of the hCCS scattering profile at very low $q$. The calculated radius of gyration $R(g)$, related to the gradient of the linear part of the plot by the Guinier approximation, is 30.5 ± 0.3 Å. This equates well with the $R(g)$ value, calculated from the $p(r)$ function (Figure 6.7), of 31.5 ± 0.3 Å. The maximum particle dimension, $D_{max}$, given by the intercept of the $p(r)$ function with the $x$ axis is 118 ± 5 Å. The asymmetric shape of the $p(r)$ function, with $D_{max}/2$ significantly larger than the peak maximum is indicative of an elongated molecule. A Kratky plot is a useful measure of the compactness of a protein. A folded protein will produce a bell-shaped plot at low angles that approaches the abscissa at high $q$ values. Conversely a non-compact or unfolded protein will remain high after the initial maximum. Figure 6.8 shows the Kratky plot for hCCS and demonstrates the largely folded nature of hCCS as the trace returns to the baseline after the primary peak.

### 6.3 *Ab initio* shape reconstruction

The scattering data described in the previous section was used to construct a three-dimensional model of the hCCS dimer using the *ab initio* shape reconstruction program GASBOR. This program finds an arrangement of residues that best describes the scattering pattern of the studied protein starting from a random collection of residues approximated by spheres [203]. Initial model building attempts using a two-fold symmetry axis resulted in higher than anticipated goodness of fit values ($2.54<\chi^2<3.39$) for the generated structures. When symmetry was not imposed on model building these values were consistently improved ($1.90<\chi^2<3.14$). This indicates there is little symmetry between the two monomers that comprise the hCCS dimer and domain I and III appear to be largely independent with respect to their counterparts in the other monomer. Using GASBOR, 20 models were constructed and the structure found to be the most typical (Figure 6.9) was then used as the reference for averaging. Of the 20 models (Figure 6.10), one was rejected from the averaging process on the basis that it showed dissimilar shape compared to others in the cohort.

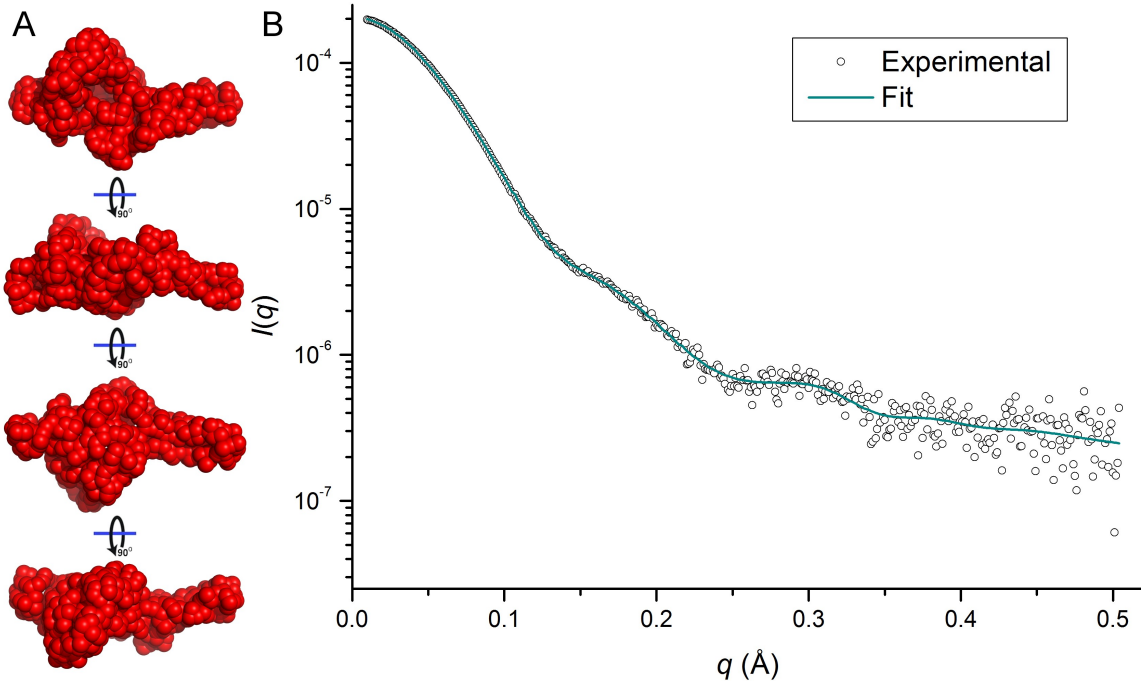


Figure 6.9. *Ab initio* P1 shape reconstruction of hCCS. (A) A single reconstruction is depicted rotating 360° along its long axis, $\chi^2$ = 1.9. (B) The computed profile of the reconstruction with the hCCS experimental scattering for comparison.

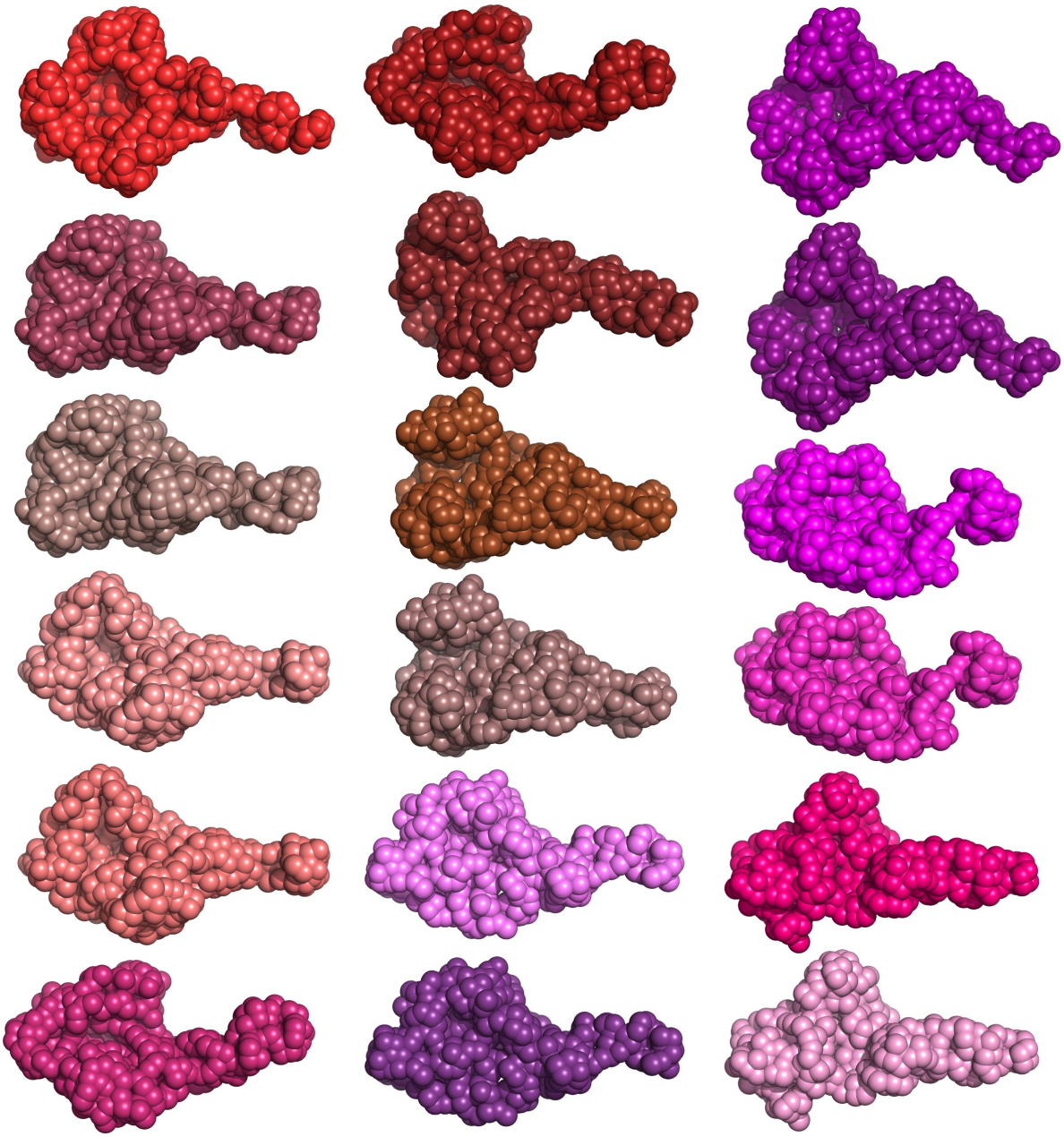

Figure 6.10. 18 *ab initio* P1 shape reconstructions of hCCS. The models presented have goodness-of-fit values $1.9<\chi^2<3.1$.

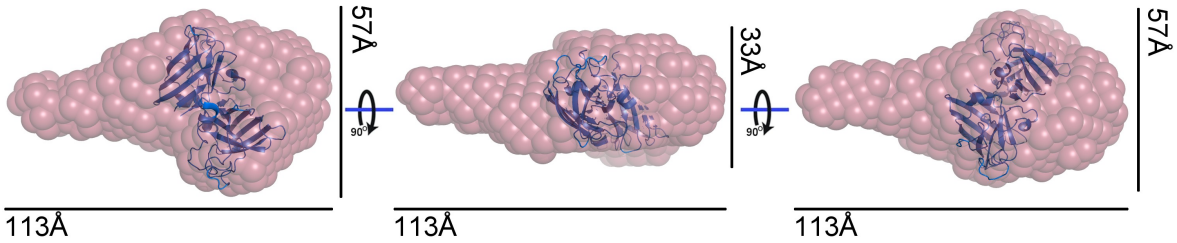


Figure 6.11. Consensus shape of all *ab initio* non-symmetrical SAXS models of hCCS. For comparison a ribbon model of the crystal structure of hCCS domain II (blue, PDB: 1DO5), which closely resembles the SOD1 dimer is superimposed on the average 3D shape model (red). The model is shown moving through a 180° rotation along the long axis with approximate dimensions added.

Domain II forms the interface between hCCS monomers and this model adequately provides volume to accommodate this interaction. In every model used to generate this average there are two regions of mass that are not accounted for by the central domain II. These areas must therefore contain domains I and III. The elongated 3D shape reflects the observation that the characteristic $p(r)$ function has an asymmetric curve shape with $D_{max}/2$ being significantly larger than the r-value at peak maximum. Moreover the *ab initio* shape reconstruction confirms that the overall conformation of hCCS in solution displays no obvious overall symmetry.

### 6.4 Rigid body modelling of hCCS

Given the multi-domains assembly with predicted flexible polypeptide segments of full-length hCCS it is not expected to exist as a rigid, globular macromolecule in solution. It is more likely to exhibit conformational plasticity with domains I and III able to move freely with respect to domain II. In fact this movement is a necessity if hCCS is to perform copper transfer by the proposed mechanism. In order to explore the conformational space occupied by hCCS and the biologically relevant interactions between these domains their arrangement and positions were modelled by fitting high resolution structures (Table 6.1) to the experimentally determined SAXS envelope. This was performed using the program BUNCH [204]. The hCCS C-terminus has no associated structure in the public databases therefore an homology model was constructed using that part of the yCCS C-terminus that is visible in the structure of the yCCS-ySOD1 complex (PDB ID: 1JK9).

| | Name | Amino acids | Source | PDB ID |
|---|---|---|---|---|
| **Domain I** | Atx1-like | 12 – 69 | NMR | 1QUP |
| **Domain II** | SOD1-like | 88 - 232 | Crystal | 1DO5 |
| **Domain III** | | 250 – 258 | Homology model | |

Table 6.1. The three hCCS domains used in rigid body modelling.

Each different rigid body model generated by this process is consistent with the SAXS data as indicated by a very good fit to the experimental scattering profile fit to the experimental results (Figure 6.12). These models collectively, therefore, represent a pool of potential

domain arrangements hCCS can adopt in solution. By taking these models together one can ascertain the likelihood that a domain will be found in a particular position. Figure 6.13 indicates that domain I forms a cloud around the central SOD1-like domain II and appears to be constrained by the length of the interdomain linker. In contrast however, domain III forms an extension into the solvent that is free to move. There is no indication of a domain swap between the two hCCS monomers and the possibility of a domain I-I or domain III-III interaction is also unlikely due to their spatial separation.

Domain I is essential for hCCS mediated incorporation of copper into SOD1 [192]. Reversible copper transfer has been observed between Ctr1 and Atx1 [175] and is likely to proceed in a similar fashion between Ctr1 and hCCS domain I. The initial stage of copper binding by domain I could be achieved by many of the models in Figure 6.13 where domain I is free, solvent exposed and receptive. These conformations would permit copper transfer to the Atx1-like domain from the C-terminus of hCtr1 while hCCS is in the dimer state. Initial acquisition seems to occur independently for each hCCS monomer due to the lack of interaction between opposing domains.

C-terminal domain III is then able to acquire copper from domain I. This interaction was postulated by *Eisses et al* based on EXAFS data [197] and is necessary if hCCS is to transfer copper between the two [192]. Transfer is facilitated by a conformation in which the two domains are physically adjacent (Figure 6.14). In this model the copper binding motifs are up to 10 Å apart allowing sufficient space for the adoption of a large multi-nuclear copper-sulphur cluster between the copper binding cysteines of each domain. In the absence of SOD1, this cluster formation presents a favourable and secure retention pocket for Cu(I) ions which may lead to a conformational change [209] that facilitates hCCS homodimer dissociation enabling realisation of the SOD1-CCS heterodimer.

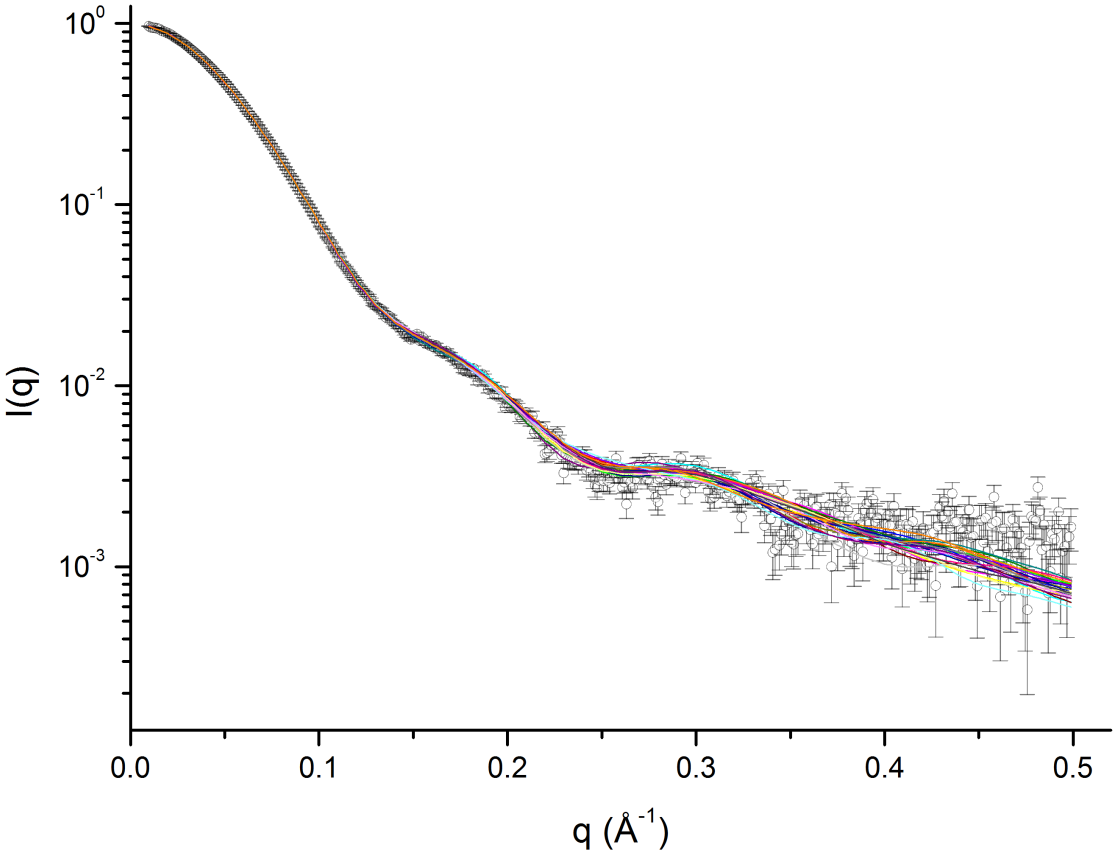


Figure 6.12 Scattering profile of 25 rigid body models of full length hCCS. The hCCS experimental scattering profile with error bars (black) with the computed profile of each individual rigid body model. The goodness-of-fit value ($\chi^2$) varies between 1.7 and 2.1.

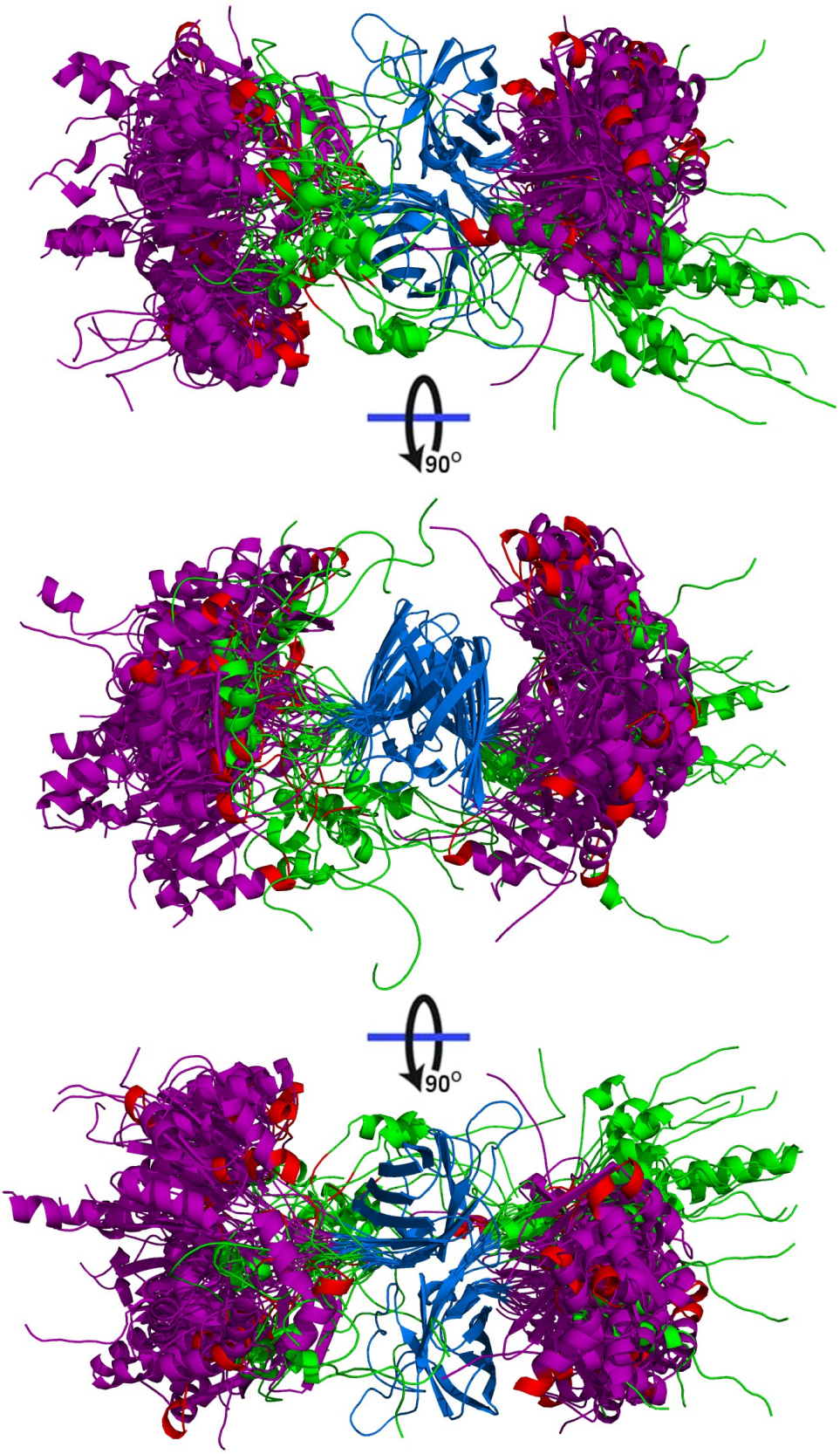


Figure 6.13. Solution structures of homodimeric hCCS. Twenty-five hCCS structures derived by rigid body modelling against experimental SAXS data rotated 180° around the long axis. Domain I is coloured purple, II-blue, III-green and copper binding motifs are depicted in red. Taken from *Wright et al* [193].

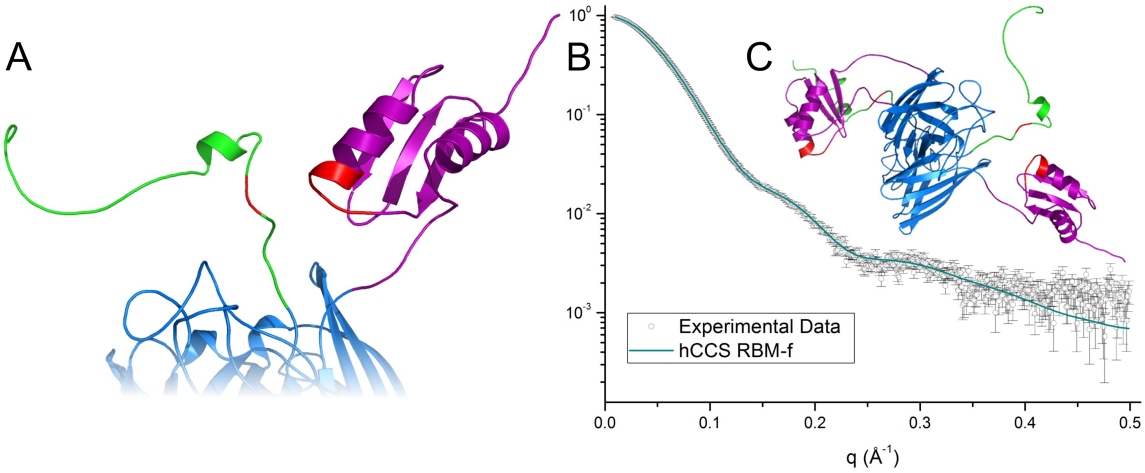


Figure 6.14. Interaction between the copper binding motifs of domains I and III. (A) Detail of the rigid body model. (B) Fit to experimental scattering data, $\chi^2 = 1.95$. (C) Complete model.

While the models of hCCS presented here lend themselves to a demonstration of the feasibility of copper movement between domains I and II they do not represent the complete spectrum of possible conformations. It is possible a mixture of conformations exist that satisfy the experimental data in totality but individually do not. Thus hyper-extended and compact structures may coexist in solution but which are not described in the pool of structures in Figure 6.13. Currently there is no substantiated and non-circuitous route with which to determine the composition of such a conformationally heterogeneous solution for oligomeric proteins.

### 6.5 Characterisation of human SOD1 by small angle X-ray scattering

Small-angle X-ray scattering has previously been used to characterise wild-type SOD1 and several fALS associated SOD1 mutants [89,212]. Large differences between wtSOD1 and A4V and I113T SOD1 mutants have been reported. These differences are illustrated by highly variable deduced scattering parameters and unusual perturbations in the proposed structural models of these two SOD1 variants. These parameters may have been affected by variable metal content and aggregation of the sample, two factors common to SOD1. To address this possibility and in order to make a valid comparison between SOD1, hCCS and their complex, wtSOD1 and two variants, each with well defined metallation state, were analysed by small-angle X-ray scattering in conjunction with size exclusion chromatography.

Figure 8.1 depicts the scattering profile of wild-type, L38V and I113T SOD1 in the copper-

apo, zinc-holo state. These profiles are of high quality with little experimental error throughout the length of the curves. Comparison of each scattering profile shows little difference (Figure 8.2). The previously reported $R_g$ and $D_{max}$ values for wtSOD1 are 20.6 Å [212] and 68 Å [89] respectively which compare well with the values reported here, 20.6 Å and 60 Å. The reported values for I113T SOD1 are however 22.9 Å and 82 Å [89] and seem to indicate a much less compact protein than those deduced here, 20.8 Å and 64 Å.

*Hough et al* reported a characteristic feature of the SOD1 scattering curve, a minimum at q = 0.25 $Å^{-1}$ [89]. This feature was found to be smoothed in the case of I113T SOD1 indicating a loss of structural integrity. There is no evidence in Figure 8.1B and C of such an effect in the I113T and L38V SOD1 mutants in comparison with wild-type.

Several lines of enquiry have implicated incorrect folding or protein unfolding in SOD1 fALS pathogenesis particularly when metal depleted [90,213,214]. Figure 8.3 portrays the Kratky analysis for the SOD1 proteins described above. In this case, L38V and I113T have almost identical Kratky plots when compared with wtSOD1 indicating that all three of these SOD1 proteins are equally well folded.

The lack of any gross structural perturbations resulting from the L38V and I113T mutations is confirmed by their *ab initio* shape reconstruction models (Figure 8.4). The dimeric nature of wtSOD1 is clearly visible in these structures as with the two mutants. However as the two SOD1 mutants are rotated along their long axis their widths and breadths appear to vary slightly with respect to wild-type SOD1. As the differences among the three scattering profiles (Figure 6.16) and structural parameters (Table 8.1) are not significant this is likely to result from slight variations in the shape restoration process rather than structural changes to the SOD1 molecules.

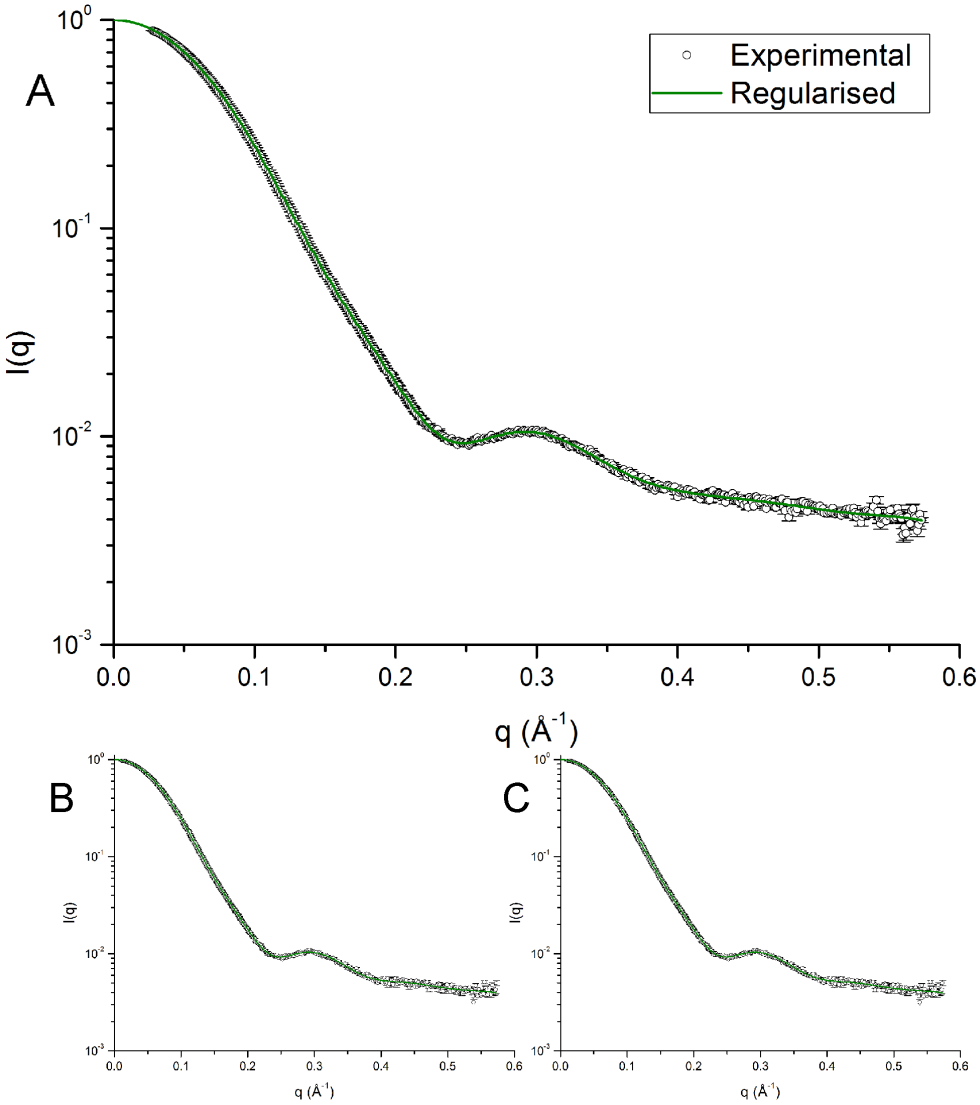


Figure 6.15. The scattering profile of human SOD1. (A) wtSOD1, (B) L38V SOD1 and (C) I113T SOD1.

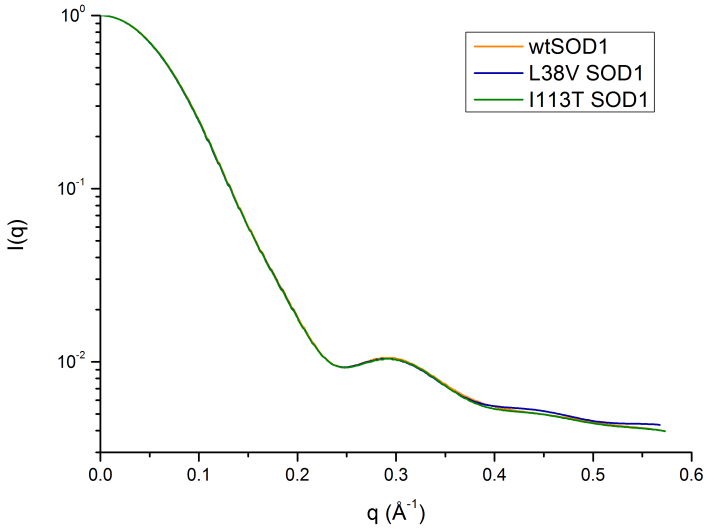


Figure 6.16. Comparison of the scattering profile of wild-type, L38V and I113T copper-apo zinc-holo SOD1.

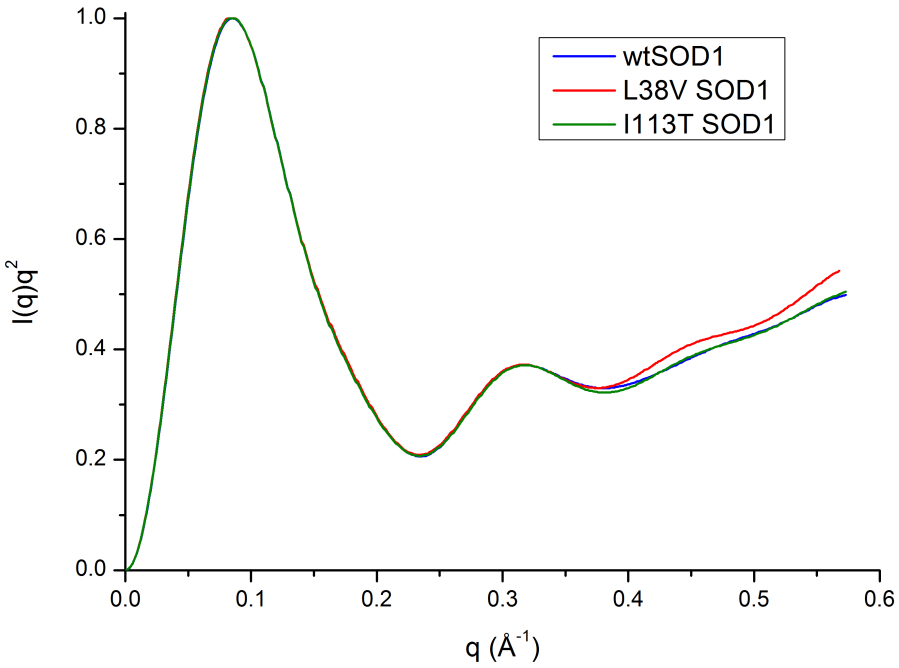


Figure 6.17. Kratky analysis of recombinant zinc loaded wild-type, L38V and I113T SOD1. The Kratky plot is normalised for the height of the peak maxima.

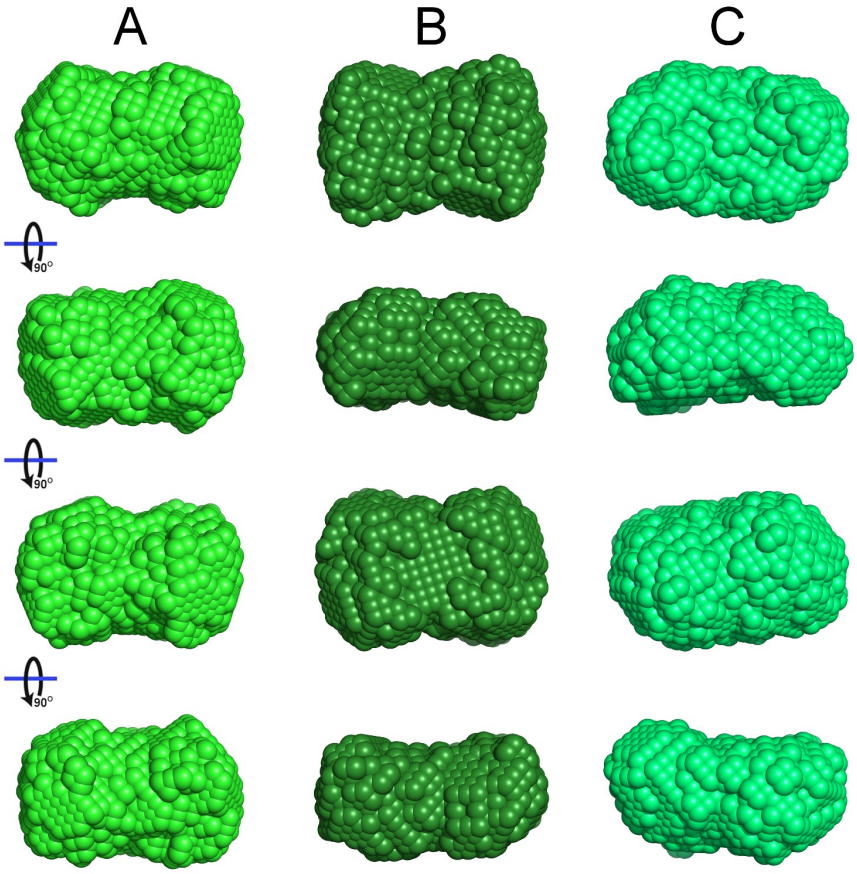


Figure 6.18. Small-angle X-ray scattering shape restoration models of human SOD1. (A) wtSOD1, (B) L38V SOD1 and (C) I113T SOD1. A two-fold symmetry axis was imposed on model building.

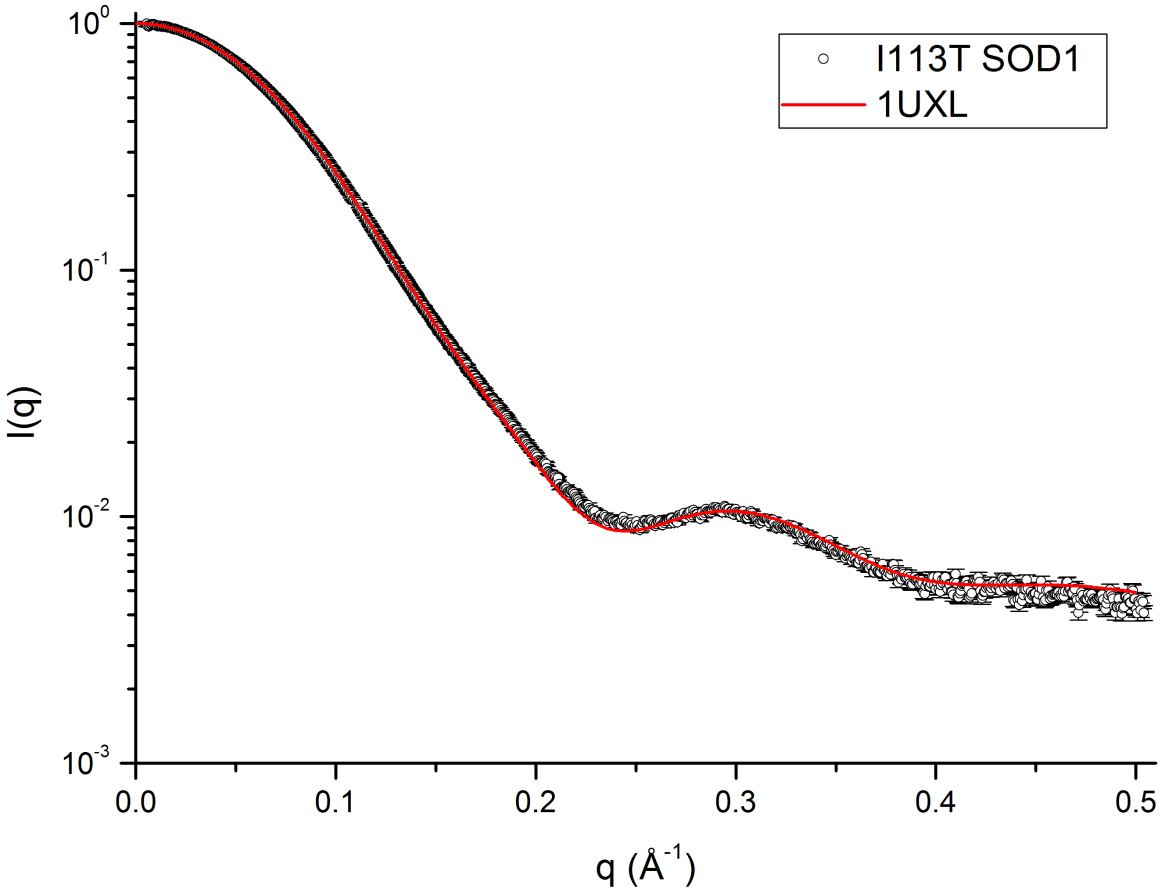


Figure 6.19. Comparison of the experimental scattering profile of I113T SOD1 with the predicted profile deduced from its crystal structure (1UXL).

The solution structure of I113T SOD1 has previously been elucidated and was found to have large extensions into the solvent originating from each monomer [89]. The data presented here indicate that L38V and I113T SOD1 have a gross structure very similar to that of wild-type with no evidence of these structural perturbations. Figure 6.19 compares the experimentally obtained scattering profile of I113T SOD1 with that of the profile deduced from its crystal structure (1UXL). It can clearly be seen from this plot that experimental and deduced profiles are very similar indicating that the protein does not adopt a conformation in solution different from that observed in the crystal.

There are two probable contributors to the discrepancy between the results described here and those of *Hough et al* [89]. Recombinant SOD1 expression in *E. coli* facilitates homogeneous metal loading, with the purified protein being more than 99 % copper-apo, zinc-holo. This results from the low copper concentration in standard LB media and the lack of a CCS bacterial homolog. Conversely, zinc is available and SOD1 seems able to bind it without the necessity of a zinc loading mechanism. The I113T SOD1 characterised

previously was expressed in *S. cereviseae* where it is metallated in a fashion akin to the situation in humans. In effect this means incomplete zinc and partial copper metallation.

Secondly, SOD1 is known to be aggregation prone, especially in its apo state. The inflated $R_g$ and $D_{max}$ values previously stated for both A4V and I113T SOD1 [89] are most likely a result of the presence of larger molecular weight species than the SOD1 dimer in the experimental sample. These species need only be trimers or tetramers, for example, in order to unduly effect the calculated $R_g$ and $D_{max}$ toward larger values without giving rise to the obvious signs of protein aggregation commonly observed in SAXS experiments. Homogenous metallation and protein separation immediately prior to data collection undoubtedly contributes to the concurrence of the scattering profiles presented here.

It must be concluded that there is no observable reorientation of the SOD1 monomers or large conformational changes that take place when SOD1 carries the L38V or I113T mutation when it is metallated as described above. As SAXS visualises the average structure present in a solution these results do not eliminate the possibility that a sub-population have perturbed and pathogenic structural features.

# Chapter VII

## Structural characterisation of the hCCS-SOD1 heterodimer by solution X-ray scattering

### 7.1 Construction of the hCCS-SOD1 heterodimer

Heterodimer formation between SOD1 and its chaperone has previously been documented for both yeast and human systems [208,215]. Both of these experiments used artificial copper site mutants to promote stable complex formation. The methodology used by these groups was followed here for the formation of the wild-type SOD1 containing complex with the addition of an incubation of SOD1 with reductant before mixing with hCCS. This incubation was necessary to reduce the SOD1 intra-subunit disulphide and 5 mM DTT at room temperature for a minimum of 4 hours was sufficient.

Complexation between hCCS and H46R/H48Q human SOD1 proceeds at stoichiometric protein ratios however yeast H48F and wild-type SOD1 require a 2 fold excess [208,215]. Here, heterodimer formation between human I113T, L38V and wtSOD1 was most effective with a 1.5 molar excess of SOD1. Figure 7.1A shows analysis of the wild-type complex by gel filtration. The size exclusion chromatography UV absorption trace obtained from the separation of 100 μM hCCS mixed with 150 μM reduced wtSOD1 indicates a maximum at 85ml. This peak is positioned between those obtained when either 100 μM hCCS (79 ml) or 150 μM wtSOD1 (90 ml) were loaded separately indicating the presence of a species of intermediate size. SDS-PAGE analysis of fractions taken over the course of this elution (Figure 7.1C) show clearly the presence of both hCCS and SOD1 in this region. For comparison, SDS-PAGE of fractions taken from hCCS and SOD1 loaded singly is presented in Figure 7.1B and C.

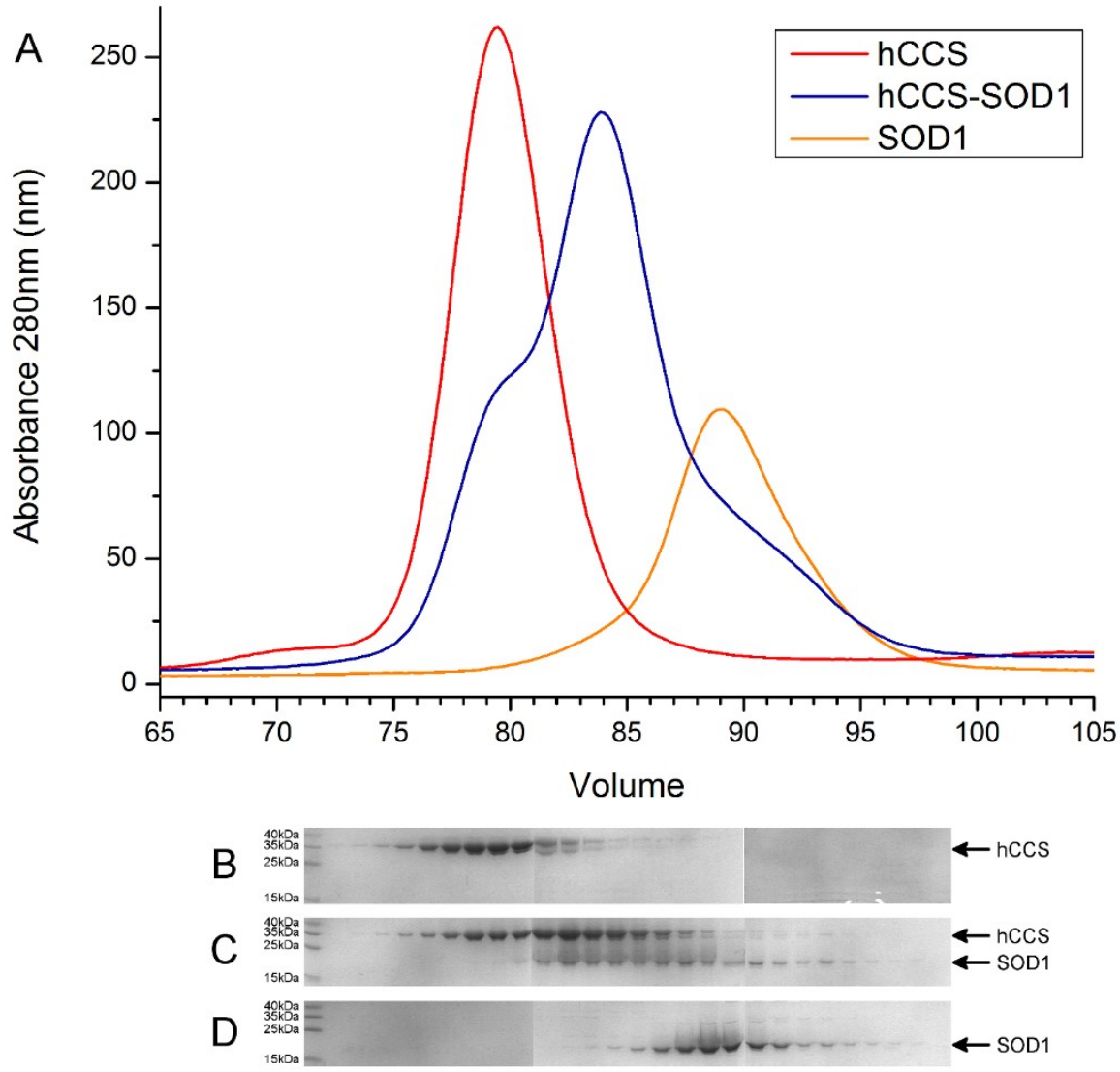


Figure 7.1. Size exclusion chromatographic and SDS-PAGE analysis of the hCCS-wtSOD1 heterodimer. (A) SEC profiles of 100 µM hCCS, 150 µM wild-type SOD1 and the hCCS-wtSOD1 complex constructed with 100 µM hCCS and 150 µM wtSOD1. 1 ml fraction were taken over the course of elution from 72 ml to 98 ml. (B) SDS-PAGE analysis of fractions from SEC of 100 µM hCCS. (C) SDS-PAGE analysis of fractions from SEC of hCCS-wtSOD1 heterodimer made with 100 µM hCCS and 150 µM SOD1. (D) SDS-PAGE analysis of fractions from SEC of 150 µM wtSOD1.

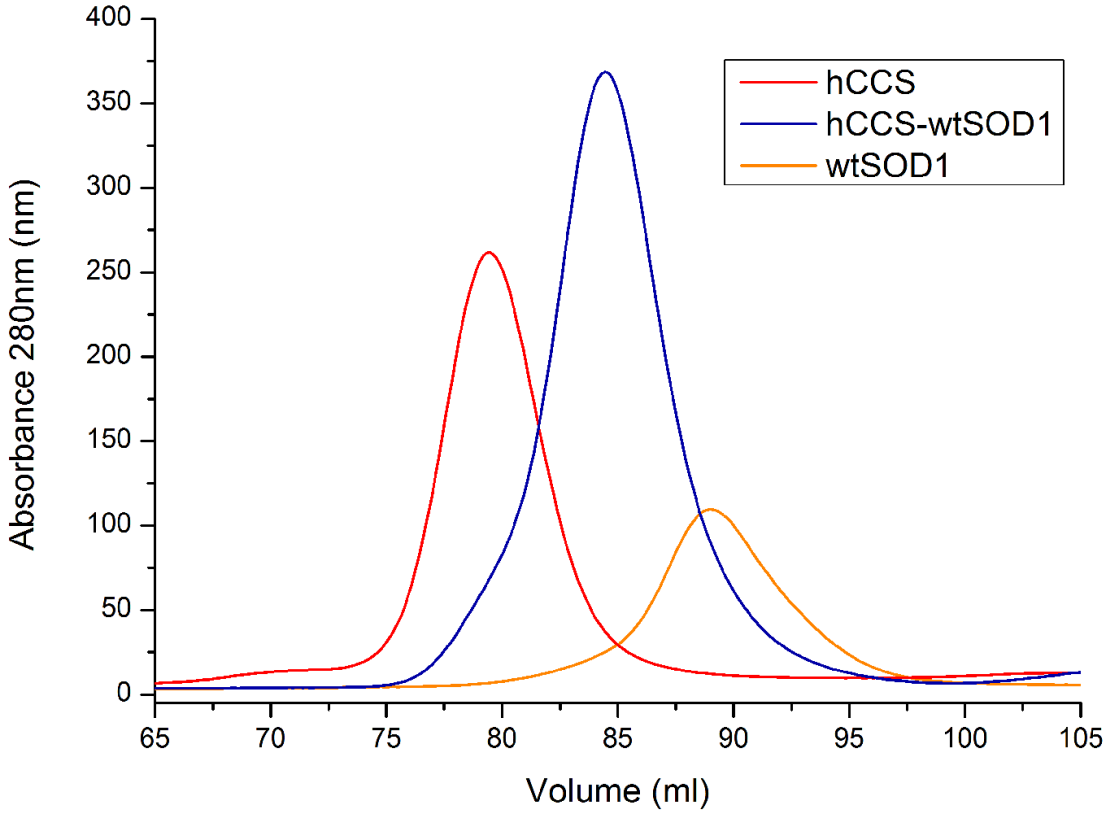


Figure 7.2. Size exclusion chromatography of the hCCS-SOD1 complex after purification and concentration. Three complexation experiments represented by Figure 7.1A-blue were pooled and incubated overnight at 4 $^{o}$C before concentrating to a 1 ml volume and reapplication to a Superdex 200 16/60 column.

Figure 7.1A-blue shows two clear shoulders on the hCCS-wtSOD1 complex gel filtration trace at positions where the maxima for homodimeric hCCS and SOD1 are found when loaded singly. These represent the native homodimer for each species and may be attributed to incomplete reduction of the SOD1 disulphide. An extended incubation of SOD1 with increased DTT did not promote complete complex formation. This would seem to indicate a dynamic equilibrium with approximately 10 % of each species remaining as the homodimer. Conversely, isolation of fractions corresponding to the hCCS-SOD1 complex followed by incubation overnight at 4 $^{o}$C and concentration before reapplication to the size exclusion chromatography column did not re-establish the equlibrium; the vast majority of protein remained in the heterodimeric state (Figure 7.2). A small amount of homodimeric hCCS is visible as a shoulder at 79 ml on this trace but this is likely to arise from incomplete separation at the previous gel filtration step and underscores the importance of the SEC-SAXS methodology used in the following sections.

### 7.2 SAXS data collection and assignment of structural parameters

Small-angle X-ray scattering data for the human CCS-SOD1 complex was collected at the SWING beamline at synchrotron SOLEIL replicating the methodology employed when measuring the hCCS homodimer with the exception of the size exclusion chromatography column. This change, to a Superdex 200 16/60 gel filtration column, was affected in order to maximise separation of the two homodimers from the heterodimer of interest.

Scattering was recorded from hCCS complexed with wild-type SOD1 and two fALS associated SOD1 mutants, L38V and I113T (Figure 7.3). Guinier analysis of the hCCS-wtSOD1 scattering profile indicates a radius of gyration for the complex of 24.8 ± 0.3 Å, indicating a dimer of size midway between the SOD1 and the hCCS homodimers. The distance distribution function indicates a maximum particle dimension ($D_{max}$) of 89 ± 3Å (Figure 7.4). A comparison of structural parameters deduced from SAXS for the three complexes studied here is presented in Table 7.1.

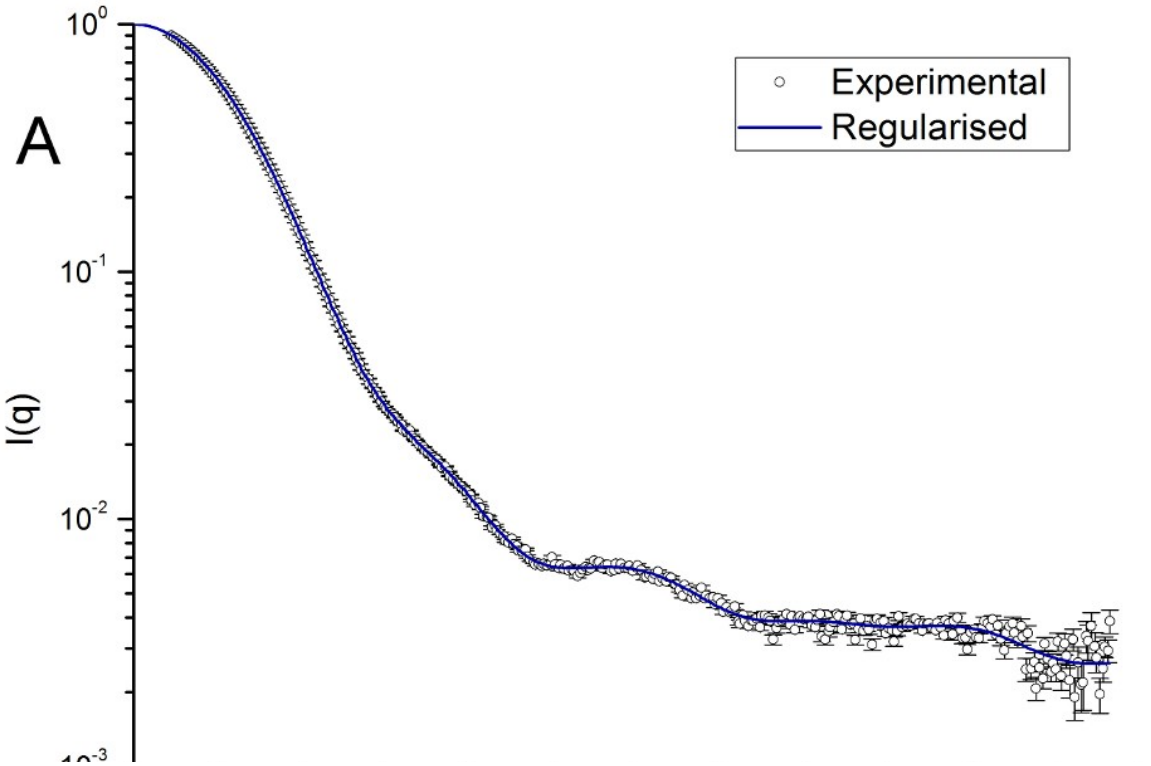
A
Experimental
Regularised
I(q)
$10^0$
$10^{-1}$
$10^{-2}$

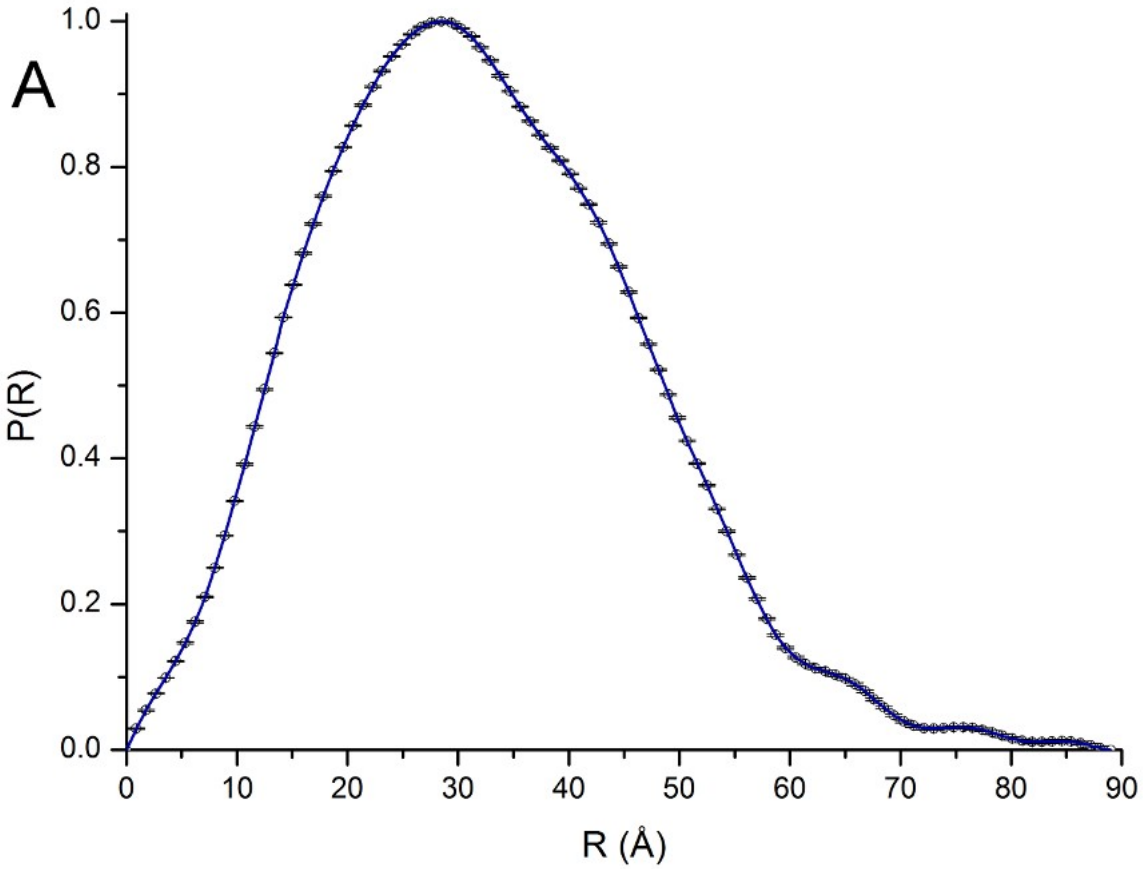
A
P(R)
R (Å)
0.0
0.2
0.4
0.6
0.8
1.0
0
10
20
30
40
50
60
70
80
90

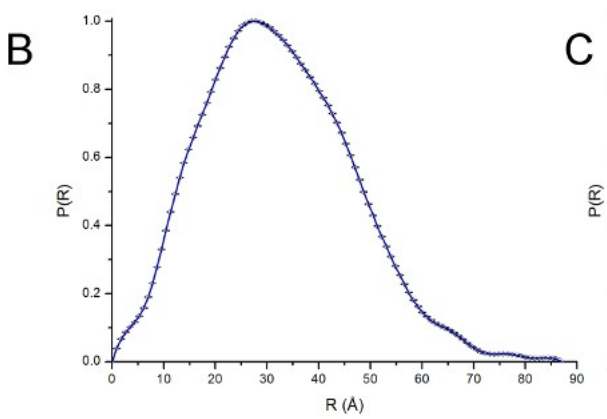
B
P(R)
R (Å)

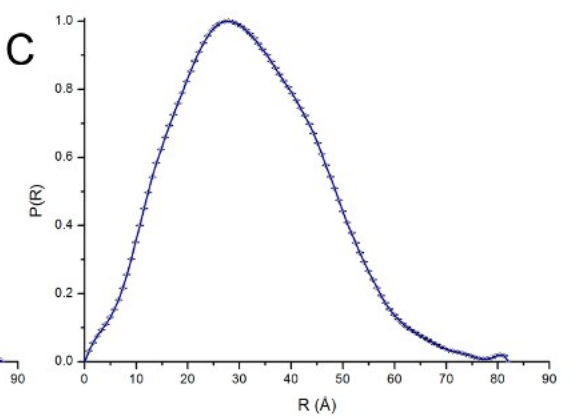
C
P(R)
R (Å)

| Complex | Real space Rg (Å) | $D_{max}$ (Å) |
|---|---|---|
| **hCCS-wtSOD1** | 24.9 ± 0.3 | 89 ± 3 |
| **hCCS-L38V SOD1** | 24.9 ± 0.3 | 87 ± 3 |
| **hCCS-I113T SOD1** | 24.6 ± 0.3 | 82 ± 3 |

Table 7.1. Comparison of deduced scattering parameters for three hCCS-SOD1 complexes.

### 7.3 *Ab initio* model reconstructions

The scattering profiles of hCCS complexed with wtSOD1, L38V and I113T SOD1 were used to create *ab initio* bead models for each heterodimer. As in the previous chapter, 20 models were generated for each complex using the GASBOR algorithm [203]. Figure 7.5 presents reconstructed three-dimensional models for the hCCS-wtSOD1 complex. For each complex the restored shape models were superimposed, compared and averaged (Figures 7.6 and 7.7).

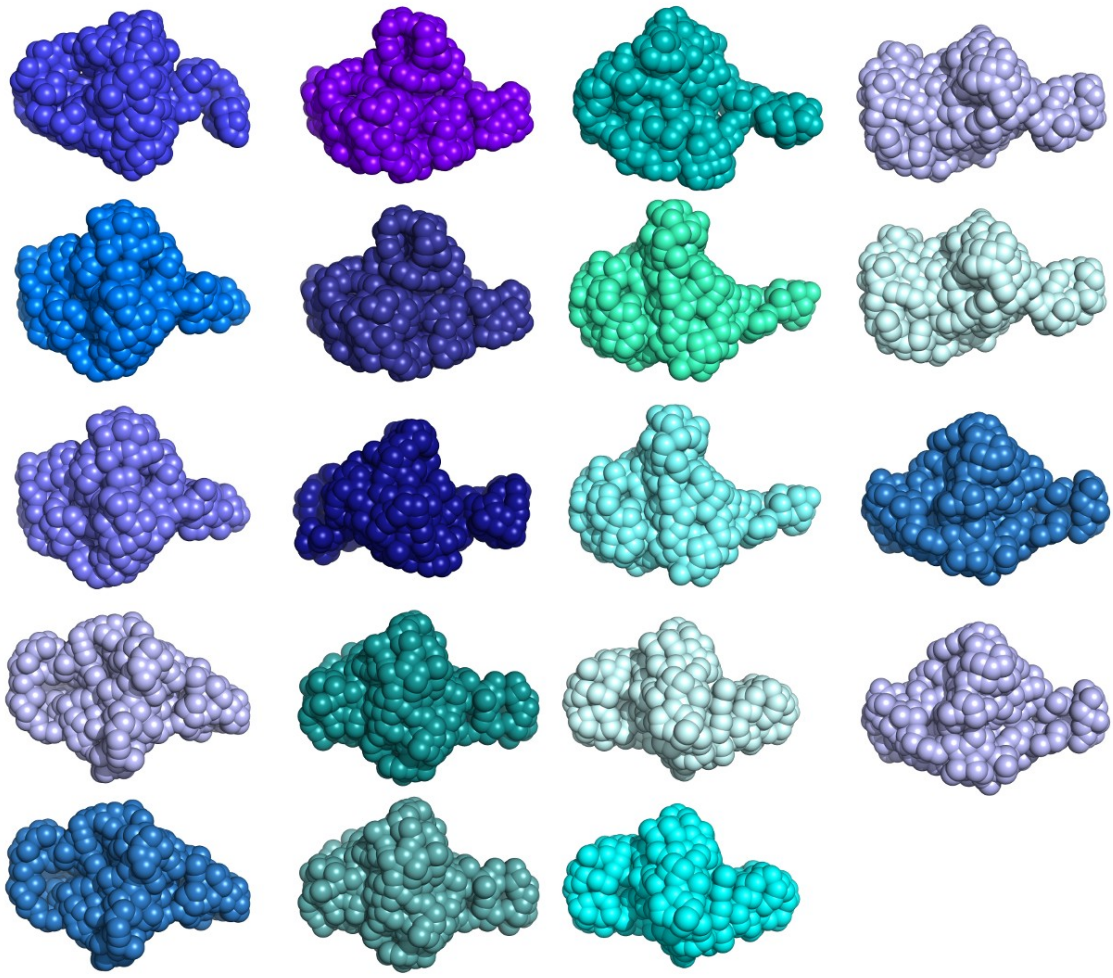

Figure 7.5. *Ab initio* bead models of the hCCS-wtSOD1 complex. $8.8<\chi^2<13.4$.

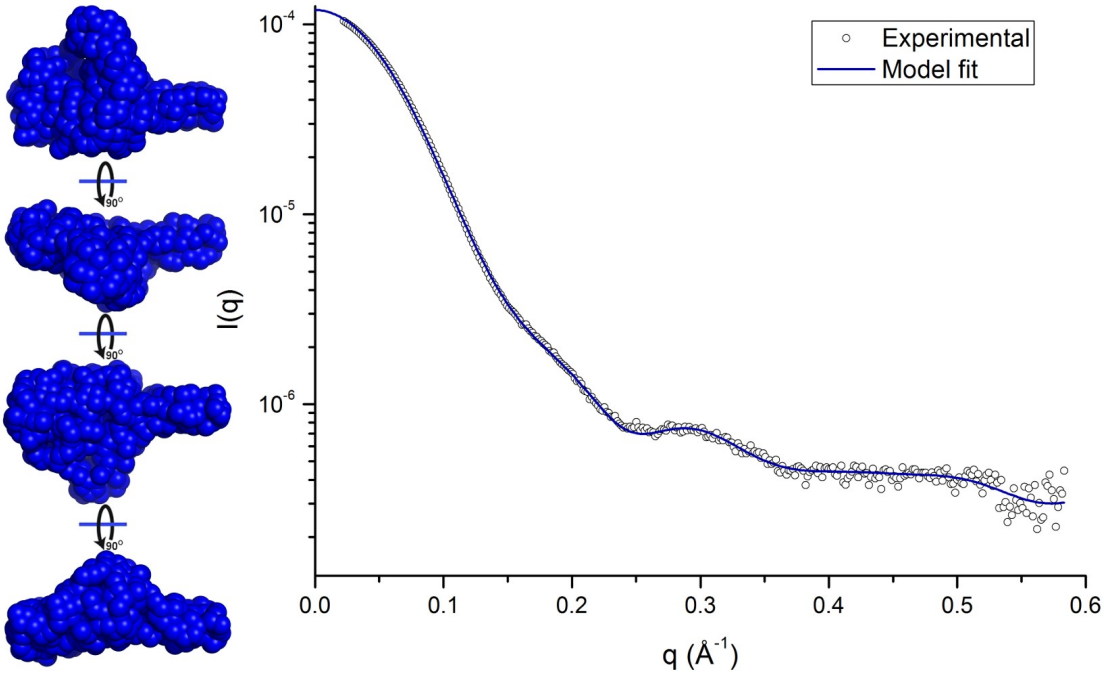


Figure 7.6. The 'most typical' hCCS-wtSOD1 complex model. This hCCS-wtSOD1 *ab initio* model was used as the reference model during averaging of those models presented in the previous figure. The goodness-of-fit value in comparison to the experimental scattering profile is $\chi^2$=11.4.

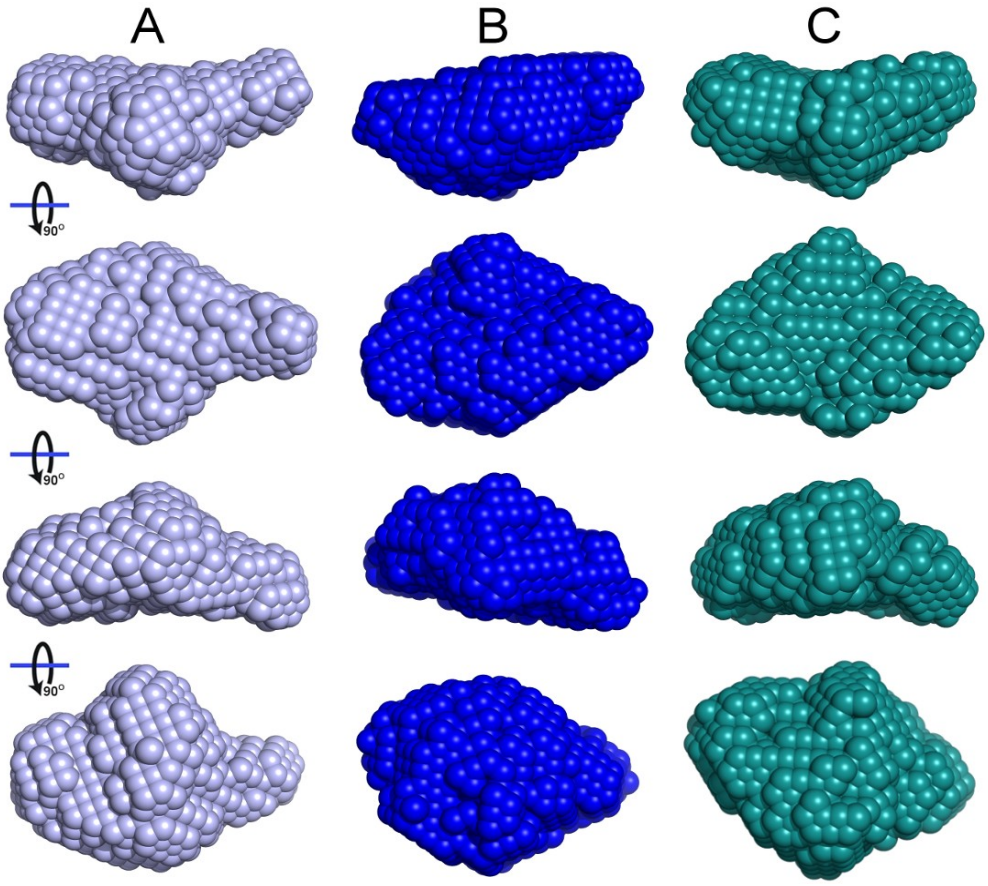


Figure 7.7. Averaged *ab initio* shape restorations of hCCS complexed with SOD1. (A) wtSOD1, (B) L38V SOD1 and (C) I113T SOD1.

*Ab initio* shape restoration from solution X-ray scattering allows one to create a consensus model of the subject protein in solution. Figure 7.7 indicates that this consensus shape is subtly different for L38V and I113T SOD1 when compared with wtSOD1 complexed with hCCS. Each model is elongated in one dimension, as dictated by the $p(r)$ function, however both mutant complexes have a more globular appearance than the contoured wild-type form. This discrepancy is not observed when comparing the three-dimensional shapes reconstituted from the scattering profiles of wild-type, L38V and I113T homodimers as described in the previous chapter. H80R and D124V SOD1 mutants have previously been observed to have perturbed interactions with the SOD1 copper chaperone characterised by abrogation of copper loading [216]. While L38V and I113T are known to be adequately copper loaded *in vivo*, assessing the state of the SOD1 intrasubunit disulphide bond is difficult. hCCS catalyses oxidation of cysteines 57 and 146 to form the SOD1 disulphide and improper oxidation is thought to be a contributor to mutant SOD1 pathogenicity. Perhaps the contrast between these structures is a manifestation of altered interaction characteristics between hCCS domain II and mutant SOD1. If this were the case, responsibility for SOD1 instability would not be a propensity for disulphide reduction of the fully post-translationally modified protein but a disturbance in the SOD1 maturation pathway.

### 7.4 Rigid body modelling the hCCS-wtSOD1 complex

Complex formation between SOD1 and CCS is known to be reliant on the SOD1-like domain of hCCS with domain III completing transfer of copper to the SOD1 active site. Using a rigid body modelling approach to curve fitting against the experimental scattering data presented thus far in conjunction with the domain structures of hCCS described in Chapter 6, Table 6.1 and crystal structures of I113T, L38V and wtSOD1 the conformational flexibility of the hCCS-SOD1 complex was sampled (Figure 7.8).

This composite of conformations is similar to that of homodimeric hCCS presented in the previous chapter. The Atx1-like domain I is mobile but forms a region of high probability of presence adjacent to, and curved around, one half of the dimer interface. Of the 20 models presented, there is one exception to this where domain I is moved across the interface. Domain III appears to have a greater degree of freedom and can be found at any

point surrounding the two domains that comprise the interface. The computed scattering profile for each hCCS-wtSOD1 rigid body model is represented in Figure 7.9 and show an excellent agreement with the experimental profile.

Comparison of these models with the crystal structure of the yCCS-ySOD1 H48F complex (PDB ID: 1JK9 [199]) indicates they occupy very similar conformational space (Figure 7.10). The SOD1-CCS interface is tethered in the rigid body models and accordingly shows high structural homology between the human and yeast complexes. Most interestingly, domain I of the yeast complex is found within a space densely populated with multiple possible positions of domain I from the human solution structures. This congruence effectively validates the modelling process used here as the initial position of domain I at the start of the modelling procedure was distant from this region of high probability of presence.

In the crystal structure of the yeast complex, domain III stretches across the unit cell to make a number of contacts with the SOD1-like domain of a second heterodimer. Domain III is found to be very mobile in the solution structures presented here however one model shows this domain in a position close to that observed in the yeast structure. This further indicates an effective modelling protocol and the complementarity of differing experimental protocols.

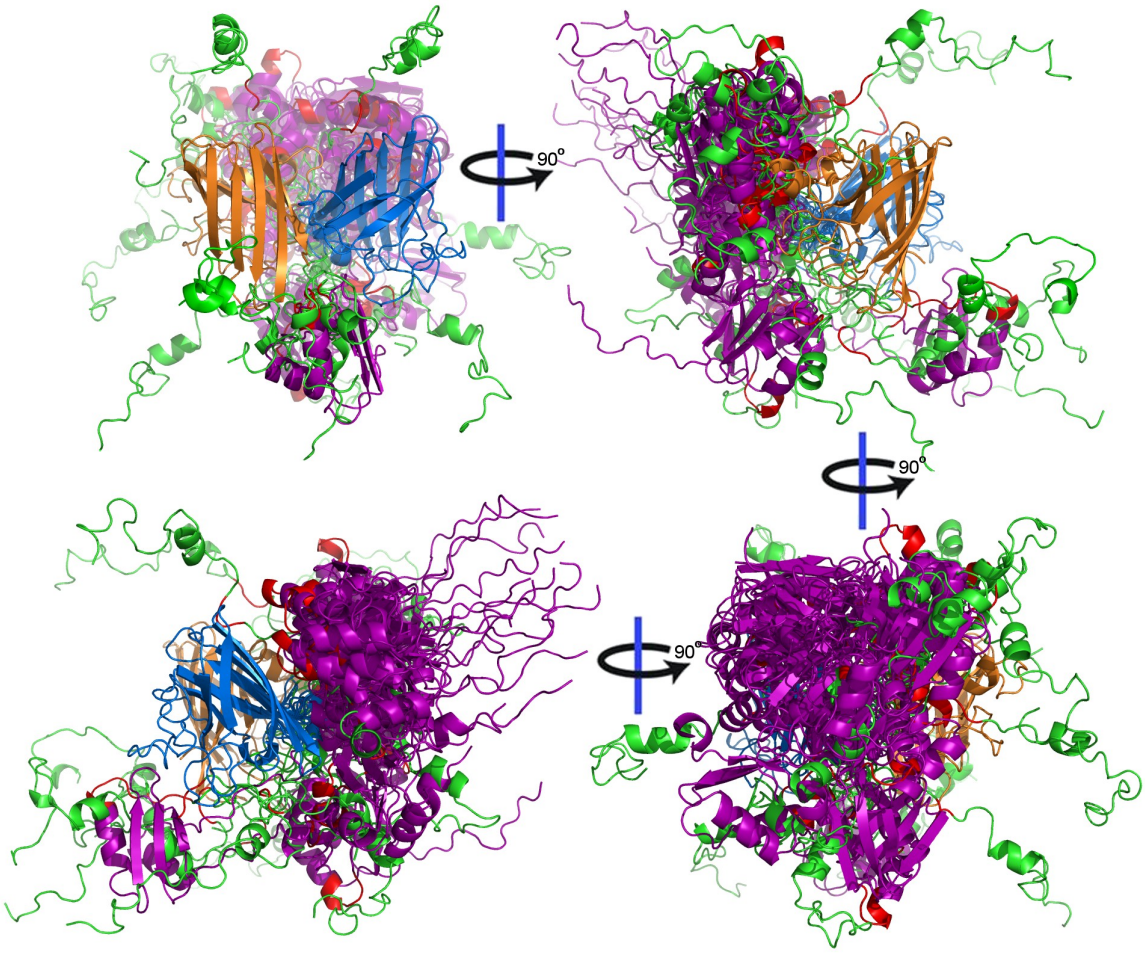


Figure 7.8. Solution structures of the hCCS-wtSOD1 complex. Models were generated against experimentally obtained SAXS data. 20 models are aligned according to the central domain II-SOD1 interface and overlaid showing the varying domain arrangement of hCCS when complexed with wild-type SOD1. Colour coding follows Figure 6.13 where hCCS domain I is coloured purple, II-blue, III-green, copper binding motifs are depicted in red and SOD1 is gold.

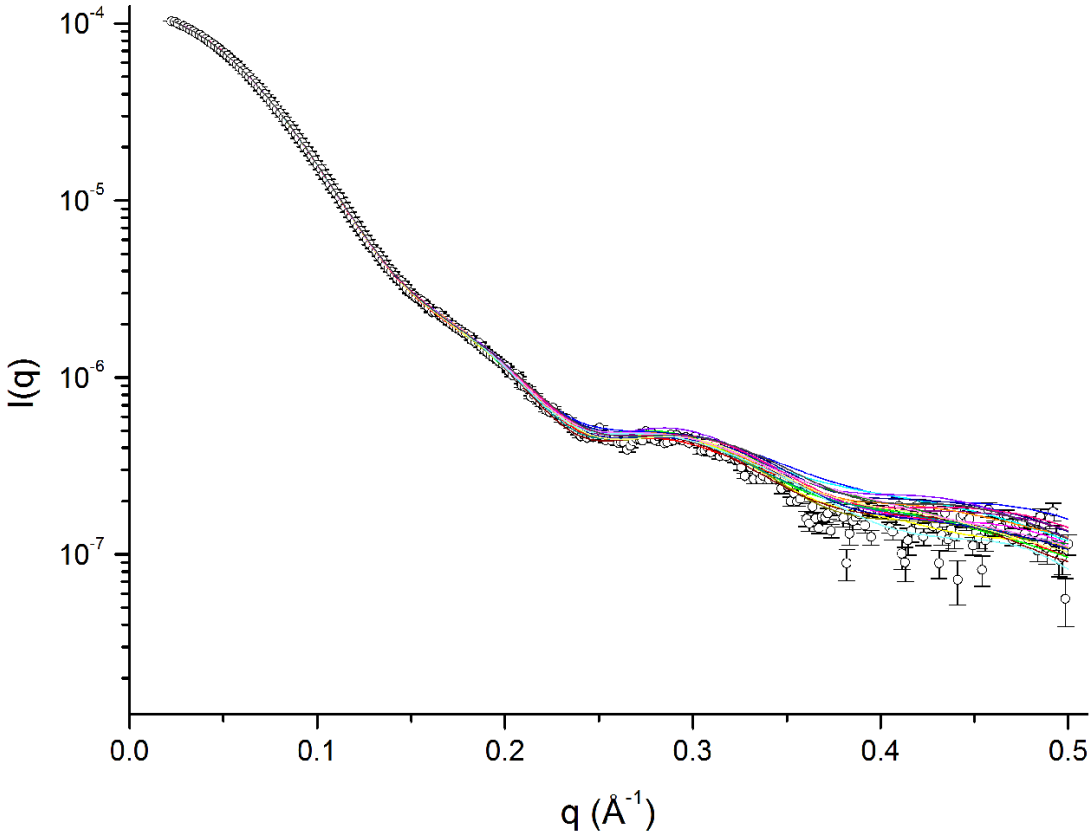


Figure 7.9. Scattering profile for the 20 rigid body models of hCCS-wtSOD1, shown in Figure 7.8. The experimental scattering profile of the complex is given with error bars (black) with the computed profile of each individual rigid body model (multi-coloured). Their goodness of-fit-values range from $2.2<\chi^2<2.6$.

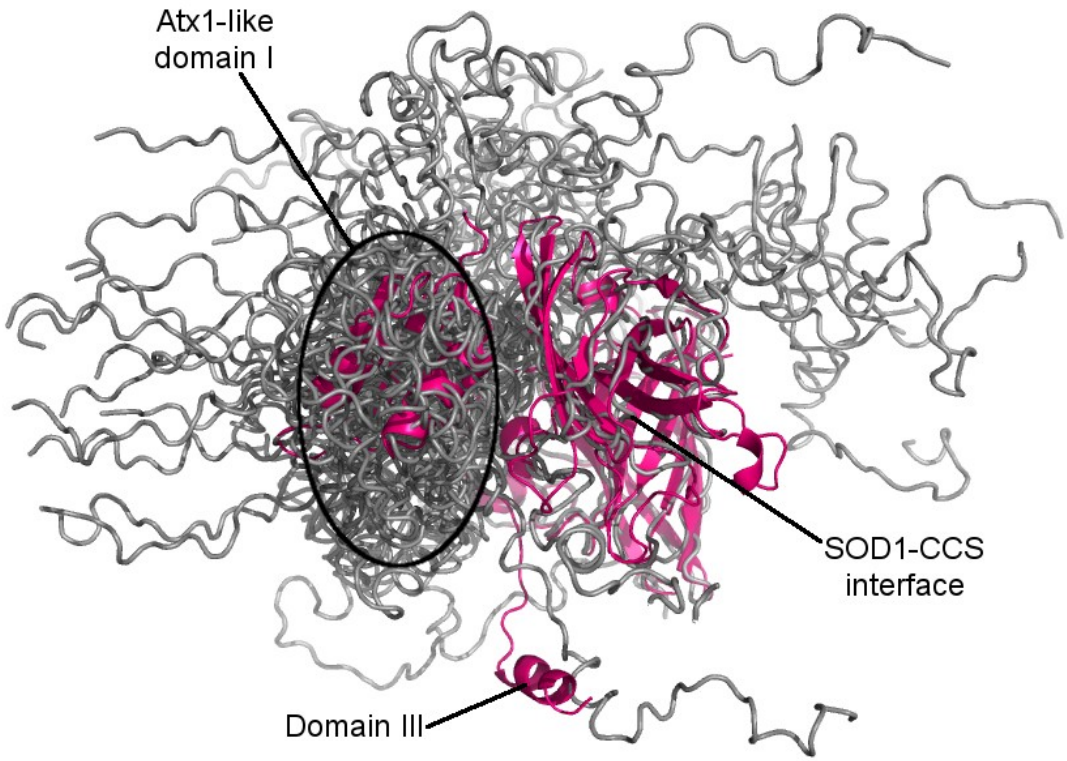


Figure 7.10. Comparison of SAXS solution structures of the human CCS-wtSOD1 complex with the crystal structure of the *S. cerevisiae* complex. The yCCS-ySOD1 H48F structure (PDB ID: 1JK9), represented in pink, is aligned with the 20 rigid body models of the human complex described in Figures 7.8 and 7.9.

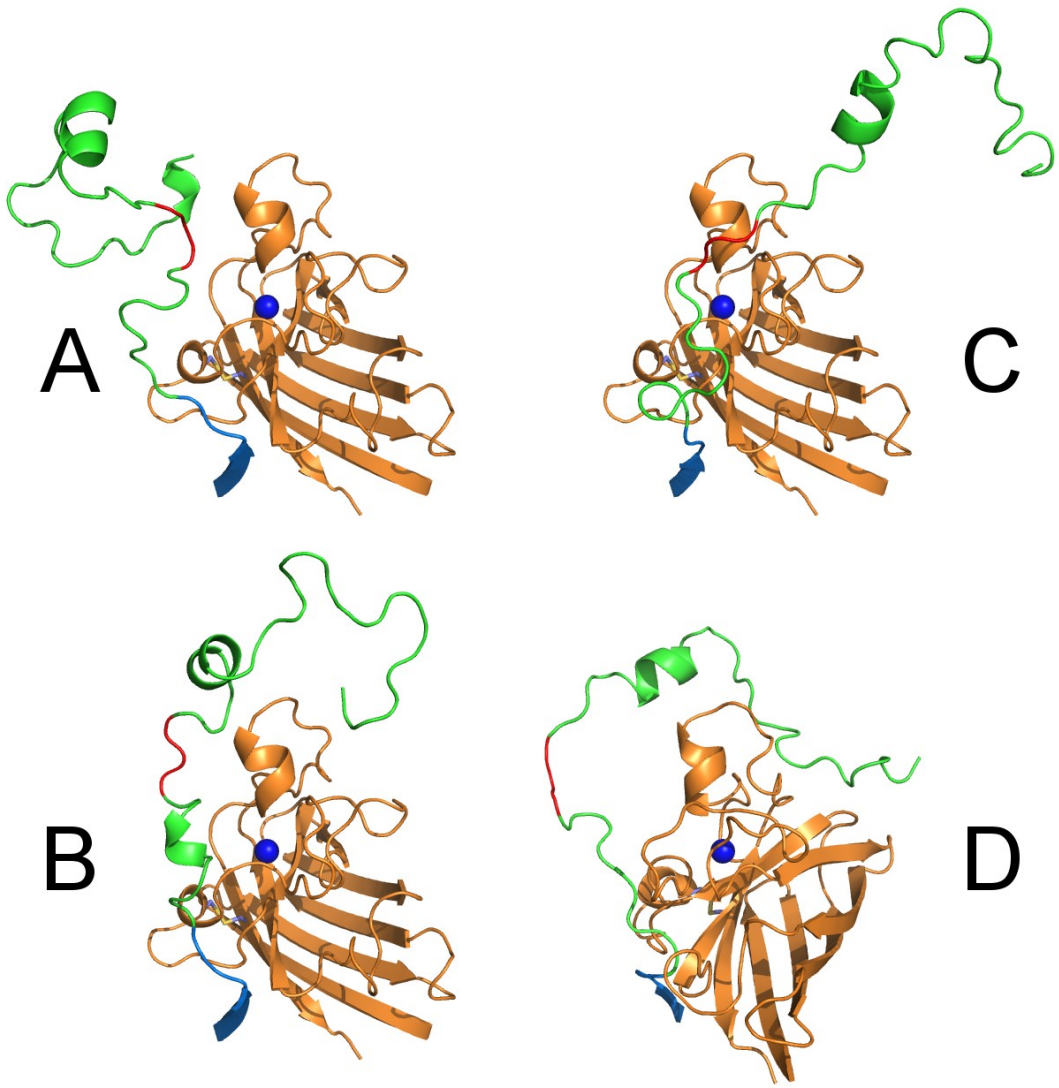


Figure 7.11. Association of hCCS domain III with SOD1. Detail of four rigid body models showing the hCCS domain III in green, the SOD1 monomer in gold. (A), (B), and (C) The copper binding motif of hCCS domain III is able to approach the SOD1 disulphide and active sites, (D) Domain III is wrapped around the SOD1 monomer.

While atomic domain models were used in the generation of these structures their atomic resolution is lost when they are used to ascertain global domain movements through rigid body modelling. Consequently the precise molecular mechanism by which hCCS domain III transfers copper to the SOD1 active site cannot be inferred from these structures. These structures do however represent a pool of possible domain arrangements hCCS-wtSOD1 could adopt in solution. Within this cohort several structures can be found where the hCCS domain III is proximal to the SOD1 copper active site and the intra-subunit disulphide. These structures are represented individually in Figure 7.11. The distance between the SOD1 copper centre and the CXC motif of hCCS domain III is, at its shortest, approximately 10 Å (Figure 7.11A). At first glance this distance appears too long for

effective transfer of copper. Two factors will enable this distance to be bridged during copper transfer. Firstly, as described in the previous chapter, the copper-sulphur clusters utilised by hCCS are much larger than mononuclear copper. Secondly, prior to copper loading and disulphide transfer from hCCS, SOD1 is immature. In this state the electrostatic loop and disulphide sub-loop are mobile and will not offer the steric resistance they exert in the rigid SOD1 structure used here. Consequently, hCCS domain III will be able to move into the region these loops occupy in the static crystal structure where it would be very close to the SOD1 active site.

### 7.5 Rigid body modelling the I113T and L38V SOD1-hCCS complex

Immature SOD1 is conjectured to be a crucial factor in the pathogenesis of amyotrophic lateral sclerosis. fALS associated SOD1 mutants have been observed to have activities ranging from nil to more than the wild-type enzyme and copper metallation which varies from nil to similar to wild-type indicating SOD1 mediated fALS has little to do with superoxide dismutase activity. SOD1 disulphide reduction is, however, known to heavily effect the stability of the protein *in vitro*. hCCS is responsible for the transfer of this stabilising intra-subunit disulphide therefore incomplete SOD1 maturation *in vivo* resulting from an atypical SOD1-CCS interaction could be an initiating factor of ALS.

In order to assess the interaction between hCCS and SOD1 mutants the complex was made and measured by SEC-SAXS using L38V and I113T as described in the previous sections. As with the wild-type complex a rigid body modelling approach was then used to probe the structure of these complexes. The scattering profiles of L38V and I113T SOD1 complexed with hCCS are presented in Figures 7.12 and 7.13.

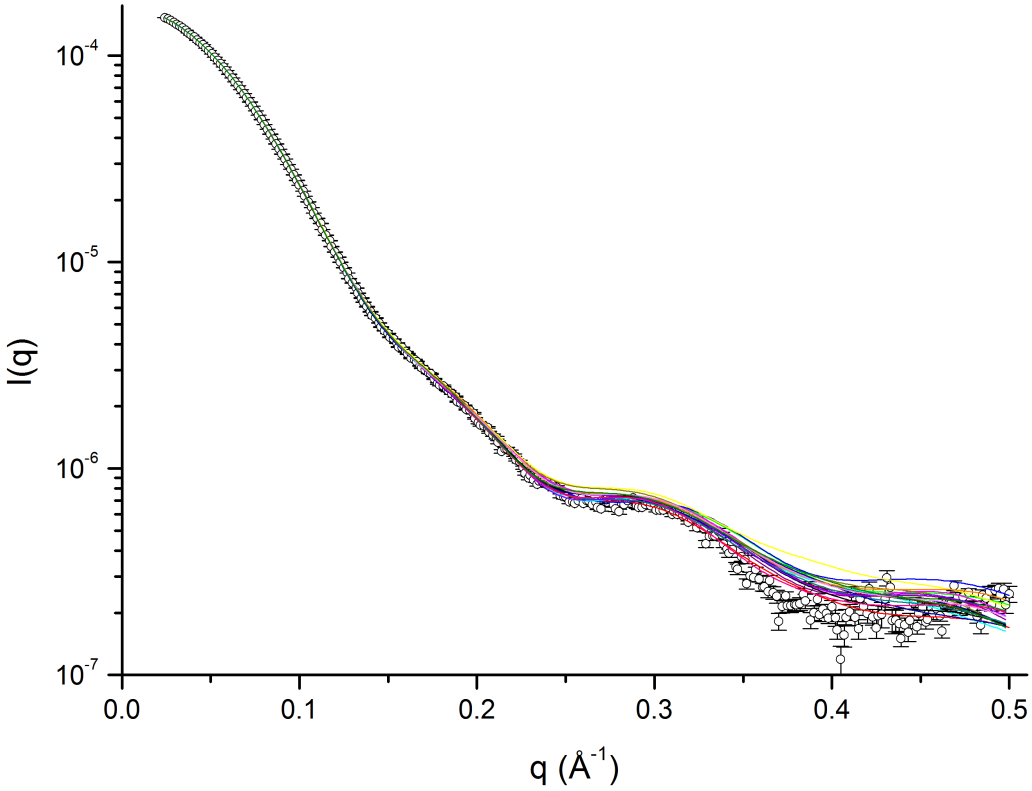


Figure 7.12. Scattering profile of 20 hCCS-L38V SOD1 models. Deduced scattering profiles (multicoloured) are superimposed on the experimental scattering profile of the complex with errors bars (black). Goodness-of-fit values are $3.4<\chi^2<4.1$.

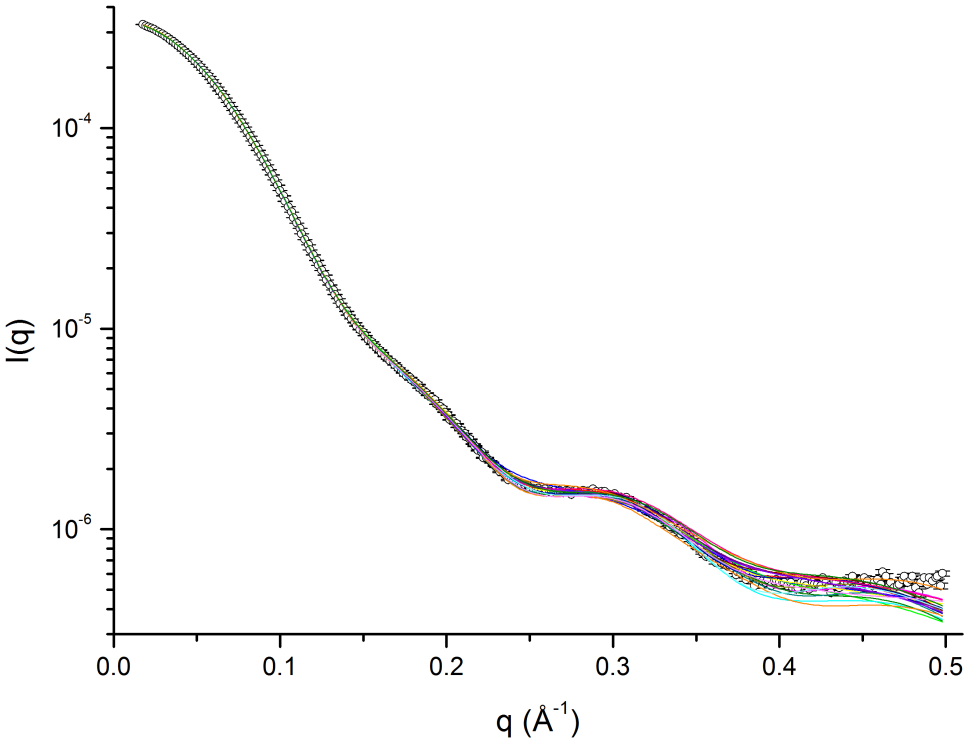


Figure 7.13. Scattering profile of 20 hCCS-I113T SOD1 models. Deduced scattering profiles (multicoloured) are superimposed on the experimental scattering profile of the complex overlaid with error bars (black). Goodness-of-fit values are $5.9<\chi^2<9.4$

Figures 7.14 and 7.15 show an overlay of 20 rigid body models of hCCS complexed with L38V and I113T SOD1 respectively. hCCS-L38V SOD1 adopts similar conformations in comparison with the wild-type complex. Domain I is found encircling one half of the complex interface while domain III is more mobile and can be found almost anywhere surrounding the interface domains. The overlapping positions of these domains when all 20 models are superimposed emphasises the possibility of an interaction between their copper binding motifs.

The I113T SOD1 complex is markedly different however (Figure 7.15). In this instance, domain III no longer forms extended protrusions into the solvent seemingly hindered only by the length of its polypeptide chain but congregates close to the SOD1 monomer. Consequently the complex appears smaller and more compact. Furthermore, there is little interaction between domains I and III with both forming separate, distinct regions where there is a high probability of their presence.

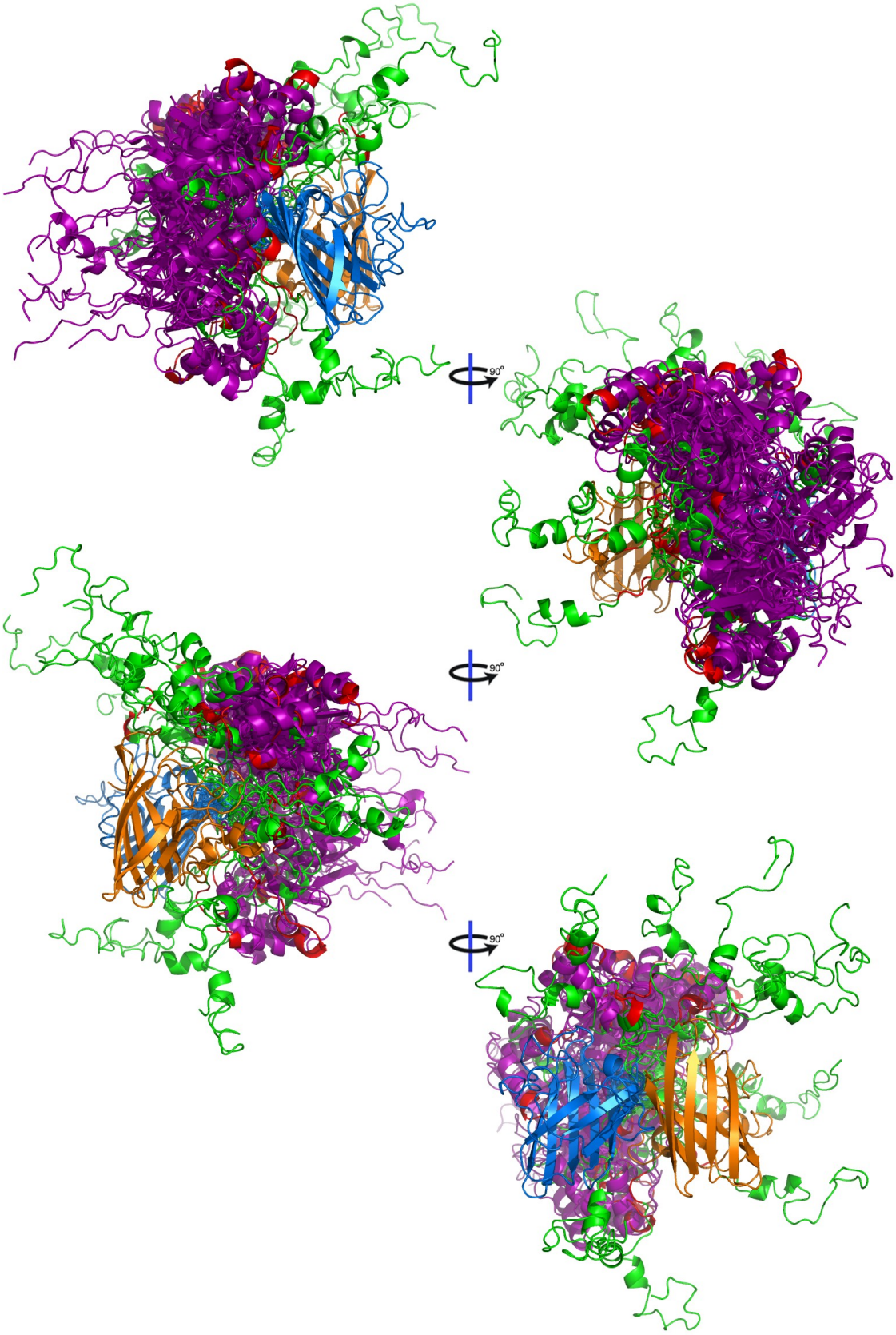


Figure 7.14. Solution structures of the hCCS-L38V SOD1 complex. 20 models are overlaid showing the domain arrangement of hCCS when complexed with SOD1. Gold – SOD1, purple – hCCS Atx1-like domain I, blue – hCCS SOD1-like domain II, green – hCCS domain III, red – hCCS copper binding motif.

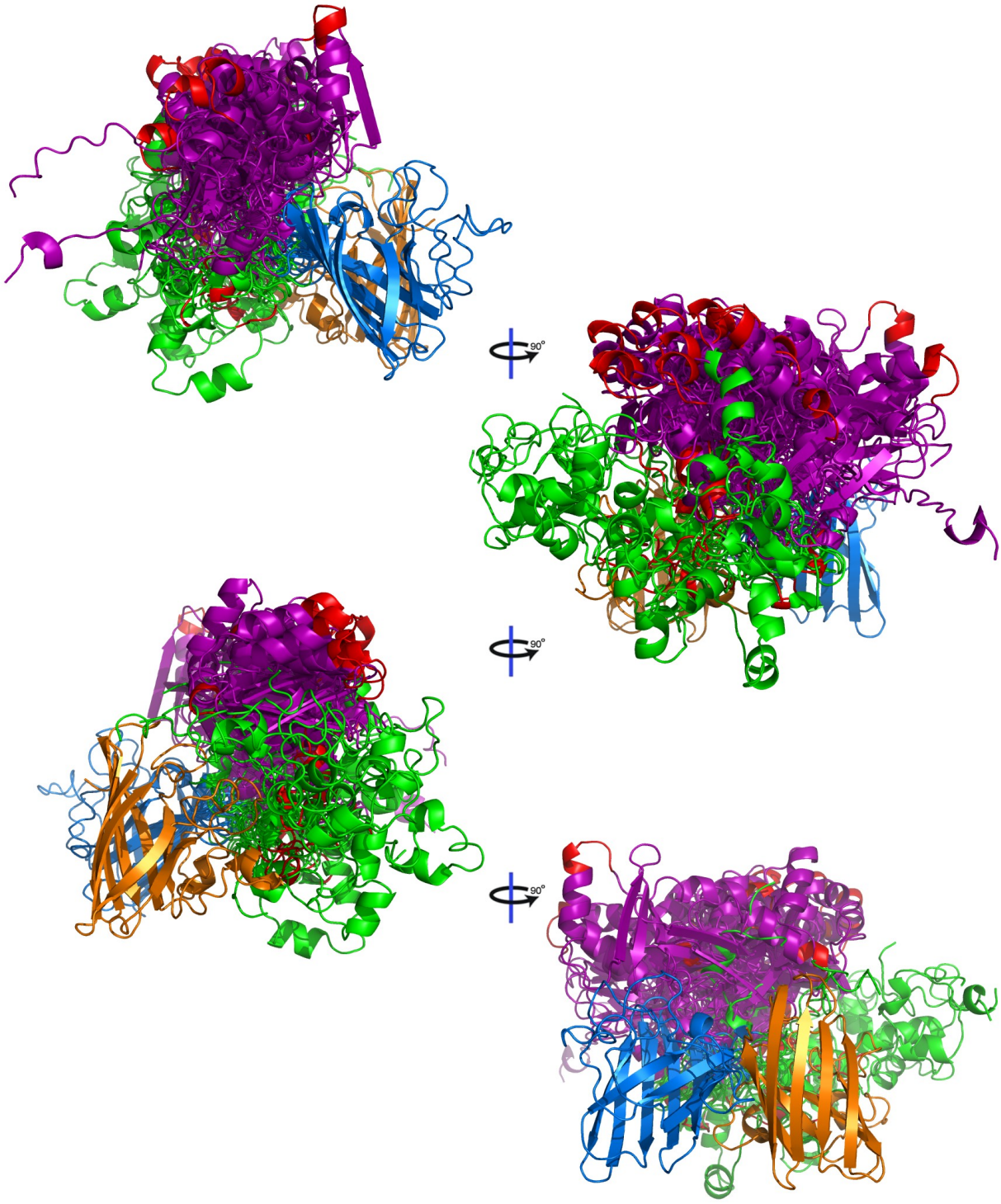


Figure 7.15. Solution structures of the hCCS-I113T SOD1 complex. 20 models are overlaid showing the domain arrangement of hCCS when complexed with SOD1. Gold – SOD1, purple – hCCS Atx1-like domain I, blue – hCCS SOD1-like domain II, green – hCCS domain III, red – hCCS copper binding motif.

## 7.6 Comparison of the solution structures of SOD1, hCCS and the hCCS-SOD1 complex

The data presented in the preceding chapters present an unparalleled opportunity for the first time to compare the solution structures of human CCS, SOD1 and the functional complex critical in the maturation of SOD1. Given the wealth of information implicating immature mutant SOD1 in the pathogenesis of amyotrophic lateral sclerosis this is also a unique opportunity to probe the structure of mutant SOD1-CCS for the crucial differences which may effect SOD1 maturation.

Figure 7.16A describes the scattering profile of SOD1, hCCS and the heterodimeric hCCS-SOD1 complex. The wtSOD1 profile shows the minimum at q = 0.25 $Å^{-1}$ characteristic of the ellipsoidal SOD1 shape. While both homodimeric hCCS and the complex show a comparable trait, this characteristic of the scattering curve it is less pronounced in both instances but its presence can be attributed to both SOD1 and the SOD1-like domain in the complex and homodimer respectively. There is an increase in the number of characteristic features present in the scattering curves of hCCS and hCCS-SOD1 compared with SOD1 and this parallels an increase in the molecular and conformational complexity of the proteins.

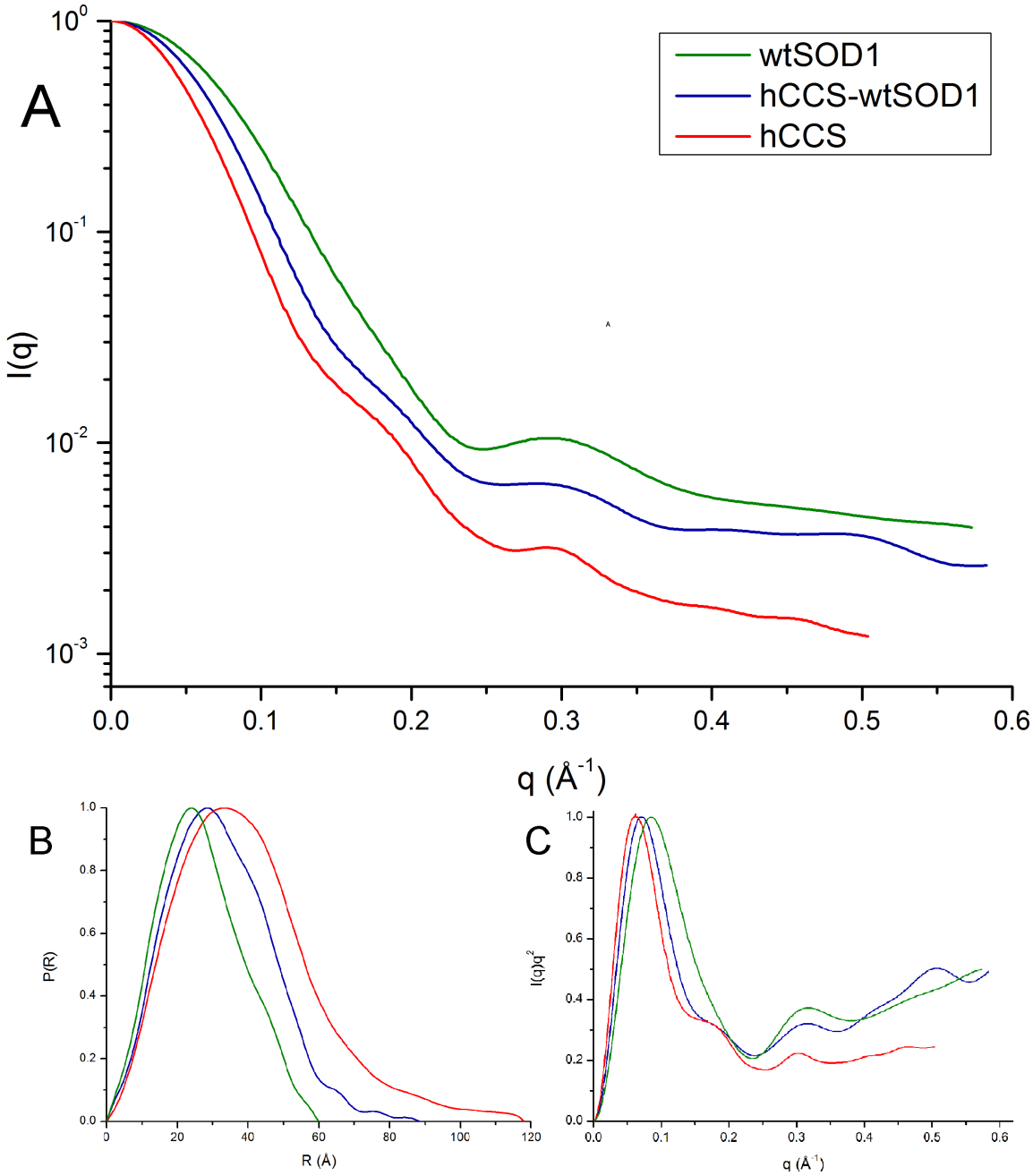


Figure 7.16. Scattering profiles of hCCS, SOD1 and their heterodimeric complex. (A) Scattering profile, (B) Distance distribution function and (C) Kratky plot. The scattering profile, *P*(*r*) function and Kratky plot are normalised to unity at the peak maxima.

| Complex | Real space Rg (Å) | $D_{max}$ (Å) |
|---|---|---|
| **wtSOD1** | 20.6 ± 0.2 | 60 ± 2 |
| **L38V SOD1** | 20.7 ± 0.2 | 65 ± 2 |
| **I113T SOD1** | 20.8 ± 0.2 | 64 ± 2 |
| **hCCS-wtSOD1** | 24.9 ± 0.3 | 89 ± 3 |
| **hCCS-L38V SOD1** | 24.9 ± 0.3 | 87 ± 3 |
| **hCCS-I113T SOD1** | 24.6 ± 0.3 | 82 ± 3 |
| **hCCS** | 31.3 ± 0.3 | 118 ± 4 |

Table 7.2 Deduced scattering parameters for SOD1, hCCS and their heterodimeric complex.

The $p(r)$ function of wtSOD1 in Figure 7.16B is indicative of a protein comprised of two domains in close contact with each other and a slight elongation. Similarly the distance distribution function of the hCCS-SOD1 complex can be equated with a protein of effectively 3 domains further indicating that the third hCCS domain does not form a compact globular structure. Due to the number of domains present in the hCCS homodimer it is difficult to distinguish features in the $p(r)$ function however the protein is clearly elongated. In general and unsurprisingly, as CCS monomers are added and SOD1 monomers are removed the oligomer becomes more elongated and more complex. This notion is reflected in Table 7.2 which also describes the effect of adding mutant SOD1 rather than the wild-type protein.

Table 7.2 highlights a counterintuitive aspect of hCCS-SOD1 heterodimer formation. Mutant homodimeric SOD1 proteins had slightly larger $D_{max}$ values the wild-type enzyme. On the other hand, the heterodimeric complexes they form with hCCS have smaller $D_{max}$ when compared with the wild-type complex. Indeed the wild-type complex is 8 % longer than the complex formed with I113T SOD1.

To draw further contrast between wild-type and I113T SOD1 complexed with hCCS, Figure 7.17 describe the likely positions of the hCCS Atx1-like domain when complexed with these two SOD1 variants.

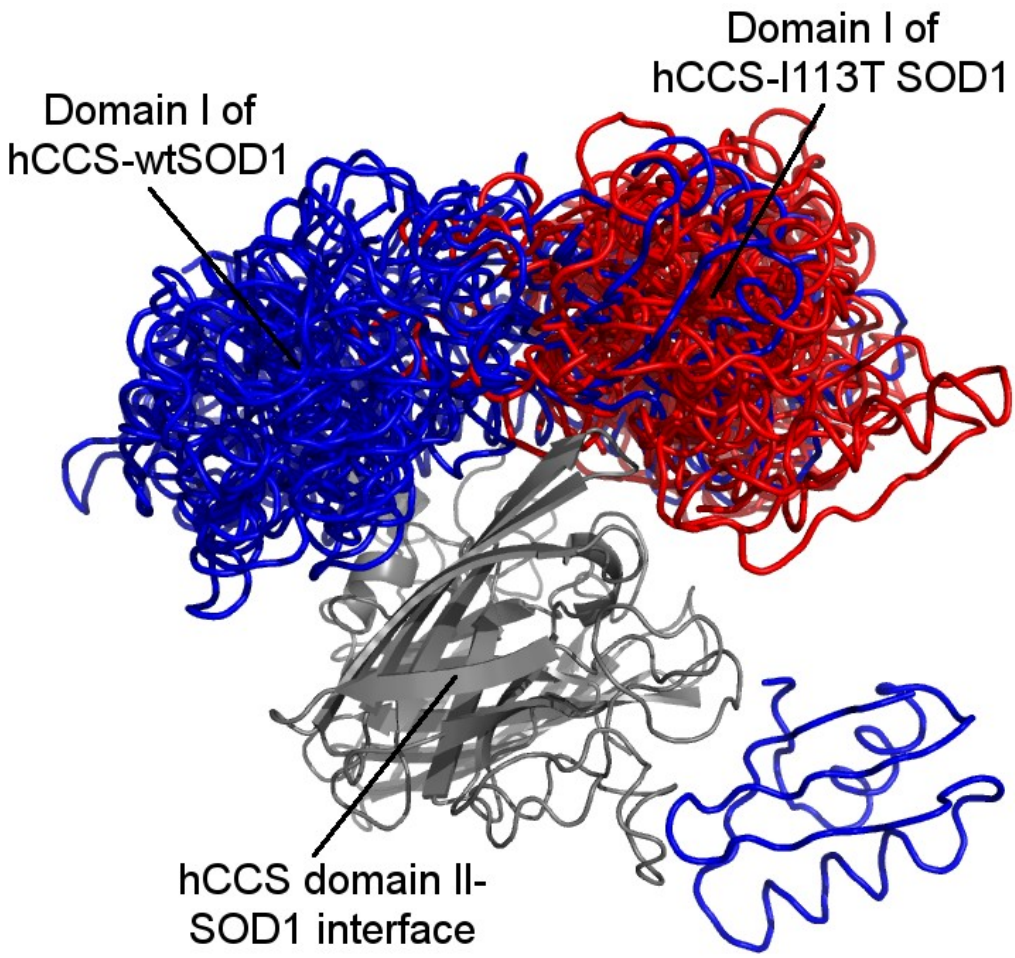


Figure 7.17. Comparison of the positions of the hCCS Atx1-like domain I when complexed with wtSOD1 and I113T SOD1. Grey - the central dimer interface comprised by a hCCS SOD1-like domain II and a SOD1 monomer. Blue – the hCCS domain I when complexed with wtSOD1. Red – the hCCS domain I when complexed with I113T SOD1. In each case 20 models are presented aligned according to the central SOD1-domainII interace each resulting from rigid body refinement against experimental scattering data.

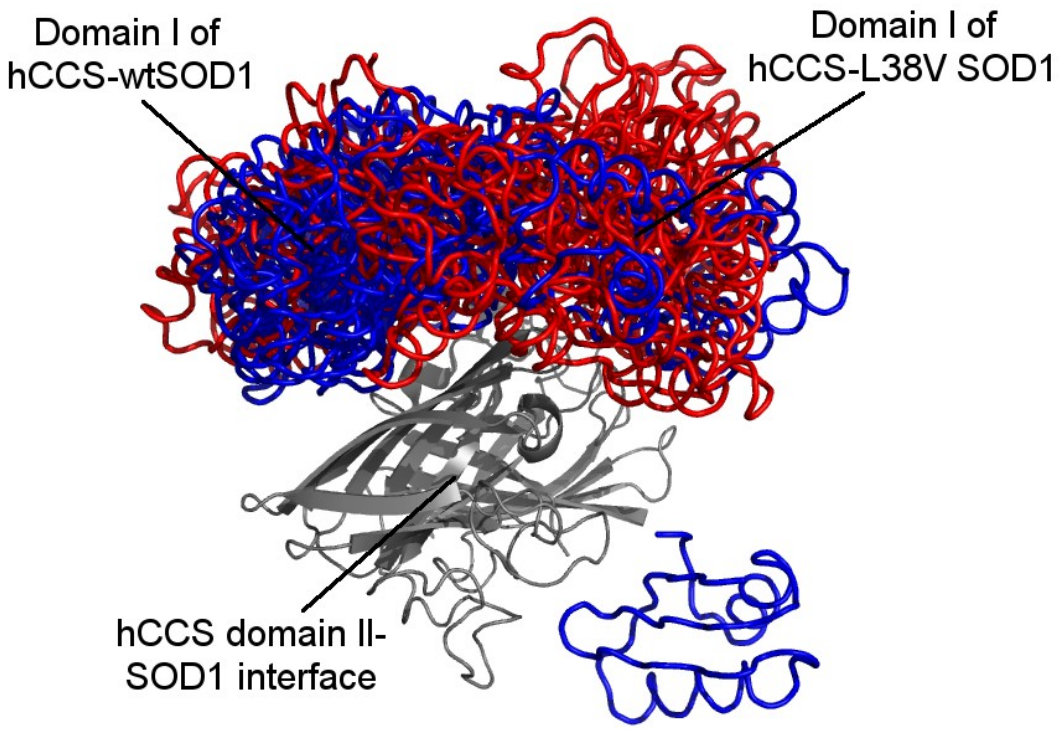


Figure 7.18. Comparison of the positions of the hCCS Atx1-like domain I when complexed with wtSOD1 and L38V SOD1. Grey - the central dimer interface comprised by a hCCS SOD1-like domain II and a SOD1 monomer. Blue – the hCCS domain I when complexed with wtSOD1. Red – the hCCS domain I when complexed with L38V SOD1. In each case 20 models are presented each resulting from rigid body refinement against experimental scattering.

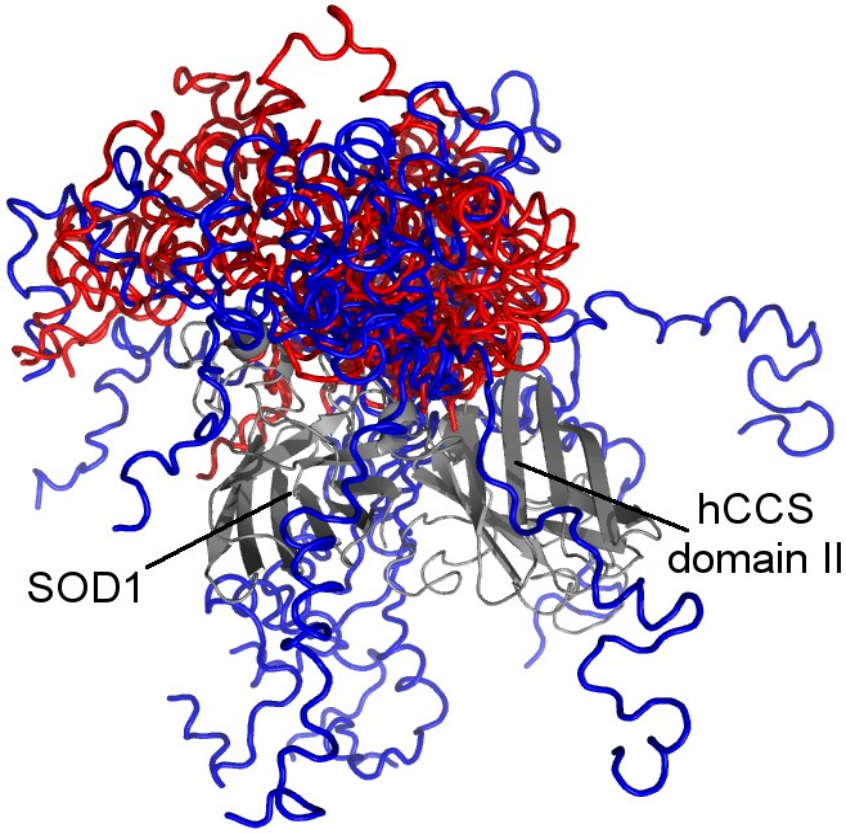


Figure 7.19. Comparison of the positions of the hCCS domain III when complexed with both wtSOD1 (blue) and I113T SOD1 (red). The central dimer interface comprised by a hCCS SOD1-like domain II and a SOD1 monomer is in grey.

For both hCCS-wtSOD1 and hCCS-I113T SOD1 complexes one can identify a region where the Atx1-like domain is found with high probability. As can be clearly seen in Figure 7.17 these regions are found to adjoin, with some overlap, but are predominantly distinct. What overlap exists is fostered by the seemingly more mobile domain I of the wild-type complex. The hCCS-L38V complex does not undergo such a dramatic shift in the position of the Atx-1like hCCS domain I, therefore the distinction between wild-type and L38V complex is less severe with a greater degree of overlap (Figure 7.18).

The copper binding motif at the C-terminus of hCCS is essential for SOD1 copper loading [191]. Figure 7.19 compares the positions of this domain when hCCS is complexed with wild-type and I113T SOD1. As described in the preceding sections the C-terminal domain of the wild-type complex is restricted only by its length and can be found surrounding the dimer domains. In complete contrast the hCCS C-terminus when complexed with I113T SOD1 appears restricted to a region of high probability of presence close to the SOD1 monomer

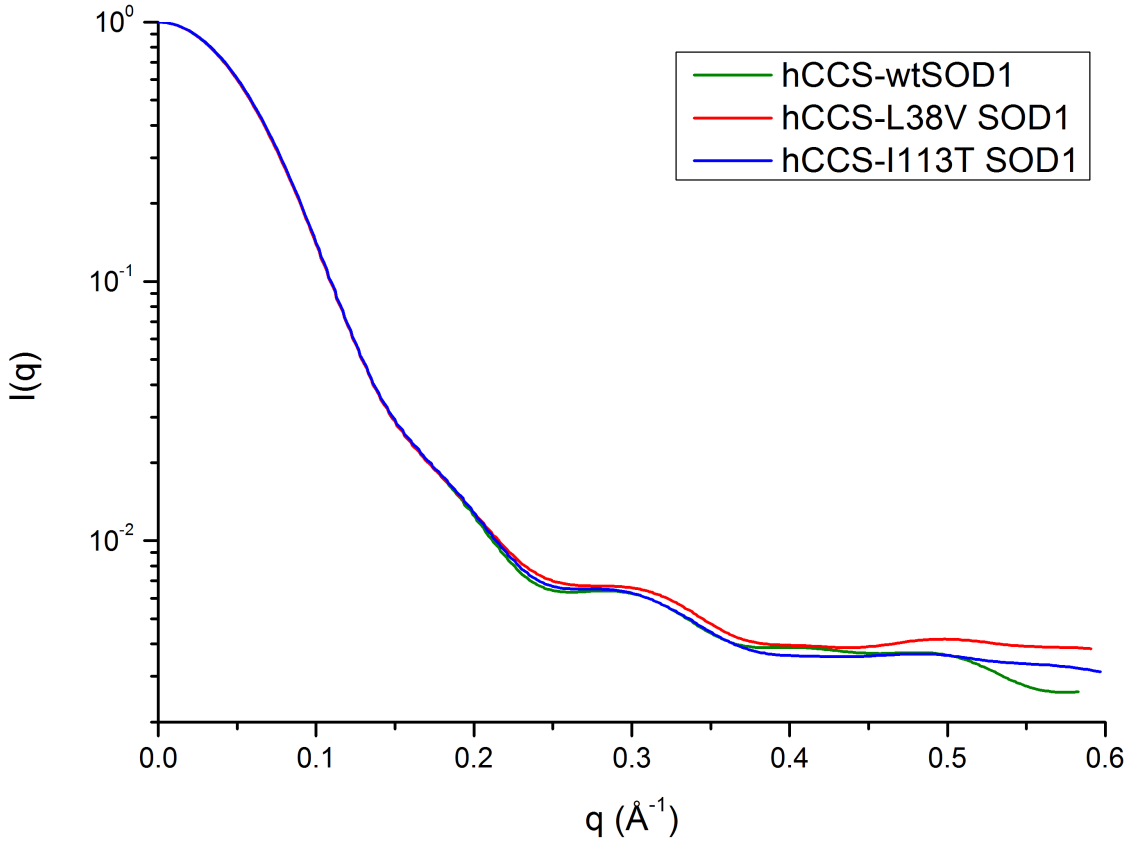


Figure 7.20. Comparison of the X-ray scattering profiles of wild-type, L38V and I113T SOD1 complexed with hCCS.

Given that the SOD1 mutations used herein are single point mutations, is there any justification from the scattering profile of the complex for such a significant domain rearrangement? Figure 7.3 shows the X-ray scattering profile for each hCCS-SOD1 complex discussed. A comparison of their smoothed scattering profiles (Figure 7.20) indicates that the complexes are indistinguishable by eye at low angles, $q < 0.2$ Å$^{-1}$. In this region scattering intensity is determined by the scatterer's shape and size. At higher scattering angles, $q > 0.2$ Å$^{-1}$, due to the use of a logarithmic scale differences in the three profiles become obvious. In this region scattering intensity is dictated by intramolecular characteristics and the differences between the three profiles infer a change in those characteristics.

While the low angle scattering is determined by the scatterers shape and size the higher angle is determined by conformations and interactions so it is reasonable infer that there should be differences between the complexes based on their scattering patterns.

These observations and comparisons lead to either of two conclusions. Movement of the Atx1-like domain into a region close to the hCCS domain II in the I113T SOD1-hCCS complex restrains the motility of domain III, or, retention of domain III in a region close to the SOD1 monomer pushes the Atx1-like domain out of the area it would normally occupy in the wild-type complex.

# Chapter VIII

## Discussion of X-ray solution scattering based structure determination of SOD1, hCCS and their complex

### 8.1 A comparison of hCCS scattering profiles collected at different X-ray sources and SAXS stations

The work described here is the first structural characterisation of full-length human CCS in solution. hCCS has implications for both the pathogenesis of amyotrophic lateral sclerosis and copper metabolism. This protein has been known for over a decade and has consistently rebutted structural characterisation by several respected groups. What follows is a review of the implications of the results in the previous chapters.

Small angle X-ray scattering is the choice method for studying large, biological macromolecules in solution. In 2004, *Mathew et al* [217] documented a combination of the standard SAXS technology with size exclusion chromatography apparatus. This synthesis facilitates the separation of impurities, different oligomeric states and aberrant high molecular weight aggregates from the species of interest, by gel filtration, directly before exposure to the x-ray beam [217]. It also eliminates any averaging contribution from such species and prevents buffer mismatch between blank and sample through the buffer exchange effect of size exclusion chromatography. To date three X-ray scattering beamlines have this capability: BioCAT at APS Chicago (US) [217], BL-10 at Photon Factory Tsukuba (Japan) [218] and SWING at SOLEIL St Aubin (France) [211].

Traditional, static SAXS analysis of recombinant hCCS at synchrotron SAXS stations 4-2 at SSRL (US) [219] and BL45XU at SPring-8 RIKEN (Japan) [220] yielded incongruence in scattering profile (Figure 8.1) and deduced structural parameters (Table 8.1 & Figure 8.2), such as a substantially increased value for the radius of gyration ($R_g$), indicating a problem with sample monodispersity. The decision to use the SEC-SAXS approach, and therefore the SWING beamline, was a direct result of these initial experiments.

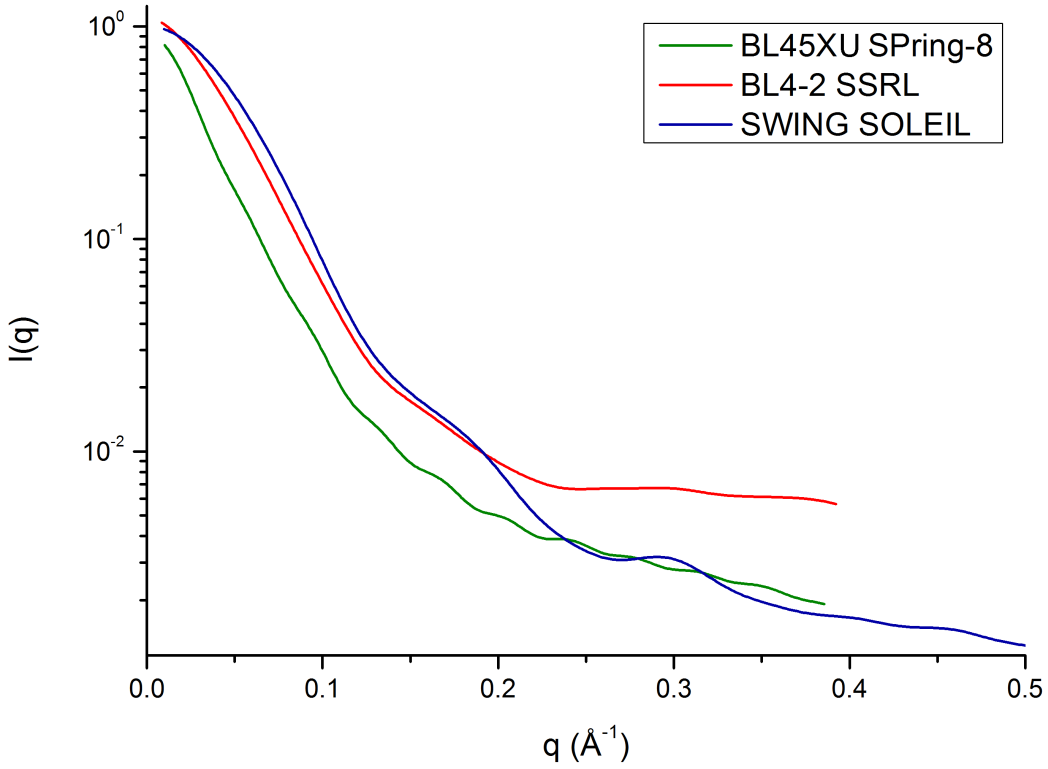


Figure 8.1. Comparison of smoothed scattering profiles from hCCS collected at three different SAXS beamlines. Curves are normalised to I(q)=1 at q=0.

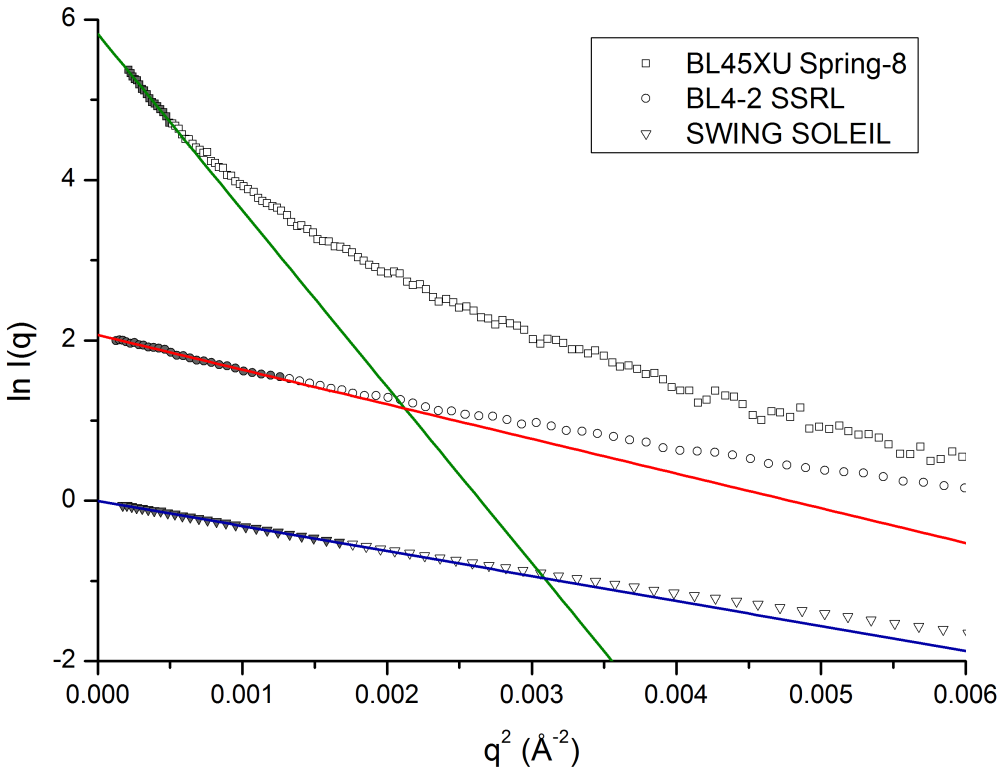


Figure 8.2 Comparison of Guinier plots for hCCS measured at three beamlines. Adapted from *Wright et al* [193].

| | | | |
|---|---|---|---|
| **Synchrotron** | SPring-8 | SSRL | SOLEIL |
| **Beamline** | BL45XU [220] | BL4-2 [219] | SWING [211] |
| **Real space $R_g$ (Å)** | 58.7 | 38.3 | 31.4 |
| **$D_{max}$ (Å)** | 174 | 160 | 118 |

Table 8.1. Deduced SAXS parameters for hCCS measured at three beamlines.

Figure 6.3 and 6.4 indicate the reason for these disparities. In solution the hCCS dimer predominates but is joined by a small amount of tetrameric protein and often higher molecule weight aggregates. These higher molecular weight species disproportionately affect scattering making the protein appear larger or less compact than it actually is. Without the combined SEC-SAXS approach recording scattering from dimeric hCCS alone would be very inaccurate.

Similarly, collecting scattering data from the hCCS-SOD1 complex would also be impossible due to incomplete formation of the heterodimer. As scattering from bulk solutions is an average, measurements taken from the hCCS-SOD1 heterodimer would comprise scattering from at least three species and any deductions made as a result would be disputable.

### 8.2 The function of hCCS and its intrinsic flexibility

The domain structure of hCCS is crucial for the transport and loading of copper into SOD1. In both the homodimeric and heterodimeric states hCCS exhibits extensive conformational flexibility made possible by two disordered, glycine rich linker regions of 11 and 17 amino acids. Indeed, hCCS domain III is largely disordered in structures of yeast CCS and homology structure predictions of hCCS other than a short α-helix that forms a long 42 amino acid flexible tail.

CCS conformational flexibility is highlighted by a comparison of the position of the Atx1-like domain I in the crystal structures of the yCCS homodimer and the yCCS-ySOD1 heterodimer (Figure 8.3). The linker between domain I and II in the yeast homolog is 6 amino acids long in comparison with 11 found in hCCS. As a crystal structure is a repeating assembly of molecules in a low energy state it can be expected that human CCS

will therefore be considerably more plastic in solution.

This flexibility is key if hCCS is to function as the accepted model of copper transfer to SOD1 suggests. The sequence of this transfer has been devised and hinges on a few key experimental observations.

Figure 8.3 Comparison of one yCCS monomer from the crystal structures of the yCCS dimer (cyan) and the yCCS-ySOD1 complex (pink). The models (1JK9 and 1QUP respectively) are aligned according to the SOD1-like domain II.

Firstly, the CXC motif of domain III is essential for SOD1 copper loading under all conditions [191]. This crucial region is therefore responsible for the ultimate transfer of copper to the SOD1 active site.

Secondly, domain I has 37 % identity to the yeast Atx-1 protein. The yeast Atx1 protein is known to exchange copper with the cytoplasmic domain of the membrane copper transporter, Ctr1 [175]. By analogy one would expect hCCS to perform the same function; initial copper acquisition.

Deletion of the Atx1-like domain I ablates hCCS function *in vivo*. This point has been disputed on the following basis. *Schmidt et al* reported this region of the yeast CCS homolog is only necessary under copper limited conditions [191]. In fact the copper limited

conditions used in yeast culture by these experimenters was 10 μM. While this is the extracellular concentration, it is safe to assume the intracellular free copper concentration will vastly exceed the $10^{-18}$ M concentration known to exist under regular culture conditions [168]. This copper flood understandably bypasses the need for domain I. Conversely, *in vivo* experiments on the human protein in human fibroblasts found this domain to be indispensable for SOD1 activation [192].

Perhaps because of this misapprehension, domain I has been proposed to function as an interaction mediator that would enable stable complex formation, with Ctr1 for example, and thus enable direct copper loading to domain III [221]. This notion is dismissed by the observation that domain I is able to perform its function in *trans* when co-expressed with a yCCS domain II/III truncation [191].

Thirdly, the interaction between hCCS and SOD1 is mediated by the amino acids at the CCS domain II and SOD1 homodimer interfaces and the SOD1 in question is fully translated when loading occurs [222]. Consequently, hCCS-SOD1 complex formation necessitates monomerisation of the native dimers.

Fourthly, the functional complex between hCCS and SOD1 is a heterodimer. Although crystallisation of the yeast complex yielded a tetramer in the unit cell this was thought to be an artefact of crystal packing [215]. As described in Chapter 8, and prior to this study [208], when analysed by size exclusion chromatography the hCCS-SOD1 complex runs at a position between the hCCS and SOD1 homodimer indicating a protein complex of intermediate size.

The commonly accepted [81,199,209] process of SOD1 activation and disulphide reduction by CCS can be summarised as follows:

1. Domain I recognises the Ctr1 cytoplasmic tail and is loaded with copper (Cu I).
2. The cysteines of domain I and III form a copper conjugate.
3. SOD1 and hCCS undergo monomerisation and heterodimer formation.
4. Copper is loaded into the SOD1 active site by domain III with concomitant formation of the SOD1 disulphide.
5. The heterodimer disintegrates followed by reformation of the homodimeric species.

This cycle of SOD1 activation and hCCS recycling is represented in Figure 5.3. Using the SAXS derived models presented in the previous chapters it is now possible to observe how the conformational flexibility of hCCS facilitates the multiple stages that take place between copper import by Ctr1 through to SOD1 activation (Figure 8.4).

Initial transfer of copper to hCCS domain I is enabled by a conformation in which the whole domain is free and receptive for interactions (Figure 8.4A). The cysteines of the copper binding motif of the yeast Atx1 protein [188] adopt a solvent exposed conformation which changes upon copper binding to bring the copper ion into the molecule. This conformational change is mimicked by the HAH1 human copper chaperone to a lesser extent [187]. However the available apo structure of hCCS domain I indicates a one-in-one-out structure with reference to the copper binding cyteines.

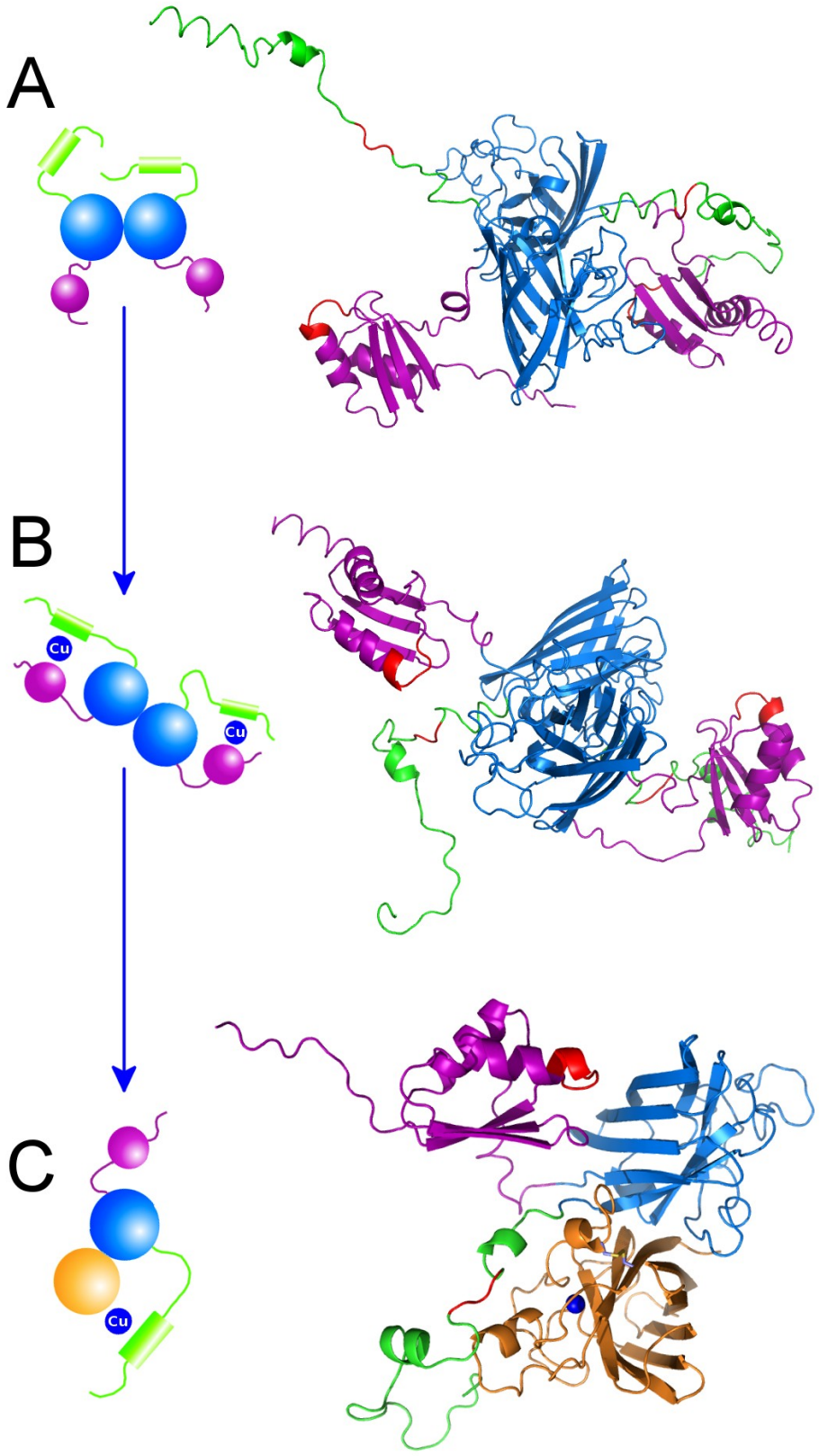


Figure 8.4. The stages of copper activation of SOD1 by hCCS. (A) The Atx1-like domain I, particularly the cycteine rich copper-binding domain, is solvent exposed and available to interact with the copper transporter Ctr1. (B) Formation of a domain I-III copper conjugate . (C) hCCS domain III is able to move toward the SOD1 active site enabling copper transfer and disulphide transfer in the heterodimeric complex. Purple – hCCS domain I, blue – hCCS domain II, green – hCCS domain III, gold – SOD1 and red – copper binding motif.

Both Atx1 and HAH1 bind copper in their monomeric form and directly load their respective targets without the need for intra-molecular transfer between domains. Transfer by hCCS is complicated by this need to move copper to domain III prior to SOD1 activation so the differences seen at this motif may be accounted for by the need to keep copper in a position accessible to domain III.

Figure 8.4B shows an hCCS conformation that would enable copper conjugation by the cysteines of domain I and III. This step is not only a necessity to primer domain III ready for loading into SOD1 but may also provide a safe environment in which poly-nuclear copper clusters can be physically transported from the cell membrane to the places where SOD1 is waiting for activation [197].

Figure 8.4C shows that hCCS domain III is able to approach the SOD1 active site. The crystal structure of the yeast SOD1-CCS heterodimer indicated that a domain III cysteine formed a disulphide with cysteine 57 of a SOD1 monomer a symmetry related heterodimer. Here we can see for the first time hCCS domain III interacting with a SOD1 monomer in the same heterodimer complex. Domain III is in a position that would facilitate copper loading into the SOD1 active site but this model does not take account of two conformational changes: Firstly, binding of copper to hCCS domain III brings about a conformational change which increases its resistance to trypsin digest [209]. Secondly, the electrostatic and zinc binding loops of SOD1 are known to be more dynamic and less rigid in the disulphide reduced state. The effect of the former is not known but the latter will indubitably open access to the SOD1 active site enabling copper loading and has been shown to increase the longevity of the heterocomplex [208].

### 8.3 Stoichiometry of hCCS-SOD1 complex formation

Previous studies have found that heterodimer formation between CCS and SOD1 occurs *in vitro* at 1:1 and 1:2 molar ratio [208,215]. In both of these cases non-natural copper site SOD1 mutants were used and wild-type SOD1 was not found to form a stable complex. The work in the previous chapter elucidates the creation of a stable complex between human CCS and wild-type, I113T and L38V SOD1.

Figures 7.1 and 7.2 characterise the production of this complex which is most effective

when the hCCS to SOD1 molar ratio was 1:1.5 when first mixed. Initial complex formation does not go to completion and homodimeric hCCS and SOD1 can be observed as minority species in gel filtration experiments. An obvious cause of this inefficiency would be the incomplete reduction of the SOD1 disulphide however longer incubation with a higher concentration of reductant did not increase conversion efficiency. Conversely, homodimeric species did not reform from isolated heterodimer upon long incubation. One must conclude that there is a barrier preventing complete complexation but once formed the complex is stable.

### 8.4 The hCCS-SOD1 heterogeneity and implications for ALS

The path from initial protein synthesis to a mature SOD1 dimer is littered with post-translation modification events. While mature SOD1 is the epitome of stability its precursors are recognised as unstable and aggregation prone with the majority of ALS SOD1 mutations enhancing this quality [78,223-225]. The copper chaperone for SOD1 is responsible for two SOD1 modifications: copper loading and disulphide oxidation. The presence or absence of the SOD1 catalytic copper centre is not thought to contribute to SOD1 disease pathogenesis [226] however the intrasubunit disulphide is of crucial importance [213,227,228]. Reduction of the SOD1 disulphide removes the anchor holding the zinc loop and must therefore promote disorder. This may lead to a decreased affinity for the structurally important zinc ion [213] or exposure of hydrophobic residues in the core of the molecule making it prone to aggregation.

Rather than functionalising freshly translated SOD1 at the ribosome, CCS is thought to cycle back and forth between the cell membrane, or an intracellular copper source, and a pool of pre-existing immature protein [222]. hCCS is not the only mechanism for SOD1 copper activation but 50 % of SOD1 molecules are found to have a reduced disulphide when CCS is deleted [229]. Thus disruption of this routine leads to an accumulation of potentially toxic immature SOD1.

The results presented in the previous chapter indicate structural differences when I113T and, to a much less extent L38V, SOD1 is complexed with hCCS in comparison with wild-type SOD1 however the reasons for this are abstruse. The hCCS-I113T SOD1 heterodimer exhibits a rearrangement of domains and a much more compact structure. The linkers

which join hCCS domain I and III to the central SOD1-like domain originate directly opposite SOD1 residue 113 in the dimer interface region. The I113T mutation is also found at the SOD1 dimer interface which it alters and induces a change in the orientation of the two monomers [89]. This reorientation of monomers is also likely to occur in the heterocomplex due to the similarity of the interface region. Thus it seems that perturbation of the hCCS-SOD1 dimer interface precipitates a conformational change in the two copper binding hCCS domains perhaps by steric hindrance at the origin of their flexible linkers.

hCCS-I113T SOD1 gives the impression of a complex that is much more globular and conformationally less flexible than the wild-type. A close inspection of Figure 7.15 and 7.19 indicate that hCCS domain III is exclusively found close to the SOD1 monomer in a position that would facilitate copper transfer and disulphide oxidation. These structures could be interpreted as domain III being locked in the conformation adopted to transfer copper and disulphide. A result of this relatively static conformation is an increase in the number of contacts between domain III and SOD1 that would stabilise the heterodimeric complex.

In both the yeast and human systems, SOD1 mutants have previously been observed to promote stable complexation with hCCS. In both cases these mutations were to the copper active sites [208,215]. The notion that stable hCCS-SOD1 complexes may prevent proper SOD1 maturation by sequestering active hCCS has been proposed previously and hinges on the excess of SOD1 compared to hCCS [230]. This normal imbalance would be exacerbated if hCCS was prevented from cycling and would effectively strand the majority of SOD1 in the immature, disulphide reduced form. What we see here is the extension of this paradigm to include the I113T mutation and by inference, all the dimer interface mutants.

### 8.5 Prospects and further work

The work presented here is the first direct evidence of a perturbed interaction between hCCS and mutant SOD1. The X-ray scattering studies undertaken here are an important foot-hold in this relatively under explored area however there are two important questions still to be answered: does this shift in the arrangement of hCCS domains occur with all SOD1 mutants and, does the shift observed have a pathogenic effect? While the first simply necessitates repetition with a wider cross-section of SOD1 mutants the second is more difficult to test. hCCS-SOD1 complexes are notoriously difficult to crystallise however the stability of the complexes presented here may facilitate characterisation by NMR methods. Alternatively, labelling either the SOD1 or hCCS component before complexation may enable dissociation rates to be calculated and compared between the wild-type complex and SOD1 mutants.

# Chapter IX

## Materials and Methods

### 9.1 SOD1 cloning and plasmid construction

SOD1 coding DNA was amplified by polymerase chain reaction (PCR) using primers 'SOD1Fwd' and 'SOD1Rev' (Appendix I) with KOD Hotstart DNA polymerase (Novagen) from yEP351-hSOD1 plasmid with cycling conditions:

| | Stage | Temperature (ºC) | Time (s) |
|---|---|---|---|
| | Initial Denaturation | 95 | 120 |
| | Denaturation | 95 | 15 |
| 30 cycles | Annealing | 55 | 15 |
| | Elongation | 70 | 15 |
| | Terminal Elongation | 70 | 600 |

Table 9.1 PCR cycling conditions for SOD1 DNA amplification.

PCR products were ligated into pCR-Zeroblunt (Appendix II) plasmid using the Zero Blunt PCR Cloning Kit (Invitrogen). Ligation products were transformed into Omnimax2 strain *E. coli* (Appendix III), plated onto selective solid media and incubated at 37 ºC overnight. Transformants were cultured in selective liquid LB media overnight at 37 ºC. Plasmid was extracted by Wizard SV Minipreps DNA Purification System (Promega) and sequenced by DNA terminator reaction at GATC Biotech. The resulting plasmid, pCR-hSOD1wt (Appendix II), was digested at 37 ºC for one hour with XbaI and XhoI (NEB) restriction enzymes. The 474 bp fragment corresponding to the hSOD1wt DNA was extracted from a 1% TAE agarose gel after electrophoresis at 120 V for 25 minutes in TAE buffer using Wizard SV Gel and PCR Clean-Up System (Promega). Purified SOD1 coding DNA was ligated into XbaI-XhoI digested pET303 vector (Appendix II) using T4 DNA ligase (NEB), transformed into Omnimax2 strain *E. coli,* plated onto selective solid media and incubated at 37 ºC overnight. Transformants were grown overnight at 37 ºC in selective liquid LB media and plasmids extracted by Wizard SV Minipreps DNA Purification System. Putative

pET303-hSOD1wt (Appendix II) plasmids were sequenced by GATC Biotech.

### 9.2 Site directed mutagenesis

Site directed mutagenesis (SDM) was carried out on pET303-hSOD1wt to introduce the I113T and L38V mutations using Stratagene's QuikChange Lightning Site-Directed Mutagenesis Kit (Agilent) and relevant DNA oligonucleotides (Appendix I). This yielded the expression plasmids pET303-hSOD1 I113T and pET303-hSOD1 L38V (Appendix II).

### 9.3 Expression of recombinant SOD1 proteins

pET303-hSOD1 expression plasmids were transformed in to BL21 (DE3) (Appendix III) strain *E. coli*. Transformants were then cultured in selective liquid LB media at 37 $^{o}$C overnight. 10 ml of overnight culture was then transferred into 1 l selective LB liquid media and incubated at 37 $^{o}$C with 220 rpm shaking. When optical density ($OD_{600}$) ~ 0.5, Isopropyl β-D-1-thiogalactopyranoside (IPTG) (Calbiochem) was added to a final concentration of 0.4 mM. Cultures were then incubated at 25$^{o}$C with shaking at 220rpm overnight. Cultures were centrifuged at 3000 g for 20 minutes at 4 $^{o}$C and the cell pellet separated from the culture media before freezing at -70 $^{o}$C for at least 30 minutes or flash freezing with liquid nitrogen.

### 9.4 SOD1 purification

Two strategies were employed to purify recombinant human SOD1 from *E. coli*. In the first instance, cells were resuspended in phenyl-sepharose lysis buffer ($KH_2PO_4$ 100mM, NaCl 150mM, lysozyme 0.2mg/ml, DNaseI 10µg/ml, 1 in 1000 protease inhibitor cocktail set III (Calbiochem), pH 7.4), lysed by sonication and the soluble and insoluble cell fractions were separated by centrifugation at 30,000 g for 2 hours. Chilled ammonium sulphate 4 M solution was slowly added to the soluble cell fraction on ice and stirred for 30 minutes before centrifugation at 8000g for 20 minutes. The supernatant was then applied to a phenyl-sepharose hydrophobic interaction chromatography column pre-equilibrated with lysis buffer containing 2 M ammonium sulphate. Recombinant SOD1 was eluted by gradually decreasing the ammonium sulphate concentration. Fractions were observed by SDS-PAGE. SOD1 containing fractions were pooled and dialysed against Tris-HCl

100mM and 150mM NaCl pH 7.4 before storage at -20$^{o}$C.

Purification of SOD1 for use in complexation experiments with hCCS occurred by re suspension of bacterial cell pellet in DEAE lysis buffer (20 mM Tris-HCl, lysozyme 0.2mg/ml, DNaseI 10µg/ml, 1 in 1000 protease inhibitor cocktail set III pH 8) with cell lysis and separation as above. The soluble fraction was then dialysed at least 3 times against 20mM Tris-HCl pH 8 in 10 kDa molecular weight cut-off dialysis tubing. The soluble fraction was then applied to DEAE-sepharose pre-equilibrated with 20mM Tris-HCl pH 8. Protein elution was achieved by increasing the concentration of NaCl. SOD1 eluted in the low millimolar range of salt concentration. Fractions were analysed by SDS-PAGE and those found to contain SOD1 were pooled, concentrated and applied to a Superdex 200 16/60 gel filtration column pre-quilibriated with 20 mM Tris HCl, 150 mM NaCl pH 7.4 operated with an ÄKTA purifyer. The peak corresponding to dimeric SOD1 was collected, concentrated and stored at -20 $^{o}$C.

**9.5 Crystallisation, soaking experiments and data collection**

Crystals in the $P2_1$ space group were grown at 20 $^{o}$C in sodium acetate 100 mM, NaCl 150mM pH 4.75 using 2.5 M ammonium sulphate as precipitant by the hanging drop vapour diffusion method from a pre-existing seed. Recombinant SOD1 crystals were also grown in 2.5 M ammonium sulphate, NaCl 150mM, Tri-HCl 100mM pH 8. These crystals formed spontaneously and were not seeded.

Appendix IV shows the compounds used throughout this study. 5-Fluorouridine, isoproteranol, dopamine and adrenaline were purchased from Sigma Aldrich UK. 4-(4-methyl-1,4-diazepan-1-yl)-2-(trifluoromethyl) quinazoline (MDTQ), 4-(4-methylpiperazin-1-yl)quinazoline (MPQ) and 4-(4-methyl-1,4-diazepan-1-yl)quinazoline (MDQ) were made in house in the Department of Chemistry at the University of Liverpool through a collaboration with Prof. P. O'Neil and Dr N. Kershaw.

Before crystal soaking, compounds were dissolved at 50 mM in a $NH_4SO_4$ 2.5 M, NaCl 150 mM, sodium acetate 100 mM pH 4.75 solution. Those compounds that were not soluble in this buffer were dissolved in 100% DMSO at a concentration of 50 mM. Crystals soaked in the former group of compounds were incubated for at least 2 hours at 20

ºC in a drop hanging over their original reservoir solution. Compounds in the latter group were mixed 1:4 with 3.3 M ammonium sulphate, NaCl 200 mM, sodium acetate 130 mM pH 4.75. Crystals were then incubated in this solution for 2 hours at 20 ºC over their original reservoir solution. Both sets of soaked crystals used paratone-N (Molecular Dimensions) as cryoprotectant and were frozen in liquid nitrogen. I113T crystals grown at pH 8 were soaked in a similar fashion however the compounds were dissolved in 3M ammonium sulphate, 150mM NaCl, 100mM Tris-HCl pH 8. A cryoprotectant of this solution with 25% glycerol was used.

X-ray crystallographic data sets were collected at Diamond Light Source station I02 and IO3, Oxford, UK and Soleil station Proxima 1, Saint-Aubin, France. Reflection data were integrated and scaled using HKL2000 [113], XDS [231] or iMosflm [112] and Scala [114]. Cycles of model building and refinement used REFMAC5 [117] and COOT [232]. A SOD1 model derived from an atomic resolution structure (PDB code: 2c9v [51]) was used as the starting model.

### 9.6 *In vitro* SOD1 aggregation assay

I113T and L38V SOD1 were purified by DEAE sepharose anion exchange chromatography as described above. A4V SOD1 was cloned expressed and purified according to *Ray et al* [86]. Metal ions were removed from the purified proteins according to the method of *McCord and Fridovich* [233]. After metal removal at pH 3.8, proteins were repeatedly dialysed against TBS pH 7.4 which had previously been demetallated with Chelex resin (Biorad). Compounds were dissolved in demetallated TBS pH 7.4. Protein and compound were mixed in each assay in a 350 µl volume and incubated at for 15 minutes before addition of 5 mM EDTA whereupon they were incubated at 37ºC for 4 or 48 hours. Samples (300 µl) were analysed on a Superose-12 using an ÄKTA purifier.

### 9.7 hCCS cloning and expression

The human CCS coding sequence was amplified by PCR using primers 'hCCSFwd' and 'hCCSRev' (Appendix I) from an EST clone (gi:8327523) containing the full hCCS sequence using KOD hotstart DNA polymerase (Novagen) according to cycling conditions:

| | Stage | Temperature (°C) | Time (s) |
|---|---|---|---|
| | Initial denaturation | 95 | 120 |
| | Denaturation | 95 | 15 |
| 30 cycles | Annealing | 55 | 15 |
| | Elongation | 70 | 15 |
| | Terminal elongation | 70 | 600 |

Table 9.2 PCR cycling conditions for hCCS DNA amplification.

PCR products were ligated into pCR-Zeroblunt (Appendix II) plasmid using the Zero Blunt PCR Cloning Kit (Invitrogen). Ligation products were transformed into Omnimax2 strain *E. coli* (Appendix III), plated onto selective solid media and incubated at 37 °C overnight. Transformants were cultured in selective liquid LB media overnight at 37 °C. Plasmid was extracted by Wizard SV Miniprep DNA Purification System (Promega) and sequenced by DNA terminator reaction at GATC Biotech. The resulting plasmid, pCR-hCSS (AppendixII), was digested at 37 °C for one hour with NcoI and XhoI (NEB) restriction enzymes. The 827 bp fragment corresponding to the hCSS DNA was extracted from a 1% TAE agarose gel after electrophoresis at 120 V for 25 minutes in TAE buffer using Wizard SV Gel and PCR Clean-Up System (Promega).

Purified hCCS coding DNA was ligated into NcoI-XhoI digested pETM11 vector (Appendix II) using T4 DNA ligase (NEB), transformed into Omnimax2 strain *E. coli,* plated onto selective solid media and incubated at 37 °C overnight. Transformants were grown overnight at 37 °C in selective liquid LB media and plasmids extracted by Wizard SV Minipreps DNA Purification System. Putative pETM11-hCCS (Appendix II) plasmids were sequenced by GATC Biotech. pETM11-hCCS was transformed into BL21 (DE3) *E. coli* (Appendix III) and plated on selective media. Colonies were then taken and cultured in 20 ml selective LB medium overnight at 37 °C with shaking at 220 rpm. 1 litre of selective

LB medium was inoculated with 10ml of this starter culture and grown at 37 ºC with 220 rpm shaking until $OD_{600}$ ~ 0.5 whereupon expression was induced with IPTG at a final concentration of 0.4 mM. Cultures were then incubated at 30 ºC with 220 rpm shaking overnight.

Large-scale cultures were then centrifuged at 3000 g for 20 minutes at 4 ºC and the cell pellet separated from the culture media before freezing at -70 ºC for at least 30 minutes. Cells were then resuspended in NiNTA lysis buffer ($NaH_2PO_4$ 50 mM, NaCl 500 mM, imidazole 10 mM, DTT 5mM, lysozyme 0.2mg/ml, DNaseI 10µg/ml, Protease inhibitor cocktail set III 1:1000 (Calbiochem), pH 7.4) and lysed by sonication on ice. Fractions were then separated by centrifugation at 30,000g for 2 hours at 4 ºC.

**9.8 Purification and tag removal**

Human recombinant CCS expressed using the system described is fused to a cleavable hexa-histidine tag that facilitates purification by nickel affinity chromatography. The soluble cell fraction generated as above was filtered through a 0.22 µm syringe filter before application to a 5 ml NiNTA HisTrap column (GE Healthcare) pre-equilibrated with NiNTA binding buffer ($NaH_2PO_4$ 20 mM, NaCl 500 mM, imidazole 10 mM, DTT 5 mM, pH 7.4). After application, the column was washed with ten column volumes of NiNTA binding buffer. The protein was then eluted by application of ten column volumes of NiNTA elution buffer ($NaH_2PO_4$ 20 mM, NaCl 500 mM, DTT 5 mM, pH 7.4) with gradually increasing imidazole concentration (10 mM – 500 mM).

The semi-pure protein was then dialysed against NiNTA binding buffer and TEV (Tobacco Etch Virus) protease subsequently added to a final concentration of 100 µg/ml and incubated at 4 ºC overnight. This solution was then reapplied to a NiNTA column and recombinant hCCS protein was collected as the flow through. The pure protein was then dialysed against storage buffer (Tris-HCl 50 mM, NaCl 150mM, DTT 5mM, pH 8.0) concentrated and applied to either a Superdex 200 10/30 or Superdex 200 16/60 column. Fractions were analysed by SDS-PAGE and those containing the 29.1 kDa protein were pooled and stored at 4 ºC or frozen at -20 ºC.

### 9.9 hCCS-SOD1 heterodimeric complex formation

hCCS-SOD1 complex formation was carried out roughly according to the protocols of *Winkler et al* [208] and *Lamb et al* [215]. SOD1 and its fALS associated mutants were expressed and purified according to the method described in the previous sections. Before mixing SOD1 and hCCS, 5 mM DTT was added to the SOD1 buffer and incubated at room temperature for at least 4hours. Protein were mixed in a 1:1.5 hCCS:SOD1 molar ratio. After mixing, the proteins were loaded on a Superdex 200 16/60 column pre-equilibriated with Tris-HCl 50 mM, NaCl 150 mM DTT 5 mM. Protein elution was monitored by UV absorption at 280 nm and 260 nm.

### 9.10 Small-angle X-ray data collection and processing

SAXS data for homodimeric hCCS were collected on the SWING beamline at SOLEIL synchrotron, St Aubin, France, using the HPLC integrated SAXS setup [211]. Protein (400 µg in 40 µl storage buffer) was loaded onto a pre-equilibrated Shodex KW402.5-4F 150 kDa SEC column at a flow rate of 80 µl/min using an Agilent 1200 series HPLC at 25 $^{o}$C before passing through the beam with wavelength 1.03 Å. The sample to detector distance was set to 180 cm. 250 exposures of 2 seconds duration were taken over the course of protein elution with 1 second dead time between each. 20 frames were taken prior to protein elution for buffer subtraction purposes.

SAXS data for the heterodimeric hCCS-SOD1 complex were acquired in a similar fashion however a Superdex 200 16/60 column was used for protein separation. Column temperature was kept at 20 $^{o}$C using a chilled water bath and a flow rate of 0.75 ml/min was established. 250 frames were taken over the course of protein elution with a 3 second exposure time separated by 1.5 seconds dead time. 100 frames were taken before the protein eluted for buffer subtraction. Samples of differing concentrations were loaded in a 900 µl volume.

Scattering intensity was recorded on an AVIEX170x170 mm CCD detector over an angular range $q_{min}$ = 0.01 Å$^{-1}$ to $q_{max}$ = 0.5 Å$^{-1}$. Data averaging and reduction, including preliminary *R*g and *I*(0) calculations, were carried out using the Foxtrot suite developed at SOLEIL for the SWING beamline. Further analysis was performed with PRIMUS [234] where radius of

gyration values were determined fulfilling the condition $qR(g)<1.3$. Particle distance distribution function $p(r)$ analysis was carried out using iterative cycles of GNOM [235] using the Guinier $R(g)$ values as guide for refinement of $D_{max}$. *Ab initio* 3-D shape reconstruction was then performed, without the imposition of symmetry restraints for hCCS and hCCS-SOD1 and with an enforced two-fold symmetry axis for SOD1, using the GASBOR web server (EMBL Hamburg) [203]. 20 models were averaged with DAMAVER [236] and the resulting structures compared in PyMOL [237].

### 9.11 Rigid body modelling

The published crystal structure of hCCS domain II [195] was used as a the structural model for the hCCS amino acid region 88 – 232 (PDB ID: 1DO5). The structure of region 12 – 69 was inferred from the NMR model of this domain (PDB ID: 2CRL). The secondary structure of the short α-helix found in domain III, amino acids 250 – 258, was inferred using I-TASSER [238]. Terminal and linker regions 1 – 11 (with the addition of two extra amino acids remaining from TEV cleavage of the hexa-histidine tag), 77 – 87, 233 – 249 and 259 – 274 are predicted to be unstructured.

The hCCS homodimer was modelled using BUNCH [204] to generate 25 hCCS models constrained by the position of the SOD1-like domain II that forms the interface between two CCS monomers. The hCCS-SOD1 heterodimer was modelled using CORAL, a variant of BUNCH that facilitates analysis of protein complexes. In both cases, unrestrained movement of hCCS domain I and III together with the flexible linker regions was permitted. BUNCH and CORAL only generate $C_\alpha$-atom positions for flexible structural segments such as linkers and peptide terminal ends. For the purposes of visualisation the protein backbone and sidechain positions of these flexible regions were reconstructed from their $C_\alpha$ traces using the SABBAC web server [239]. The scattering profile of each reconstructed and complete model was then computed with CRYSOL [240].

# References


1. Mitchell J.D. & Borasio G.D. Amyotrophic lateral sclerosis. *Lancet* **369**, 2031-2041 (2007).
2. Logroscino G, Traynor B.J, Hardiman O, Chiò A, Mitchell D, Swingler R.J, Millul A, Benn E. & Beghi E. Incidence of amyotrophic lateral sclerosis in Europe. *J. Neurol. Neurosurg. Psychiatr.* **81**, 385-390 (2010).
3. Beghi E, Logroscino G, Chiò A, Hardiman O, Mitchell D, Swingler R. & Traynor B.J. The epidemiology of ALS and the role of population-based registries. *Biochim. Biophys. Acta* **1762**, 1150-1157 (2006).
4. Hirtz D, Thurman DJ, Gwinn-Hardy K, Mohamed M, Chaudhuri A.R. & Zalutsky R. How common are the "common" neurologic disorders? *Neurology* **68**, 326-337 (2007).
5. Reitz C, Brayne C. & Mayeux R. Epidemiology of Alzheimer disease. *Nat. Rev. Neurol.* **7**, 137-152 (2011).
6. Traynor B.J, Codd M.B, Corr B, Forde C, Frost E. & Hardiman O.M. Clinical features of amyotrophic lateral sclerosis according to the El Escorial and Airlie House diagnostic criteria: A population-based study. *Arch. Neurol.* **57**, 1171-1176 (2000).
7. Silani V, Messina S, Poletti B, Morelli C, Doretti A, Ticozzi N. & Maderna L. The diagnosis of Amyotrophic Lateral Sclerosis in 2010. *Arch. Ital. Biol.* **149**, 5-27 (2011).
8. Polkey M.I, Lyall R.A, Moxham J. & Leigh P.N. Respiratory aspects of neurological disease. *J. Neurol. Neurosurg. Psychiatr.* **66**, 5-15 (1999).
9. Ramirez C, Piemonte M.E.P, Callegaro D. & Da Silva H.C.A. Fatigue in amyotrophic lateral sclerosis: frequency and associated factors. *Amyotroph. Lateral Scler.* **9**, 75-80 (2008).
10. Simmons Z. Management strategies for patients with amyotrophic lateral sclerosis from diagnosis through death. *Neurologist* **11**, 257-270 (2005).
11. Neudert C, Oliver D, Wasner M. & Borasio, G.D. The course of the terminal phase in patients with amyotrophic lateral sclerosis. *J. Neurol.* **248**, 612-616 (2001).
12. Schymick J.C, Talbot K. & Traynor B.J. Genetics of sporadic amyotrophic lateral sclerosis. *Hum. Mol. Genet.* **16 Spec No. 2**, R233-242 (2007).
13. Mulder D.W, Kurland L.T, Offord K.P. & Beard C.M. Familial adult motor neuron disease: amyotrophic lateral sclerosis. *Neurology* **36**, 511-517 (1986).
14. Hadano S, Hand C.K, Osuga H, Yanagisawa Y, Otomo A, Devon R.S, Miyamoto N, Showguchi-Miyata J, Okada Y, Singaraja R, Figlewicz D.A, Kwiatkowski T, Hosler B.A, Sagie T, Skaug J, Nasir J, Brown R.H. Jr, Scherer S.W, Rouleau G.A, Hayden M.R. & Ikeda J.E. A gene encoding a putative GTPase regulator is mutated in familial amyotrophic lateral sclerosis 2. *Nat. Genet.* **29**, 166-173 (2001).
15. Hentati A, Ouahchi K, Pericak-Vance M.A, Nijhawan D, Ahmad A, Yang Y, Rimmler J, Hung W, Schlotter B, Ahmed A, Ben Hamida M, Hentati F. & Siddique T. Linkage of a commoner form of recessive amyotrophic lateral sclerosis to chromosome 15q15-q22 markers. *Neurogenetics* **2**, 55-60 (1998).
16. Chen Y.Z, Bennett C.L, Huynh H.M, Blair I.P, Puls I, Irobi J, Dierick I, Abel A, Kennerson M.L, Rabin B.A, Nicholson G.A, Auer-Grumbach M, Wagner K, De Jonghe P, Griffin J.W, Fischbeck K.H, Timmerman V, Cornblath D.R. & Chance P.F. DNA/RNA helicase gene mutations in a form of juvenile amyotrophic lateral sclerosis (ALS4). *Am. J. Hum. Genet.* **74**, 1128-1135 (2004).
17. Rosen D.R, Siddique T, Patterson D, Figlewicz D.A, Sapp P, Hentati A, Donaldson D, Goto J, O'Regan J.P, Deng H.X, Rahmani Z, Krizus A, McKenna-Yasek D, Cayabyab

A, Gaston S.M, Berger R, Tanzi R.E, Halperin J.J, Herzfeldt B, Van den Bergh R, Hung W.Y, Bird T, Deng G, Mulder D.W, Smyth C, Laing N.G, Soriano E, Pericak–Vance M.A, Haines J, Rouleau G.A, Gusella J.S, Horvitz H.R. & Brown R.H. Jr. Mutations in Cu/Zn superoxide dismutase gene are associated with familial amyotrophic lateral sclerosis. *Nature* **362**, 59-62 (1993).
18. Kabashi E, Valdmanis P.N, Dion P, Spiegelman D, McConkey B.J, Vande Velde C, Bouchard J.P, Lacomblez L, Pochigaeva K, Salachas F, Pradat P.F, Camu W, Meininger V, Dupre N. & Rouleau G.A. TARDBP mutations in individuals with sporadic and familial amyotrophic lateral sclerosis. *Nat. Genet.* **40**, 572-574 (2008).
19. Yang Y, Hentati A, Deng H.X, Dabbagh O, Sasaki T, Hirano M, Hung W.Y, Ouahchi K, Yan J, Azim A.C, Cole N, Gascon G, Yagmour A, Ben-Hamida M, Pericak-Vance M, Hentati F. & Siddique T. The gene encoding alsin, a protein with three guanine-nucleotide exchange factor domains, is mutated in a form of recessive amyotrophic lateral sclerosis. *Nat. Genet.* **29**, 160-165 (2001).
20. Maruyama H, Morino H, Ito H, Izumi Y, Kato H, Watanabe Y, Kinoshita Y, Kamada M, Nodera H, Suzuki H, Komure O, Matsuura S, Kobatake K, Morimoto N, Abe K, Suzuki N, Aoki M, Kawata A, Hirai T, Kato T, Ogasawara K, Hirano A, Takumi T, Kusaka H, Hagiwara K, Kaji R. & Kawakami H. Mutations of optineurin in amyotrophic lateral sclerosis. *Nature* **465**, 223-226 (2010).
21. Nishimura A.L, Mitne-Neto M, Silva H,C, Richieri-Costa A, Middleton S, Cascio D, Kok F, Oliveira J,R, Gillingwater T, Webb J, Skehel P. & Zatz M. A mutation in the vesicle-trafficking protein VAPB causes late-onset spinal muscular atrophy and amyotrophic lateral sclerosis. *Am. J. Hum. Genet.* **75**, 822-831 (2004).
22. Chen H.J, Anagnostou G, Chai A, Withers J, Morris A, Adhikaree J, Pennetta G. & de Belleroche J.S. Characterization of the properties of a novel mutation in VAPB in familial amyotrophic lateral sclerosis. *J. Biol. Chem.* **285**, 40266-40281 (2010).
23. Wang H.Y, Wang I.F, Bose J. & Shen C.K. Structural diversity and functional implications of the eukaryotic TDP gene family. *Genomics* **83**, 130-139 (2004).
24. Rabbitts T.H, Forster A, Larson R. & Nathan P. Fusion of the dominant negative transcription regulator CHOP with a novel gene FUS by translocation t(12;16) in malignant liposarcoma. *Nat. Genet.* **4**, 175-180 (1993).
25. Ou S.H, Wu F, Harrich D, García-Martínez L.F. & Gaynor R.B. Cloning and characterization of a novel cellular protein, TDP-43, that binds to human immunodeficiency virus type 1 TAR DNA sequence motifs. *J. Virol.* **69**, 3584-3596 (1995).
26. Kwiatkowski T.J. Jr, Bosco D.A, Leclerc A.L, Tamrazian E, Vanderburg C.R, Russ C, Davis A, Gilchrist J, Kasarskis E.J, Munsat T, Valdmanis P, Rouleau G.A, Hosler B.A, Cortelli P, de Jong P.J, Yoshinaga Y, Haines J.L, Pericak-Vance M.A, Yan J, Ticozzi N, Siddique T, McKenna-Yasek D, Sapp P.C, Horvitz H.R, Landers J.E. & Brown R.H. Jr. Mutations in the FUS/TLS gene on chromosome 16 cause familial amyotrophic lateral sclerosis. *Science* **323**, 1205-1208 (2009).
27. Neumann M, Sampathu D.M, Kwong L.K, Truax A.C, Micsenyi M.C, Chou T.T, Bruce J, Schuck T, Grossman M, Clark C.M, McCluskey L.F, Miller B.L, Masliah E, Mackenzie I.R, Feldman H, Feiden W, Kretzschmar H.A, Trojanowski J.Q. & Lee V.M. Ubiquitinated TDP-43 in frontotemporal lobar degeneration and amyotrophic lateral sclerosis. *Science* **314**, 130-133 (2006).
28. Wroe R, Wai-Ling Butler A, Andersen P.M, Powell J.F. & Al-Chalabi A. ALSOD: the Amyotrophic Lateral Sclerosis Online Database. *Amyotroph. Lateral Scler.* **9**, 249-250 (2008).
29. Radunovíc A. & Leigh P.N. Cu/Zn superoxide dismutase gene mutations in

amyotrophic lateral sclerosis: correlation between genotype and clinical features. *J. Neurol. Neurosurg. Psychiatr.* **61**, 565-572 (1996).
30. Cleveland D.W, Laing N, Hurse P.V. & Brown R.H. Jr. Toxic mutants in Charcot's sclerosis. *Nature* **378**, 342-343 (1995).
31. Zinman L, Liu H.N, Sato C, Wakutani Y, Marvelle A.F, Moreno D, Morrison K.E, Mohlke K.L, Bilbao J, Robertson J, Rogaeva E. A mechanism for low penetrance in an ALS family with a novel SOD1 deletion. *Neurology* **72**, 1153-1159 (2009).
32. Sapp P.C, Rosen D.R, Hosler B.A, Esteban J, McKenna-Yasek D, O'Regan J.P, Horvitz H.R. & Brown R.H. Jr. Identification of three novel mutations in the gene for Cu/Zn superoxide dismutase in patients with familial amyotrophic lateral sclerosis. *Neuromuscul. Disord.* **5**, 353-357 (1995).
33. Shaw P.J, Tomkins J, Slade J.Y, Usher P, Curtis A, Bushby K. & Ince P.G.CNS tissue Cu/Zn superoxide dismutase (SOD1) mutations in motor neurone disease (MND). *Neuroreport* **8**, 3923-3927 (1997).
34. Shi S, Li L, Chen K. & Liu X. Identification of the mutation of SOD1 gene in a familial amyotrophic lateral sclerosis. *Zhonghua Yi Xue Yi Chuan Xue Za Zhi* **21**, 149-152 (2004).
35. Hayward C, Brock D.J, Minns R.A. & Swingler R.J. Homozygosity for Asn86Ser mutation in the CuZn-superoxide dismutase gene produces a severe clinical phenotype in a juvenile onset case of familial amyotrophic lateral sclerosis. *J. Med. Genet.* **35**, 174 (1998).
36. Andersen P.M, Nilsson P, Ala-Hurula V, Keränen M.L, Tarvainen I, Haltia T, Nilsson L, Binzer M, Forsgren L. & Marklund S.L. Amyotrophic lateral sclerosis associated with homozygosity for an Asp90Ala mutation in CuZn-superoxide dismutase. *Nat. Genet.* **10**, 61-66 (1995).
37. Pauling L. The discovery of the superoxide radical. *Trends in Biochemical Sciences* **4**, N270-N271 (1979).
38. Gruber J, Schaffer S. & Halliwell B. The mitochondrial free radical theory of ageing--where do we stand? *Front. Biosci.* **13**, 6554-6579 (2008).
39. Fridovich I. Superoxide dismutases. *Annu. Rev. Biochem.* **44**, 147-159 (1975).
40. Valentine J.S, Doucette P.A. & Zittin Potter S. Copper-zinc superoxide dismutase and amyotrophic lateral sclerosis. *Annu. Rev. Biochem.* **74**, 563-593 (2005).
41. Klug D, Rabani J. & Fridovich I. A direct demonstration of the catalytic action of superoxide dismutase through the use of pulse radiolysis. *J. Biol. Chem.* **247**, 4839-4842 (1972).
42. Riley D.P, Rivers W.J. & Weiss R.H. Stopped-flow kinetic analysis for monitoring superoxide decay in aqueous systems. *Anal. Biochem.* **196**, 344-349 (1991).
43. Smith M.W. & Doolittle R.F. A comparison of evolutionary rates of the two major kinds of superoxide dismutase. *J. Mol. Evol.* **34**, 175-184 (1992).
44. Bannister W.H, Bannister J.V, Barra D, Bond J. & Bossa, F. Evolutionary aspects of superoxide dismutase: the copper/zinc enzyme. *Free Radic. Res. Commun.* **12-13 Pt 1**, 349-361 (1991).
45. Kurobe N, Suzuki F, Okajima K. & Kato K. Sensitive enzyme immunoassay for human Cu/Zn superoxide dismutase. *Clin. Chim. Acta* **187**, 11-20 (1990).
46. Crapo J.D, Oury T, Rabouille C, Slot J.W. & Chang L.Y. Copper,zinc superoxide dismutase is primarily a cytosolic protein in human cells. *Proc. Natl. Acad. Sci. U.S.A* **89**, 10405-10409 (1992).
47. Kawamata H. & Manfredi G. Different regulation of wild-type and mutant Cu,Zn superoxide dismutase localization in mammalian mitochondria. *Hum. Mol. Genet* **17**, 3303-3317 (2008).

48. Chang L.Y, Slot J.W, Geuze H.J. & Crapo J.D. Molecular immunocytochemistry of the CuZn superoxide dismutase in rat hepatocytes. *J. Cell Biol.* **107**, 2169-2179 (1988).
49. Tainer J.A, Getzoff E.D, Beem K.M, Richardson J.S. & Richardson D.C. Determination and analysis of the 2 A-structure of copper, zinc superoxide dismutase. *J. Mol. Biol.* **160**, 181-217 (1982).
50. Parge H.E, Hallewell R.A. & Tainer J.A. Atomic structures of wild-type and thermostable mutant recombinant human Cu,Zn superoxide dismutase. *Proc. Natl. Acad. Sci. U.S.A* **89**, 6109-6113 (1992).
51. Strange R.W, Antonyuk S.V, Hough M.A, Doucette P.A, Valentine J.S, Hasnain S.S. Variable metallation of human superoxide dismutase: atomic resolution crystal structures of Cu-Zn, Zn-Zn and as-isolated wild-type enzymes. *J. Mol. Biol.* **356**, 1152-1162 (2006)
52. Alexander M.D, Traynor BJ, Miller N, Corr B, Frost E, McQuaid S, Brett F.M, Green A. & Hardiman O. "True" sporadic ALS associated with a novel SOD-1 mutation. *Ann. Neurol* **52**, 680-683 (2002).
53. Millecamps S, Salachas F, Cazeneuve C, Gordon P, Bricka B, Camuzat A, Guillot-Noël L, Russaouen O, Bruneteau G, Pradat P.F, Le Forestier N, Vandenberghe N, Danel-Brunaud V, Guy N, Thauvin-Robinet C, Lacomblez L, Couratier P, Hannequin D, Seilhean D, Le Ber I, Corcia P, Camu W, Brice A, Rouleau G, LeGuern E. & Meininger V. SOD1, ANG, VAPB, TARDBP, and FUS mutations in familial amyotrophic lateral sclerosis: genotype-phenotype correlations. *J. Med. Genet.* **47**, 554-560 (2010).
54. Aoki M, Ofgasawara M, Matsubara Y, Narisawa K, Nakamura S, Itoyama Y. & Abe K. Mild ALS in Japan associated with novel SOD mutation. *Nat. Genet.* **5**, 323-324 (1993).
55. Enayat Z.E, Orrell R.W, Claus A, Ludolph A, Bachus R, Brockmüller J, Ray-Chaudhuri K, Radunovic A, Shaw C, Wilkinson J, King A, Swash , Leigh P.N, de Belleroche J. & Powell J. Two novel mutations in the gene for copper zinc superoxide dismutase in UK families with amyotrophic lateral sclerosis. *Hum. Mol. Genet.* **4**, 1239-1240 (1995).
56. Andersen P.M, Nilsson P, Keränen M.L, Forsgren L, Hägglund J, Karlsborg M, Ronnevi L.O, Gredal O. & Marklund S.L. Phenotypic heterogeneity in motor neuron disease patients with CuZn-superoxide dismutase mutations in Scandinavia. *Brain* **120 ( Pt 10)**, 1723-1737 (1997).
57. Borchelt D.R, Lee M.K, Slunt H.S, Guarnieri M, Xu Z.S, Wong P.C, Brown R.H. Jr, Price D.L, Sisodia S.S. & Cleveland D.W. Superoxide dismutase 1 with mutations linked to familial amyotrophic lateral sclerosis possesses significant activity. *Proc. Natl. Acad. Sci. U.S.A* **91**, 8292-8296 (1994).
58. Kadekawa J, Fujimura H, Ogawa Y, Hattori N, Kaido M, Nishimura T, Yoshikawa H, Shirahata N, Sakoda S. & Yanagihara T. A clinicopathological study of a patient with familial amyotrophic lateral sclerosis associated with a two base pair deletion in the copper/zinc superoxide dismutase (SOD1) gene. *Acta Neuropathol.* **94**, 617-622 (1997).
59. Ratovitski T, Corson L.B, Strain J, Wong P, Cleveland D.W, Culotta V.C. & Borchelt DR. Variation in the biochemical/biophysical properties of mutant superoxide dismutase 1 enzymes and the rate of disease progression in familial amyotrophic lateral sclerosis kindreds. *Hum. Mol. Genet.* **8**, 1451-1460 (1999).
60. Gurney M.E, Pu H, Chiu A.Y, Dal Canto M.C, Polchow C.Y, Alexander D.D, Caliendo J, Hentati A, Kwon Y.W, Deng H.X, Chen W, Zhai P, Sufit R.L. & Siddique

T. Motor neuron degeneration in mice that express a human Cu,Zn superoxide dismutase mutation. *Science* **264**, 1772-1775 (1994).
61. Bruijn L.I, Houseweart M.K, Kato S, Anderson K.L, Anderson S.D, Ohama E, Reaume A.G, Scott R.W. & Cleveland D.W. Aggregation and motor neuron toxicity of an ALS-linked SOD1 mutant independent from wild-type SOD1. *Science* **281**, 1851-1854 (1998).
62. Kotulska K, LePecheur M, Marcol W, Lewin-Kowalik J, Larysz-Brysz M, Paly E, Matuszek I. & London J. Overexpression of copper/zinc-superoxide dismutase in transgenic mice markedly impairs regeneration and increases development of neuropathic pain after sciatic nerve injury. *J. Neurosci. Res.* **84**, 1091-1097 (2006).
63. Epstein C.J, Avraham K.B, Lovett M, Smith S, Elroy-Stein O, Rotman G, Bry C, Groner Y. Transgenic mice with increased Cu/Zn-superoxide dismutase activity: animal model of dosage effects in Down syndrome. *Proc. Natl. Acad. Sci. U.S.A* **84**, 8044-8048 (1987).
64. Reaume A.G, Elliott J.L, Hoffman E.K, Kowall N.W, Ferrante R.J, Siwek D.F, Wilcox H.M, Flood D.G, Beal M.F, Brown R.H. Jr, Scott R.W. & Snider W.D. Motor neurons in Cu/Zn superoxide dismutase-deficient mice develop normally but exhibit enhanced cell death after axonal injury. *Nat. Genet.* **13**, 43-47 (1996).
65. Kato S, Takikawa M, Nakashima K, Hirano A, Cleveland D.W, Kusaka H, Shibata N, Kato M, Nakano I. & Ohama E. New consensus research on neuropathological aspects of familial amyotrophic lateral sclerosis with superoxide dismutase 1 (SOD1) gene mutations: inclusions containing SOD1 in neurons and astrocytes. *Amyotroph. Lateral Scler. Other Motor Neuron Disord.* **1**, 163-184 (2000).
66. Brown R.H. Jr. SOD1 aggregates in ALS: Cause, correlate or consequence? *Nat. Med.* **4**, 1362-1364 (1998).
67. Wang J, Xu G. & Borchelt D.R. High molecular weight complexes of mutant superoxide dismutase 1: age-dependent and tissue-specific accumulation. *Neurobiol. Dis.* **9**, 139-148 (2002).
68. Kato S, Shimoda M, Watanabe Y, Nakashima K, Takahashi K. & Ohama E. Familial amyotrophic lateral sclerosis with a two base pair deletion in superoxide dismutase 1: gene multisystem degeneration with intracytoplasmic hyaline inclusions in astrocytes. *J. Neuropathol. Exp. Neurol.* **55**, 1089-1101 (1996).
69. De Vos K.J, Chapman A.L, Tennant M.E, Manser C, Tudor E.L, Lau K.F, Brownlees J, Ackerley S, Shaw P.J, McLoughlin D.M, Shaw C.E, Leigh P.N, Miller C.C. & Grierson AJ. Familial amyotrophic lateral sclerosis-linked SOD1 mutants perturb fast axonal transport to reduce axonal mitochondria content. *Hum. Mol. Genet.* **16**, 2720-2728 (2007).
70. Williamson T.L. & Cleveland D.W. Slowing of axonal transport is a very early event in the toxicity of ALS-linked SOD1 mutants to motor neurons. *Nat. Neurosci.* **2**, 50-56 (1999).
71. Pasinelli P, Belford M.E, Lennon N, Bacskai B.J, Hyman B.T, Trotti D. & Brown R.H. Jr. Amyotrophic lateral sclerosis-associated SOD1 mutant proteins bind and aggregate with Bcl-2 in spinal cord mitochondria. *Neuron* **43**, 19-30 (2004).
72. Hervias I, Beal M.F. & Manfredi G. Mitochondrial dysfunction and amyotrophic lateral sclerosis. *Muscle Nerve* **33**, 598-608 (2006).
73. Matsumoto G, Stojanovic A, Holmberg C.I, Kim S. & Morimoto, R.I. Structural properties and neuronal toxicity of amyotrophic lateral sclerosis-associated Cu/Zn superoxide dismutase 1 aggregates. *J. Cell Biol.* **171**, 75-85 (2005).
74. Rodriguez J.A, Valentine J.S, Eggers D.K, Roe J.A, Tiwari A, Brown R.H. Jr. & Hayward L.J. Familial amyotrophic lateral sclerosis-associated mutations decrease

the thermal stability of distinctly metallated species of human copper/zinc superoxide dismutase. *J. Biol. Chem.* **277**, 15932-15937 (2002).
75. Arnesano F, Banci L, Bertini I, Martinelli M, Furukawa Y. & O'Halloran T.V. The unusually stable quaternary structure of human Cu,Zn-superoxide dismutase 1 is controlled by both metal occupancy and disulfide status. *J. Biol. Chem.* **279**, 47998-48003 (2004).
76. Strange R.W, Antonyuk S, Hough M.A, Doucette P.A, Rodriguez J.A, Hart P.J, Hayward L.J, Valentine J.S. & Hasnain S.S. The structure of holo and metal-deficient wild-type human Cu, Zn superoxide dismutase and its relevance to familial amyotrophic lateral sclerosis. *J. Mol. Biol.* **328**, 877-891 (2003).
77. Elam J.S, Taylor A.B, Strange R, Antonyuk S, Doucette P.A, Rodriguez J.A, Hasnain S.S, Hayward L.J, Valentine J.S, Yeates T.O. & Hart P.J. Amyloid-like filaments and water-filled nanotubes formed by SOD1 mutant proteins linked to familial ALS. *Nat. Struct. Biol.* **10**, 461-467 (2003).
78. Banci L, Bertini I, Boca M, Girotto S, Martinelli M, Valentine J.S. & Vieru M. SOD1 and amyotrophic lateral sclerosis: mutations and oligomerization. *PLoS ONE* **3**, e1677 (2008).
79. Banci L, Bertini I, Durazo A, Girotto S, Gralla E.B, Martinelli M, Valentine J.S, Vieru M. & Whitelegge J.P. Metal-free superoxide dismutase forms soluble oligomers under physiological conditions: a possible general mechanism for familial ALS. *Proc. Natl. Acad. Sci. U.S.A* **104**, 11263-11267 (2007).
80. Furukawa Y, Torres A.S. & O'Halloran T.V. Oxygen-induced maturation of SOD1: a key role for disulfide formation by the copper chaperone CCS. *EMBO J.* **23**, 2872-2881 (2004).
81. Culotta V.C, Yang M. & O'Halloran T.V. Activation of superoxide dismutases: putting the metal to the pedal. *Biochim. Biophys. Acta* **1763**, 747-58 (2006).
82. Carroll M.C, Girouard J.B, Ulloa J.L, Subramaniam J.R, Wong P.C, Valentine J.S. & Culotta V.C. Mechanisms for activating Cu- and Zn-containing superoxide dismutase in the absence of the CCS Cu chaperone. *Proc. Natl. Acad. Sci. U.S.A* **101**, 5964-5969 (2004).
83. Tiwari A. & Hayward L.J. Familial Amyotrophic Lateral Sclerosis Mutants of Copper/Zinc Superoxide Dismutase Are Susceptible to Disulfide Reduction. *J. Biol. Chem.* **278**, 5984-5992 (2003).
84. Rakhit R, Crow J.P, Lepock J.R, Kondejewski L.H, Cashman N.R. & Chakrabartty A. Monomeric Cu,Zn-superoxide dismutase is a common misfolding intermediate in the oxidation models of sporadic and familial amyotrophic lateral sclerosis. *J. Biol. Chem* **279**, 15499-15504 (2004).
85. Khare S.D, Caplow M. & Dokholyan N.V. The rate and equilibrium constants for a multistep reaction sequence for the aggregation of superoxide dismutase in amyotrophic lateral sclerosis. *Proc. Natl. Acad. Sci. U.S.A* **101**, 15094-15099 (2004).
86. Ray S.S, Nowak R.J, Strokovich K, Brown R.H. Jr, Walz T. & Lansbury P.T. Jr. An intersubunit disulfide bond prevents in vitro aggregation of a superoxide dismutase-1 mutant linked to familial amytrophic lateral sclerosis. *Biochemistry* **43**, 4899-4905 (2004).
87. Auclair J.R, Boggio K.J, Petsko G.A, Ringe D. & Agar J.N. Strategies for stabilizing superoxide dismutase (SOD1), the protein destabilized in the most common form of familial amyotrophic lateral sclerosis. *Proc Natl Acad Sci U.S.A* **50** 21394-21399 (2010).
88. Ding F. & Dokholyan N.V. Dynamical roles of metal ions and the disulfide bond in Cu, Zn superoxide dismutase folding and aggregation. *Proc. Natl. Acad. Sci. U.S.A*

**105**, 19696-19701 (2008).
89. Hough M.A, Grossmann J.G, Antonyuk S.V, Strange R.W, Doucette P.A, Rodriguez J.A, Whitson L.J, Hart P.J, Hayward L.J, Valentine J.S. & Hasnain S.S. Dimer destabilization in superoxide dismutase may result in disease-causing properties: structures of motor neuron disease mutants. *Proc. Natl. Acad. Sci. U.S.A* **101**, 5976-5981 (2004).
90. Miller R.G, Mitchell J.D, Lyon M. & Moore D.H. Riluzole for amyotrophic lateral sclerosis (ALS)/motor neuron disease (MND). *Amyotroph. Lateral Scler. Other Motor Neuron Disord.* **4**, 191-206 (2003).
91. CytRx`s Arimoclomol to be Administered in a Phase 2/Phase 3 Adaptive Clinical Trial in a Subset of Patients with Familial ALS. *Reuters* (2009) http://www.reuters.com/article/pressRelease/idUS139511+23-Feb-2009+BW20090223
92. Benn, S.C. & Brown, R.H. Putting the heat on ALS. *Nat. Med.* **10**, 345-347 (2004).
93. Kiernan M.C, Vucic S, Cheah B.C, Turner M.R, Eisen A, Hardiman O, Burrell J.R. & Zoing MC. Amyotrophic lateral sclerosis. *Lancet* **377**, 942-955 (2011).
94. Kalmar B, Novoselov S, Gray A, Cheetham M.E, Margulis B. & Greensmith L. Late stage treatment with arimoclomol delays disease progression and prevents protein aggregation in the SOD1 mouse model of ALS. *J. Neurochem.* **107**, 339-350 (2008).
95. Dykxhoorn D.M, Novina C.D. & Sharp P.A. Killing the messenger: short RNAs that silence gene expression. *Nat. Rev. Mol. Cell Biol* **4**, 457-467 (2003).
96. Smith R.A, Miller T.M, Yamanaka K, Monia B.P, Condon T.P, Hung G, Lobsiger C.S, Ward C.M, McAlonis-Downes M, Wei H, Wancewicz E.V, Bennett C.F. & Cleveland D.W. Antisense oligonucleotide therapy for neurodegenerative disease. *J. Clin. Invest.* **116**, 2290-2296 (2006).
97. Towne C, Raoul C, Schneider B.L. & Aebischer P. Systemic AAV6 delivery mediating RNA interference against SOD1: neuromuscular transduction does not alter disease progression in fALS mice. *Mol. Ther.* **16**, 1018-1025 (2008).
98. Raoul C, Abbas-Terki T, Bensadoun J.C, Guillot S, Haase G, Szulc J, Henderson C.E. & Aebischer P. Lentiviral-mediated silencing of SOD1 through RNA interference retards disease onset and progression in a mouse model of ALS. *Nat. Med.* **11**, 423-428 (2005).
99. Lange D. Session 9B Clinical trials & trial design: C79 Pyrimethamine as a therapy for SOD1 associated fALS: Early findings. *Amyotrophic Lateral Sclerosis* **9**, 45-47 (2008).
100. Wright P.D, Huang M, Weiss A, Matthews J, Wightman N, Glicksman M. & Brown R.H. Jr. Screening for inhibitors of the SOD1 gene promoter: Pyrimethamine does not reduce SOD1 levels in cell and animal models. *Neurosci. Lett.* (2010).doi:10.1016/j.neulet.2010.07.020
101. Burbaum J.J. & Sigal N.H. New technologies for high-throughput screening. *Curr. Opin. Chem. Biol.* **1**, 72-78 (1997).
102. Hann M.M, Leach A.R. & Harper G. Molecular complexity and its impact on the probability of finding leads for drug discovery. *J. Chem. Inf. Comput. Sci.* **41**, 856-864 (2001).
103. Oprea T.I, Davis A.M, Teague S.J. & Leeson P.D. Is there a difference between leads and drugs? A historical perspective. *J. Chem. Inf. Comput. Sci.* **41**, 1308-1315 (2001).
104. Trouiller P, Olliaro P, Torreele E, Orbinski J, Laing R. & Ford N. Drug development for neglected diseases: a deficient market and a public-health policy failure. *Lancet* **359**, 2188-2194 (2002).
105. Rees D.C, Congreve M, Murray C.W. & Carr R. Fragment-based lead discovery. *Nat. Rev. Drug. Discov.* **3**, 660-672 (2004).

106. Nienaber V.L, Richardson P.L, Klighofer V, Bouska J.J, Giranda V.L. & Greer J. Discovering novel ligands for macromolecules using X-ray crystallographic screening. *Nat. Biotechnol.* **18**, 1105-1108 (2000).
107. de Kloe G.E, Bailey D, Leurs R. & de Esch I.J.P. Transforming fragments into candidates: small becomes big in medicinal chemistry. *Drug Discov. Today* **14**, 630-646 (2009).
108. Hopkins A.L, Groom C.R. & Alex A. Ligand efficiency: a useful metric for lead selection. *Drug Discov. Today* **9**, 430-431 (2004).
109. Lipinski C.A, Lombardo F, Dominy B.W. & Feeney P.J. Experimental and computational approaches to estimate solubility and permeability in drug discovery and development settings. *Adv. Drug Deliv. Rev* **46**, 3-26 (2001).
110. Gill A.L, Frederickson M, Cleasby A, Woodhead S.J, Carr M.G, Woodhead A.J, Walker M.T, Congreve M.S, Devine L.A, Tisi D, O'Reilly M, Seavers L.C, Davis D.J, Curry J, Anthony R, Padova A, Murray C.W, Carr R.A. & Jhoti H. Identification of novel p38alpha MAP kinase inhibitors using fragment-based lead generation. *J. Med. Chem* **48**, 414-426 (2005).
111. Battye T.G.G, Kontogiannis L, Johnson O, Powell H.R. & Leslie A.G.W. iMOSFLM: A new graphical interface for diffraction-image processing with MOSFLM. *Acta Crystallographica Section D: Biol, Crystallogr.* **67**, 271-281 (2011).
112. Otwinowski Z. & Minor W. Processing of X-ray diffraction data collected in oscillation mode. *Methods in Enzymology* **276**, 307-326 (1997).
113. The CCP4 suite: programs for protein crystallography. *Acta Crystallogr. D Biol. Crystallogr* **50**, 760-763 (1994).
114. Vagin A. & Teplyakov A. MOLREP: an Automated Program for Molecular Replacement. *J. Appl. Cryst.* **30**, 1022-1025 (1997).
115. Emsley P, Lohkamp B, Scott W.G. & Cowtan K. Features and development of Coot. *Acta Crystallogr. D Biol. Crystallogr* **66**, 486-501 (2010).
116. Murshudov G.N, Vagin A.A. & Dodson E.J. Refinement of macromolecular structures by the maximum-likelihood method. *Acta Crystallogr. D Biol. Crystallogr* **53**, 240-255 (1997).
117. Orrell R.W, Habgood J.J, Malaspina A, Mitchell J, Greenwood J, Lane R.J. & deBelleroche J.S. Clinical characteristics of SOD1 gene mutations in UK families with ALS. *J. Neurol. Sci* **169**, 56-60 (1999).
118. Jones C.T, Swingler R.J, Simpson S.A. & Brock D.J. Superoxide dismutase mutations in an unselected cohort of Scottish amyotrophic lateral sclerosis patients. *J. Med. Genet.* **32**, 290-292 (1995).
119. Orrell R.W, King A.W, Hilton D.A, Campbell M.J, Lane R.J. & de Belleroche J.S. Familial amyotrophic lateral sclerosis with a point mutation of SOD-1: intrafamilial heterogeneity of disease duration associated with neurofibrillary tangles. *J. Neurol. Neurosurg. Psychiatr.* **59**, 266-270 (1995).
120. Lopate G, Baloh R.H, Al-Lozi M.T, Miller T.M, Fernandes Filho J.A, Ni O, Leston A, Florence J, Schierbecker J. & Allred P. Familial ALS with extreme phenotypic variability due to the I113T SOD1 mutation. *Amyotroph. Lateral. Scler.* **11**, 232-236 (2010).
121. Suthers G, Laing N, Wilton S, Dorosz S. & Waddy H. “Sporadic” motoneuron disease due to familial SOD1 mutation with low penetrance. *Lancet* **344**, 1773 (1994).
122. Antonyuk S, Strange R.W. & Hasnain S.S. Structural discovery of small molecule binding sites in Cu-Zn human superoxide dismutase familial amyotrophic lateral sclerosis mutants provides insights for lead optimization. *J. Med. Chem.* **53**, 1402-1406 (2010).

123. Strange R.W, Antonyuk S.V, Hough M.A, Doucette P.A, Valentine J.S. & Hasnain S.S. Variable metallation of human superoxide dismutase: atomic resolution crystal structures of Cu-Zn, Zn-Zn and as-isolated wild-type enzymes. *J. Mol. Biol.* **356**, 1152-1162 (2006).
124. Eisenberg D, Schwarz E, Komaromy M. & Wall R. Analysis of membrane and surface protein sequences with the hydrophobic moment plot. *J. Mol. Biol.* **179**, 125-142 (1984).
125. Jantová S, Greif G, Spirková K, Stankovský S. & Oravcová M. Antibacterial effects of trisubstituted quinazoline derivatives. *Folia Microbiol. (Praha)* **45**, 133-137 (2000).
126. Castera-Ducros C, Azas N, Verhaeghe P, Hutter S, Garrigue P, Dumètre A, Mbatchi L, Laget M, Remusat V, Sifredi F, Rault S, Rathelot P. & Vanelle P. Targeting the human malaria parasite Plasmodium falciparum: In vitro identification of a new antiplasmodial hit in 4-phenoxy-2-trichloromethylquinazoline series. *Eur. J. Med. Chem.* **46**, 4184-4191 (2011).
127. Partin J.V, Anglin I.E. & Kyprianou N. Quinazoline-based alpha 1-adrenoceptor antagonists induce prostate cancer cell apoptosis via TGF-beta signalling and I kappa B alpha induction. *Br. J. Cancer* **88**, 1615-1621 (2003).
128. Rioja I, Terencio M.C, Ubeda A, Molina P, Tárraga A, Gonzalez-Tejero A. & Alcaraz M.J. A pyrroloquinazoline derivative with anti-inflammatory and analgesic activity by dual inhibition of cyclo-oxygenase-2 and 5-lipoxygenase. *Eur. J. Pharmacol.* **434**, 177-185 (2002).
129. Longley D.B, Harkin D.P. & Johnston P.G. 5-fluorouracil: mechanisms of action and clinical strategies. *Nat. Rev. Cancer* **3**, 330-338 (2003).
130. Nowak R.J, Cuny G.D, Choi S, Lansbury P.T. & Ray S.S. Improving binding specificity of pharmacological chaperones that target mutant superoxide dismutase-1 linked to familial amyotrophic lateral sclerosis using computational methods. *J. Med. Chem.* **53**, 2709-2718 (2010).
131. Ray S.S, Nowak R.J, Brown R.H. & Lansbury P.T. Small-molecule-mediated stabilization of familial amyotrophic lateral sclerosis-linked superoxide dismutase mutants against unfolding and aggregation. *Proc. Natl. Acad. Sci. U.S.A* **102**, 3639-3644 (2005).
132. Joint Formulary Committee *British National Formulary*. (BMJ Group and Pharmaceutical Press: 2011).
133. Stolley P.D. & Schinnar R. Association between asthma mortality and isoproterenol aerosols: a review. *Prev. Med.* **7**, 519-538 (1978).
134. Liang Y, Liu D, Ochs T, Tang C, Chen S, Zhang S, Geng B, Jin H. & Du J. Endogenous sulfur dioxide protects against isoproterenol-induced myocardial injury and increases myocardial antioxidant capacity in rats. *Lab. Invest.* **91**, 12-23 (2010).
135. Purves D. *Neuroscience*. (Sinauer Associates, Inc.: 2004).
136. National Asthma Education and Prevention Program. Expert Panel Report: Guidelines for the Diagnosis and Management of Asthma Update on Selected Topics--2002. *J. Allergy Clin. Immunol.* **110**, S141-219 (2002).
137. Hartling L, Bialy L.M, Vandermeer B, Tjosvold L, Johnson D.W, Plint A.C, Klassen T.P, Patel H. & Fernandes R.M. Epinephrine for bronchiolitis. *Cochrane Database Syst. Rev.* **5** (2011).
138. Keet C. Recognition and management of food-induced anaphylaxis. *Pediatr. Clin. North Am.* **58**, 377-388, x (2011).
139. Temiño V.M. & Peeble, R.S. Jr. The spectrum and treatment of angioedema. *Am. J. Med.* **121**, 282-286 (2008).

140. Williams G.V. & Castner S.A. Under the curve: critical issues for elucidating D1 receptor function in working memory. *Neuroscience* **139**, 263-276 (2006).
141. Contreras F, Fouillioux C, Bolívar A, Simonovis N, Hernández-Hernández R, Armas-Hernandez M.J. & Velasco M. Dopamine, hypertension and obesity. *J. Hum. Hypertens.* **16 Suppl 1**, S13-17 (2002).
142. Faraone S.V. & Khan S.A. Candidate gene studies of attention-deficit/hyperactivity disorder. *J. Clin. Psychiatry* **67 Suppl 8**, 13-20 (2006).
143. Heinz A. & Schlagenhauf F. Dopaminergic dysfunction in schizophrenia: salience attribution revisited. *Schizophr. Bull.* **36**, 472-485 (2010).
144. Kranzler H.R. & Edenberg H.J. Pharmacogenetics of alcohol and alcohol dependence treatment. *Curr. Pharm. Des.* **16**, 2141-2148 (2010).
145. Leong S.L, Cappai R, Barnham K.J. & Pham C.L.L. Modulation of alpha-synuclein aggregation by dopamine: a review. *Neurochem. Res.* **34**, 1838-1846 (2009).
146. Bruijn L.I, Becher M.W, Lee M.K, Anderson K.L, Jenkins N.A, Copeland N.G, Sisodia S.S, Rothstein J.D, Borchelt D.R, Price D.L. & Cleveland D.W. ALS-linked SOD1 mutant G85R mediates damage to astrocytes and promotes rapidly progressive disease with SOD1-containing inclusions. *Neuron* **18**, 327-338 (1997).
147. Rosen D.R, Bowling A.C, Patterson D, Usdin T.B, Sapp P, Mezey E, McKenna-Yasek D, O'Regan J, Rahmani Z, Ferrante R.J, Brownstein M.J, Kowall N.W, Beal M.F, Horvitz H.R. & Brown R.H. Jr. A frequent ala 4 to val superoxide dismutase-1 mutation is associated with a rapidly progressive familial amyotrophic lateral sclerosis. *Hum. Mol. Genet.* **3**, 981-987 (1994).
148. Cardoso R.M, Thayer M.M, DiDonato M, Lo T.P, Bruns C.K, Getzoff E.D. & Tainer J.A. Insights into Lou Gehrig's disease from the structure and instability of the A4V mutant of human Cu,Zn superoxide dismutase. *J. Mol. Biol.* **324**, 247-256 (2002).
149. Cordingley M.G, Callahan P.L, Sardana V.V, Garsky V.M. & Colonno R.J. Substrate requirements of human rhinovirus 3C protease for peptide cleavage in vitro. *J. Biol. Chem.* **265**, 9062-9065 (1990).
150. Graham D.G. Oxidative pathways for catecholamines in the genesis of neuromelanin and cytotoxic quinones. *Mol. Pharmacol.* **14**, 633-643 (1978).
151. Ray S.S. & Lansbury P.T. A possible therapeutic target for Lou Gehrig's disease. *Proc. Natl. Acad. Sci. U.S.A* **101**, 5701-5702 (2004).
152. Saraiva M.J, Birken S, Costa P.P. & Goodman D.S. Amyloid fibril protein in familial amyloidotic polyneuropathy, Portuguese type. Definition of molecular abnormality in transthyretin (prealbumin). *J. Clin. Invest.* **74**, 104-119 (1984).
153. Damas A.M. & Saraiva M.J. Review: TTR amyloidosis-structural features leading to protein aggregation and their implications on therapeutic strategies. *J. Struct. Biol.* **130**, 290-299 (2000).
154. Sekijima Y, Dendle M.A. & Kelly J.W. Orally administered diflunisal stabilizes transthyretin against dissociation required for amyloidogenesis. *Amyloid* **13**, 236-249 (2006).
155. Furukawa, Y., Kaneko, K., Yamanaka, K. & Nukina, N. Mutation-dependent polymorphism of Cu,Zn-superoxide dismutase aggregates in the familial form of amyotrophic lateral sclerosis. *J. Biol. Chem.* **285**, 22221-22231 (2010).
156. Oliveberg, M. Waltz, an exciting new move in amyloid prediction. *Nat. Methods* **7**, 187-188 (2010).
157. Zhang H, Andrekopoulos C, Joseph J, Chandran K, Karoui H, Crow J.P. & Kalyanaraman B. Bicarbonate-dependent peroxidase activity of human Cu,Zn-superoxide dismutase induces covalent aggregation of protein: intermediacy of tryptophan-derived oxidation products. *J. Biol. Chem.* **278**, 24078-24089 (2003).

158. Zhang H, Joseph J, Crow J. & Kalyanaraman B. Mass spectral evidence for carbonate-anion-radical-induced posttranslational modification of tryptophan to kynurenine in human Cu, Zn superoxide dismutase. *Free Radic. Biol. Med.* **37**, 2018-2026 (2004).
159. Zhang H, Andrekopoulos C, Joseph J, Chandran K, Karoui H, Crow J.P. & Kalyanaraman B. Tryptophan 32 potentiates aggregation and cytotoxicity of a copper/zinc superoxide dismutase mutant associated with familial amyotrophic lateral sclerosis. *J. Biol. Chem.* **282**, 16329-16335 (2007).
160. Grad L.I, Guest W.C, Yanai A, Pokrishevsky E, O'Neill M.A, Gibbs E, Semenchenko V, Yousefi M, Wishart D.S, Plotkin S.S. & Cashman NR. Intermolecular transmission of superoxide dismutase 1 misfolding in living cells. *Proc. Natl. Acad. Sci. U.S.A* 108, 16398-16403 (2011).
161. Ladbury J.E, Klebe G. & Freire E. Adding calorimetric data to decision making in lead discovery: a hot tip. *Nat .Rev. Drug Discov.* **9**, 23-27 (2010).
162. Howard N, Abell C, Blakemore W, Chessari G, Congreve M, Howard S, Jhoti H, Murray C.W, Seavers L.C. & van Montfort RL. Application of fragment screening and fragment linking to the discovery of novel thrombin inhibitors. *J. Med. Chem.* **49**, 1346-1355 (2006).
163. Benmohamed R, Arvanites A.C, Kim J, Ferrante R.J, Silverman R.B, Morimoto R.I. & Kirsch DR. Identification of compounds protective against G93A-SOD1 toxicity for the treatment of amyotrophic lateral sclerosis. *Amyotroph. Lateral Scler.* **12**, 87-96 (2011).
164. Yoo Y.E. & Ko C.P. Treatment with trichostatin A initiated after disease onset delays disease progression and increases survival in a mouse model of amyotrophic lateral sclerosis. *Exp. Neurol.* **231**, 147-159 (2011).
165. Crichton R.R. & Pierre J.L. Old iron, young copper: from Mars to Venus. *Biometals* **14**, 99-112 (2001).
166. Andreini C, Banci L, Bertini I. & Rosato A. Occurrence of copper proteins through the three domains of life: a bioinformatic approach. *J. Proteome Res.* **7**, 209-216 (2008).
167. Gaetke L.M. & Chow C.K. Copper toxicity, oxidative stress, and antioxidant nutrients. *Toxicology* **189**, 147-163 (2003).
168. Rae T.D, Schmidt P.J, Pufahl R.A, Culotta V.C. & O'Halloran T.V. Undetectable intracellular free copper: the requirement of a copper chaperone for superoxide dismutase. *Science* **284**, 805-808 (1999).
169. O'Halloran T.V. & Culotta V.C. Metallochaperones, an intracellular shuttle service for metal ions. *J. Biol. Chem* **275**, 25057-25060 (2000).
170. Zhou B. & Gitschier J. hCTR1: a human gene for copper uptake identified by complementation in yeast. *Proc. Natl. Acad. Sci. U.S.A* **94**, 7481-7486 (1997).
171. Banci L, Bertini I, Ciofi-Baffoni S, Kozyreva T, Zovo K. & Palumaa P. Affinity gradients drive copper to cellular destinations. *Nature* **465**, 645-648 (2010).
172. Lee J, Peña M.M.O, Nose Y. & Thiele D.J. Biochemical characterization of the human copper transporter Ctr1. *J. Biol. Chem.* **277**, 4380-4387 (2002).
173. De Feo C.J, Aller S.G, Siluvai G.S, Blackburn N.J. & Unger V.M. Three-dimensional structure of the human copper transporter hCTR1. *Proc. Natl. Acad. Sci. U.S.A* **106**, 4237-4242 (2009).
174. Eisses J.F. & Kaplan J.H. Molecular characterization of hCTR1, the human copper uptake protein. *J. Biol. Chem* **277**, 29162-29171 (2002).
175. Xiao Z. & Wedd A.G. A C-terminal domain of the membrane copper pump Ctr1 exchanges copper(I) with the copper chaperone Atx1. *Chem. Commun. (Camb.)* 588-

589 (2002).
176. Huffman D.L. & O'Halloran T.V. Energetics of copper trafficking between the Atx1 metallochaperone and the intracellular copper transporter, Ccc2. *J. Biol. Chem.* **275**, 18611-18614 (2000).
177. Banci L, Bertini I, Cantini F, Felli I.C, Gonnelli L, Hadjiliadis N, Pierattelli R, Rosato A. & Voulgaris P. The Atx1-Ccc2 complex is a metal-mediated protein-protein interaction. *Nat. Chem. Biol.* **2**, 367-368 (2006).
178. Cobine P.A, Pierrel F. & Winge D.R. Copper trafficking to the mitochondrion and assembly of copper metalloenzymes. *Biochim. Biophys. Acta* **1763**, 759-772 (2006).
179. Henikoff S. & Henikoff J.G. Amino acid substitution matrices from protein blocks. *Proc. Natl. Acad. Sci. U.S.A* **89**, 10915-10919 (1992).
180. Okado-Matsumoto A. & Fridovich I. Subcellular distribution of superoxide dismutases (SOD) in rat liver: Cu,Zn-SOD in mitochondria. *J. Biol. Chem.* **276**, 38388-38393 (2001).
181. Kawamata H. & Manfredi G. Import, Maturation, and Function of SOD1 and Its Copper Chaperone CCS in the Mitochondrial Intermembrane Space. *Antioxid. Redox Signal.* **13**, 1375-1384 (2010).
182. Culotta V.C, Klomp L.W, Strain J, Casareno R.L, Krems B. & Gitlin J.D. The copper chaperone for superoxide dismutase. *J. Biol. Chem* **272**, 23469-23472 (1997).
183. Casareno R.L, Waggoner D. & Gitlin J.D. The copper chaperone CCS directly interacts with copper/zinc superoxide dismutase. *J. Biol. Chem.* **273**, 23625-23628 (1998).
184. Yamaguchi Y, Heiny M.E. & Gitlin J.D. Isolation and characterization of a human liver cDNA as a candidate gene for Wilson disease. *Biochem. Biophys. Res. Commun.* **197**, 271-277 (1993).
185. Klomp L.W, Lin S.J, Yuan D.S, Klausner R.D, Culotta V.C. & Gitlin J.D. Identification and functional expression of HAH1, a novel human gene involved in copper homeostasis. *J. Biol. Chem.* **272**, 9221-9226 (1997).
186. Chelly J, Tümer Z, Tønnesen T, Petterson A, Ishikawa-Brush Y, Tommerup N, Horn N. & Monaco A.P. Isolation of a candidate gene for Menkes disease that encodes a potential heavy metal binding protein. *Nat. Genet.* **3**, 14-19 (1993).
187. Anastassopoulou I, Banci L, Bertini I, Cantini F, Katsari E. & Rosato A. Solution structure of the apo and copper(I)-loaded human metallochaperone HAH1. *Biochemistry* **43**, 13046-13053 (2004).
188. Arnesano F, Banci L, Bertini I, Huffman D.L. & O'Halloran T.V. Solution structure of the Cu(I) and apo forms of the yeast metallochaperone, Atx1. *Biochemistry* **40**, 1528-1539 (2001).
189. Leech H.K, Raux E, McLean K.J, Munro A.W, Robinson N.J, Borrelly G.P, Malten M, Jahn D, Rigby S.E, Heathcote P. & Warren MJ. Characterization of the cobaltochelatase CbiXL: evidence for a 4Fe-4S center housed within an MXCXXC motif. *J. Biol. Chem.* **278**, 41900-41907 (2003).
190. Rousselot-Pailley P, Sénèque O, Lebrun C, Crouzy S, Boturyn D, Dumy P, Ferrand M. & Delangle P. Model peptides based on the binding loop of the copper metallochaperone Atx1: selectivity of the consensus sequence MxCxxC for metal ions Hg(II), Cu(I), Cd(II), Pb(II), and Zn(II). *Inorg Chem* **45**, 5510-5520 (2006).
191. Schmidt P.J, Rae T.D, Pufahl R.A, Hamma T, Strain J, O'Halloran T.V. & Culotta V.C. Multiple protein domains contribute to the action of the copper chaperone for superoxide dismutase. *J. Biol. Chem* **274**, 23719-23725 (1999).
192. Caruano-Yzermans A.L, Bartnikas T.B. & Gitlin J.D. Mechanisms of the copper-dependent turnover of the copper chaperone for superoxide dismutase. *J. Biol. Chem*

**281**, 13581-13587 (2006).
193. Wright G.S.A, Hasnain S.S. & Grossmann J.G. The structural plasticity of the human copper chaperone for SOD1: insights from combined size-exclusion chromatographic and solution X-ray scattering studies. *Biochem. J.* **439**, 39-44 (2011).
194. Schmidt P.J, Ramos-Gomez M. & Culotta V.C. A gain of superoxide dismutase (SOD) activity obtained with CCS, the copper metallochaperone for SOD1. *J. Biol. Chem.* **274**, 36952-36956 (1999).
195. Lamb A.L, Wernimont A.K, Pufahl R.A, O'Halloran T.V. & Rosenzweig A.C. Crystal structure of the second domain of the human copper chaperone for superoxide dismutase. *Biochemistry* **39**, 1589-95 (2000).
196. Stasser J.P, Eisses J.F, Barry A.N, Kaplan J.H. & Blackburn N.J. Cysteine-to-serine mutants of the human copper chaperone for superoxide dismutase reveal a copper cluster at a domain III dimer interface. *Biochemistry* **44**, 3143-3152 (2005).
197. Eisses J.F, Stasser J.P, Ralle M, Kaplan J.H. & Blackburn N.J. Domains I and III of the human copper chaperone for superoxide dismutase interact via a cysteine-bridged Dicopper(I) cluster. *Biochemistry* **39**, 7337-7342 (2000).
198. Brown N.M, Torres A.S, Doan P.E. & O'Halloran T.V. Oxygen and the copper chaperone CCS regulate posttranslational activation of Cu,Zn superoxide dismutase. *Proc. Natl. Acad. Sci. U.S.A* **101**, 5518-5523 (2004).
199. Lamb A.L, Torres A.S, O'Halloran T.V. & Rosenzweig A.C. Heterodimeric structure of superoxide dismutase in complex with its metallochaperone. *Nat. Struct. Biol.* **8**, 751-755 (2001).
200. Pike R. & Sabatier P. Scattering: Scattering and inverse scattering in pure and applied science. Academic Press (2002).
201. Debye P. Scattering from non-crystalline substances. *Ann. Phys.* **46**, 809-823 (1915).
202. Svergun D.I. & Koch M.H.J. Small-angle scattering studies of biological macromolecules in solution. *Reports on Progress in Physics* **66**, 1735-1782 (2003).
203. Svergun D.I, Petoukhov M.V. & Koch M.H. Determination of domain structure of proteins from X-ray solution scattering. *Biophys. J* **80**, 2946-2953 (2001).
204. Petoukhov M.V. & Svergun D.I. Global Rigid Body Modeling of Macromolecular Complexes against Small-Angle Scattering Data. *Biophys. J.* **89**, 1237-1250 (2005).
205. Studier F.W, Rosenberg A.H, Dunn J.J. & Dubendorff J.W. Use of T7 RNA polymerase to direct expression of cloned genes. *Methods Enzymol.* **185**, 60-89 (1990).
206. Van Dyke M.W, Sirito M. & Sawadogo M. Single-step purification of bacterially expressed polypeptides containing an oligo-histidine domain. *Gene* **111**, 99-104 (1992).
207. Carrington J.C. & Dougherty W.G. A viral cleavage site cassette: identification of amino acid sequences required for tobacco etch virus polyprotein processing. *Proc. Natl. Acad. Sci. U.S.A.* **85**, 3391-5 (1988).
208. Winkler D.D, Schuermann J.P, Cao X, Holloway S.P, Borchelt D.R, Carroll M.C, Proescher J.B, Culotta V.C. & Hart PJ. Structural and biophysical properties of the pathogenic SOD1 variant H46R/H48Q. *Biochemistry* **48**, 3436-3447 (2009).
209. Rae T.D, Torres A.S, Pufahl R.A. & O'Halloran T.V. Mechanism of Cu,Zn-superoxide dismutase activation by the human metallochaperone hCCS. *J. Biol. Chem.* **276**, 5166-5176 (2001).
210. Lamb A.L, Wernimont A.K, Pufahl R.A, Culotta V.C, O'Halloran T.V. & Rosenzweig A.C. Crystal structure of the copper chaperone for superoxide dismutase. *Nat. Struct. Mol. Biol.* **6**, 724-729 (1999).
211. David G. & Perez J. Combined sampler robot and high-performance liquid

chromatography: a fully automated system for biological small-angle X-ray scattering experiments at the Synchrotron SOLEIL SWING beamline. *J. Appl. Cryst.* **42**, 892-900 (2009).
212. Yonga C.W, Glabb J, Strange R.W, Smitha W, Hasnain S.S. & Grossmann J.G. Assessment of long-term molecular dynamics calculations with experimental information on protein shape from X-ray scattering - SOD1 as a case study. *Chemical Physics Letters* **481**, 112-117 (2009).
213. Kayatekin C, Zitzewitz J.A. & Matthews C.R. Disulfide-reduced ALS variants of Cu, Zn superoxide dismutase exhibit increased populations of unfolded species. *J. Mol. Biol.* **398**, 320-331 (2010).
214. Ip P, Mulligan V.K. & Chakrabartty A. ALS-causing SOD1 mutations promote production of copper-deficient misfolded species. *J. Mol. Biol.* **409**, 839-852 (2011).
215. Lamb A.L, Torres A.S, O'Halloran T.V. & Rosenzweig A.C. Heterodimer formation between superoxide dismutase and its copper chaperone. *Biochemistry* **39**, 14720-14727 (2000).
216. Seetharaman S.V, Winkler D.D, Taylor A.B, Cao X, Whitson L.J, Doucette P.A, Valentine J.S, Schirf V, Demeler B, Carroll M.C, Culotta V.C. & Hart PJ. Disrupted zinc-binding sites in structures of pathogenic SOD1 variants D124V and H80R. *Biochemistry* **49**, 5714-5725 (2010).
217. Mathew E, Mirza A. & Menhart N. Liquid-chromatography-coupled SAXS for accurate sizing of aggregating proteins. *J. Synchrotron Rad.* **11**, 314-318 (2004).
218. Watanabe Y. & Inoko Y. Size-exclusion chromatography combined with small-angle X-ray scattering optics. *Journal of Chromatography A* **1216**, 7461-7465 (2009).
219. Smolsky I.L, Liu P, Niebuhr M, Ito K, Weiss T.M. & Tsuruta H. Biological small-angle X-ray scattering facility at the Stanford Synchrotron Radiation Laboratory. *J. Appl. Cryst.* **40**, s453-s458 (2007).
220. Fujisawa T, Inoue K, Oka T, Iwamoto H, Uruga T, Kumasaka T, Inoko Y, Yagi N, Yamamoto M & Ueki T. Small-angle x-ray scattering station at the SPring-8 RIKEN beamline. *J. Appl. Cryst.* **33**, 797-800 (2000).
221. Leitch J.M, Yick P.J. & Culotta V.L. The right to choose: Multiple pathways for activating Cu/Zn superoxide dismutase. *J. Biol. Chem.* **284**, 24679-24683.
222. Schmidt P.J, Kunst C. & Culotta V.C. Copper activation of superoxide dismutase 1 (SOD1) in vivo. Role for protein-protein interactions with the copper chaperone for SOD1. *J. Biol. Chem.* **275**, 33771-33776 (2000).
223. Vassall K.A, Stubbs H.R, Primmer H.A, Tong M.S, Sullivan S.M, Sobering R, Srinivasan S, Briere L.A, Dunn S.D, Colón W. & Meiering E.M. Decreased stability and increased formation of soluble aggregates by immature superoxide dismutase do not account for disease severity in ALS. *Proc. Natl. Acad. Sci. U.S.A* **108**, 2210-2215 (2011).
224. Furukawa Y. & O'Halloran T.V. Amyotrophic lateral sclerosis mutations have the greatest destabilizing effect on the apo- and reduced form of SOD1, leading to unfolding and oxidative aggregation. *J. Biol. Chem.* **280**, 17266-17274 (2005).
225. Furukawa Y, Kaneko K, Yamanaka K, O'Halloran T.V. & Nukina N. Complete Loss of Post-translational Modifications Triggers Fibrillar Aggregation of SOD1 in the Familial Form of Amyotrophic Lateral Sclerosis. *J. Biol. Chem.* **283**, 24167-24176 (2008).
226. Corson L.B, Strain J.J, Culotta V.C. & Cleveland D.W. Chaperone-facilitated copper binding is a property common to several classes of familial amyotrophic lateral sclerosis-linked superoxide dismutase mutants. *Proc. Natl. Acad. Sci. U.S.A* **95**, 6361-6366 (1998).

227. Karch C.M, Prudencio M, Winkler D.D, Hart P.J. & Borchelt D.R. Role of mutant SOD1 disulfide oxidation and aggregation in the pathogenesis of familial ALS. *Proc. Natl. Acad. Sci. U.S.A* **106**, 7774-7779 (2009).
228. Jonsson P.A, Graffmo K.S, Andersen P.M, Brännström T, Lindberg M, Oliveberg M. & Marklund S.L. Disulphide-reduced superoxide dismutase-1 in CNS of transgenic amyotrophic lateral sclerosis models. *Brain* **129**, 451-464 (2006).
229. Leitch J.M, Jensen L.T, Bouldin S.D, Outten C.E, Hart P.J. & Culotta V.C. Activation of Cu/Zn superoxide dismutase in the absence of oxygen and the copper chaperone CCS. *J. Biol. Chem.* (2009).doi:10.1074/jbc.M109.000489
230. Seetharaman S.V, Prudencio M, Karch C, Holloway S.P, Borchelt D.R. & Hart P.J. Immature copper-zinc superoxide dismutase and familial amyotrophic lateral sclerosis. *Exp. Biol. Med.* **234**, 1140-1154 (2009).
231. Kabsch W. Integration, scaling, space-group assignment and post-refinement. *Acta Crystallogr. D Biol. Crystallogr.* **66**, 133-144 (2010).
232. Emsley P. & Cowtan K. Coot: model-building tools for molecular graphics. *Acta Crystallogr. D Biol. Crystallogr* **60**, 2126-2132 (2004).
233. McCord J.M. & Fridovich I. Superoxide dismutase. An enzymic function for erythrocuprein (hemocuprein). *J. Biol. Chem.* **244**, 6049-6055 (1969).
234. Konarev P.V, Volkov V.V, Sokolova A.V, Koch M.H.J. & Svergun D.I. PRIMUS: a Windows PC-based system for small-angle scattering data analysis. *J. Appl. Cryst.* **36**, 1277-1282 (2003).
235. Svergun D.I. Determination of the regularization parameter in indirect-transform methods using perceptual criteria. *J. Appl. Cryst.* **25**, 495-503 (1992).
236. Volkov V. & Svergun D. Uniqueness of ab initio shape determination in small-angle scattering. *J. Appl. Cryst.* **36**, 860-864 (2003).
237. The PyMOL Molecular Graphics System. (Schrödinger, LLC).
238. Roy A, Kucukural A. & Zhang Y. I-TASSER: a unified platform for automated protein structure and function prediction. *Nat. Protoc.* **5**, 725-738 (2010).
239. Maupetit J, Gautier R. & Tufféry P. SABBAC: online Structural Alphabet-based protein BackBone reconstruction from Alpha-Carbon trace. *Nucleic Acids Res.* **34**, W147-151 (2006).
240. Svergun D, Barberato C. & Koch M. CRYSOL - a Program to Evaluate X-ray Solution Scattering of Biological Macromolecules from Atomic Coordinates. *J. Appl. Cryst.* **28**, 768-773

# Appendices

## Appendix I – Summary of Oligonucleotides

| Name | Restriction Site | Sequence |
|---|---|---|
| SOD1Fwd | XbaI | 5'-TCTAGAATGGCGACGAAGGCC-3' |
| SOD1Rev | XhoI | 5'-CTCGAGTCAAAGGTGGGCAGGGGGC-3' |
| L38V | N/A | 5'-TGTGGGGAAGCATTAAAGGAGTGACTGAAGGCCT-3' |
| L38V-AS | N/A | 5'-AGGCCTTCAGTCACTCCTTTAATGCTTCCCCACA-3' |
| I113T | N/A | 5'-TCTCAGGAGACCATTGCATCACTGGCCGCACAC-3' |
| I113T-AS | N/A | 5'-GTGTGCGGCCAGTGATGCAATGGTCTCCTGAGA-3' |
| A4V | N/A | 5'-CCGCGACGAAGGTCGTGTGCGTGCT-3' |
| A4V-AS | N/A | 5'-AGCACGCACACGACCTTCGTCGCGG-3' |
| hCCSFwd | NcoI | 5'-CCATGGCTTCGGATTCGGGGAAC-3' |
| hCCSRev | XhoI | 5'-CTCGAGTCAAAGGTGGGCAGGGGGC-3' |

## Appendix II – Summary of Plasmids

| Name | Source | Insert | Size (bp) | Resistance |
|---|---|---|---|---|
| pCR-Blunt | Invitrogen | N/A | 3512 | Kanamycin |
| pCR-hSOD1wt | N/A | Human wild-type SOD1 | 3985 | Kanamycin |
| pETM-11 | EMBL | N/A | 5400 | Kanamycin |
| pGEX6P1 | GE Healthcare | N/A | 4984 | Ampicillin |
| pET303 | Invitrogen | N/A | 5369 | Ampicillin |
| pET303-hSOD1wt | N/A | Human wild-type SOD1 | 5828 | Ampicillin |
| pET303-hSOD1 L38V | N/A | hSOD1 with L38V mutation | 5828 | Ampicillin |
| pET303-hSOD1 I113T | N/A | hSOD1 with I113T mutation | 5828 | Ampicillin |
| pETM11-hCCS | N/A | Human wild-type CCS | 6137 | Kanamycin |
| pGEX6-hSOD1 A4V | N/A | hSOD1 with A4V mutation | 5428 | Ampicillin |

## Appendix III – *E. coli* Strains

| Name | Supplier | Genotype |
|---|---|---|
| Omnimax 2 | Invitrogen | F {proAB+ lacIq lacZΔM15 Tn10(TetR) Δ(ccdAB)} mcrA Δ(mrr-hsdRMS-mcrBC) φ80(lacZ)ΔM15 Δ(lacZYA-argF) U169 endA1 recA1 supE44 thi-1 gyrA96 relA1 tonA panD |
| BL21 (DE3) | Novagen | F– ompT hsdSB(rB- mB-) dcm gal λ(DE3) |

## Appendix IV – Compounds

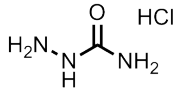

**1**

Chemical Formula: $CH_6ClN_3O$
Exact Mass: 111.02

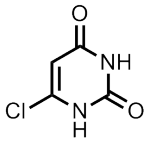

**2**

Chemical Formula: $C_4H_3ClN_2O_2$
Exact Mass: 145.99

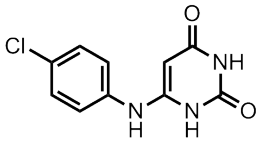

**3**

Chemical Formula: $C_{10}H_8ClN_3O_2$
Exact Mass: 237.03

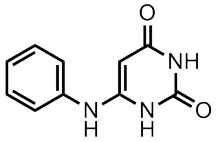

**4**

Chemical Formula: $C_{10}H_9N_3O_2$
Exact Mass: 203.07

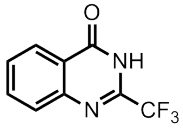

**5**

Chemical Formula: $C_9H_5F_3N_2O$
Exact Mass: 214.04

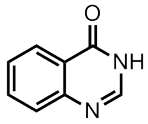

**6**

Chemical Formula: $C_8H_6N_2O$
Exact Mass: 146.05

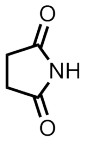

**7**

Chemical Formula: $C_4H_5NO_2$
Exact Mass: 99.03

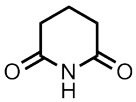

**8**

Chemical Formula: $C_5H_7NO_2$
Exact Mass: 113.05

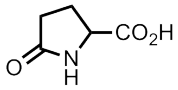

**9**

Chemical Formula: $C_5H_7NO_3$
Exact Mass: 129.04

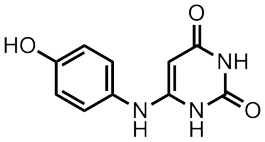

**10**

Chemical Formula: $C_{10}H_9N_3O_3$
Exact Mass: 219.06

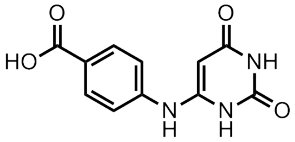

**11**

Chemical Formula: $C_{11}H_9N_3O_4$
Exact Mass: 247.06

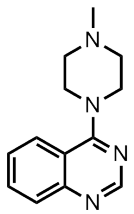

**12**

Chemical Formula: $C_{13}H_{16}N_4$
Exact Mass: 228.14

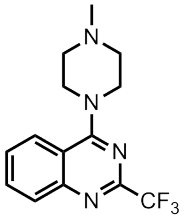

**13**

Chemical Formula: $C_{14}H_{15}F_3N_4$
Exact Mass: 296.12

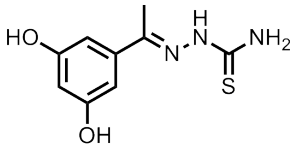

**14**

Chemical Formula: $C_9H_{11}N_3O_2S$
Exact Mass: 225.06

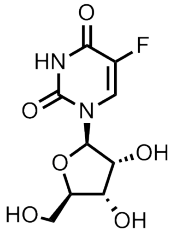

**15**

Chemical Formula: $C_9H_{11}FN_2O_6$
Exact Mass: 262.06

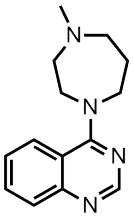

**16**

Chemical Formula: $C_{14}H_{18}N_4$
Exact Mass: 242.15

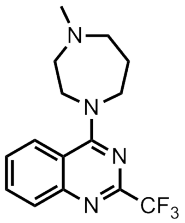

**17**

Chemical Formula: $C_{15}H_{17}F_3N_4$
Exact Mass: 310.14

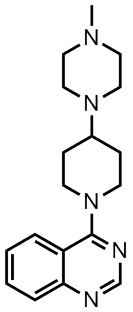

**18**

Chemical Formula: $C_{18}H_{25}N_5$
Exact Mass: 311.21

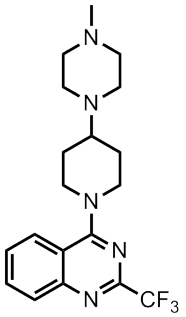

**19**

Chemical Formula:
$C_{19}H_{24}F_3N_5$
Exact Mass: 379.20

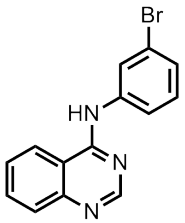

**20**

Chemical Formula: $C_{14}H_{10}BrN_3$
Exact Mass: 299.01

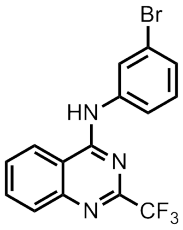

**21**

Chemical Formula: $C_{15}H_9BrF_3N_3$
Exact Mass: 366.99

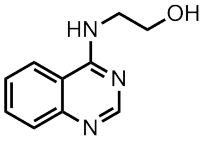

**22**

Chemical Formula:
$C_{10}H_{11}N_3O$
Exact Mass: 189.09

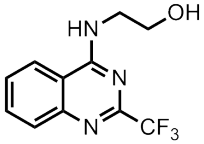

**23**

Chemical Formula: $C_{11}H_{10}F_3N_3O$
Exact Mass: 257.08

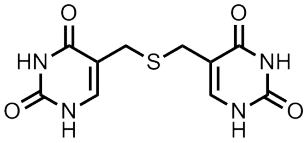

**24**

Chemical Formula: $C_{10}H_{10}N_4O_4S$
Exact Mass: 282.04

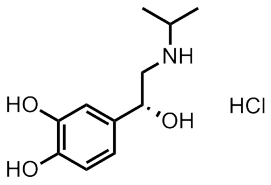

**25**

Chemical Formula: $C_{11}H_{18}ClNO_3$
Exact Mass: 247.10

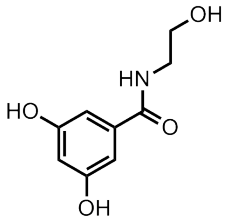

**26**

Chemical Formula: $C_9H_{11}NO_4$
Exact Mass: 197.07

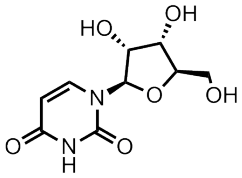

**27**

Chemical Formula: $C_9H_{12}N_2O_6$
Exact Mass: 244.07

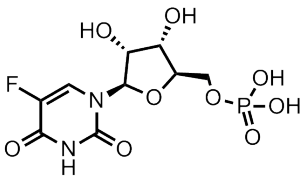

**28**

Chemical Formula: $C_9H_{12}FN_2O_9P$
Exact Mass: 342.03

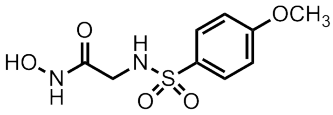

**29**

Chemical Formula: $C_9H_{12}N_2O_5S$
Exact Mass: 260.05

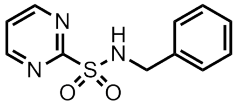

**30**

Chemical Formula: $C_{11}H_{11}N_3O_2S$
Exact Mass: 249.06

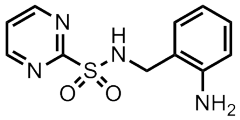

**31**

Chemical Formula: $C_{11}H_{12}N_4O_2S$
Exact Mass: 264.07

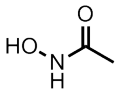

**32**

Chemical Formula: $C_2H_5NO_2$
Exact Mass: 75.03

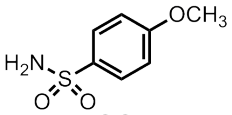

**33**

Chemical Formula: $C_7H_9NO_3S$
Exact Mass: 187.03

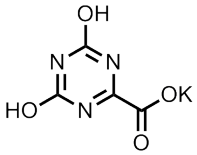

**34**

Chemical Formula: $C_4H_2KN_3O_4$
Exact Mass: 194.97

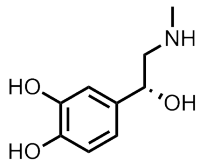

**35**

Chemical Formula: $C_9H_{13}NO_3$
Exact Mass: 183.09

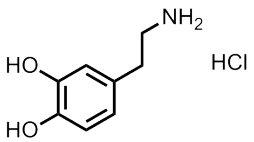

**36**

Chemical Formula: $C_8H_{12}ClNO_2$
Exact Mass: 189.06

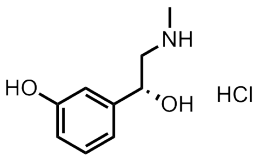

**37**

Chemical Formula: $C_9H_{14}ClNO_2$
Exact Mass: 203.07

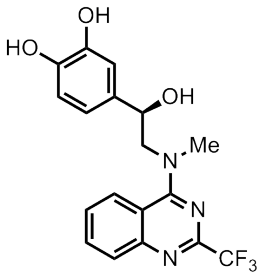

**38**

Chemical Formula: $C_{18}H_{16}F_3N_3O_3$
Exact Mass: 379.11

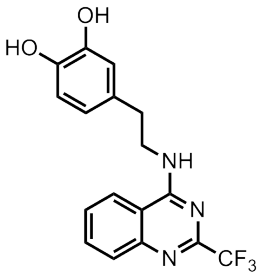

**39**

Chemical Formula: $C_{17}H_{14}F_3N_3O_2$
Exact Mass: 349.10

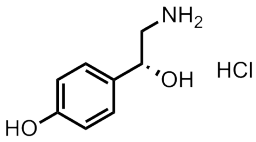

**40**

Chemical Formula: $C_8H_{12}ClNO_2$
Exact Mass: 189.06

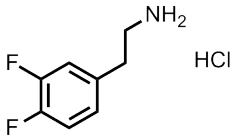

**41**

Chemical Formula: $C_8H_{10}ClF_2N$
Exact Mass: 193.05

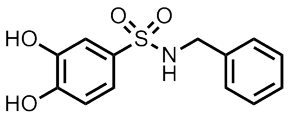

**42**

Chemical Formula: $C_{13}H_{13}NO_4S$
Exact Mass: 279.06

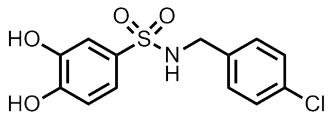

**43**

Chemical Formula: $C_{13}H_{12}ClNO_4S$
Exact Mass: 313.02